The Catalytic Decomposition of Nitrous Oxide

Thesis submitted in accordance with the requirement of Cardiff University for the degree of Doctor of Philosophy

Nia Richards

Graham J. Hutchings

Stanislaw E. Golunski

School of Chemistry

Cardiff University

2015 - 2019

Appendix 1 – Statements and declarations signed by the candidate and included in the thesis

STATEMENT 1

This thesis is being submitted in partial fulfilment of the requirements for the degree of PhD

Signed …… (candidate) Date ……

STATEMENT 2

This work has not been submitted in substance for any other degree or award at this or any other university or place of learning, nor is it being submitted concurrently for any other degree or award (outside of any formal collaboration agreement between the university and a partner organisation).

Signed …… (candidate) Date ……

STATEMENT 3

I hereby give consent for my thesis, if accepted, to be available online in the University's Open Access repository (or, where approved to be available in the University's library and for inter-library loan), and for the title and summary to be made available to outside organisations, subject to the expiry of a University-approved bar on access if applicable.

Signed …… (candidate) Date ……

DECLARATION

This thesis is the result of my own independent work, except where otherwise stated, and the views expressed are my own. Other sources are acknowledged by explicit references. The thesis has not been edited by a third party beyond what is permitted by Cardiff University's Use of Third Party Editors by Research Degree Students Procedure.

Signed …… (candidate) Date ……

Word Count ……

(Excluding summary, acknowledgments, declarations, contents pages, appendices, tables, diagrams and figures, references, bibliography, footnotes and endnotes)

Acknowledgements

Firstly I would like to thank my supervisors Graham Hutchings and Stan Golunski for giving me an opportunity to study a PhD and for their supervision and guidance throughout the entirety of my PhD. Secondly I would like to thank the rest of the "After the GoldRush" team, Nick Dummer, Ewa Nowicka, James Carter, Sam Pattisson and Rebecca Engel, whose day to day supervision was instrumental in keeping me focussed and on the path to completion, even when the end was nowhere near in sight.

There are a lot of people who have contributed greatly to this thesis, some of who are Dave Morgan whose expertise with XPS was greatly received, Qian He whose imaging knowledge and skills are way beyond me, and Greg Shaw forever coolheaded when what seemed like impending doom struck in the lab. Following on from that the entire workshop team, Steve, Alun, Lee and Julian, just Thank you!

I have thoroughly enjoyed my PhD, and that is mainly due to the people I have worked with along the way. Thank you to Luke, Parag, Meg, Eoin and Simon for putting up with me from day one. It wouldn't have been the same without you all. To everyone else in the office, thank you for making it feel like a second home, where no question was too stupid.

I would like to thank my family, they have no idea what I've done for the last three years other than 'catalysts' and go on holiday (apparently), but have supported me the whole way. Finally, to Ross, the biggest thank you for listening to me and helping me through the tough times.

Abstract

N_2O is an extremely potent greenhouse gas that has been shown to have devastating effects on the atmosphere. There are many natural and anthropogenic sources of N_2O emissions, such as oceans, atmospheric chemical reactions, industrial chemical processes, by-product from fuel combustion, and contributions from the agricultural sector. Therefore a catalyst that converts N_2O into N_2 and O_2 at low temperatures is highly desirable. Throughout this thesis the common aim is to produce a catalyst that can decompose N_2O at temperatures lower than 300 °C.

Three different classes of catalysts were investigated in this thesis, the first is a Fe-ZSM-5 catalyst. The work focusses on the effect of different Fe species in Fe-ZSM-5 for the decomposition of N_2O in the presence and absence of a reductant, propane. The effect of Si:Al ratio and Fe weight loading was initially investigated before focussing on a single weight loading and the effects of acid washing on catalyst activity and iron speciation.

The second class of catalysts were based on Pd-Al_2O_3 with the focus being on the importance of surface species and particle size of Pd for the decomposition of N_2O. The effect of removal of surface species such as water and chloride ions were investigated by different catalyst pre-treatments and support pre-treatments. Through pre-treatment of the catalyst support prior to metal deposition, catalytic activity significantly increased, resulting in a decrease of the T_{100} by 150 °C to 400 °C.

The third class of catalysts studied were a range of perovskite structured materials. Most notably studying how the surface area, phase purity and oxygen species present effected the catalytic activity. The factors were investigated by changing the ratio of elements in the A and B sites, which lead to increased perovskite purities requiring lower calcination temperatures leading to higher surface areas. The ratios that produced the highest phase purity were prepared by two alternative preparation method to the original citric acid preparation, supercritical anti-solvent preparation and oxalic acid preparation.

Publication List:

Investigating the Influence of Fe Speciation on N_2O Decomposition Over Fe–ZSM-5 Catalysts. N. Richards, E. Nowicka, J. H. Carter, D. J. Morgan, N. F. Dummer, S. Golunski and G. J. Hutchings, *Top. Catal.*, 2018, **61**, 1983–1992.

Submitted: Structure-sensitivity of alumina supported palladium catalysts for N_2O decomposition. N. Richards, J. H. Carter, E. Nowicka, L. A. Parker, S. Pattisson, Q. He, N. F. Dummer, S. Golunski and G. J. Hutchings. Applied Catalysis B: Environmental.

Abbreviations and Units

%	Percent
°C	Degrees Celsius
Å	Angstrom (10^{-10} metres)
a.u.	Arbitrary units
AW	Acid Washing
BET	Brunauer, Emmet and Teller
cm	Centimetre
CVI	Catalysts prepared by Chemical Vapour Impregnation
D	Support dried before catalyst preparation
DRIFTS	Diffuse Reflectance Infrared Fourier Transform Spectroscopy
eV	Electron Volts
FID	Flame ionisation detector
g	Gram
GC	Gas Chromatography
GHSV	Gas hourly space velocity
h	Hours
HAADF-STEM	High Angle Annular Dark-Field Scanning Transmission Electron Microscopy
ICP-OES	Inductively Coupled Plasma Optical Emission Spectroscopy
IR	InfraRed
M	Molar
MAS-NMR	Magic Angle Spin Nuclear Magnetic Resonance
MFC	Mass Flow Controllers
mg	Milligram (10^{-3} g)
min	Minutes
mL	Millilitre
mol	Moles
MP-AES	Microwave Plasma Atomic Emission Spectroscopy
MSI	Metal support interaction
nm	Nanometre (10^{-9} metres)
N_2O	Nitrous Oxide
PZC	Point of Zero Charge
SAS	Supercritical Anti-Solvent Preparation
SC	Support calcined before catalyst preparation

SEM	Scanning electron microscopy
Si/Al	Molar ratio of SiO_2 to Al_2O_3 in a zeolite
SMSI	Strong metal support interaction
SS	Stainless Steel
TCD	Thermal conductivity detector
TEM	Transmission electron microscopy
Temp	Temperature
TGA	Thermogravimetric analysis
TOF	Turnover frequency
TPR	Temperature programmed reduction
UV/Vis	Ultraviolet- Visible spectroscopy
v/v%	Volume by volume %
wt. %	Weight percent
XPS	X-ray photoelectron spectroscopy
XRD	X-ray diffraction
ZSM-5	Zeolite Socony Mobil–5

Table of Contents

1 Introduction

1.1 Introduction

A catalyst is described by Bond *et al.* as *a substance which increases the rate at which a chemical reaction approaches equilibrium, without being consumed in the process*. [1] When a catalyst is used in a reaction it is termed catalysis. The first noted use of catalysts in literature was by Berzelius in 1836 who noted the effect of trace substances on the rates of reactions. As defined by IUPAC, the catalyst is both a reactant and a product of the reaction. [2] The word catalysis comes from two Greek words, *cata-* meaning down and *lyesin* meaning to split or break. Catalysis or catalyst is commonly used in the popular press, but usually with the meaning to 'accelerate' usually referring to a sports team, this is the incorrect definition of the term catalysis and should not be thought of when using the term.

Catalysts do not change the thermodynamic equilibrium; they enable the rate of a reaction to be increased. Consequently, an increase in the rate coefficient is observed, whilst the Gibbs free energy remains the same. The laws of thermodynamics limit the change of the equilibrium position. Therefore, the initial and final states must remain unchanged. This allows the catalyst to provide a different pathway through which the reaction can proceed, of which the intermediate stages are different. When a catalyst is used there are usually a number of catalysed reaction intermediates, but the highest activation barrier of these states is still lower than that of the un-catalysed reaction. Therefore, catalysts offer an energetically favourable pathway, distinct to that of the un-catalysed reaction.[1]

There are three important characteristics of an effective catalyst: catalytic activity, product selectivity and stability. Catalytic activity is the level at which the reaction is promoted by the catalyst, *i.e.* the proficiency of the catalyst. This can be demonstrated by an increase in conversion of the starting reactant at a consistent temperature. The choice of catalyst can have a demonstrable influence in the formation of different final products in reactions with the same initial reagents.

Therefore, the ratio of these final products is termed selectivity. A catalyst that produces desirable products is termed a selective catalyst, a catalyst that produces undesirable products is termed an unselective catalyst. Finally, the stability of the catalyst relates to the length of time over which the catalyst is active for. The longer the time in which the catalyst is active without any change in activity, the more stable the catalyst. If a decrease in activity is noted after a short period of time, this is an unstable catalyst and has gone through a process of deactivation. Deactivation can occur through chemical, mechanical or thermal processes. Examples of chemically induced deactivation are described by "poisoning" through the chemisorption of species on the active site, or by "coking", which is the deposition of often strongly adsorbed carbonaceous material. When heat is applied to a catalyst, the metal species present can agglomerate, to form larger metal nanoparticles. The increase in particle size leads to a decrease in metal surface area available for reactions, this process is known as sintering. In some systems mechanical processes such as attrition or crushing lead to the loss of catalytic material, due to abrasion leading to a decreased in surface area. For example, in a FCC fluidised bed, attrition of the catalyst leads to a smoothed catalyst, and decreased surface area; [3,4] However, in some cases attrition leads to the formation of smaller particles and an increased surface area, but can lead to blockages as the finer powder blocks pores and channels.

There are two classes of catalysts: homogeneous and heterogeneous. [5] Homogenous catalysts are in the same state as the reactants, therefore, if the reactants are liquid phase the catalyst will also be in the liquid phase. Heterogeneous catalysts are in a different phase to the reactants, for example a solid catalyst used in a gas phase reaction. In these cases, the catalyst is easily recoverable after a reaction has taken place. One of the first industrial uses of a heterogeneous catalyst was in the Haber process, which produces ammonia from nitrogen and hydrogen. This was implemented in Germany just before the First World War as a way of securing the supply of fertilizer that had previously been imported from South America (along with speculation that ammonia was produced for explosives). The application of this technology is now used worldwide with little change to the original Fe catalyst. A final class of catalyst that will not be discussed further than this mention is enzymes; these do not fit into either of the classes

above and are biocatalysts. [6] In this thesis all reactions are heterogeneous with gas phase reactants and a solid catalyst.

A heterogeneous catalysed gas phase reaction using a solid catalyst normally consists of five steps as shown in Fig. 1.1. They are:

1) Diffusion of reactants from the reaction mixture to the catalyst surface.
2) Adsorption of reactants at the active site on the surface of the catalyst.
3) Reaction takes place on the surface, breaking and formation of new bonds.
4) Desorption of products from surface.
5) Finally, the products diffuse into the reaction mixture.

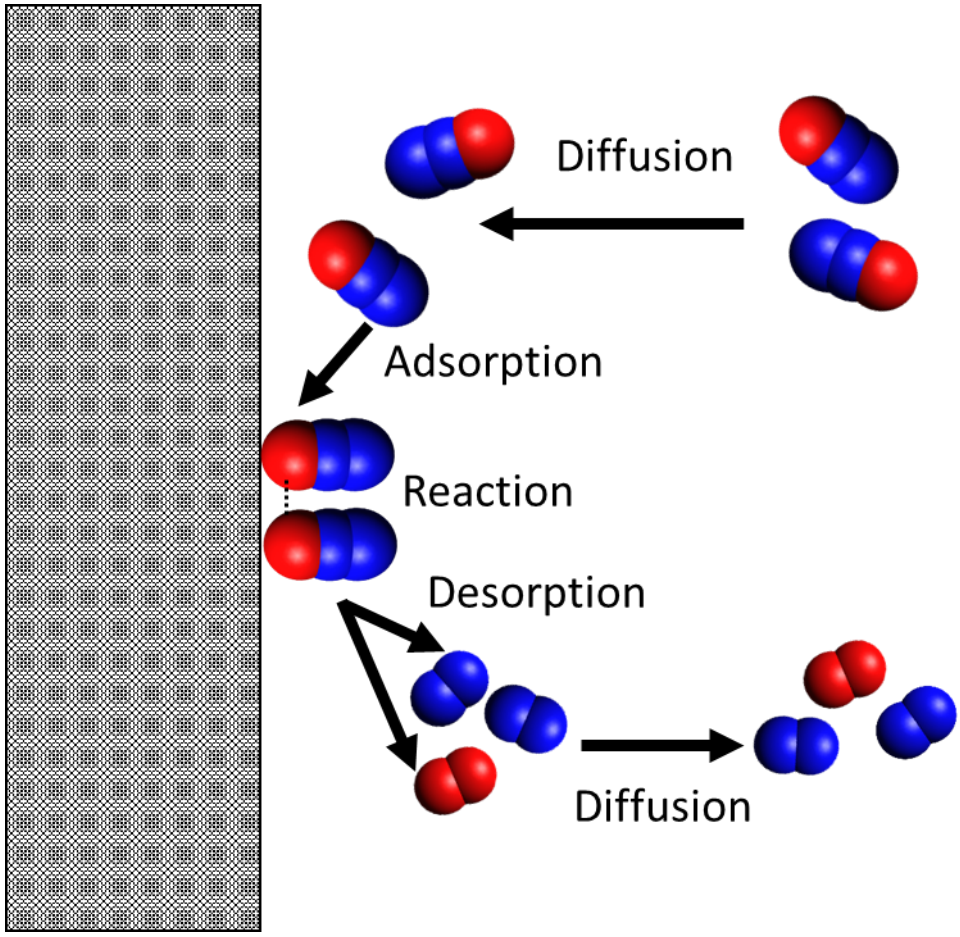

Fig. 1.1 Example reaction on a catalyst surface following the Langmuir – Hinshelwood mechanism. Legend: Grey block – Catalysts surface, Red – Oxygen atom, Blue – Nitrogen atom, When combined red and blue atoms form N_2O, the process shows the decomposition of N_2O into nitrogen and oxygen.

Generally, adsorption is the first step in the reaction mechanism. When discussing the reaction $A + B \rightarrow C$ there are three types of mechanisms that can take place. The first is Langmuir-Hinshelwood which assumes that both reactants (A and B) are

adsorbed on to the surface of the catalyst before a reaction can take place. Following the diagram in Fig. 1.2. the reactants adsorb on to the catalysts surface (A+B), the adsorbed species then undergo surface migration, combine and desorb as the product C. The second is the Eley-Ridel mechanism whereby only one of the reactants are adsorbed onto the surface of the catalyst. As shown in Fig. 1.2, A is adsorbed on the surface and reacts with reactant B that is in the reaction mixture to produce C. The third mechanism is the Mars Van Krevelen, where the surface contributes in the reaction. One of the reactants (A) forms a chemical bond with the catalytic surface and forms a metal-reactant intermediate, such as N_2O binding via the oxygen terminal to fill an oxygen vacancy on a surface such as ceria, that then reacts further with the other reactants (B) to form the product C. In heterogeneous catalysis the most common mechanism is the Langmuir-Hinshelwood as many reactants are activated by the adsorption on the catalytic surface. [5]

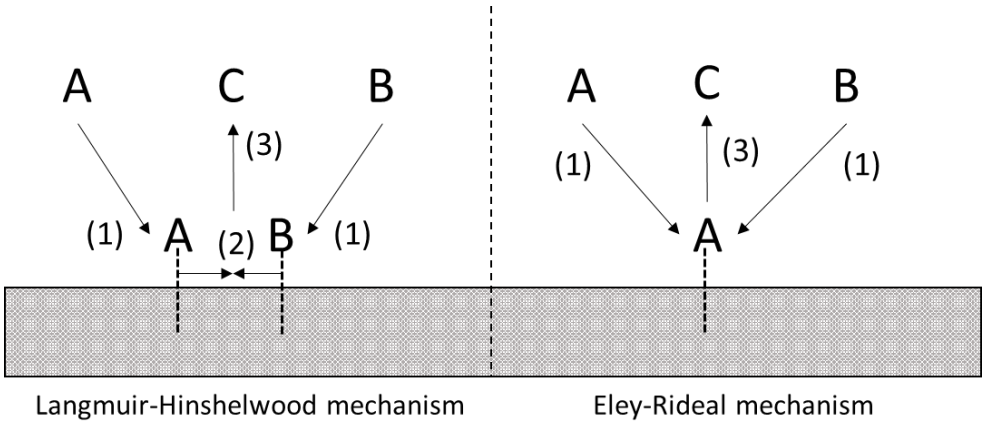

Fig. 1.2. Diagram showing the difference between Langmuir-Hinshelwood and Eley-Rideal mechanism. Legend: Grey block - catalyst surface, A + B – reactants, C – product.

As mentioned previously the catalyst is not consumed in the reaction, with the active site constantly being regenerated and as such can be used in consecutive cycles. Therefore, a small ratio of catalyst to reactant is required due to the efficiency of the catalyst, this ratio can be measured as a turnover number (TON) or turn over frequency (TOF). As shown in equation 1 below, TON is defined as the number of moles of reactant that one mole of catalyst can convert before becoming inactive, based on the calculation of the moles of product formed divided by the moles of catalysts.

$$Eq.1 \qquad Turn\ Over\ Number\ (TON) = \frac{moles\ of\ N_2O\ converted}{total\ moles\ of\ metal}$$

$$Eq.2 \quad Turn\ Over\ Frequency\ (TOF) = \frac{moles\ of\ N_2O\ converted\ per\ second}{total\ moles\ of\ metal}$$

As shown in Eq.2, TOF is defined as the molecules reacting per active site in unit of time. [7] This is typically calculated using the number of moles of reactant consumed and either the active site weight or total metal loading converted to moles of active metal. The active site is usually a metal species on the surface that contains nanoparticles. Nano-particles are in the range 1-100 nm and are defined as being between the bulk and molecular state of matter. It is not always possible to quantitatively measure the active moles of metal, therefore throughout this thesis total moles of metal is used to calculate TON or TOF. [8]

There are many classes of catalysts, for example, metal oxides, zeolites, and supported metal nano-particles. The most common materials used as catalysts are metals and various oxides. Metals generally have a high surface energy and are therefore very active for many catalytic reactions, and in some cases too active, for example in selective oxidation reactions the catalyst can be too active, leading to an over oxidised product, such as the conversion of propene to acrolein, with very low selectivity to the desired product. [9] In the case of these overactive catalysts, mixed metal oxides can be used instead, for example $FeSbO_4$ is used to produce a high selectivity to acrolein from propene. [10] To increase stability of high surface area metal nanoparticles under reaction conditions, the nanoparticles are dispersed on a support, usually a metal oxide such as alumina or silica (Al_2O_3 or SiO_2). This helps to limit sintering and maintain high catalytic activity. [1,6] An example of supported metal nanoparticles on an oxide is the use of Au supported on NiO or Fe_2O_3 for the low temperature oxidation of CO to CO_2. [11] Until 1985, gold was thought of as being an inactive metal, that was until Graham Hutchings predicted that nano-particles of gold would be active for the hydro-chlorination of acetylene to produce vinyl chloride.[12] Vinyl chloride is one of the key reactants in the production of PVC, one of the most commonly used plastics around the world. The chemistry described here has been implemented at an industrial level, with plants in China now using a gold catalyst instead of the problematic and toxic mercury catalyst that had been used previously in the production of vinyl chloride. [13]

Zeolites are another class of catalyst that are composed of two different oxides, silica and alumina, amorphous materials that when prepared correctly form a crystalline zeolite. When *ca.* 10 % alumina is dispersed through a silica matrix, an increase in acidity of the solid is observed. The increase in acidity is due to the build-up of the structure between SiO_4^{4-} and AlO_4^{5-} ions. The imbalance between the two units requires a proton to balance the charge, leading to a highly acidic solid. The interlinking of the two tetrahedra building blocks leads to the production of relatively open three dimensional crystal structures, or cages, with high surface areas. The cages can limit adsorbing molecules based on the size of the molecules and whether they fit in the openings, this phenomenon is known as acting as a molecular sieve.[1] There are many everyday applications for zeolites such as in water softeners, water filters, and pet litter. These applications make use of the crystalline structure trapping un-wanted liquids, ions or odour molecules.[14] Zeolites are also commonly used in the petroleum industry, with zeolites the main constituent in catalytic crackers used to crack large hydrocarbon molecules into petrol and diesel.[15–17]

1.2 Ozone Depletion and Global Warming

Ozone depletion is the term used to describe the decrease in concentration of ozone with in the earth's stratosphere. The ozone layer helps to protect the earth from the sun's ultra violet (UV) radiation. Ozone is formed with in the earth's stratosphere by the following reactions:

$$h\nu + O_2 \rightarrow 2\,O \qquad (1)$$

$$O + O_2 \rightarrow O_3 \qquad (2)$$

The UV radiation from the sun strikes an oxygen molecule in the stratosphere causing the molecule to split, creating two oxygen atoms (step 1). These oxygen atoms then combine with an oxygen molecule to form ozone (O_3) and heat (step 2). Due to the high concentration of oxygen molecules in the upper atmosphere, the UV radiation is fully absorbed into the stratosphere. Ozone depletion occurs when compounds containing nitrogen, hydrogen, bromine and chlorine react with the highly unstable ozone molecules, normally producing oxygen and an oxygen containing compound of the original molecule.[18]

Ozone depletion can occur in two ways, either by a thinning of the ozone layer, where more ozone is destroyed than produced in the ozone cycle,[19] or by the formation of ozone holes.[20,21] These holes occur over the north and south poles when the temperature in the stratosphere cools rapidly to form polar stratospheric clouds (PSC). In the stratosphere one of the many ozone depleting atoms, Cl, is in unreactive forms such as HCl and $ClNO_3$, however when PSC form the inactive Cl species can react with the surface of the PSC forming very reactive Cl species that react with ozone, creating ozone holes. In the areas on the earth under the ozone holes, the intensity of UV radiation is far higher than in places where the ozone layer is thicker.

A higher intensity of UV radiation hitting the earth's surface produces many problems. For example, the temperature in these areas increases and distributes around the world leading to a phenomenon known as global warming. The increased temperature in the polar regions leads to an increase in the speed at which the polar icecaps are melting. As the polar icecaps melt, eventually into the world's oceans, this leads to an increase in sea levels. As sea levels rise communities and life that live on shore close to sea level are threatened.[22–26] A secondary effect of the thinning of the ozone layer is an increase in people getting skin cancer, this is due to an increased everyday exposure to UV radiation which has been shown to cause skin cancer.[27–30] Overall there have yet to be any positive effects of global warming.

1.3 N_2O and the environment

Nitrous Oxide (N_2O) is a colourless non-flammable gas that was discovered in 1772 by Joseph Priestly. Priestly discovered N_2O by dampening iron filaments with nitric acid and heating to produce what he called "nitrous air diminished".[31] In 1794 Thomas Beddoes and James Watt first claimed that N_2O could be used to treat tuberculosis and other lung diseases. A clinical trial was started under the supervision of Sir Humphry Davy, who noted that, when inhaled, an analgesic effect was felt, indicating that the gas could be used for surgical operations and called N_2O "laughing gas".[32] The gas was not implemented for use in surgery for another 44 years, but it is still in use today in both dental practices and in hospitals as "gas and air".

N_2O is a linear molecule that is isoelectronic to CO_2. There are two resonance structures of N_2O, shown in Fig. 1.3, either with a negatively charged oxygen or a negatively charged nitrogen but always a positively charged central nitrogen atom.

Fig. 1.3. Resonance structures of Nitrous Oxide.

Levels of N_2O in the atmosphere have remained constant at around 270 ppb until the early 1800s as shown in Fig. 1.4; this is noted as the pre-industrial era. For the time period up up to 2000 years ago, levels of N_2O in the atmosphere can be deduced by measuring the composition of air found in ice cores from Antarctica. For the period up until 1977, Law Dome ice cores, East Antarctica, have been used. From 1997 to the present day, the National Oceanic and Atmospheric Administration's Earth system Research Laboratory (NOAA/ESRL) measure the current concentration of N_2O in the atmosphere at sites around the world such as Mauna Loa, Hawaii.[33–36] The onset of widespread industrialisation resulted in a dramatic increase in atmospheric N_2O, with levels rising to the current day level of 327 ppb.[37] Furthermore, the level of atmospheric N_2O has increased at the same rate since around the 1980s year-on-year. Industrialisation and an increase in agriculture have led to the increase in the levels of N_2O in the atmosphere.

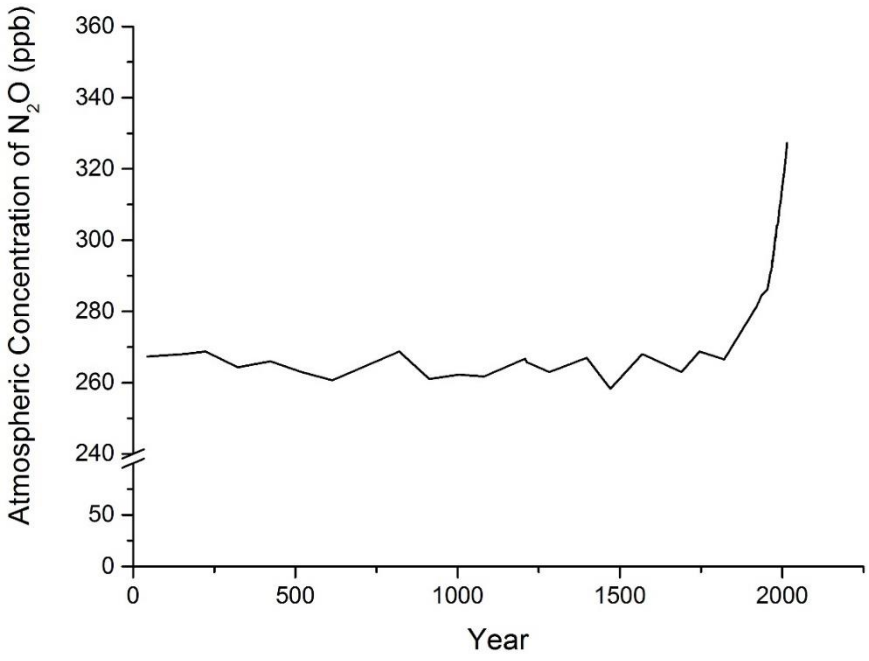

Fig. 1.4. Graph showing how the concentration of N_2O in the atmosphere has changed in the last 2000 years.[34,38–40]

There are both natural and anthropogenic sources of N_2O,[41–43] with natural sources contributing 62 % of the world emissions and anthropogenic sources contributing to the remaining 38 %. Oceans, soils that are undergoing natural vegetation (micro -organisms such as nitrifiers and denitrifiers produce N_2O during the decomposition of the nitrogen based fertilisers in soils, converting ammonium to nitrates)[44], and atmospheric chemical reactions are natural sources of N_2O.[45] However, natural vegetation of soils is the largest natural contributor to N_2O emissions. Emissions of N_2O are closely related to microbial production processes in soils, sediments and water bodies.[46]

Examples of anthropogenic sources are sewage treatment, fuel and biomass combustion, industrial chemical processes, and contributions from the agricultural sector.[41] Approximately 60 % of global anthropogenic emissions come from the agricultural sector and the use of nitrogen based fertilisers.[47] Adipic and nitric acid are the main industrial processes that lead to the formation of N_2O,[48] adipic acid production leads to around 80 % of the global industrial emission of N_2O (10 % in total).[43,49] Dental surgeries and hospitals also use N_2O for treatment of patients, in the form of a sedative. These emissions are unregulated and uncontrolled.[50] Another anthropogenic source of N_2O is a by-product of the combustion of fuels in cars. Here, three-way catalytic (TWC) converters are installed in all petrol cars worldwide, and are used to abate nitrogen oxides such a nitric oxide and nitrogen dioxide, carbon monoxide, and hydrocarbons. The levels of N_2O emitted are dependent on many factors such as the driving cycle, the age and composition of the TWC, the temperature at which it is operating and the concentration of sulphur in the fuel source which leads to catalyst deactivation.[49,51–54]

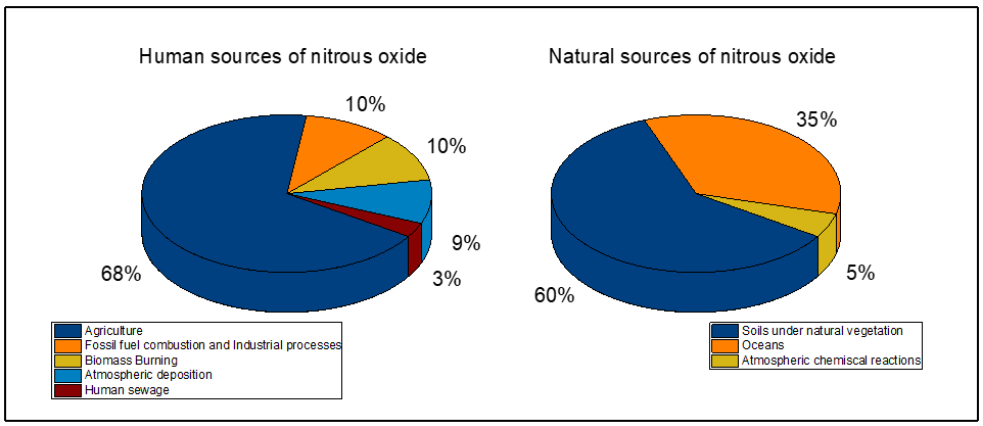

Fig. 1.5. Graphs showing the distribution of anthropogenic and natural sources of N_2O. Figure reproduced from IPCC fourth assessment report: Climate change 2007, intergovernmental panel on climate change.[41]

As a result, it is extremely important to decompose N_2O before it is released into the atmosphere. Decomposition of N_2O takes place through dissociation into O_2 and N_2 as shown below.[55]

$$2\ N_2O \rightarrow\ 2N_2 + O_2 \qquad (\Delta_r H^0(298) = -163\ kJ\ mol^{-1})\ ^{56}$$

The effect of nitrous oxide (N_2O) on the atmosphere is far more devastating than CO_2 (global warming potential = 1) due to having a global warming potential of roughly 300, as seen in Fig. 1.6, and a half-life of greater than 100 years.[48,57,58] With such a long lifetime, the effect of N_2O on the atmosphere is seen for extended periods of time.

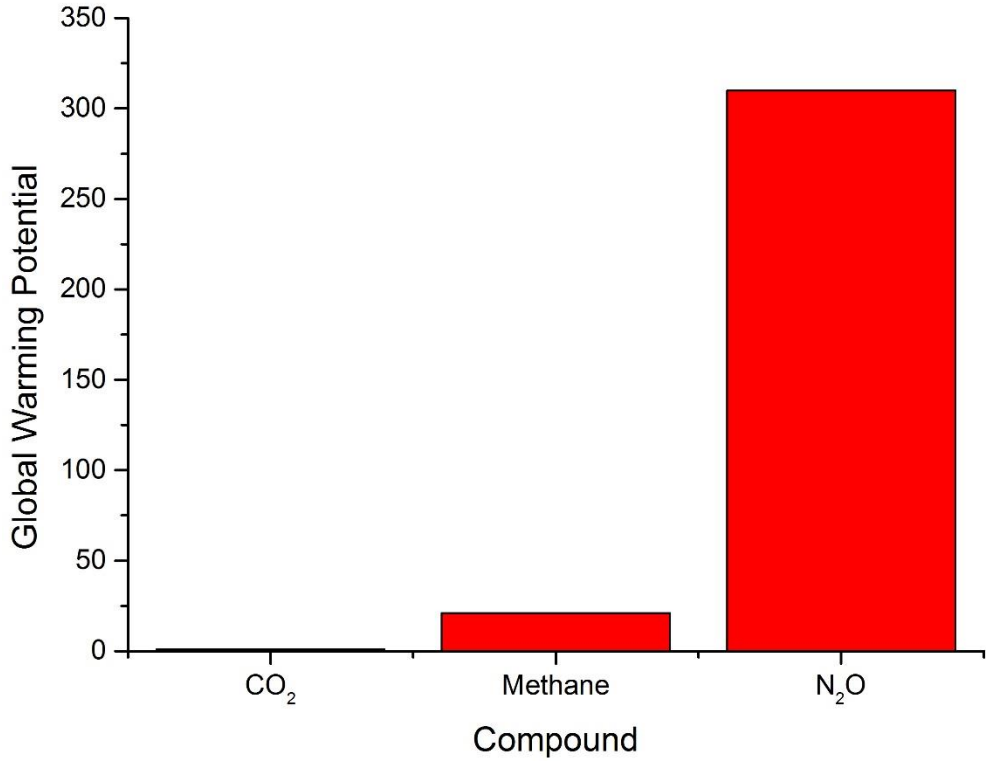

Fig. 1.6. Graph showing the global warming potential of three well-known greenhouse gases, CO_2, methane and N_2O.[59]

Increasing levels of N_2O leads to an increase in ozone depletion, which in turn leads to global warming. As described previously, ozone depletion is the decrease in levels of ozone from the stratosphere, which can either lead to a thinning of the ozone layer or the formation of ozone holes. Presence of N_2O in the stratosphere enables ozone depletion through the following mechanism:[60]

$$N_2O + hv \rightarrow N_2 + O^* \qquad (3)$$

$$N_2O + O^* \rightarrow 2\,NO \qquad (4)$$

$$NO + O_3 \rightarrow NO_2 + O_2 \qquad (5)$$

$$NO_2 + O^* \rightarrow NO + O_2 \qquad (6)$$

In the first step N_2O reacts with UV light to form radical oxygen species, which then react with N_2O in step two to form nitric oxide. Nitric oxide then reacts with ozone to form nitrogen dioxide and oxygen, this is one of the ozone depletion steps. In step 4 nitrogen dioxide reacts with ozone to form nitric oxide and oxygen, another ozone depleting step. The formation of NO enables step 5 to happen again, which in turn enables step 6 to happen. The constant cycling between steps 5 and 6, shows how the effect on the ozone layer is so devastating. [60]

There are many forms of legislation that cover carbon emissions around the globe; however, most do not explicitly cover N_2O emissions. One that does is the Climate Change Act 2008 that was introduced by the UK government, with aims to reduce the emissions of N_2O to pre-1990 levels by 2050.[61] This is in line with the Kyoto protocol implemented worldwide in 1997 by the United Nations Framework Convention on Climate Change (UNFCC), with aims to reduce emissions of multiple greenhouse gases to pre-1990 levels by 2050 but with aims to do this in the first period of the protocol (2008-2012).[62] The Kyoto protocol is the world's only legally binding treaty to reduce greenhouse gas emissions. However, because many emitters are not part of The Kyoto Agreement, only 18 % of the world's total emissions are covered by the protocol. Now in the second commitment period (2013-2020), the European union countries have vowed to decrease their greenhouse gas emissions to levels 20 % lower than pre-1990 levels, by following guidelines set out in the 2020 climate and energy package.[63]

In December 2015, the Paris Agreement was created that strengthens the global response to the threat of climate change by trying to cap a global temperature rise to below 2 °C above pre-industrial levels and to try to limit the increase to + 1.5 °C. This agreement requires all the parties to frequently report on their emissions and implementation efforts, with a global stocktake every 5 years to keep track of efforts. In January 2019, 184 out of 197 countries had joined the Paris Agreement, making it a truly worldwide initiative.[64]

With one of the major anthropogenic sources of N_2O being from vehicle emissions (Fig. 1.5)[41], it would be natural to expect there to be legislation surrounding the emissions from mobile exhaust streams. This is not the case; the latest legislation, Euro 6, does not mention N_2O specifically, but instead particulate matter, NO_x, CO and hydrocarbons. With the focus of the legislation aiming more towards the emission of air pollutants rather than the emission of greenhouse gases, with aims to improve health rather than limit global warming.[65]

The reduction of greenhouse gas emissions lies hand-in-hand with the 12 principles of green chemistry.[66] Green chemistry or sustainable chemistry is the use of chemistry that minimises the use or production of hazardous substances. The twelve principles are as follows:

1. Prevent Waste
2. Atom Economy
3. Less Hazardous Synthesis
4. Design Benign Chemicals
5. Benign Solvents and Auxiliaries
6. Design for Energy Efficiency
7. Use of Renewable Feedstocks
8. Reduce Derivatives
9. Catalysis (vs. Stoichiometric)
10. Design for Degradation
11. Real-Time Analysis for Pollution Prevention
12. Inherently Benign Chemistry for Accident Prevention

The use of the 12 principles of green chemistry design will enable the reduction in greenhouse gas emissions and allow control over the currently changing global temperature. The key principles that will be utilised to do this are number 3. less hazardous synthesis, 6. Design for energy efficiency, 7. Use of renewable feedstocks, and real-time analysis for pollution prevention.

1.4 N_2O Decomposition

1.4.1 Mechanism

The following mechanism is generally accepted for the catalytic decomposition of N_2O into $N_2$and O_2.[56,67]

$$N_2O_{(gas)} + * \rightarrow N_2O *_{(ads)} \quad (7)$$

$$N_2O *_{(ads)} \rightarrow N_{2(gas)} + O *_{(ads)} \quad (8)$$

$$2\ O *_{(ads)} \rightarrow O_{2(gas)} + 2 * \quad (9)$$

$$O *_{(ads)} + N_2O_{(gas)} \rightarrow O_{2(gas)} + N_{2(gas)} + * \quad (10)$$

* = active site

Initially, N_2O binds via the oxygen atom to the active site (Eq.7), the second step shows the breakdown of the N_2O molecule into nitrogen and an absorbed oxygen atom at the active site (Eq.8). Based on this mechanism the catalyst becomes oxidised in the 2nd step and needs to be able to reduce the active site by removal of oxygen to regenerate the active site for further reactions. The reduction can take place via two routes: Eq. 9, by the Langmuir-Hinshelwood mechanism,[68] or by Eq. 10, which follows the principles of Eley-Rideal mechanism.[56] As described previously the Eley-Rideal mechanism involves only one of the reactants being absorbed onto the surface of the catalyst, in this case absorbed oxygen species, which react with N_2O to form oxygen, nitrogen and regenerate the active site. Equation 8 takes place via the Langmuir-Hinshelwood mechanism, whereby both the reactants are absorbed on to the surface of the catalyst; in this case, two bound oxygen atoms come together to form molecular oxygen, regenerating two active sites.

1.4.2 N_2O decomposition rate limiting step and the effect of adding a reductant to the gas feed.

During the decomposition of N_2O, the rate limiting step is the recombination of oxygen to form O_2 (Eq. 13). This is because the oxygen atoms need to be within close proximity of each other to be able to react to form an oxygen molecule. This

is unlikely to be the case, which leads to the blocking of the active site due to oxidation. To combat the oxidation of active sites, a reductant can be added to the gas feed to act as an oxygen scavenger. The presence of a reductant in the gas feed has been shown to assist the abstraction of oxygen from the oxidised active site, significantly increasing the observed rate of N_2O decomposition at lower temperatures, normally lowering the T_{50} by 150 °C. Propane,[69–73] ethane, methane and CO [73–78] have all been used as a reductant, however my work focuses on the use of propane as a reductant, altering the reaction mechanism to the following:

$$N_2O_{(gas)} + * \rightarrow N_2O*_{(ads)} \quad (11)$$

$$N_2O*_{(ads)} \rightarrow N_{2(gas)} + O*_{(ads)} \quad (12)$$

$$10\,O*_{(ads)} + C_3H_{8(gas)} \rightarrow 3\,CO_{2(gas)} + 4\,H_2O_{(gas)} + 10* \quad (13)$$

Eq.11 and 12 are the same as previously described but the addition of propane to the gas feed allows one propane molecule to regenerate 10 oxidised active sites, as described in Eq. 13. This is an ideal situation; if there is not enough oxidised active sites present to produce CO_2 then CO can also be formed, as follows:

$$7\,O*_{(ads)} + C_3H_{8(gas)} \rightarrow 3\,CO_{(gas)} + 4\,H_2O_{(gas)} + 7* \quad (14)$$

In this case, only 7 active sites are regenerated. As the reaction proceeds to higher temperatures, it is more common to see CO form as more propane is converted because there are less oxygen species present on the surface of the catalyst for scavenging. This is expected as the gas feed the ratio of C to O is 3:1 in most reaction conditions when propane is present in the feed, therefore a high conversion of propane will always convert all the oxygen species present.

1.5 Catalysts for N_2O decomposition

Over the last century there have been many classes of catalysts that have been used for the decomposition of N_2O. Prominent examples are iron zeolites, perovskites and others such as spinels and vanadium catalysts and some are discussed herein.

1.5.1 Iron Zeolites

Zeolites are a class of crystalline, microporous solids that consist of silicon, aluminium and oxygen. The elements come together to form frameworks in cage

like structures, where cations, or small molecules may be present inside the channels. There are many different both naturally occurring and man-made zeolite framework structures, which have different sized cages. The differing cage sizes lead to the ability to trap and block different size molecules in the cavities, which enables the zeolite to act as a molecular sieve. Based on this property, zeolites have been used as adsorbents for industrial purification for many years.[79]

The zeolite framework consists of tetrahedrally coordinated Si and Al atoms that are linked by shared oxygen atoms to form regular cavities with in the crystalline structure. Small cations are present inside the channels to balance out the negatively charged framework. This results in a three-dimensional microporous crystalline structure, with channels and tunnels of differing dimensions as shown in Fig. 1.7.[80] There are nearly 50 different types of naturally occurring zeolites and over 200 synthetic zeolites, such as chabazite and mordenite, all of which have different physical and chemical properties. Different chemical composition, such as the ratio of silicon to aluminium atoms, can result in these different properties such as the pore size of the channels and the cation selectivity.[81,82] The pore size of the channel can range from approximately 3 to 8 Å, within the micropore range of less than 2 nm.[83] Every time that a new structure is thought to be produced, the structure is submitted to the Structure Commission of the International Zeolite Association (IZA-SC) to confirm whether the framework is unique.[84] If the framework is unique then the IZA-SC will assign a unique three letter code to the framework. For example, MFI is used to signify the family of zeolites derived from Zeolite Socony Mobil – five (ZSM-5), with MFI taken from the M for Mobil and FI from five. Some of the most common commercially available zeolites are denoted by their colloquial names; A, beta, Y and ZSM-5 (Fig. 1.7).

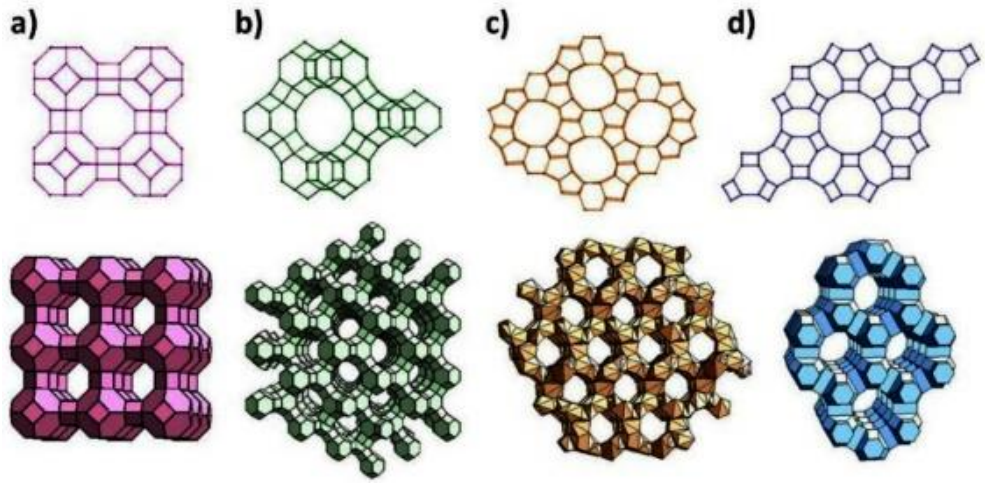

Fig. 1.7. Representative siliceous frameworks of (**a**) zeolite A; (**b**) zeolite Y; (**c**) Zeolite L; (**d**) ZSM-5.[80]

Naturally occurring zeolites are not commonly used in catalysis due to the impurity of the phases present, along with varying chemical compositions between deposits and sometimes even with in deposits, leading to irreproducible catalysis.[85] Therefore, synthetically produced zeolites are favourable for catalysis. Zeolite X and Y have been used on an industrial scale for the use in fluid catalytic cracking (FCC) of large hydrocarbon molecules into petrol and diesel.[15–17] The implementation of zeolites as a catalyst in this reaction improved the yield of petrol significantly over the previous amorphous silica-alumina catalysts due to the removal of any impurities.

Zeolites can be doped with a wide variety of metals such as silver, cobalt, nickel and iron to alter the catalytic activity. For example, silver can be added to a zeolite to produce an antimicrobial material that can be applied to wounds to enable better healing and limit infection.[86] Cobalt doped zeolites have been used for Fischer-Tropsch (FT) synthesis to produce hydrocarbons from syngas (CO and H_2). Cobalt is used as the metal in this reaction due to its low cost, high activity and selectivity to liquid fuels.[87]

When aluminium cations are substituted into the zeolite framework a charge imbalance is created, a cation is required to satisfy the Al tetrahedron, SiO_4^{4-} compared to AlO_4^{5-}. Often this is a proton, which increases the Bronsted acidity of the zeolite due to the proton acting as a Bronsted acid. [88] Other size limited cations can also be present in the zeolite channels to balance the charge created on the Al ion, such as, potassium, sodium and ammonium ions. [89]

Iron zeolites have been commonly used for the decomposition of N_2O,[68] with H-ZSM-5 frequently being used as a support.[90–92] Both high and low weight loading Fe-ZSM-5 catalysts have been reported in literature, Xie *et al.* reported 100 % conversion at 450 °C using 7.46 wt. % Fe [73] while Wood and co-workers [93] reported 84 % conversion at 500 °C using an Fe-ZSM-5 catalyst with a loading of 0.57 wt. %. Sobalik *et al.* showed that when using ferrierite (FER) a Si:Al ratio of 8.5 outperformed Si:Al 10.5 when the same Fe loading was used for N_2O decomposition.[94] Rauscher *et al*. reported that low Si:Al ratios are more effective for N_2O decomposition catalysts.[90] Iron doped zeolites (Fe-ZSM-5) (Si:Al = 11.4) exhibited 95 % conversion of N_2O at 500 °C in contrast to Fe-BEA (93) achieved just 20 % conversion of N_2O at 575 °C.[95] The work of both these groups show that the Si:Al ratio of the zeolite is an important factor for activity of an N_2O decomposition catalyst.

Additionally, it has been shown that zeolites with different framework structures can be used for the decomposition of N_2O with ZSM-5 (MFI), beta (BEA) and Ferrierite (FER) zeolites acting as supports for Fe.[95–97] Jisa *et al.* showed that a low loaded Fe-FER was the most active, achieving 85 % conversion at 450 °C.[98] The Si:Al ratio for the FER was the lowest (8.6) of all the zeolites tested, compared to BEA (15.5) and MFI (13.4). This supports the earlier findings that a low Si:Al ratio is necessary for high N_2O conversion, due to the presence of active Fe species that form on the Al moiety of the zeolite framework. Therefore, low Si:Al ratios can lead to a higher concentration of active species.[73]

The rate limiting step of N_2O decomposition is the recombination of deposited oxygen to form O_2. In the case of Fe-zeolites, the dissociation of N_2O on the active Fe species is facile and results in an oxidised Fe active site. The oxygen left on the surface must recombine with another oxygen atom to form O_2, which is slow. Propane [69–73] ethane, methane and CO [73–78] have all been used as a reductant.

Fe-ZSM-5 can be prepared by various ion-exchange methods, including *via* wet [99–102] or solid state,[90,101,103] or sublimation [94,98,104–107] methodologies. Solid state methods use solventless mechanical mixing, while wet ion exchange makes use of solvents. Salts with low temperatures of evaporation can be used during a sublimation technique, for example $FeCl_3$ precursors. Generally, when this technique is used, chlorine ions remain after sublimation. Therefore, a post

preparation washing step may be necessary to remove any remaining chlorine species.[108–110]

When iron is deposited on zeolites it is possible to form four distinct Fe species as shown in Fig. 1.8. These are framework Fe^{3+}, isolated Fe^{3+} or Fe^{2+}, Fe oxo-species and FeO_x species. Framework Fe^{3+} is formed by isomorphous substitution of Al or Si ions, whereas isolated $Fe^{2+/3+}$ species are anchored to the zeolite framework by either Si-O-Fe or Al-O-Fe bridges or di-nuclear Fe-O-Fe species, either in the framework or in the channels. Iron oxide (FeO_x) can exist as both small nanoparticles or bulk FeO_x particles.[73,110–112]

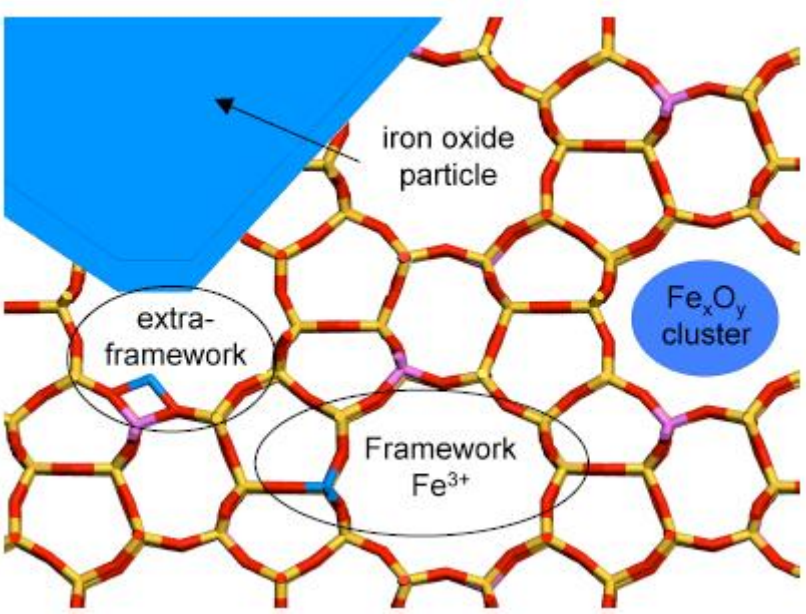

Fig. 1.8. Visual representation of the Fe sites that can form after the introduction of Fe into ZSM-5 framework. Reproduced from Fig 1.14, Hammond 2011.[113] Legend: Red - Oxygen, Yellow – Silicon, Pink – Aluminium, Blue – Iron.

Therefore, determination of the active species is challenging, with nano-particulate iron [73,114] and extra-framework Fe [97,115,116] having been reported as the active site for N_2O decomposition. Extra framework Fe is considered the dominate active species, due to the formation of α-Oxygen in the presence of N_2O.[117–123] α-Oxygen (an oxygen vacancy) is formed by decomposing N_2O over reversible redox α-Fe sites that have the capacity to switch between Fe^{2+} and Fe^{3+} as shown in the mechanism below.[124,125]

$$N_2O + (Fe^{2+})_\alpha \rightarrow (Fe^{3+} - O^{\cdot-})_\alpha + N_2 \quad [126]$$

Acid washing Fe-ZSM-5 catalysts have been shown to increase both the catalytic activity and stability. This is due to the removal of spectator Fe species such as FeO_x nano-particulates and clusters. These species can be removed in relatively short periods of time such as 10 mins; with extended periods of time, the amount of iron removed was not found to increase.[110] As zeolites are relatively stable to short acid washing, it does not affect the pore channels and mesopores are not created. As the acid conditions are relatively mild (10 vol.%), only a small quantity of surface Al is removed.[127] This stability indicates that only the Fe species present will be effected by the acid washing and the zeolite will remain unchanged.[128] Alternatively, steaming pre-treatments can be used to extract iron from the pores and into the extra-framework sites; [129–133] however, as this technique has been extensively studied this was not a focus of this work.

1.5.2 Pd-γAl_2O_3 Catalysts

Palladium/alumina (Pd-Al_2O_3) catalysts have not been extensively studied for the decomposition of N_2O [103,134–137]; however, similar catalytic Pd-Al_2O_3 systems have been demonstrated to exhibit high activity and stability in other applications.[138–143] Pekridis *et al.* reported a T_{100} (i.e. the temperature to reach 100 % conversion) of 425 °C using a 2 wt. % Pd-Al_2O_3 catalyst prepared by wet-impregnation, for the decomposition of N_2O. The group also showed that the addition of propane to the gas feed lowered the T_{100} to 400 °C.[134] As described previously the rate limiting step in the decomposition of N_2O is typically the recombination of oxygen to form O_2 and free the active site to adsorb an incoming N_2O molecule.[123,144–149] Therefore, propane acts as reductant that can facilitate the abstraction of oxygen from the oxidised active site, significantly increasing the observed rate of N_2O decomposition at lower temperatures.[103,134] In the case of Pd-Al_2O_3 catalysts, addition of propane [69–73] ethane, methane and CO [73–78] have also been used as reductants. Christoforou *et al.* reported that 72 % conversion was possible using 2 wt. % Pd-Al_2O_3 at 600 °C and the addition of propane to the feed lowers this temperature by over 200 °C, while still achieving 100 % N_2O conversion.[103] Doi *et al.* utilised a higher weight loading of Pd (5 wt.%) with only 60 ppm N_2O in the gas feed and showed that it was possible to decompose this low concentration at 300 °C. However, air was used as the balance gas during this reaction, and it has been shown in this case that the addition of oxygen to the feed increases the activity.[137] It is important to note that

in most cases the addition of oxygen to the gas feed limits the conversion of N_2O, as the oxygen present oxidises the active site of the catalyst.[134,150,151]

Tateishi *et al.* also demonstrated that a higher weight loading was suitable for the decomposition of N_2O with a commercial 5 wt.% Pd-Al_2O_3 catalyst achieving 100 % conversion at 320 °C. However, when compared to the catalyst prepared by wet impregnation in house by the group, the same loading catalyst required 500 °C to achieve the same conversion under the same conditions.[136] Pekridis *et. al.* prepared a 2 wt. % Pd-Al_2O_3 catalyst that at 350 °C achieved 90 % N_2O conversion when propane is present in the gas feed.[134]

1.5.3 Perovskites

Perovskites are a well-known class of mineral structures with the chemical formula ABO_3. Calcium Titanate ($CaTiO_3$) was the first mineral discovered with the ABO_3 structure and was named a perovskite after the Russian Mineralogist Lev Perovski.[152] A perovskite forms a cubic structure, as shown in Fig. 1.9. The A cation is typically larger than the B cation. The A site cation sits on the corners of the cubic structure (12 fold coordination to oxygen atoms), whereas the B site atom typically sits at the centre of the structure (6 fold coordination to oxygen atoms). Whilst the oxygen species are located in face centered positions and binds to both cations present in the structure. The A site cation is typically an ion with a large ionic radius such as a rare earth element, La, whilst the B site cation is a transition metal element such as Fe or Co that has a smaller ionic radius. The A site cation is generally catalytically inactive but alters the oxidation state of the B site therefore creating oxygen vacancies.[153] The A sites are typically 2+/3+ cations, whereas, the B sites are 3+/4+ cations. A second A site cation can be incorporated into the structure, the difference in valence state between the cations can lead to further oxygen vacancies as shown in Fig. 1.9, below, in orange. Because of the structural flexibility of a perovskite, around 90 % of the natural metallic elements of the periodic table could be incorporated into the structure.[154]

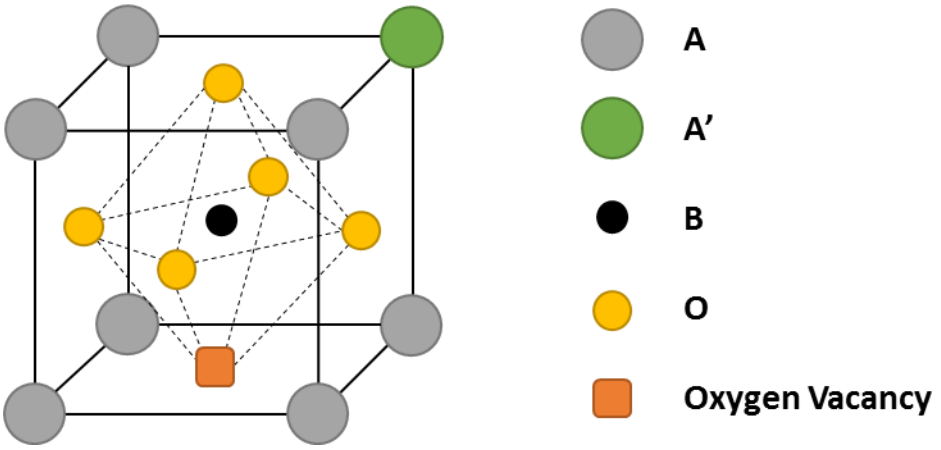

Fig. 1.9. Ideal ABO_3 structure of perovskite oxide, the green dot represents the substitution of an A-site cation by an alternative cation, orange squares represent an oxygen vacancies.[155]

A perovskite consists of two or more simple oxides that have a high melting point, therefore the preparation of a perovskite structure requires high temperature and a long calcination time, which typically leads to low surface areas. Common properties of a perovskite include high thermal stability for use under gas phase reactions at high temperatures, or high hydrothermal stability for use under liquid reaction at low temperatures. Perovskites are well known for their ease of preparation, high thermal stability, low cost and good catalytic activity despite their low surface area. For examples perovskite catalysts are commonly used in photochemistry, electrochemistry, CHO_x/NO_x oxidation, TWC catalytic converters and CO_2 reduction.[68,156–160]

Surface area has been a very important driving force behind the design of different preparation method to produce perovskite structures. Initially most preparation methods produced perovskites with specific surface areas (SSA) of *ca.* 2 m^2g^{-1}. An example solid-state chemistry preparation method that produces low surface area perovskites is ball milling: single oxides are milled together to form a homogenous oxide mixture before calcination at temperatures greater than 900 °C.[161] The high temperature required to form a phase pure perovskite results in a low SSA. Solution chemistry preparation methods, such as sol-gel, spray drying and co-precipitation, have been used to produce highly crystalline and phase pure materials at lower temperatures between the range of 700 – 800 °C, resulting in surface areas of up to 30 m^2g^{-1}, which is a vast improvement on the solid-state methods used previously. An example of this is the citric acid combustion method, whereby nitrate precursors were combined with citric acid, dissolved, dried and then

calcined at temperatures between 700 – 800 °C, for a shorter period of time.[162–164] This preparation method produces a higher surface area material due to the use of an organic complexing agent, which coordinates the metal ions, followed by the combustion of the nitrate precursors and the organic complex to form small homogenised metal oxide particles which are the precursors of perovskites.

Oxygen vacancies have been shown to previously influence the catalytic activity of perovskites.[165–168] The oxidation sate of the B site cation and the resulting oxygen vacancy can be controlled by substitution of an external cation into the matrix. For example, if a B site cation oxidation state is reduced from B^{4+} to B^{3+} an oxygen vacancy can be formed, due to less oxygen atoms being required to balance the charge of the cation. Alternatively, an oxygen vacancy can also be formed by the substitution of an A^{3+} cation with that of an A^{2+} one in the ABO_3 structure. The control of the oxidation state of the B site cation and as a result the number of oxygen vacancies is crucial as a lot of catalytic cycles depend on the redox properties of the B site metal cation. Oxygen vacancies can provide the site at which coordination of the reactant and subsequent activation can take place, owing to the importance of their presence in the perovskite structure for catalytic activity.[155]

Perovskites have been reported as effective catalysts for the decomposition of N_2O. For example, Russo *et al* prepared a $LaCoO_3$ perovskite by a solution combustion synthesis method and reported 100 % conversion of 0.5 % N_2O in He at 550 °C, with a T_{50} of 455 °C.[169] Ivanov and co-workers prepared a series of $LaSrMnO_3$ catalysts, investigating the effects of the ratio of La and Sr in the A site. The group found the optimal ratio to be $La_{0.75}Sr_{0.25}$, with a T_{50} of 725 °C under conditions of 0.15 % N_2O, and a Gas Hourly Space Velocity (GHSV) of 30 800 h^{-1}.[170,171] The same group then went on to study the effect of oxygen mobility based on the doping of $La_{0.4}Sr_{0.6}FeO_3$ catalysts with $LaSrFeO_4$ ferrite. Ivanov found that the $La_{0.4}Sr_{0.6}FeO_3$ doped with *ca.* 10 wt. % $LaSrFeO_4$ produced the most active catalyst, with a T_{50} of 815 °C under conditions of 0.15 % N_2O, and a GHSV of 30 800 h^{-1}. This catalyst outperforms others that were tested by Ivanov due to the increased oxygen surface exchange, which was suggested to be due to the formation of intergrown boundaries between the perovskite and layered-perovskite phases, which leads to the increased incorporation of surface oxygen in to the lattice.[172]

Takita and co workers investigated the effect of multiple A and B site atoms and ratios on the decomposition of N_2O using a $LaBaMnInO_3$ catalytic system. The group concluded that the $La_{0.7}Ba_{0.3}Mn_{0.8}In_{0.2}O_3$ ratios provided the most active catalyst for the decomposition of N_2O; decomposing 92 % at 500 °C, with a T_{50} at 443 °C under conditions of 10 % N_2O in He at 20 ml min^{-1} [173]; Kumar and co-workers reported a similar T_{50} by preparing a $Pr_{0.8}Ba_{0.2}MnO_3$ catalyst, initially by co-precipitation and then impregnation. The group achieved 100 % conversion at 550 °C under conditions of 0.5 % N_2O, balance He and a GHSV of 7500 h^{-1}.[174] The catalyst prepared by Kumar *et al.* are amongst the most active perovskites for N_2O decomposition reported in literature to date; a summary is provided in Table 1.1.

Table 1.1 The most relevant perovskite systems for N_2O decomposition and the temperature required for 50 % conversion (T_{50}).

Catalyst	**Conditions**	**T_{50} (°C)**	**Ref**
$LaCoO_3$	0.5 % N_2O, Helium, WHSV = 120 000 mL g^{-1} h^{-1}	445 (100 % at 550 °C)	169
$Pr_{0.8}Ba_{0.2}MnO_3$	0.5 g, 0.5 % N_2O, He balance. GHSV = 7500 h^{-1}	442 (100 % at 550 °C)	174
$La_{0.7}Ba_{0.3}Mn_{0.8}In_{0.2}O_3$	10 % N_2O in He, 20 ml min^{-1} W/F = 3.0 g s cm^{-3}	443 (92 % at 500 °C)	173
$La_{0.75}Sr_{0.25}MnO_3$	0.15 % N_2O GHSV = 30 800 h^{-1}	725	170,171
$La_{0.4}Sr_{0.6}FeO_3$	0.15 % N_2O GHSV = 30 800 h^{-1}	815	172

1.6 Project outline

The aim of the PhD is to advance understandings in the area of N_2O decomposition, initially trying to elucidate further information regarding the current catalysts used in literature and to use this new understanding of catalysts to prepare novel catalysts for the decomposition of N_2O. As mentioned at the start of this chapter it is extremely important to decompose N_2O as it has drastic consequences if released into the atmosphere.

Chapter 2 provides an outline of all the experimental techniques used in this thesis, from catalyst preparation and characterisation through to catalyst testing.

Chapter 3 looks at the importance of different Fe species in Fe-ZSM-5 for the decomposition of N_2O in the presence and absence of a reductant, propane. In

addition to comparing different Fe loadings, the efficacy of acid washing to increase the efficiency of the Fe in the active catalyst was investigated. UV/Vis spectroscopy was used to identify the different Fe species present and elucidate the active Fe species for the decomposition of N_2O. To overcome the issue of chlorine contamination, a modified sublimation technique denoted as Chemical Vapour impregnation (CVI) was used to prepare the series of catalysts, iron acetylacetonate {$Fe(acac)_3$} is used in place of $FeCl_3$, as acetylacetonate precursors are easily removed under vacuum.[108–110]

Chapter 4 studies the importance of surface species and particle size on Pd-Al_2O_3 catalysts for the decomposition of N_2O in the presence and absence of a reductant, propane. The effect of removal of surface species such as water and chloride ions have been investigated by different pre-treatments and support pre-treatments. In addition to comparing how activity changes based on these pre-treatments, the control of subsequent particle size and the effect this has on catalytic activity is evaluated. Through pre-treatment of the catalyst support prior to metal deposition, catalytic activity significantly increased, resulting in a decrease of the T_{100} from 550 °C to 400 °C.

Chapter 5 investigates the use of Perovskites for N_2O decomposition, most notably studying how the surface area, phase purity and oxygen species present effect the catalytic activity. The factors were investigated by changing the ratio of elements in the A and B sites, which lead to increased purities, requiring lower calcination temperatures and thus higher surface areas. The ratios that gave the highest phase purity were prepared by two alternative preparation methods to the original citric acid preparation, namely supercritical anti-solvent preparation and oxalic acid preparation. The preparation methods were compared for two catalysts, with no single preparation method being best for both. Instead, a factor of things made an improved perovskite catalyst for N_2O decomposition. For example, in the case of the $La_{0.75}Sr_{0.25}Co_{0.81}Fe_{0.19}O_x$, more lattice oxygen present resulted in a more active catalyst, whereas, for $Pr_{0.75}Ba_{0.25}CoO_x$, the catalyst with the most mobile lattice oxygen was the most active. Both these catalysts convert > 85 % N_2O at 500 °C, which is an improvement on the state of the art. [174]

1.7 References

1 G. Bond, *Heterogenous Catalysis: principles and applications*, Oxford University Press, 1974.

2 IUPAC Compendium of Chemical Terminology, *https://goldbook.iupac.org/html/C/C00876.html*, 2018-12–12.

3 R. H. Harding, A. W. Peters and J. R. D. Nee, *Appl. Catal. A Gen.*, 2001, **221**, 389–396.

4 J. Reppenhagen and J. Werther, *AIChE J.*, 2000, **45**, 2001–2010.

5 P. Atkins and J. de Paula, *Atkins Physical Chemistry*, Oxford University Press, 2006.

6 M. Bowker, *The Basis and Applications of Heterogenous Catalysis*, Oxford Science Publications, 1998.

7 IUPAC, in *Manual of Symbols and Terminology for Physicochemical Quantities and Units - Appendix II. Definitions, Terminology and Symbols in Colloid and Surface Chemistry. Part II: Heterogeneous Catalysis*, IUPAC, Research Triagle Park, NC, 1976, vol. 46, p. 81.

8 IUPAC Compendium of Chemical Terminology, *IUPAC Compendium of Chemical Terminology*, IUPAC, Research Triagle Park, NC, 2009.

9 N. W. Cant and W. K. Hall, *J. Phys. Chem.*, 1971, **75**, 2914–2921.

10 M. D. Allen and M. Bowker, *Catal. Letters*, 1995, **33**, 269–277.

11 M. Haruta, T. Kobayashi, H. Sano and N. Yamada, *Chem. Lett.*, 1987, 405–408.

12 G. J. Hutchings, *J. Catal.*, 1985, **96**, 292–295.

13 J. Zhang, N. Liu, W. Li and B. Dai, *Front. Chem. Sci. Eng.*, 2011, **5**, 514–520.

14 C. Woodford, *https://www.explainthatstuff.com/zeolites.html*, 2009, 2019-01–28.

15 N. Rahimi and R. Karimzadeh, *Appl. Catal. A Gen.*, 2011, **398**, 1–17.

16 J. Aguado, D. P. Serrano, J. M. Escola and A. Peral, *J. Anal. Appl. Pyrolysis*,

2009, **85**, 352–358.

17 J. S. Jung, J. W. Park and G. Seo, *Appl. Catal. A Gen.*, 2005, **288**, 149–157.

18 NASA, *https://www.nasa.gov/audience/foreducators/postsecondary/features/F_Ozone.html*, 2019-01–14.

19 S. Stolarski and J. Cicerone, *Can. J. Chem.*, 1974, **52**, 1610–1615.

20 D. J. Hofmann and T. Deshler, *J. Geophys. Res.*, 1991, **96**, 2897–2912.

21 J. Austin, N. Butchart and K. P. Shine, *Nature*, 1992, **360**, 221–225.

22 J. Hansen, M. Sato, P. Hearty, R. Ruedy, M. Kelley, V. Masson-delmotte, G. Russell, G. Tselioudis, J. Cao, E. Rignot, I. Velicogna, B. Tormey, B. Donovan, E. Kandiano, K. Von Schuckmann, P. Kharecha, A. N. Legrande and M. Bauer, *Atmos. Chem. Phys.*, 2016, **16**, 3761–3812.

23 S. Rahmstorf, *Science*, 2007, **315**, 368–370.

24 M. Meinshausen, N. Meinshausen, W. Hare, S. C. B. Raper, K. Frieler, R. Knutti, D. J. Frame and M. R. Allen, *Nature*, 2009, **458**, 1158–1162.

25 G. A. Meehl, W. M. Washington, W. D. Collins, J. M. Arblaster, A. Hu, L. E. Buja, W. G. Strand and H. Teng, *Science*, 2005, **307**, 1769–1772.

26 J. Oerlemans, *Science*, 1994, **264**, 243–245.

27 J. M. Last, *Annu. Rev. Public Health*, 1993, **14**, 115–136.

28 W. J. M. Martens, *Environ. Health Perspect.*, 1998, **106**, 241–251.

29 D. L. Hartmann, J. M. Wallace, V. Limpasuvan, D. W. J. Thompson and J. R. Holton, *Proc. Natl. Acad. Sci. U. S. A.*, 2000, **97**.

30 B. Diffey, *Phys. Med. Biol.*, 2004, **49**, R1–R11.

31 J. Priestly, *Experiments and Observations on Different Kinds of Air*, London, Vol II., 1776.

32 H. Davy, *Researches, chemical and philosophical: Chiefly concerning Nitrous Oxide or Dephlogisticated Nitrous Air and its respiration*, Oxford University, 1800.

33 J. Spahni R. amd Chapellaz, T. F. Stocker, L. Loulergue, G. Hasamman, K. Kawamura, J. Fluckiger, J. Schwander, D. Raynaud, J.-M. Barnola, H. Fischer, V. Masson-Delmotte and J. Jouzel, *Science*, 2005, **310**, 1317–1321.

34 A. Schilt, M. Baumgartner, T. Blunier, J. Schwander, R. Spahni, H. Fischer and T. F. Stocker, *Quarternary Sci. Rev.*, 2010, **29**, 182–192.

35 D. M. Etheridge, L. P. Steele, R. J. Francey and R. L. Langenfelds, *J. Geophys. Res. Atmos.*, 1998, **103**, 15979–15993.

36 D. M. Etheridge, L. P. Steele, R. L. Langenfelds, R. J. Francey, J. M. Barnola and V. I. Morgan, *J. Geophys. Res.*, 1996, **101**, 4115–4128.

37 NASA and AGAGE (Advanced Global Atmospheric Gases Experiment), 2018, 13-01–2019.

38 M. Battle, M. Bender, T. Sowers, P. Tans, J. Butler, J. Elkins, J. Ellis, T. Conway, N. Zhang, P. Lang and A. Clarke, *Nature*, 1996, **383**, 231–235.

39 AGAGE (Advanced Global Atmospheric Gases Experiment), *http://ds.data.jma.go.jp/gmd/wdcgg/cgi-bin/wdcgg/catalogue.cgi*, 13-01–2019.

40 NOAA (National Oceanic and Atmospheric Administration)., *www.esrl.noaa.gov/gmd/hats/insitu/cats/cats_conc.html*, 13-01–2019.

41 Intergovernmental Panel on Climate Change, *Climate Change 2007 Synthesis Report*, 2008.

42 L. Li, J. Xu, J. Hu and J. Han, *Environ. Sci. Technol.*, 2014, **48**, 5290–5297.

43 Intergovernmental Panel on Climate Change, *Climate Change 2013: The Physical Science Basis. Contribution of Working Group I to the Fifth Assessment Report of the Intergovernmental Panel on Climate Change*, 2013.

44 K. Pilegaard, *Philos. Trans. R. Soc. B Biol. Sci.*, 2013, **368**.

45 Z. Hu, J. W. Lee, K. Chandran, S. Kim and S. K. Khanal, *Environ. Sci. Technol.*, 2012, **46**, 6470–80.

46 K. Butterbach-bahl, E. M. Baggs, M. Dannenmann, R. Kiese and S.

Zechmeister-boltenstern, *Phil. Trans. R Soc. B*, 2013, **368**, 1–20.

47 D. S. Reay, E. A. Davidson, K. A. Smith, P. Smith, J. M. Melillo, F. Dentener and P. J. Crutzen, *Nat. Clim. Chang.*, 2012, **2**, 410–416.

48 J. Pérez-Ramírez, F. Kapteijn, K. Schöffel and J. A. Moulijn, *Appl. Catal. B Environ.*, 2003, **44**, 117–151.

49 United Nations Environment Programme (UNEP), *Drawing Down N2O To Protect Climate and the Ozone Layer*, 2013.

50 S. S. Maroufi, M. J. Gharavi, M. Behnam and A. Samadikuchaksaraei, *Iran. J. Public Health*, 2011, **40**, 75–79.

51 M. Odaka, N. Koike and H. Suzuki, *Chemosph. - Glob. Chang. Sci.*, 2000, **2**, 413–423.

52 J. Baronick, B. Heller, G. Lach and B. Ramacher, in *SAE Technical Paper*, 2000.

53 M. G. M. Berges, R. M. Hofmann, D. Scharffe and P. J. Crutzen, *J. Geophys. Res. Atmos.*, 1993, **98**, 18527–18531.

54 J. M. Dasch, *J. Air Waste Manag. Assoc.*, 1992, **42**, 63–67.

55 Space Propulsion Group, *http://www.spg-corp.com/nitrous-oxide-safety.html*, 2015-10–29.

56 F. Kapteijn, J. Rodriguez-Mirasol and J. A. Moulijn, *Appl. Catal. B Environ.*, 1996, **9**, 25–64.

57 J. Weimann, *Best Pract. Res. Clin. Anaesthesiol.*, 2003, **17**, 47–61.

58 P. Grace and L. Barton, *http://theconversation.com/meet-n2o-the-greenhouse-gas-300-times-worse-than-co2-35204*, 2015-10–29.

59 Green House Protocol, *Global Warming Potential Values (AR5)*, 2015, vol. 2014.

60 R. W. Portmann, J. S. Daniel and A. R. Ravishankara, *Philos. Trans. R. Soc. B Biol. Sci.*, 2012, **367**, 1256–1264.

61 Parliament of the United Kingdom, *Climate Change Act 2008*, 2008.

62 United Nations, *Kyoto Protocol To the United Nations Framework Kyoto*

Protocol To the United Nations Framework, 1998, vol. 7.

63 European Parliament; European Council, *Directive 2009/28/EC on the promotion of the use of energy from renewable sources*, 2009, vol. 140.

64 United Nations, *Convention on Climate Change: Climate Agreement of Paris.*, 2015.

65 J. European Union, *DIRECTIVE 2007/46/EC OF THE EUROPEAN PARLIAMENT AND OF THE COUNCIL of 5 September 2007 establishing a framework for the approval of motor vehicles and their trailers, and of systems, com- ponents and separate technical units intended for such vehicles*, 2007.

66 P. Anastas and J. C. Warner, *Green Chemistry: Theory and Practice*, Oxford University Press, New Ed., 2000.

67 N. Russo, D. Mescia, D. Fino, G. Saracco and V. Specchia, *Ind. Eng. Chem. Res.*, 2007, **46**, 4226–4231.

68 M. I. Konsolakis, *ACS Catal.*, 2015, **5**, 6397–6421.

69 H. Ohtsuka, T. Tabata, O. Okada, L. M. F. Sabatino and G. Bellussi, *Catal. Letters*, 1997, **44**, 265–270.

70 H. Ohtsuka, T. Tabata, O. Okada, L. M. . Sabatino and G. Bellussi, *Catal. Today*, 1998, **42**, 45–50.

71 R. W. Van Den Brink, S. Booneveld, M. J. F. M. Verhaak and F. A. De Bruijn, *Catal. Today*, 2002, **75**, 227–232.

72 G. Centi and F. Vazzana, *Catal. Today*, 1999, **53**, 683–693.

73 H. Abdulhamid, E. Fridell and M. Skoglundh, *Top. Catal.*, 2004, **30/31**, 161–168.

74 G. Djéga-Mariadassou, F. Fajardie, J. F. Tempère, J. M. Manoli, O. Touret and G. Blanchard, *J. Mol. Catal. A Chem.*, 2000, **161**, 179–189.

75 L. He, L. C. Wang, H. Sun, J. Ni, Y. Cao, Y. He and K. N. Fan, *Angew. Chemie - Int. Ed.*, 2009, **48**, 9538–9541.

76 K. Teramura, T. Tanaka, H. Ishikawa, Y. Kohno and T. Funabiki, *J. Phys. Chem. B*, 2004, **108**, 346–354.

77 K. Yogo, M. Ihara, I. Terasaki and E. Kikuchi, *Chem. Lett.*, 1993, **22**, 229–232.

78 R. Burch and P. K. Loader, *Appl. Catal. B Environ.*, 1994, **5**, 149–164.

79 S. Kesraoui-Ouki, C. R. Cheeseman and R. Perry, *J. Chem. Technol. Biotechnol.*, 1994, **59**, 121–126.

80 Y. Zheng, X. Li and P. K. Dutta, *Sensors*, 2012, **12**, 5170–5194.

81 J. Li, H. Chang, L. Ma, J. Hao and R. T. Yang, *Catal. Today*, 2011, **175**, 147–156.

82 B. Bogdanov, D. Georgiev, K. Angelova and K. Yaneva, in *International Science Conference*, 2009, vol. I, pp. 482–487.

83 Lenntech, *https://www.lenntech.pl/zeolites-structure-types.htm*, 2019-01–31.

84 C. Baerlocher and L. B. McCusker, *www.iza-structure.org/databases/*, 2019-01–31.

85 J. Weitkamp, *Solid State Ionics*, 2000, **131**, 175–188.

86 M. Rai, A. Yadav and A. Gade, *Biotechnol. Adv.*, 2009, **27**, 76–83.

87 D. Farrusseng and A. Tuel, *New J. Chem.*, 2016, **40**, 3933–3949.

88 D. Coster, A. L. Blumenfeld and J. J. Fripiat, *J. Phys. Chem.*, 1994, **98**, 6201–6211.

89 R. A. Van Santen, in *Studies in Surface Science and Catalysis*, 1994, vol. 85, pp. 273–294.

90 M. Rauscher, K. Kesore, R. Mönnig, W. Schwieger, A. Tißler and T. Turek, *Appl. Catal. A Gen.*, 1999, **184**, 249–256.

91 B. M. Abu-Zied, W. Schwieger and A. Unger, *Appl. Catal. B Environ.*, 2008, **84**, 277–288.

92 S. Sklenak, P. C. Andrikopoulos, B. Boekfa, B. Jansang, J. Nováková, L. Benco, T. Bucko, J. Hafner, J. Ddeek and Z. Sobalík, *J. Catal.*, 2010, **272**, 262–274.

93 B. R.Wood, J. A. Reimer and A. T. Bell, *J. Catal.*, 2002, **209**, 151–158.

94 Z. Sobalik, J. Novakova, J. Dedecek, N. K. Sathu, E. Tabor, P. Sazama, P.

Stastny and B. Wichterlova, *Micropor. Mesopor. Mat.*, 2011, **146**, 172–183.

95 I. Melián-Cabrera, E. R. H. van Eck, S. Espinosa, S. Siles-Quesada, L. Falco, A. P. M. Kentgens, F. Kapteijn and J. A. Moulijn, *Appl. Catal. B Environ.*, 2017, **203**, 218–226.

96 M. Mauvezin, G. Delahay, B. Coq, S. Kieger, J. C. Jumas and J. Olivier-Fourcade, *J. Phys. Chem. B*, 2001, **105**, 928–935.

97 A. H. Øygarden and J. Pérez-Ramírez, *Appl. Catal. B Environ.*, 2006, **65**, 163–167.

98 K. Jíša, J. Nováková, M. Schwarze, A. Vondrová, S. Sklenák and Z. Sobalik, *J. Catal.*, 2009, **262**, 27–34.

99 J. A. Z. Pieterse, S. Booneveld and R. W. Van Den Brink, *Appl. Catal. B Environ.*, 2004, **51**, 215–228.

100 L. Li, Q. Shen, J. Li, Z. Hao, Z. P. Xu and G. Q. M. Lu, *Appl. Catal. A Gen.*, 2008, **344**, 131–141.

101 J. H. Park, J. H. Choung, I. S. Nam and S. W. Ham, *Appl. Catal. B Environ.*, 2008, **78**, 342–354.

102 B. Chen, N. Liu, X. Liu, R. Zhang, Y. Li, Y. Li and X. Sun, *Catal. Today*, 2011, **175**, 245–255.

103 S. C. Christoforou, E. A. Efthimiadis and I. A. Vasalos, *Catal. Letters*, 2002, **79**, 137–147.

104 Q. Zhu, E. J. Hensen, B. L. Mojet, J. H. van Wolput and R. A. van Santen, *Chem Commun*, 2002, 1232–1233.

105 A. V Kucherov, C. N. Montreuil, T. N. Kucherova and M. Shelef, *Catal. Letters*, 1998, **56**, 173–181.

106 H.-T. Lee and H.-K. Rhee, *Catal. Letters*, 1999, **61**, 71–76.

107 L. J. Lobree, I. Hwang, J. A. Reimer and A. T. Bell, 1999, **63**, 233–240.

108 M. M. Forde, R. D. Armstrong, C. Hammond, Q. He, R. L. Jenkins, S. A. Kondrat, N. Dimitratos, J. A. Lopez-Sanchez, S. H. Taylor, D. Willock, C. J. Kiely and G. J. Hutchings, *J. Am. Chem. Soc.*, 2013, **135**, 11087–11099.

109 M. M. Forde, R. D. Armstrong, R. McVicker, P. P. Wells, N. Dimitratos, Q. He, L. Lu, R. L. Jenkins, C. Hammond, J. A. Lopez-Sanchez, C. J. Kiely and G. J. Hutchings, *Chem. Sci.*, 2014, 3603–3616.

110 V. Peneau, R. D. Armstrong, G. Shaw, J. Xu, R. L. Jenkins, D. J. Morgan, N. Dimitratos, S. H. Taylor, H. W. Zanthoff, S. Peitz, G. Stochniol, Q. He, C. J. Kiely and G. J. Hutchings, *ChemCatChem*, 2017, **9**, 642–650.

111 A. Ates, C. Hardacre and A. Goguet, *Appl. Catal. A Gen.*, 2012, **441**–**442**, 30–41.

112 J. Pérez-Ramírez, J. C. Groen, A. Brückner, M. S. Kumar, U. Bentrup, M. N. Debbagh and L. A. Villaescusa, *J. Catal.*, 2005, **232**, 318–334.

113 C. Hammond, Cardiff University, 2011.

114 F. Kapteijn, G. Mul, J. a Moulijn and J. Perez-Ramirez, 2002, **35**, 227–234.

115 G. Li, E. A. Pidko, I. A. W. Filot, R. A. Van Santen, C. Li and E. J. M. Hensen, *J. Catal.*, 2013, **308**, 386–397.

116 J. Perez-Ramirez, F. Kapteijn, J. C. Groen, A. Domenech, G. Mul and J. A. Moulijn, *J. Catal.*, 2003, **214**, 33–45.

117 K. Sun, H. Zhang, H. Xia, Y. Lian, Y. Li, Z. Feng, P. Ying and C. Li, *Chem. Commun.*, 2004, 2480–2481.

118 E. J. M. Hensen, Q. Zhu, M. M. R. M. Hendrix, A. R. Overweg, P. J. Kooyman, M. V. Sychev and R. A. Van Santen, *J. Catal.*, 2004, **221**, 569–583.

119 J. Pérez-Ramírez, F. Kapteijn and A. Brückner, *J. Catal.*, 2003, **218**, 234–238.

120 V. I. Sobolev, G. I. Panov, A. S. Kharitonov, V. N. Romannikov, A. M. Volodin and K. G. Ione, *J. Catal.*, 1993, **139**, 435–443.

121 G. I. Panov, A. S. Kharitonov and V. I. Sobolev, *Appl. Catal. A, Gen.*, 1993, **98**, 1–20.

122 G. I. Panov, V. I. Sobolev and A. S. Kharitonov, *J. Mol. Catal.*, 1990, **61**, 85–97.

123 G. D. Pirngruber, *J. Catal.*, 2003, **219**, 456–463.

124 G. I. Panov, E. V. Starokon, L. V. Pirutko, E. A. Paukshtis and V. N. Parmon, *J.*

Catal., 2008, **254**, 110–120.

125 M. V. Parfenov, E. V. Starokon, L. V. Pirutko and G. I. Panov, *J. Catal.*, 2014, **318**, 14–21.

126 Y. K. Chow, N. F. Dummer, J. H. Carter, C. Williams, G. Shaw, D. J. Willock, S. H. Taylor, S. Yacob, R. J. Meyer, M. M. Bhasin and G. J. Hutchings, *Catal. Sci. Technol.*, 2017, 154–163.

127 C. Fernandez, I. Stan, J. P. Gilson, K. Thomas, A. Vicente, A. Bonilla and J. Pérez-Ramírez, *Chem. - A Eur. J.*, 2010, **16**, 6224–6233.

128 M. Wu, H. Wang, L. Zhong, X. Zhang, Z. Hao, Q. Shen, W. Wei, G. Qian and Y. Sun, *Cuihua Xuebao/Chinese J. Catal.*, 2016, **37**, 898–907.

129 K. Sun, H. Zhang, H. Xia, Y. Lian, Y. Li, Z. Feng, P. Ying and C. Li, *Chem. Commun.*, 2004, **216**, 2480–2481.

130 K. A. Dubkov, N. S. Ovanesyan, A. A. Shteinman, E. V. Starokon and G. I. Panov, *J. Catal.*, 2002, **207**, 341–352.

131 A. Ribera, I. W. C. E. Arends, S. De Vries, J. Pérez-Ramírez and R. A. Sheldon, *J. Catal.*, 2000, **195**, 287–297.

132 G. I. Panov, A. K. Uriarte, M. A. Rodkin and V. I. Sobolev, *Catal. Today*, 1998, **41**, 365–385.

133 Q. Zhu, E. J. Hensen, B. L. Mojet, J. H. van Wolput and R. A. van Santen, *Chem Commun*, 2002, 1232–1233.

134 G. Pekridis, C. Athanasiou, M. Konsolakis, I. V. Yentekakis and G. E. Marnellos, *Top. Catal.*, 2009, **52**, 1880–1887.

135 M. Machida, T. Watanabe, S. Ikeda and T. Kijima, *Catal. Commun.*, 2002, **3**, 233–238.

136 Y. Tateishi, T. Tsuneyuki, H. Furukawa, S. Kagawa, I. Moriguchi, Y. Kanmura and Y. Teraoka, *Catal. Today*, 2008, **139**, 59–63.

137 K. Doi, Y. Y. Wu, R. Takeda, A. Matsunami, N. Arai, T. Tagawa and S. Goto, *Appl. Catal. B Environ.*, 2001, **35**, 43–51.

138 K. Zorn, S. Giorgio, E. Halwax, C. R. Henry, H. Gronbeck and G. Rupprechter,

J. Phys. Chem. C, 2011, **115**, 1103–1111.

139 T. Maillet, C. Solleau, J. Barbier and D. Duprez, *Appl. Catal. B Environ.*, 1997, **14**, 85–95.

140 A. S. Ivanova, E. M. Slavinskaya, R. V. Gulyaev, V. I. Zaikovskii, O. A. Stonkus, I. G. Danilova, L. M. Plyasova, I. A. Polukhina and A. I. Boronin, *Appl. Catal. B Environ.*, 2010, **97**, 57–71.

141 D. Roth, P. Gélin, A. Kaddouri, E. Garbowski, M. Primet and E. Tena, *Catal. Today*, 2006, **112**, 134–138.

142 D. Gao, C. Zhang, S. Wang, Z. Yuan and S. Wang, *Catal. Commun.*, 2008, **9**, 2583–2587.

143 J. Lu, B. Fu, M. C. Kung, G. Xiao, J. W. Elam, H. H. Kung and P. C. Stair, *Science*, 2012, **335**, 1205–1208.

144 H. Guesmi, D. Berthomieu and L. Kiwi-Minsker, *J. Phys. Chem. C*, 2008, **112**, 20319–20328.

145 C. Sang, B. H. Kim and C. R. F. Lund, *J. Phys. Chem. B*, 2005, **109**, 2295–2301.

146 N. Hansen, A. Heyden, A. T. Bell and F. J. Keil, *J. Phys. Chem. C*, 2007, **111**, 2092–2101.

147 D. A. Bulushev, L. Kiwi-minsker and A. Renken, *Ind. Eng. Chem. Res.*, 2004, **211**, 2004.

148 K. Sun, H. Xia, E. Hensen, R. van Santen and C. Li, *J. Catal.*, 2006, **238**, 186–195.

149 B. R.Wood, J. A. Reimer and A. T. Bell, *J. Catal.*, 2002, **209**, 151–158.

150 S. Parres-Esclapez, M. J. Illan-Gomez, C. S. M. de Lecea and A. Bueno-Lopez, *Appl. Catal. B Environ.*, 2010, **96**, 370–378.

151 M. Konsolakis, I. V. Yentekakis, G. Pekridis, N. Kaklidis, A. C. Psarras and G. E. Marnellos, *Appl. Catal. B Environ.*, 2013, **138**–**139**, 191–198.

152 M. De Graef and M. E. McHenry, *Structure of Materials: An introduction to Crystallography, Diffraction and Symmetry*, 2007.

153 N. Labhasetwar, G. Saravanan, S. Kumar Megarajan, N. Manwar, R.

Khobragade, P. Doggali and F. Grasset, *Sci. Technol. Adv. Mater.*, 2015, **16**, 036002.

154 A. S. Bhalla, R. Guo and R. Roy, *Mater. Res. Innov.*, 2000, **4**, 3–26.

155 J. Zhu, H. Li, L. Zhong, P. Xiao, X. Xu, X. Yang, Z. Zhao and J. Li, *ACS Catal.*, 2014, **4**, 2917–2940.

156 J. Hwang, R. R. Rao, L. Giordano, Y. Katayama, Y. Yu and Y. Shao-Horn, *Science*, 2017, **358**, 751–756.

157 R. J. H. Voorhoeve, D. W. Johnson, J. P. Remeika and P. K. Gallagher, *Science*, 1977, **195**, 827–833.

158 M. A. Peña and J. L. G. Fierro, *Chem. Rev.*, 2001, **101**, 1981–2017.

159 G. Centi and S. Perathoner, *Micropor. Mesopor. Mat.*, 2008, **107**, 3–15.

160 S. Keav, S. Matam, D. Ferri and A. Weidenkaff, *Catalysts*, 2014, **4**, 226–255.

161 L. A. Isupova, G. M. Alikina, S. V Tsybulya, N. N. Boldyreva, G. N. Kryukova, I. S. Yakovleva, V. P. Isupov and V. A. Sadykov, *Int. J. Inorg. Mater.*, 2001, **3**, 559–562.

162 J. Zhu, D. Xiao, J. Li, X. Xie, X. Yang and Y. Wu, *J. Mol. Catal. A Chem.*, 2005, **233**, 29–34.

163 J. Zhu, X. Yang, X. Xu and K. Wei, *J. Phys. Chem. C*, 2007, **111**, 1487–1490.

164 J. Zhu, Z. Zhao, D. Xiao, J. Li, X. Yang and Y. Wu, *J. Mol. Catal. A Chem.*, 2005, **238**, 35–40.

165 H. Tanaka and M. Misono, *Curr. Opin. Solid State Mater. Sci.*, 2001, **5**, 381–387.

166 L. Marchetti and L. Forni, *Appl. Catal. B Environ.*, 1998, **15**, 179–187.

167 R. J. H. Voorhoeve, J. P. Remeika and L. E. Trimble, *Ann. N. Y. Acad. Sci.*, 1976, **272**, 3–21.

168 J. Il Jung, H. Y. Jeong, J. S. Lee, M. G. Kim and J. Cho, *Angew. Chemie - Int. Ed.*, 2014, **53**, 4582–4586.

169 N. Russo, D. Mescia, D. Fino, G. Saracco and V. Specchia, *Ind. Eng. Chem.*

Res., 2007, **46**, 4226–4231.

170 D. V. Ivanov, E. M. Sadovskaya, L. G. Pinaeva and L. A. Isupova, *J. Catal.*, 2009, **267**, 5–13.

171 D. V. Ivanov, L. G. Pinaeva, L. A. Isupova, A. N. Nadeev, I. P. Prosvirin and L. S. Dovlitova, *Catal. Letters*, 2011, **141**, 322–331.

172 D. V. Ivanov, L. G. Pinaeva, L. A. Isupova, E. M. Sadovskaya, I. P. Prosvirin, E. Y. Gerasimov and I. S. Yakovleva, *Appl. Catal. A Gen.*, 2013, **457**, 42–51.

173 T. Ishihara, M. Ando, K. Sada, K. Takiishi, K. Yamada, H. Nishiguchi and Y. Takita, *J. Catal.*, 2003, **220**, 104–114.

174 S. Kumar, A. Vinu, J. Subrt, S. Bakardjieva, S. Rayalu, Y. Teraoka and N. Labhsetwar, *Catal. Today*, 2012, **198**, 125–132.

2 Experimental

This chapter outlines the experimental methods used in this thesis. Catalyst preparation methods are explained, including the chemicals and their suppliers. The characterisation techniques used are also described along with the principles behind them. The catalyst testing and reactor set-ups are also described.

2.1 List of Chemicals

Table 2.1 lists the chemicals used in this thesis, the supplier and purity of the substances. All reagents were used as received without further purification.

Table 2.1. List of chemicals used

Substance	Supplier	Purity
γ-Al_2O_3	Sigma Aldrich	> 99.5 %
$PdCl_2$	Sigma Aldrich	99 %
H-ZSM-5	Zeolyst	99 %
Fe(acetylacetonate)$_3$	Sigma Aldrich	99.9 %
HNO_3 (70 %)	Fisher Scientific	Extra Pure
HCl (37 %)	Fisher Scientific	Extra Pure
Oxalic Acid	Sigma Aldrich	> 99 %
Citric Acid	Sigma Aldrich	> 99.5 %
$La(NO_3)_2.6H_2O$	Sigma Aldrich	99.999 %
$Sr(NO_3)_2$	Sigma Aldrich	99.995 %
$Co(NO_3)_2.6H_2O$	Sigma Aldrich	99.999 %
$Fe(NO_3)_3.9H_2O$	Sigma Aldrich	> 99.95 %
$Ba(NO_3)_2$	Sigma Aldrich	99.999 %
$Pr(NO_3)_3.6H_2O$	Sigma Aldrich	99.9 %
$Sr(CH_3CO_2)_2$	Sigma Aldrich	99.995 %
$Co(CH_3CO_2)_2.4H_2O$	Sigma Aldrich	99.999 %
$Fe(CH_3CO_2)_2$	Sigma Aldrich	95 %
$Ba(CH_3CO_2)_2$	Sigma Aldrich	99.999 %
$Pr(CH_3CO_2)_2.xH_2O$	Sigma Aldrich	99.9 %
La(acetylacetonate)$_3$.xH_2O	Sigma Aldrich	99.9 %
Ethanol	Sigma Aldrich	99.8 %
N_2O	BOC	99.9 %
Propane	BOC	99.99 %
Ethane	BOC	99.99 %
Methane	BOC	99.99 %

Helium	BOC	99.99 %
Nitrogen	BOC	> 99.99%
Oxygen	BOC	> 99.99 %

2.2 Catalyst Preparation

A number of catalysts were prepared during the course of this thesis. Examples of each procedure are provided below.

2.2.1 Wet impregnation

Supported metal catalysts were prepared by impregnation as described by Pekridis *et al*. [1] $PdCl_2$ was dissolved in deionised water to give a solution with a concentration of 6 mg mL^{-1}. To this metal solution (4.6 mL), γ-Al_2O_3 support (0.98 g, Sigma Aldrich) was added and heated slowly to 55 °C until a slurry was formed. The slurry was then dried in an oven at 120 °C for 2 h, and calcined at 600 °C for 4 h at 10 °C min^{-1} in flowing air. Further heat treatments carried out at 600 °C for 1 h at 20 °C min^{-1} in flowing air.

The impregnation preparation method stated in 2.2.1 was followed to prepare the following catalysts:

- 2 wt. % Pd-Al_2O_3
- 2 wt. % Pd-Al_2O_3 support calcined before catalyst preparation at 600 °C for 4 h at 10 °C min^{-1} in flowing air, indicated by "SC".

2.2.2 Support calcination before catalyst preparation

Commercially sourced Al_2O_3 was treated at high temperatures to remove any impurities and excess water before catalyst preparation. γ-Al_2O_3 (~3 g) was placed in a high alumina combustion boat and placed inside a quartz tube within a combustion furnace. The glass tube was sealed so that flowing air could be passed over the sample. The furnace was heated to 600 °C at a rate of 10 °C min^{-1} and held for 4 h. The calcined support was left to cool to room temperature under flowing air, before being removed for catalyst preparation.

2.2.3 Hydrochloric acid Modified Impregnation Preparation

2 wt.% Pd-Al_2O_3 was prepared by modified impregnation as described by Morad and co-workers.[2] $PdCl_2$ was dissolved in water to give a solution with a concentration of 5.725 mg mL^{-1}, HCl was added to acidify the solution until a concentration of 0.58 M was achieved. De-ionised water was added to the solution (3.49 mL) to a total volume of 16 mL in a 50 mL round bottom flask. The solution was heated to 60 °C in an oil bath. γAl_2O_3 (0.98 g, Sigma Aldrich) was added to the solution slowly over a period of 10 min. The slurry was left to stir for 15 min and then the temperature was increased to 95 °C and left to dry for 16 h. The resulting sample was calcined at 600 °C for 4 h at 10 °C min^{-1} in flowing air.

The modified impregnation preparation method described in 2.2.3 was followed to prepare the following catalysts:

- 2 wt. % Pd-Al_2O_3 MI
- 2 wt. % Pd-Al_2O_3 SC MI

2.2.4 Chemical Vapour Impregnation (CVI)

A series of supported metal catalysts were prepared by CVI following the procedure described by Forde *et al*.[3,4] Prior to catalyst preparation, zeolite supports were dried under vacuum, and then placed into a Schlenk flask and evacuated at room temperature using a vacuum line, followed by heating at 150 °C for 1 h under continuous vacuum to remove any surface water species. The metal acetylacetonate precursor and support were placed into a glass vial and mixed by manual shaking. The obtained mixture was transferred to a 50 mL Schlenk flask fitted with a magnetic stirrer bar and sealed. The flask was then evacuated at room temperature using a vacuum line followed by heating at 150 °C for 2 h, under continuous vacuum conditions, with stirring to induce sublimation and deposition of the organometallic precursor onto the support. The flask was brought up to atmospheric pressure with air and the sample removed and calcined at 550 °C in static air for 3 h for zeolite catalysts.

The chemical vapour impregnation preparation method described in 2.2.4 was followed to prepare the following catalysts:

- 2.5 wt. % Fe-ZSM-5 (23)
- 2.5 wt. % Fe-ZSM-5 (30)
- 1.25 wt. % Fe-ZSM-5 (23)
- 1.25 wt. % Fe-ZSM-5 (30)
- 0.4 wt. % Fe-ZSM-5 (23)
- 0.4 wt. % Fe-ZSM-5 (30)
- 0.16 wt. % Fe-ZSM-5 (23)

Brackets represents the SiAl ratio of the zeolites used.

2.2.5 Acid washing

Acid washing was performed by heating 10 v/v% $HNO_{3(aq)}$ (50 mL) to 50 °C, adding the catalyst (0.25 g) and stirring for 10 min. The solution was filtered and washed with deionised water (1 L g^{-1}) followed by drying in an oven at 110 °C for 16 h. The samples obtained using this method were denoted as Acid Washed (AW).

2.2.6 Citric Acid Preparation

Perovskite based catalysts were prepared by citric acid preparation as described by Fierro *et al.*[5,6] Deionised water (50 mL) was stirred and heated to 50 °C in a round bottom flask. Metal nitrates were added to the solution and allowed to dissolve. Citric acid (metal : citric acid = 1:2 molar ratio) was added to the solution and the temperature increased to 90 °C, after 30 min the temperature was increased to 110 °C and left for 16 h. Following grinding, all catalysts were pre-treated in a chamber oven at 1 °C min^{-1} at a temperature greater than 200 °C to pass the point of citric acid combustion, as inferred by TGA, as this can lead to explosions if not controlled. Finally the materials were calcined in flowing air at a suitable temperature to form a pure phase perovskite, as determined by in-situ XRD.

The citric acid preparation method described in 2.2.6 was followed to prepare the following catalysts:

- $Ba_{0.5}Pr_{0.5}CoO_x$
- $SrCo_{0.81}Fe_{0.19}O_x$
- $La_{0.75}Sr_{0.25}CoO_x$
- $La_{0.75}Sr_{0.25}Co_{0.81}Fe_{0.19}O_x$

- $Pr_{0.75}Ba_{0.25}CoO_x$

2.2.7 Oxalic Acid Preparation

Perovskite catalysts were prepared using oxalic acid as a precipitation agent, based on the work by Fan *et al.*[7–9] Metal nitrates were added in the appropriate ratios totalling 0.02 moles of metal to ethanol (200 mL, Sigma Aldrich 99.8 %) and stirred. Once the metal salts were dissolved oxalic acid (0.024 moles, Sigma Aldrich, > 99 %) was added and the solution was left to age for 2 h at room temperature. After aging, the solution was filtered and washed with ethanol (500 mL) and dried in oven at 110 °C for 16 h. The resulting solid was pre-treated in a chamber oven at 300 °C, followed by calcination in flowing air at a suitable temperature to form a pure phase perovskite, as determined by in-situ XRD.

The oxalic acid preparation method described in 2.2.7 was followed to prepare the following catalysts:

- $La_{0.75}Sr_{0.25}Co_{0.81}Fe_{0.19}O_x$
- $Pr_{0.75}Ba_{0.25}CoO_x$

2.2.8 Supercritical Anti-Solvent (SAS) Preparation, equipment set-up, conditions and method

The Supercritical Anti-Solvent (SAS) operational mode involves a flowing system when high-pressure CO_2 and metal solvent solutions are fed into the precipitation vessel at the same time using a co-axial nozzle system. The nozzle contains an inner tube through which the metal precursor solution is pumped and an outer tube through which the CO_2 anti solvent is pumped. The CO_2 flow rate is controlled by the pump and the pressure of the system is controlled by the position of the needle valve with in the backpressure regulator (BPR) which is located downstream of the precipitation vessel. The metal precursor solution flow rate (4 mL min^{-1}) was controlled using a HPLC pump (Agilent 1200 series isocratic).

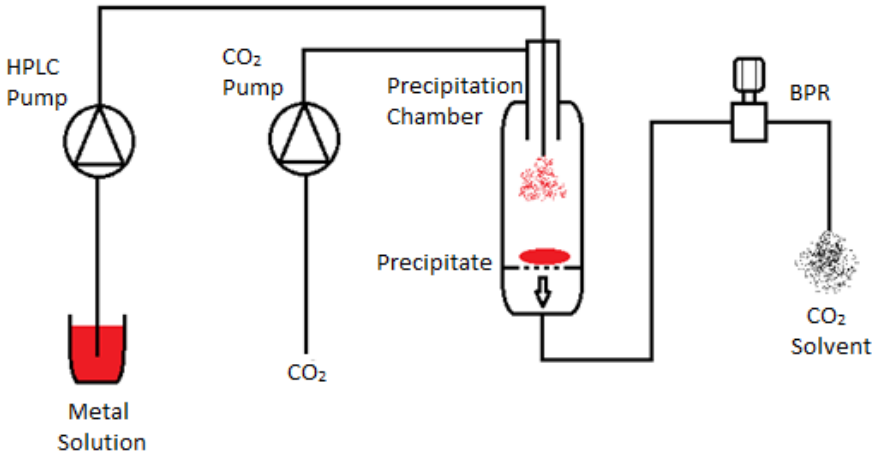

Fig. 2.1. Diagram showing set up of the SAS precipitation rig as used in the experimental.

Using the apparatus set up described above, perovskite precursors were synthesised. Solutions of metal salts dissolved in ethanol (1000 mL) with ~ 5 % deionised water were made prior to the SAS process with all precursors being dissolved at the same time.

The SAS experiments were performed by first pressurising the system with CO_2 to the required pressure of 150 bar using a flow rate of 12 kg h^{-1}. The heated jacket around the precipitation chamber was maintained at 40 ^{o}C. Pure solvent was pumped through the system for 10 minutes to allow the system to equilibrate and clean the residual waste from the system. Then the metal solution was pumped at a flow rate of 4 mL min^{-1} for approximately 2 h. To remove any remaining solvent and dry the precipitate, $scCO_2$ was flowed for 1 h with the HPLC pump turned off. The system was then brought back to atmospheric pressure by first turning off the $scCO_2$ flow and then unwinding the needle valve within the BPR before finally venting the system.

The SAS preparation method stated in 2.2.8 was followed to prepare the following catalysts:

- $La_{0.75}Sr_{0.25}Co_{0.81}Fe_{0.19}O_x$
- $Pr_{0.75}Ba_{0.25}CoO_x$

2.3 Characterisation Techniques

Many catalyst characterisation techniques have been used throughout this thesis. A summary of the theory and the experimental procedure required for each technique are provided.

2.3.1 Powder X-ray Diffraction (XRD)

XRD is a commonly used technique for the analysis of the bulk phases of powdered samples. The aim of this method is to use constructive interference of diffracted waves from a sample to form a diffraction pattern that can be used to identify the phases present and determine the crystallite sizes using the Scherrer equation.[10,11] Every crystalline compound produces a characteristic fingerprint under XRD which can be compared to the Powder Diffraction File to identify the compound.[12] It is important to note that amorphous solids will not produce a diffraction pattern as they do not possess long range order. The file contains detailed information on the d spacing and the estimated lines of diffraction. The method requires the sample to have long range order to produce constructive interference, such as a repeating unit cell. Therefore amorphous samples produce no diffraction data. The diffraction from a crystal can be described in terms of reflection from a set of lattice planes. Constructive interference is a results of satisfying the Bragg Equation. [13]

$$n\lambda = 2dsin\theta$$

Eq. 1. Bragg Equation, where *n* is the order of reflection (integer), λ is the wavelength of the X-rays, *d* is the distance between the lattice planes and θ is the angle of incidence.

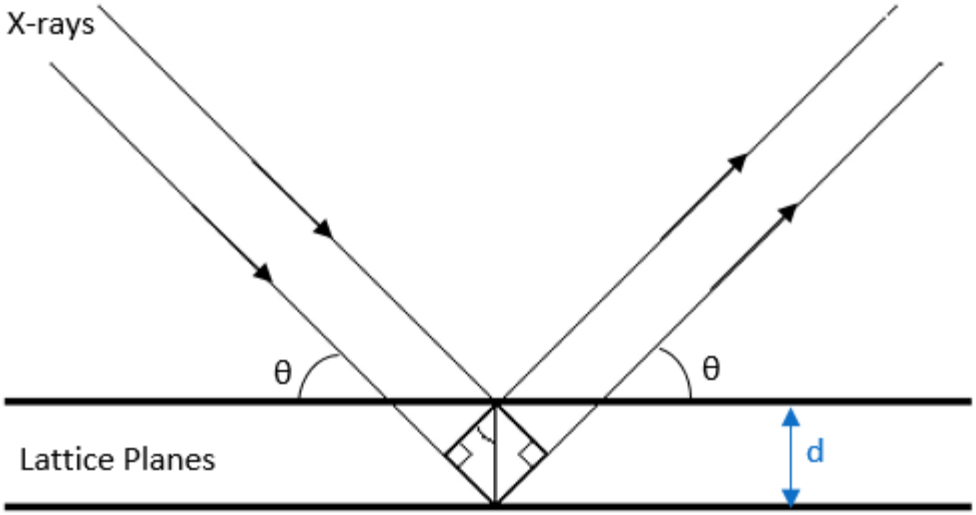

Fig. 2.2. Bragg Reflection from crystal planes with spacing d

Standard powder XRD involves the use of a static or moving mono-chromatic X-ray source that bombards a sample creating cones of constructive interference. Diffraction occurs when waves scattering with an object constructively and destructively interfere with each other. Destructive interference occurs when X-rays are out of phase and cancel out diffracted radiation. Constructive interference is a result of the randomly orientated crystallites, that allow the incident X-rays to be in phase with each other. The random orientation of the crystallites ensures that all lattice planes will interact with the X-rays at all possible angles and therefore satisfying Bragg's Law for each plane. A detector follows an arch path to intersect the diffraction cones, which allows the determination of X-ray intensity with respect to 2θ.

The Scherrer equation can be used to calculate the average crystallite size of the powdered sample [10,11]. This is based on the requirement of long-range order or crystallinity for XRD diffractograms to be produced. The larger the crystallite the narrower and sharper the reflections that are seen. However, below 100 nm particle size line broadening takes place due to incomplete destructive interference of out of phase X-rays. This broadening of the reflections is used in the calculation of the crystallite sizer using the Scherrer equation shown below.[14]

$$< L > = \frac{K\lambda}{\beta cos\theta}$$

Eq. 2. Scherrer equation, where $< L >$ is the crystallite size in the direction perpendicular to the lattice planes being analysed, K is a numerical factor frequently referred to as the crystallite shape factor, λ is the wavelength of the X-

rays, β is the full width half maximum of the diffraction peak in radians and ϑ is the Bragg angle in radians.

Powder X-ray diffraction (XRD) analysis was performed using a PANalytical X'pert Pro diffractometer with a Cu X-ray source operating at 40 keV and 40 mA, with $K_{\alpha 1}$ X-rays selected using a Ge (111) single crystal monochromator. Patterns were recorded over the 2θ angular range 10 - 80° using a step size of 0.016° (resulting in a total run time of 40 minutes) using a back filled sample holder. Diffraction patterns were identified using the International Centre for Diffraction Data (ICCD) Powder Diffraction File. [12]

2.3.2 *In-situ* X-ray Diffraction (XRD)

In-situ XRD uses the same theory as XRD stated in 2.3.1 but the spectrometer focuses the X-rays onto a cell containing a sample holder that can be heated and have gases flowed over it. This allows for XRD to be performed during either pre-treatment conditions or reaction conditions.

In-situ XRD was performed using a PANalytical X'pert Pro diffractometer with a Cu X-ray source operating at 40 keV and 40 mA, with $K_{\alpha 1}$ X-rays selected using a Ge (111) single crystal monochromator. The sample cell allows temperature control and gas flow using Bronkhorst mass flow controllers (MFC's). A computer program called 'High Score Data collector' was used to control the temperature settings, run time and scan repeats. The cell was packed with sample and loaded inside the scan unit of the diffractometer, with flow rates set and temperature controlled. Reflections within each sample were identified and compared to the ICDD Powder Diffraction File [12] which contains a database of reference patterns, enabling identification of compounds. Compounds can be compared based on elemental composition and the '% match' between the database file and the data.

For phase determination of perovskites the following *in situ* XRD profile was performed.

1. Set air flow to 25 ml min^{-1}.
2. Heat to 50 °C, wait 10 min, perform 2 scans from 15 to 70 °.
3. Heat to 400 °C at 10 °C min^{-1}, wait 10 min, perform 2 scans from 15 to 70 °.
4. Heat in 50 °C intervals at 10 °C min^{-1} and wait 10 min, perform 2 scans from 15 to 70 ° at each temperature up to 850 °C.

5. Cool to 50 °C, wait 10 min, perform 2 scans from 5 to 70 °.
6. Cool to room temperature and shut off gas flow.

2.3.3 Raman Spectroscopy

Raman spectroscopy measures the vibrational energy of molecules based on the changes of polarizability of the molecule. The excitation energies in Raman spectroscopy result in promotion to virtual energy states and then the relaxation back to the vibrational energy states. Excitation and relaxation to and from the same vibrational state is referred to as Raleigh Scattering. Raleigh scattering is an elastic process meaning both energy and momentum are conserved. Raman scattering is defined by a change in energy, both positive and negative. Stokes scattering is characterised by the kinetic energy of the incident radiation and the scattered photon being different; if the scattered photon gains energy then it is referred to as anti-stokes scattering where as if the photon loses energy then it is defined as stokes scattering.[15,16] Therefore only Stokes scattering is observed. For a molecule to be Raman active, the molecule must have changeable polarizability and not have any centres of symmetry, with selection rules stating that only bond vibrations and rotations are allowed. A change in frequency of the scattered light is due to a change in the vibration state on relaxation, which is a Raman effect. The measurement of this change in frequency from a sample irradiated with a laser allows the calculation of the vibrational energy states, providing information about the chemical bonds present and molecular structure that are characteristic to each sample.

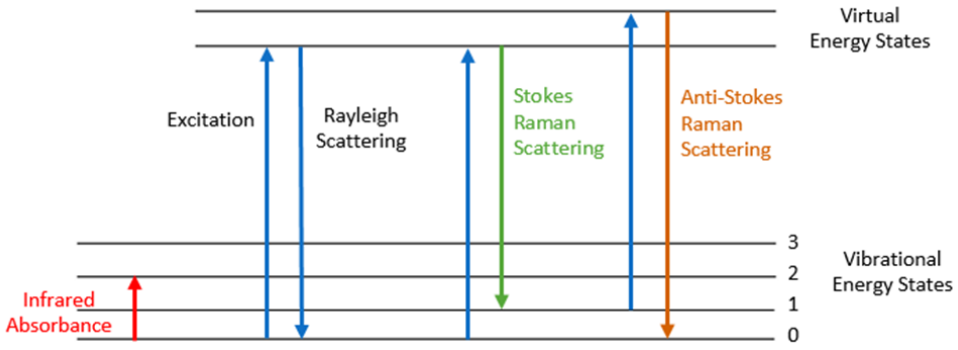

Fig. 2.3. Transitions between energy levels in IR and Raman Spectroscopy [15]

Raman spectroscopy was carried out using a Renishaw in Via Raman microscope fitted with a Stellar-REN 3B green Ar^+ laser (λ = 514 nm) operated at a power of 20 mW.

2.3.4 Thermogravimetric Analysis (TGA)

TGA allows the mass of a sample to be monitored as a function of time as the temperature is increased at a controlled rate. Volatile molecules and water loss or decomposition shows up as mass loss, whereas oxidation or adsorption shows as mass gain, however if total oxidation occurs this is seen as a mass loss. This technique can be performed under many different atmospheres. TGA provides quantitative information on sample composition based on specific weight loss correlating to functional groups at known temperatures. [17]

Analysis was carried out using a Perkin Elmer TGA 4000 to determine information on the decomposition pathways of catalyst precursors. The default TGA profile used between 20 – 30 mg sample with 50 mL min^{-1} air and a ramp rate of 5 °C min^{-1} unless otherwise stated. Perovskite catalysts require a more controlled temperature increase and therefore in the case of these catalysts the temperature ramp rate used was 1 °C min^{-1} with < 10 mg sample. Mass losses were recorded as changes in mg and converted into a percentage of the total mass of the sample.

2.3.5 Microwave Plasma Atomic Emission Spectroscopy (MP-AES)

MP-AES allows elemental analysis of a compound to be carried out in one run. Multi-element analysis can be carried out using AES with greater sensitivity than in atomic absorption spectroscopy (AAS) due to lower interference. A microwave nitrogen plasma heat source was used to create high temperatures to excite electrons to create a radiation source. The wavelength of this radiation is characteristic of the specific element used, and allows elemental concentrations to be determined.

A solution is sprayed through a nebuliser into a detection chamber that lies just below the microwave nitrogen plasma. The electrons within the sample are excited to a higher energy state by the plasma and then emit energy in the form of radiation (visible to UV) which is directed to the charge coupled device detector by a

diffraction grating where it is separated into its component wavelengths in an optical spectrometer. The intensity of the light is measured by photomultiplier tubes and correlated against known intensities at certain wavelengths to produce a concentration value in parts per million (PPM). Before any analysis is carried out, standards containing the known concentrations of the elements expected within the sample must be run to calibrate the AES equipment. [18,19]

AES was carried out using an Agilent 4100 MP-AES utilising Agilent MP expert software. Calibration samples were prepared by dilution of a standard metal solution with deionised water. A minimum of 4 calibration plots were used per analysis. Solid catalyst samples (50 mg) were dissolved in aqua regia (4 mL diluted to 50 mL with deionised water) to give a pre-calculated approximate metal concentration.

2.3.6 Inductively Coupled Plasma – Optical Emission Spectroscopy (ICP-OES)

Inductively Coupled Plasma – Optical Emission Spectroscopy uses the same technique as descried in 2.3.5 but, instead of a microwave plasma being used as a heat source, an inductively coupled plasma is used instead as the temperature achieved is much higher and therefore all elements are fully ionised. ICP-OES is used instead of MP-AES as the detection limits are much lower in ICP-OES.

Inductively Coupled Plasma – Optical Emission Spectroscopy (ICP-OES) was performed by Exeter Analytical Services using HF digestion to get an accurate Fe loading. The sample was digested by an Anton Paar Multiwave 3000 microwave with nitric acid and HF – then the HF was neutralised with the addition of boric acid. A reagent blank was carried out. An internal standard was added to the resulting solutions, and the blank and sample were run against Fe standards by ICP-OES using Thermo Fisher iCAP Duo 7400.

2.3.7 Temperature Programmed Reduction (TPR)

Temperature programmed reduction measures the reducibility of a sample and the reducible species present. This is achieved by heating the sample in a reducing

atmosphere such as diluted hydrogen at various temperatures controlled by a program to ensure a linear ramp rate.

The sample was heated as a function of time in a furnace under a flowing gas mixture of 10% H_2 in Ar. The results show the different species present in the sample and how easily they are reduced (i.e. temperature required). These results give information on the presence of different oxidation states or the effect of a dopant in a lattice. This technique is useful for measuring the temperature required for complete reduction of a catalyst and is commonly used to analyse the interaction of a metal with its support. Hydrogen has a high thermal conductivity meaning a decrease in hydrogen concentration is marked by a decrease in conductivity of the gas mixture. This change is measured by a thermal conductivity cell as a function of either time or temperature. The peaks in a TPR spectrum show the temperature at which various reduction steps take place. If a species is reduced, and hydrogen is consumed, a positive peak is seen on the TCD signal that is used to monitor the H_2 flow. Sometimes a negative peak is seen due to the sample releasing H_2 when heated, an example of is this Pd which can exist as Pd-H before reduction takes place. The volume of hydrogen consumed can be determined by the area under the peak, when compared to a CuO calibration.[17]

TPR was carried out using a ChemBET TPR/TPD equipped with a TCD to monitor hydrogen uptake. A pre-treatment in He up to 150 ^{o}C was performed, followed by a reduction in 10 %H_2/Ar up to 800 ^{o}C, held for 30 min at T_{max}, using an attenuation of 4, TCD sensitivity of 150 and flow 15 mL min^{-1}. The sample mass used was typically between 40 – 50 mg.

2.3.8 CO Chemisorption

CO chemisorption can be used to determine the dispersion, metal surface area and average crystallite size of active metal in a catalyst sample.

Chemisorption takes place when an interaction such as bond formation takes place between an adsorbates and the sample surface, whereas physisorption refers to a weak physical interaction. Initially chemisorption involves the formation of a monolayer of adsorbate on the surface of the active sites by bond formation. However, it is possible for further absorption to take place on top of the mono-layer and form multi-layers which should be considered when chemisorption techniques

are performed. Multi-layers form when CO binds to a monolayer of CO that has already formed on the surface of the active metal. This only normally happens when a molecule is polar and both physical and chemical adsorption may occur at the surface at the same time. A layer of molecules may be physically adsorbed on top of an underlying chemisorbed layer. [20]

The CO chemisorption process involves reducing an active component of a catalyst and then pulsing a known volume of CO (adsorbate) over the catalyst and recording the volume that is not adsorbed on the metal by the TCD response. Initially no response should be seen for the first couple of pulses, and as the metal becomes saturated more of a response is registered, until the response does not change and the metal is fully saturated, and no further CO is adsorbed. The total volume of CO absorbed can be converted into a dispersion value when the stoichiometry, binding modes and metal loading are considered. The 'TPR Win' software makes use of three key equations, metal surface area, dispersion, and average crystallite size.

Metal surface area is defined as the surface area of active sites present in the sample surface as $m^2\ g^{-1}$ from the following equation:

$$Metal\ Surface\ Area\ (MSA) = \frac{N_a\ V_m}{S_f S_d}$$

Eq. 3. Metal surface area equation, where: N_a = Avogadro's number, V_m = Gas adsorbed at monolayer (mol g^{-1}), S_f = Stoichiometric factor of reaction, S_d = Metal surface density.

Dispersion is defined as the amount of metal atoms exposed and available to act as catalyst and propagate the reaction, given as a percentage of the total metal loading from the following reaction:

$$Dispersion = \frac{V_m\ M\ 10^4}{S_f\ x}$$

Eq. 4. Dispersion equation, where: V_m = Gas adsorbed at monolayer (mol g^{-1}), M = molecular weight of the active metal, S_f = Stoichiometric factor of reaction and x = total metal loading of the sample.

Average particle size is defined as the using the metal surface area as follows:

$$Average\ Particle\ Size = \frac{100\ N\ f}{MSA\ \rho}$$

Eq. 5. Average particle size equation in nm, where: *N* = mass of the active metal, *f* = shape correlation factor, *MSA* = metal surface area, and *ρ* = active metal density.

CO Chemisorption was performed using a ChemBET TPR/TPD pulsar with a reduction in 10 %H_2/Ar up to 120 °C before carrying out CO chemisorption at room temperature using 10 % CO/He using an attenuation of 2, TCD sensitivity of 150 and CO flow of 15 mL min^{-1}. An automated pulse program was used with a pulse length of 400 seconds, loop volume 125 µL, 16 pulses and a stable baseline.

2.3.9 Oxygen Temperature Programmed Desorption (O_2 TPD)

Temperature programmed desorption of oxygen measures the oxygen mobility of the species present, i.e. the more mobile the oxygen the lower the temperature at which desorption will take place at. This is achieved by heating the sample in a clean atmosphere such as helium to remove any surface species, followed by dosing of oxygen at high temperatures and cooling to room temperature, followed by the desorption of oxygen in helium environment controlled by a program to ensure a linear ramp rate.

The sample was pre-treated to 550 °C at 10 °C min^{-1} and held for 30 min in helium (30 ml min^{-1}) to remove any surface species that may give a false TCD response such as water. After completion of the pre-treatment, the gas was switched to 10 % O_2/He and held at 550 °C for 30 mins to allow adsorption of oxygen. The sample was then cooled in the O_2 atmosphere to room temperature and the gas switched to He, after a wait of 1 h the temperature programmed desorption was performed. This involved heating the sample to 850 °C at 10 °C min^{-1}, whilst measuring the TCD signal and temperature.

The results show the different oxygen species present in the sample and how mobile they are (i.e. the temperature required for desorption). The more labile the oxygen, the more available it is for reaction and subsequently the more active the catalyst.

Oxygen has a different thermal conductivity to helium, meaning the desorption of oxygen leads to a difference of conductivity of the gas mixture. This change is

measured by a thermal conductivity detector (TCD) as a function of either time or temperature. TPD curves are the representation of the TCD signal versus temperature.

Oxygen TPD was carried out using a ChemBET TPR/TPD equipped with a TCD to monitor oxygen evolution. A pre-treatment in He up to 550 ^{o}C was performed, followed by dosing of oxygen using 10 %O_2/He at 550 ^{o}C, the sample was cooled to room temperature and the gas changed to He, followed by desorption of oxygen up to 850 °C at 10 °C min^{-1} and held for 10 min at the maximum temperature (T_{max}), using an attenuation of 2, TCD sensitivity of 150 and flow 30 mL min^{-1}. The sample mass used was typically 60 mg.

2.3.10 Brunauer Emmett Teller surface area determination (BET)

Total surface area is an important characteristic of a catalyst and is commonly determined using the Brunauer Emmett Teller (BET) technique.[21] The data produced is characterised by a specific isotherm which plots the number of molecules adsorbed relative to pressure. The number of molecules can be converted to volume of gas physisorbed or surface coverage. The BET isotherm allows multilayer adsorption and enables the different enthalpies of these layers to be accounted for.

The pore structure defines the isotherm shape that is produced when N_2 adsorption takes place. There are 4 different types of isotherms shown in Fig. 2.4, with the BET isotherm being based on either type I or type II. Type I refers to the formation of a monolayer, whilst type II refers to the gradual formation of a monolayer and pressure increase that leads to the formation of a multilayer. Type IV refers to the formation of a monolayer followed by the filling of the micropores. The black dot in the isotherms in Fig. 2.4 represent the point at which a monolayer has formed.

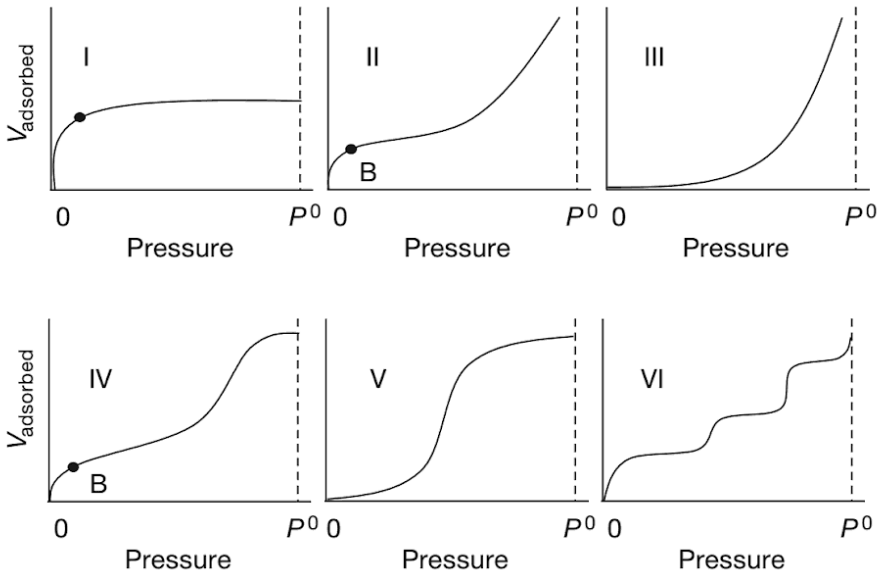

Fig. 2.4. Nitrogen adsorption isotherm types, showing the many types of adsorption that are possible with the dot representing the point at which a monolayer has formed, adapted from reference [22]

The BET equation can be represented in a linear form to give a gradient of [(C-1)/V_mC], which equates to the volume of surface adsorbed gas. Based on the molecules adsorbed, the surface area can be determined, i.e. molecule size multiplied by number of molecules adsorbed. [23]

$$\frac{P}{V(P_o - P)} = \frac{1}{V_m C} + \frac{(C-1)}{V_m C} \cdot \frac{P}{P_o}$$

Eq. 6. BET equation where V = Volume of gas adsorbed, V_m = monolayer volume, P_o = saturation gas pressure, P = specific gas pressure, C = BET constant that accounts for the enthalpies of adsorption for the monolayer and subsequent layers.

$$C = e^{\frac{\Delta H_D^o - \Delta H_{VAP}^o}{RT}}$$

Eq. 7. Equation for the C constant described above, where $\Delta H_D{}^o$ is the enthalpy of desorption (strength of adsorbate – surface interaction) and $\Delta H_{VAP}{}^o$ is the enthalpy of vaporisation (Adsorbate – adsorbate interaction in multilayer) [24].

Nitrogen adsorption isotherms were collected using either Quantachrome Quadrasorb evo or a Micrometric 3Flex (where necessary i.e zeolites, which have micropores which can not be analysed using the Quantachrome Quadrasorb evo). For the Quantachrome Quadrasorb evo a 20-point analysis was performed using N_2 as the adsorbate gas. Samples were degassed for 14 h at 300 °C prior to analysis. With the 3Flex, samples (0.050 g) were degassed (250 °C, 9 h) prior to analysis. Analyses was carried out at -196 °C with P_0 measured continuously. Free space was

measured post analysis with He. Pore size analysis was carried out using Density Functional Theory (DFT) (N_2-Cylindrical Pores-Oxide surface) via the Micrometrics 3Flex software.

2.3.11 X-Ray Photoelectron Spectroscopy (XPS)

XPS is a commonly used characterisation technique that can be used for the analysis of surface species, such as surface elemental analysis and determination of the metal oxidation state. XPS is a surface technique and therefore information is only obtained to a depth of 1 - 5 nm, depending on the photoelectron kinetic energy.

XPS is based upon the photoelectric effect; if a sample is irradiated with light of a small enough wavelength electrons will be emitted, with the sample atoms irradiated by a monochromatic X-Ray radiation source. If the energy of the incident photon is equal to or greater than that of the binding energy of a core or valence electron then the electron is ejected and has a resulting kinetic energy [25] as given by the equation:

$$E_k = h\upsilon - E_b - \varphi$$

Eq. 8. Equation used to calculate the resulting kinetic energy of an electron after being ejected from core. Where E_k = ejected electrons kinetic energy, h = Planck's constant, υ = frequency of the incident radiation, E_b = binding energy of the electron, ϕ = work function of the spectrometer.

The binding energy depends on a number of factors such as; the element the electron is emitted from, the orbital from which the electron is ejected and the chemical environment of the atom from which the electron was emitted. All elements have a characteristic binding energy of an ejected electron. Intensity at a binding energy can therefore be correlated back to a specific element. It is also possible to determine the oxidation state of the element present as the energy levels of the core electrons depend on the oxidation state of the atom. For example, a metal in an oxide form has a higher binding energy compared to that of the metallic form due to having a higher resulting kinetic energy as the binding energy of the electron is lower.

X-ray photoelectron spectroscopy (XPS) was performed using a Thermo Fisher Scientific K-alpha$^+$ spectrometer. A micro-focused monochromatic Al X-ray source (72 W) was used to analyse samples over an area of 400 microns. Data was recorded

at pass energies of 150 eV for survey scans and 40 eV for high resolution scan with 1 eV and 0.1 eV step sizes respectively. A combination of both low energy electrons and argon gas were used for charge neutralisation of the sample. Data analysis was performed in CasaXPS using a Shirley type background and Scofield cross sections, with an energy dependence of -0.6.

2.3.12 Solid State magic angle spin nuclear magnetic resonance (MAS-NMR)

MAS-NMR spectroscopy is an experimental technique that provides information on the chemical environment of atoms present in a solid sample. Solid State NMR allows the study of atoms that have a magnetic moment due to having an uneven number of protons and/or neutrons in the nucleus. Nuclear spin is quantised (I) which can be either a whole or half number depending on the number of unpaired protons and neutrons. There are $2I + 1$ levels that are associated to nuclear spin, when no magnetic field is applied these are the same. When a magnetic field is applied these levels become different with $2I + 1$ states that can either align or oppose the magnetic field. The applied magnetic field causes the molecules to resonate between the energy levels and this frequency that this occurs at is characteristic of a molecule.

In liquid samples line broadening is not a problem as they are removed by rapid molecular motions, i.e. tumbling. In solids this is not the case and therefore the sample must be spun quickly (> 5 kHz) around the magic angle of $\theta = 54.7\ °$. Both dipolar and chemical shielding interactions contain $(3\cos^2\theta\text{-}1)$ terms, in the liquid state rapid isotropic tumbling occurs, averaging this spatial component to zero. In the solid state by spinning at 54.7 °, the magic angle, it is possible to average the anisotropic interaction to zero by using a rate of MAS greater than the interaction. This makes the equation $3\cos^2\theta\text{-}1$ negligible and therefore removes the line broadening, by mimicking the rapid tumbling that occurs in liquids and allows higher resolution spectra to be obtained. Without satisfying this equation, i.e. spinning at an angle that is not 54.7 °, the line broadening would not be removed and the spectra would resemble an agglomeration of all species present in the sample.[13]

Solid-state NMR spectra were obtained at the EPSRC UK National Solid-state NMR Service at Durham. Solid state ^{1}H Proton and ^{27}Al spectra were recorded at 399.88 MHz using a Varian VNMRS spectrometer and a 4 mm (rotor outer diameter) magic-angle spinning probe. They were obtained using a background suppression pulse sequence, 128 repetitions with a 1 s recycle delay and a spin-rate of approximately 14 kHz. Spectral referencing was to external, neat tetramethylsilane carried out by setting the resonance from adamantane to 1.9 ppm.

2.3.13 Diffuse Reflectance UV/Vis Spectroscopy (UV/Vis)

Diffuse Reflectance UV/Vis spectroscopy is a characterisation technique that can be used to define the different species of an element present based on their response to UV radiation. UV radiation exhibits wavelengths in the region of 200 – 400 nm. In this region it is possible to promote valence electrons (HOMO) to higher energy levels (LUMO), by absorbing photons of specific energy. The energy needed to promote an electron from the HOMO to the LUMO depends on the bonding system and atoms involved, therefore the wavelength at which an absorption band is observed provides information on the ionic charge, environment and electronic bonding, all of which have an effect on the transition energy.[26] The Beer Lambert law can be used to calculate the concentration of absorbing species based on the absorbance as long as the correct molar extinction coefficient is used.

$$A = \varepsilon[c]l$$

Eq. 9. Beer lambert law, where A = absorbance, ε = molar extinction coefficient, $[c]$ = concentration, l = path length of sample cell.

Allowed electronic transitions are determined by the spin and Laporte selection rules. The spin selection rule ($\Delta S = 0$) means that changes in spin multiplicity are forbidden. The Laporte selection states that for a transition to occur a change in symmetry of the complex is needed. Some useful transitions such as d → d absorptions in transition metals are 'not allowed' due to the lack of change in the symmetry, so does not satisfies the Laporte selection rule.

UV/Vis spectra are produced when a UV light source is shone on a catalyst and the light that is reflected is measured, the wavelengths at which light is absorbed are shown as peaks, where as troughs are seen when light is emitted. The higher the absorbance value, the more of a particular wavelength is being absorbed. The

wavelength that corresponds to the highest absorption is usually referred to as 'lambda-max' λ_{max}.

Diffuse Reflectance UV/Vis spectra was collected using an Agilent Cary 4000 UV/Vis spectrophotometer. Prior to analysis samples were ground into a fine powder using an agate pestle and mortar, then loaded into a sample cell. Background scans were run on a high purity PTFE disc. Samples were scanned between 200 and 800 nm at a scan rate of 150 nm min^{-1}, with a UV-visible changeover wavelength of 350 nm.

2.3.14 Electron Microscope Techniques

Electron Microscopy (EM) is an extremely useful characterisation technique that is used to determine the topology, morphology and elemental composition of a sample. EM can also be used to determine the size and shape of supported metal nano-particles, leading to particle size distributions. [25]

EM is based on the interaction of an electron beam with a sample. As electrons have wavelengths in the range of an atomic radius (< 1 Å) it is therefore possible to obtain images with atomic detail.

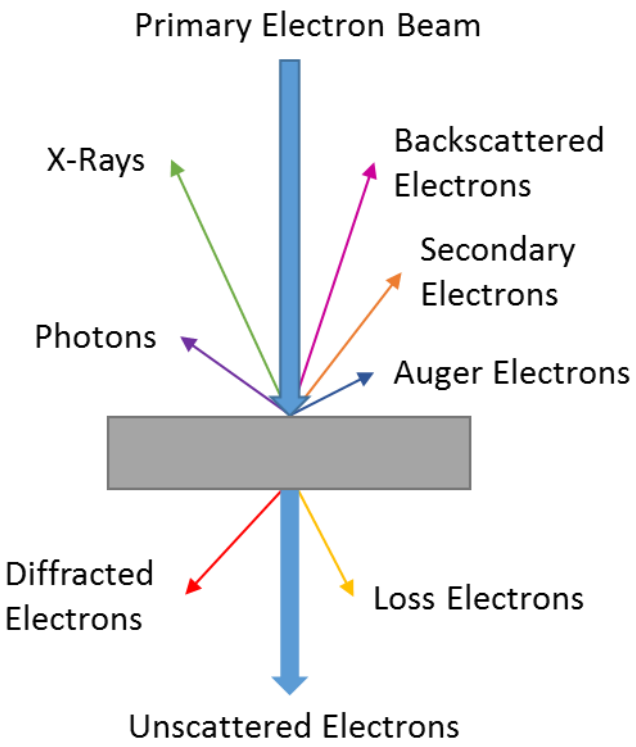

Fig. 2.5. Diagram explaining how the electron beam interacts with the sample in electron microscope.

Fig. 2.5. shows the main processes of the electrons as they pass through the sample that provide different information about the specimen. For instance, diffracted electrons can give information about the crystallographic structure. Backscattered electrons are also useful as these provide information about the distribution of atoms in the sample, as the electron beam is scattered by the collision with atoms in the sample, the heavier the atoms the greater the chance of an elastic collision occurring due to their greater cross-sectional area. To keep the electron beam focussed a vacuum is used. Different types of apertures and lenses are used to focus the beam into a fine point on the sample and to produce different types of emissions.

Scanning Electron Microscopy (SEM) detects either secondary or backscattered electrons based on the beam position. SEM can be used to determine topology, morphology and composition of a sample, up to a depth of 3 – 10 nm.

Transmission Electron Microscopy (TEM) detects both transmitted scattered and unscattered electrons. Bright field images represent a 2D projection of the transmitted electrons, with intensity dependent on the mass distribution of atoms and the density and thickness of the sample. Dark field electrons represent those electrons that have been diffracted by the sample and therefore are at an angle that is different to that of the transmitted beam. It is possible to increase contrast in the image by altering the attenuation of the electron beam and by altering the thickness and density of the sample. TEM is commonly used in catalysis to determine dispersion, particle size, morphology and chemical composition of supported metal nano-particles.

STEM combines both Scanning Electron Microscopy (SEM) and Transmission Electron Microscopy (TEM) operational modes. The user can select a specific region of the sample to irradiate with the primary electron beam and obtain a bright or dark field image. To obtain an image with an increased contrast of supported metal nanoparticles, an image can be produced by the electrons that are diffracted by the metal nano-particles, this is referred to as a dark field image. The intensity of a HAADF image is proportional to the square of the atomic number, by the equation $((1.4)^2 \times \text{atomic number})^2$, therefore heavy atoms are observed brighter but light atoms can be difficult to observe.

High-Angle Annular Dark-Field Scanning Transmission Electron Microscopy (HAADF-STEM) was performed by Dr. Qian He initially at Lehigh University and then finally Diamond Light source. In both, a JEOL ARM 200CF AC-STEM instrument was used and the samples were prepared using the dry dispersion route: The catalyst powder was ground between two clean glass slides and then dry transferred onto a holey carbon TEM grid.

2.3.15 Point of Zero Charge (PZC)

The point of zero charge (PZC) of an oxide support can have a significant effect on metal dispersion and particle size during impregnation preparation of a catalyst. An oxide support contains terminal hydroxyl groups that are protonated or deprotonated depending on the acidity of the solution, the pH at which the hydroxyl groups are overall neutral is the point of zero charge. It is important to determine the point of zero charge of an oxide support before catalyst preparation if an impregnation technique is to be used, as the pH of the impregnation solution affects the species that will bind to the support. For example, if the pH of the solution is below that of the PZC, the hydroxyl groups are protonated and become positively charged, then the surface can absorb anionic metal complexes; above the PZC, the hydroxyl groups are deprotonated and become negatively charged and cations will be strongly absorbed. In the case of platinum, two different precursors are used for preparation depending on the support PZC: if the pH < PZC, chloroplatinic acid is used; if the pH > PZC platinum tetraamine is used (2.6), this is termed electrostatic absorption. [27] The PZC of Al_2O_3 was determined and the pH of the Pd solution used for impregnation were determined to see the effect of electrostatic absorption on the catalysts preparation.

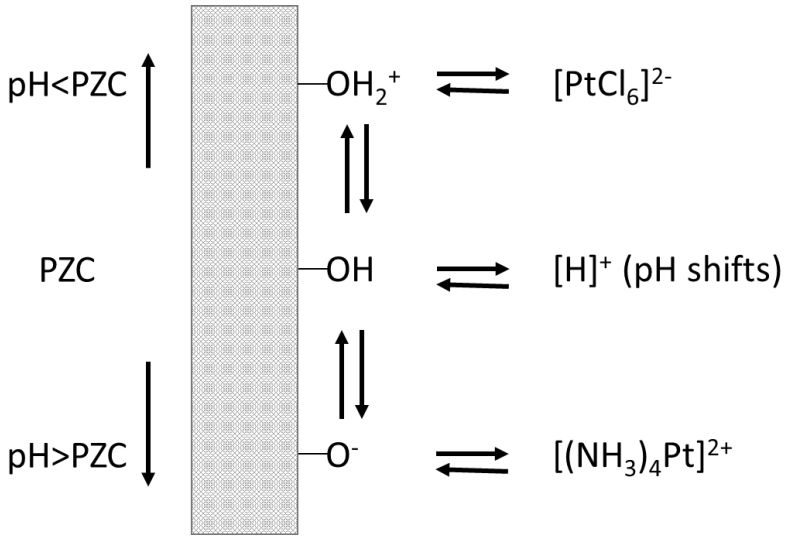

Fig. 2.6. Components of electrostatic adsorption mechanism, surface charging, metal adsorption and proton transfer. Reproduced from 'Synthesis of solid catalysts' pg 34. [27]

PZC is determined by measuring the initial pH of a solution, adding a known mass of support and measuring the final pH. Done over a range of pH from 1 – 14, these two values are plotted against each other and the point at which a plateau is observed is the point of zero charge. In this case, solutions of known pH were prepared by serial dilution of 0.1 M NaOH and 0.1 M HCl to prepare 10 mL of solution, of which 1 mL was used for the next dilution to leave 9 mL for experiment. The initial pH was recorded, using a pH meter calibrated using pH 4, 7 and 9 buffer solutions, followed by the addition of Al_2O_3 (0.9 g). The solution was stirred and left to equilibrate for 15 minutes, and the final pH was recorded. The volumes and weights used were selected in relation to the fact that the higher the $m^2 L^{-1}$ (surface area per litre), the more obvious the plateau (Fig. 2.7). As the surface area of the support is *ca.* 120 $m^2 g^{-1}$, this equates to 12000 $m^2 L^{-1}$, and based on the information provided should provide an obvious plateau.

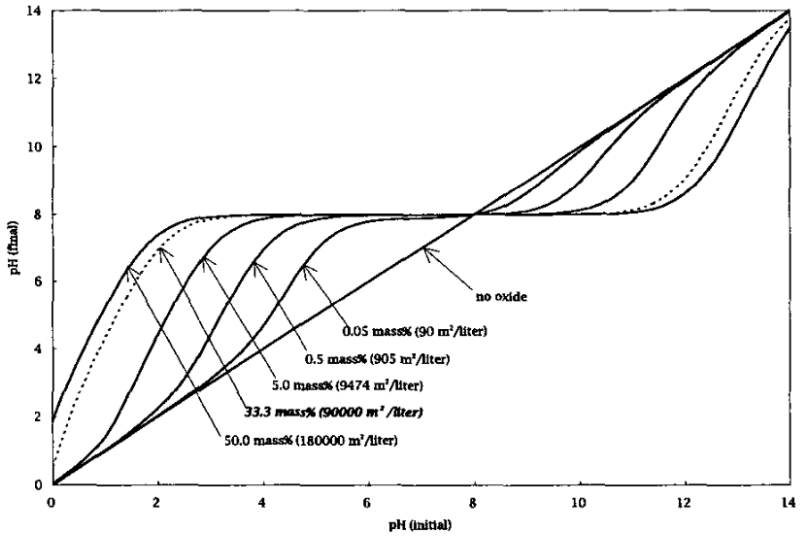

Fig. 2.7. Simulation of γ-alumina EpHL for various mass loadings (PZC = 8.0, Dp*K* = 5.0 s, s = 180 $m^2 g^{-1}$). Reproduced from "A simple, accurate determination of Oxide PZC and the strong buffering effect of Oxide surfaces at incipient wetness." [28]

2.4 Reactor Experimental

2.4.1 Reactor set up and catalyst testing

All reported reactions were performed at atmospheric pressure in a continuous flow fixed-bed reactor. Both stainless steel and quartz reactor tubes can be used for this reactor, so either a 35 cm length of 6.5 mm outer diameter stainless steel tube or a 20 cm length quartz tube with an internal diameter of 7 mm was packed with 0.0625 g of catalyst, which was then sandwiched between two layers of glass wool. The temperature range tested was 200 - 600 °C, with the temperature measured on a N-type thermocouple. The temperature was held at each temperature for 2 h to enable a steady state to be achieved before data was collected. A mixture of Bronkhorst and MKS mass flow controllers were used to control the incoming N_2O, nitrogen, oxygen, methane, ethane, propane and helium, for testing under a GHSV of 45,000 – 70,000 h^{-1}, with a total flow of 100 mL min^{-1}. Two gas regimes were tested, N_2O or N_2O and C_3H_8 at either a composition of 1 % reactants or 5 % reactants. All outgoing gaseous products were analysed online using an Agilent 7890B Gas Chromatograph (GC) (columns: Haysep Q (80-100 mesh, 1.8 m) MolSieve 5A (80-100 mesh, 2 m) fitted with a thermal conductivity detector (TCD) and flame ionisation detector (FID). The reactor scheme is shown in Scheme 2.1 with an image of the set up in Fig. 2.8.

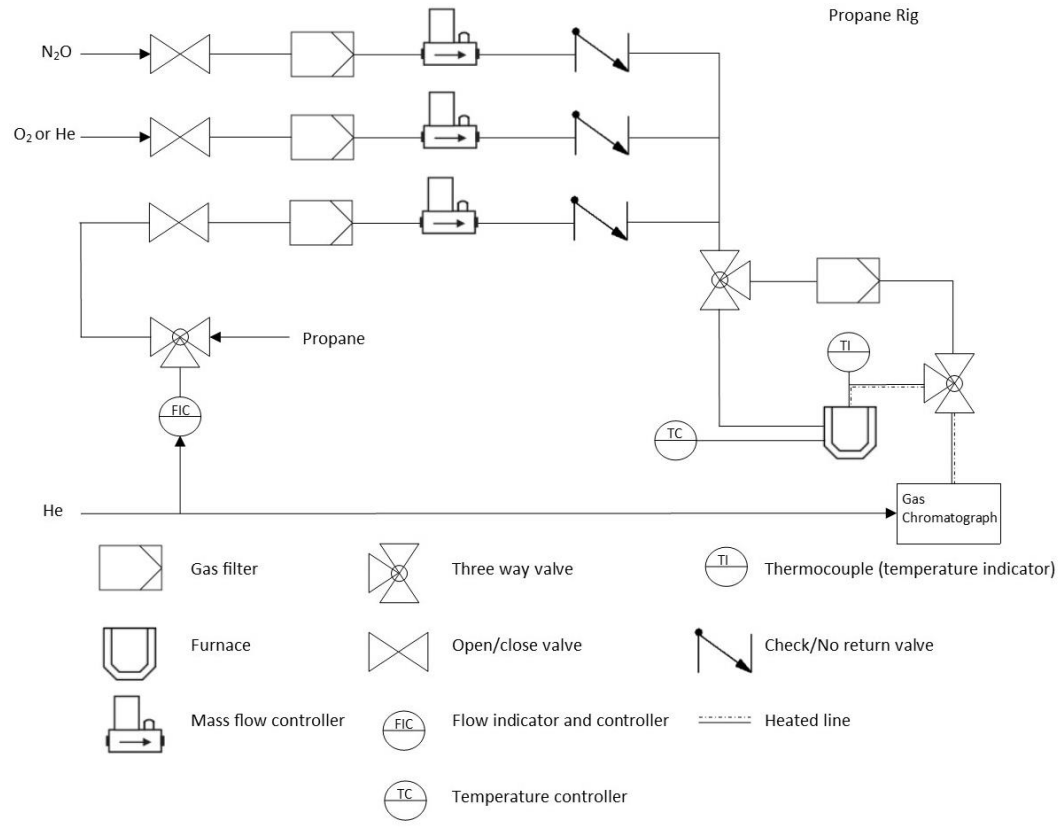

Scheme 2.1. P&ID diagram of the propane ODH Reactor used to test catalysts throughout this thesis.

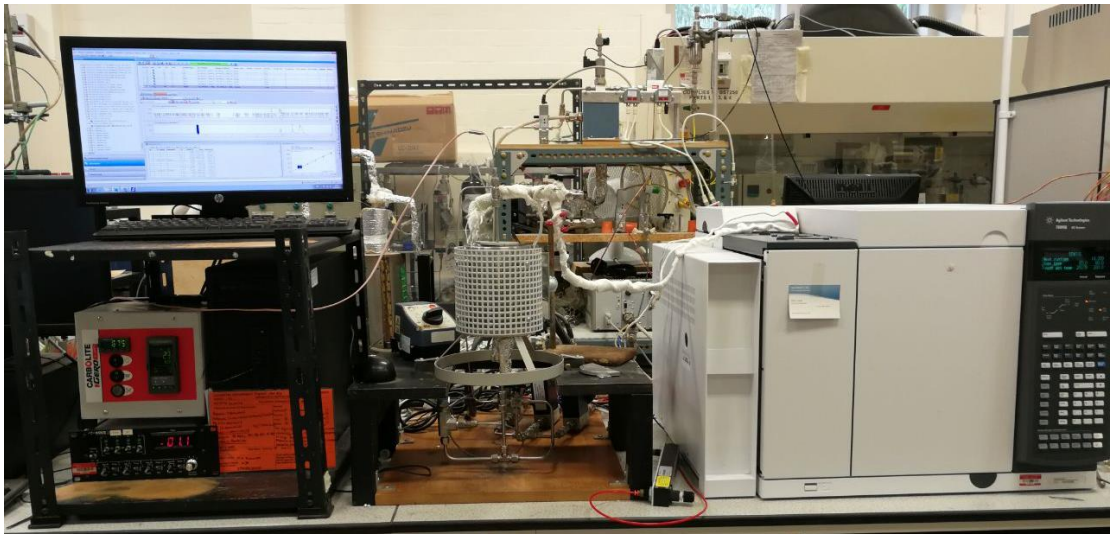

Fig. 2.8. Image of the propane ODH Reactor used to test catalysts throughout this thesis, located in Lab 1.86 in Cardiff Catalysis institute, Cardiff University Main Building.

2.4.2 Product analysis:

Agilent 7890B Gas Chromatograph (GC) fitted with an FID and TCD was used to separate analytes. The reaction gas was injected into the GC using a six port valve heated to 150 °C, with He used as the carrier gas. There are 3 six port valves in the GC that are used to control the flow of analytes through each column and detector, as shown in Table 2.2. At 0.5 min V3 is used to inject the analytes on to the HayeSep Q and Mol Sieve column, after 2 mins, the Mol Sieve column is switched out and the light analytes such as O_2 and N_2 are trapped on this column. This allows hydrocarbons and CO_2 top be eluted from the HayeSep Q column without compromising the integrity of the Mol Sieve column, as CO_2 irreversibly binds to it. At 13 minutes, the Mol Sieve column is brought back into sequence by the switching of valve 2, allowing the elution of the light gases.

Table 2.2. Valve sequence program, + = on, - = off.

Time (min)	**V3 Sample injection Fill (-) Inject (+)**	**V1 (Methaniser bypass) Series (+) Bypass (-)**	**V2 (Bypass) Series (+) Bypass (-)**
0.5	+	-	+
2	-	-	-
13	-	+	+

Hydrocarbons and CO_2 were separated using a HayeSep Q column (80-100 mesh, 1.8 m). O_2, N_2 and other light gases were separated using a MolSieve 5A (80-100 mesh, 2 m) column.

To start the GC method, analyte sample is injected onto the GC columns by the switching of valve 3 from the fill to inject position as shown in Fig. 2.9. In this instance the second valve is in the series position that allows the gas to elute onto both columns.

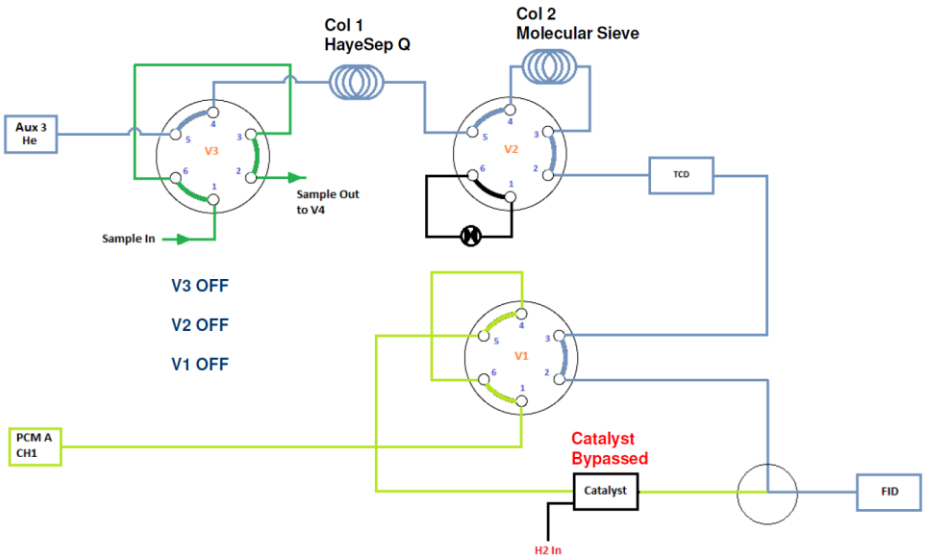

Fig. 2.9. Gas injection onto GC columns during analysis of N_2O decomposition products using propane as a reductant.

After a short period of time, the light gases such as N_2 and O_2 have eluted from the HayeSep Q column. The second valve switches so that the MolSieve column is bypassed, (highlighted in red) this is because CO_2 irreversibly binds to molecular sieve columns and would therefore cause damage to the GC if allowed to elute onto said column, as shown in Fig. 2.10.

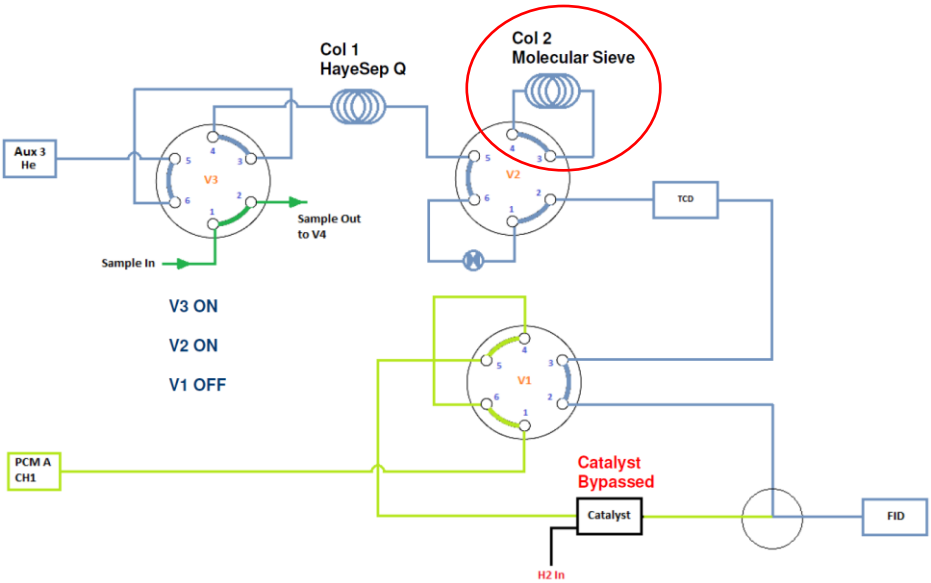

Fig. 2.10. Column change during analysis of N_2O decomposition products using propane as a reductant.

After the valve change shown in Fig. 2.10. CO_2, propane and other cracked products are eluted; after these gases have eluted the second valve switches to the series position to allow the elution of the trapped O_2 and N_2 gases that have been isolated in the bypassed MolSieve column as shown in Fig. 2.11.

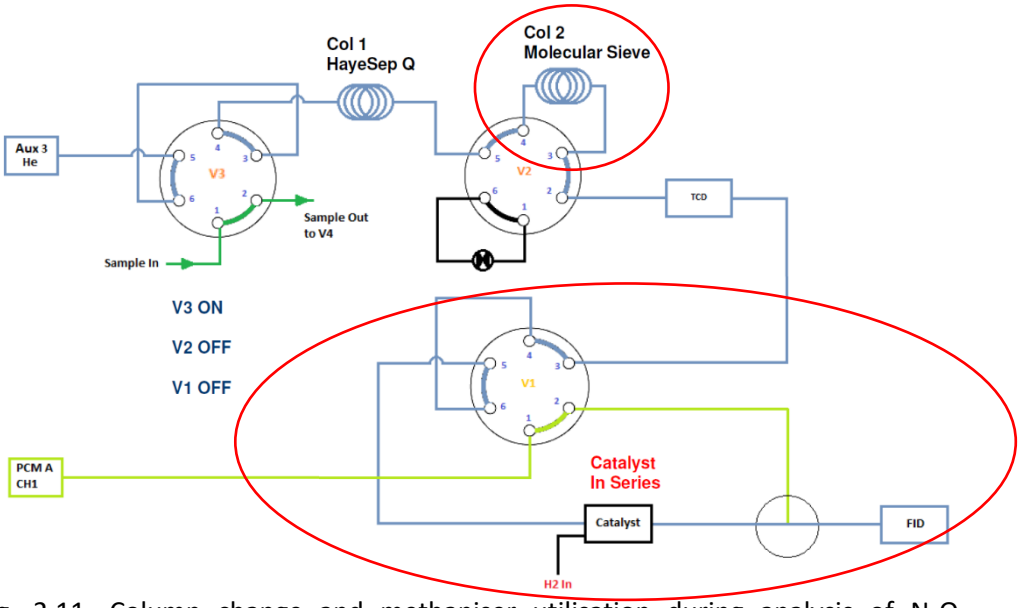

Fig. 2.11. Column change and methaniser utilisation during analysis of N_2O decomposition products using propane as a reductant.

Finally the methaniser (Ni catalyst at 350 °C) must be brought inline to allow the combustion of all gases to methane before being analysed by the FID, as shown in Fig. 2.11. This is done so that CO_2 and CO can be analysed on the FID channel rather than the TCD channel and give better response.

To achieve an effective separation and elution of all products the column oven was set to an isothermal program at 125 °C. Analytes were identified by comparing their retention times with those of commercial standards. O_2, N_2 and N_2O were detected in the TCD channel whilst C_3H_8, CO_2, CO and other carbon based products were detected in the FID channel that is fitted with a methaniser. TCD is a universal detector generally used for the detection of gaseous compounds by measuring the difference in thermal conductivity of the analyte gas and the carrier gas. FID is commonly used in the industry for the determination of hydrocarbon concentrations based on the detection of ions formed during the combustion of hydrocarbons in a hydrogen flame, with the response being proportional to the concentrations of hydrocarbon present.

The retention times for all products are as follows:

Table 2.3. Retention times of all analytes seen in GC chromatograph.

Compound	**TCD Retention Time (min)**	**FID Retention Time (min)**
Carbon Dioxide	2.75	2.75
Nitrous Oxide	3.1	-
Water	5.44	-
Ethene	-	3.95
Ethane	-	4.42
Propene	-	10.58
Propane	-	11.54
Oxygen	14.54	-
Nitrogen	15.59	-
Methane	-	17.8
Carbon Monoxide	18.62	18.62

Quantitative analysis was performed by quantifying reactants consumed and products formed.

Propane and N_2O conversion (%) were determined from the gas consumption with the difference between the inlet and outlet concentration using the following equations:

$$Propane\ conversion\ (\%) = \left(\left(\frac{C_3H_{8_{in}} - C_3H_{8_{out}}}{C_3H_{8_{in}}}\right) * 100\right)$$

Eq. 10. Equation showing how propane conversion is calculated.

$$N_2O\ conversion\ (\%) = \left(\left(\frac{N_2O_{in} - N_2O_{out}}{N_2O_{in}}\right) * 100\right)$$

Eq. 11. Equation showing how N_2O conversion is calculated.

All products (apart from water) were calibrated for by injecting known concentrations of each gas. The response factor (RF = peak area/analyte concentration) was obtained from the calibration plot that correlates the concentration with peak area.

Blank experiments conducted in an unfilled reactor tube showed insignificant activity over the temperature range tested. Repeat experiments were performed

to enable the error of the testing methodology to be calculated, with an error of ± 3 % N_2O conversion. Where propane was present in the reaction carbon balances were in the range of 100 ± 5 %.

Error bars are not shown through this thesis as the errors produced are so small that the bars are smaller than the figure icons used on the graphs and are therefore not visible.

Repeat experiments were performed for all catalyst tests, along with most characterisation data that has a source of intrinsic error that could not be eliminated. For example, BET surface area measurements are an average of three. Where there was doubt over an XRD measurement, these were performed again to check any phases present. If the decomposition pathway of a catalyst precursor was not comparable to literature the TGA was run again. For some techniques, it was only possible to run the analysis once, such as ICP, SS NMR, HAADF-STEM and XPS where there are costs associated with the analysis. In some catalyst cases it was not possible to perform repeats due to limited catalyst quantity produced, i.e. a used catalyst.

2.5 References

1 G. Pekridis, C. Athanasiou, M. Konsolakis, I. V. Yentekakis and G. E. Marnellos, *Top. Catal.*, 2009, **52**, 1880–1887.

2 M. Morad, M. Sankar, E. Cao, E. Nowicka, T. E. Davies, P. J. Miedziak, D. J. Morgan, D. W. Knight, D. Bethell, A. Gavriilidis and G. J. Hutchings, *Catal. Sci. Technol.*, 2014, **4**, 3120–3128.

3 M. M. Forde, L. Kesavan, M. I. Bin Saiman, Q. He, N. Dimitratos, J. A. Lopez-Sanchez, R. L. Jenkins, S. H. Taylor, C. J. Kiely and G. J. Hutchings, *ACS Nano*, 2014, **8**, 957–969.

4 M. M. Forde, R. D. Armstrong, R. McVicker, P. P. Wells, N. Dimitratos, Q. He, L. Lu, R. L. Jenkins, C. Hammond, J. A. Lopez-Sanchez, C. J. Kiely and G. J. Hutchings, *Chem. Sci.*, 2014, 3603–3616.

5 M. A. Peña and J. L. G. Fierro, *Chem. Rev.*, 2001, **101**, 1981–2017.

6 P. N. Trikalitis and P. J. Pomonis, *Appl. Catal. A Gen.*, 1995, **131**, 309–322.

7 S. Ishikawa, D. R. Jones, S. Iqbal, C. Reece, D. J. Morgan, D. J. Willock, P. J. Miedziak, J. K. Bartley, J. K. Edwards, T. Murayama, W. Ueda and G. J. Hutchings, *Green Chem.*, 2017, **19**, 225–236.

8 J. Yuan, S. S. Li, L. Yu, Y. M. Liu, Y. Cao, H. Y. He and K. N. Fan, *Energy Environ. Sci.*, 2013, **6**, 3308–3313.

9 L.-C. Wang, Q. Liu, M. Chen, Y.-M. Liu, Y. Cao, He and K.-N. Fan, *J. Phys. Chem. C*, 2007, **111**, 16549–16557.

10 U. Holzwarth and N. Gibson, *Nat. Nanotechnol.*, 2011, **6**, 534.

11 P. Scherrer, *Göttinger Nachrichten Math. Phys.*, 1918, **2**, 98–100.

12 International Centre for Diffraction Data, *www.icdd.com/profile/overview.htm*, 03-05–2018.

13 A. Cheetham and P. Day, *Solid State Chemistry Techniques*, Oxford Science Publications, 1st edn., 1987.

14 J. W. Niemantsverdriet and I. Chorkendorff, *Concepts of Modern Catalysis and Kinetics*, Wiley, 1st edn., 2003.

15 T. Gilson and P. Hendra, *Laser Raman Spectroscopy*, John Wiley & Sons Ltd, United Kindgom, 1st edn., 1970.

16 A. Cheetham and P. Day, *Solid-State Chemistry: Techniques*, United Kindgom, 1st edn., 1990.

17 L. Smart and E. Moore, *Solid State Chemistry: An Introduction*, Taylor & Francis, United States, 3rd edn., 2005.

18 Agilent Technologies, *http://www.chem.agilent.com/Library/brochures/5991-3696EN.pdf*, 2013, 20-05–2018.

19 E. Metcalfe, *Atomic Absorption and Emission Spectroscopy*, Wiley-Blackwell, 1st edn., 1987.

20 P. A. Webb, *MIC Tech. Publ.*, 2003, **13**, 1–4.

21 S. Brunauer, P. H. Emmett and E. Teller, *J. Am. Chem. Soc.*, 1938, **60**, 309.

22 G. Rothenberg, in *Applied Organometallic Chemistry*, Wiley-VCH Verlag

GmbH & Co. KGaA, 2008, vol. 22, pp. 412–412.

23 K. W. Kolasinski, *Surface Science: Foundations of Catalysis and Nanoscience*, Wiley-Blackwell, 2nd edn., 2008.

24 G. Attard and C. Barnes, *Surfaces*, Oxford University Press, 1st edn., 1998.

25 J. W. Niemantsverdriet, *Spectroscopy in Catalysis*, Wiley-VCH Verlag GmbH & Co. KGaA, 3rd edn., 2000.

26 R. A. Schoonheydt, *Chem. Soc. Rev.*, 2010, **39**, 5051–5066.

27 K. P. De Jong, *Synthesis of Solid Catalysts*, Wiley-VCH Verlag GmbH & Co. KGaA, 1st edn., 2009, vol. 39.

28 J. Park and J. R. Regalbuto, *J. Colloid Interf. Sci.*, 1995, **175**, 239–252.

3 Identifying the active Fe species for N_2O decomposition in Fe-ZSM-5 catalysts

3.1 Abstract

The influence of active Fe species on the decomposition of N_2O over Fe-ZSM-5 catalysts prepared by Chemical Vapour Impregnation (CVI) were investigated. Two parent H-ZSM-5 zeolites (Si:Al ratio 23 or 30) were used to prepare various weight loadings of Fe-ZSM-5 catalysts. Initially Si:Al ratio and Fe weight loading were tested before focussing on the effect of acid treatment and Fe speciation on a single weight loading. Characterisation by UV/vis, XPS and ICP-OES showed that acid washing lead to a reduction of *ca.* 60 % Fe loading compared to the parent 0.4 wt. % Fe-ZSM-5 catalyst. At 600 °C, the TOF of N_2O decomposition increased from 1.60 s^{-1} for the parent catalyst to 3.99 s^{-1} for the acid washed catalyst with a weight loading of 0.16 %. The rate limiting step of this reaction is the removal of oxygen from the surface of the catalyst after the decomposition of N_2O has taken place. Therefore propane was added to the gas feed as a reductant to remove any inhibiting oxygen species that remain on the surface of the catalyst. When propane is present the loading of Fe is not important as it is possible to achieve similar decomposition levels using both high and low loaded catalysts. However, when only N_2O is present in the gas feed, low metal loadings Fe-ZSM-5 catalysts are not capable of achieving high conversions due to the low proximity of active framework Fe^{3+} ions and extra-framework α-Fe species, which limits oxygen recombination and desorption. Acid washing removes Fe from these active sites and deposits it on the surface of the catalyst as Fe_xO_y, leading to a drop in activity. UV/Vis spectroscopy was used to identify the Fe species present in the catalyst and to speculate on the active species. High loadings of Fe do not lead to an active catalyst when propane is present, due to the formation of Fe_xO_y nanoparticles and clusters during catalyst preparation. These are inactive species which lead to a decrease in overall efficiency of the Fe ions and consequentially a lower TOF.

3.2 Keywords

Nitrous Oxide, Iron Zeolites, Fe-ZSM-5, N_2O Decomposition, Acid Washing, Iron Species, Chemical Vapour Impregnation, UV/Vis, XPS.

3.3 Introduction

Iron zeolites have been commonly used for the decomposition of N_2O [1], with H-ZSM-5 frequently being used as a support.[2–4] Low Si:Al ratios are necessary for high N_2O conversion, due to the presence of active Fe species that form on the Al moiety of the zeolite framework. Therefor low Si:Al ratios can lead to a higher concentration of active species. [2,5,6]

During the decomposition of N_2O, the rate limiting step is the recombination of oxygen to form O_2, as N_2O binds to the active site, N_2 desorbs, leaving an oxidised active site. Adding a reductant to the gas feed can promote the removal of oxygen and increase the rate of reaction at lower temperatures. Propane [5,7–10] ethane, methane and CO [5,11–15] have all been used as a reductant.

When iron is deposited on zeolites it is possible to form four distinct Fe species: [5,16–18]

- Framework Fe^{3+},
- Isolated Fe^{3+} or Fe^{2+},
- Fe oxo-species,
- FeO_x species.

Extra framework Fe is considered the active species, due to having the ability to form α-Oxygen.[19–25] α-Oxygen is formed by decomposing N_2O over reversible redox α-Fe sites that have the capacity to switch between Fe^{2+} and Fe^{3+} as shown in the mechanism below.[26,27]

$$N_2O + (Fe^{2+})_\alpha \rightarrow (Fe^{3+} - O^{\cdot-})_\alpha + N_2 \quad [28]$$

The aim of this chapter is to investigate the importance of different Fe species in Fe-ZSM-5 for the decomposition of N_2O in the presence and absence of a reductant, such as propane. In addition, comparing different Fe loadings, the merit of acid washing to increase the efficiency of the Fe in the active catalyst is discussed. UV-

Vis spectroscopy used to identify the different Fe species, and to suggest the active Fe component for N_2O decomposition.

3.4 Effect of Si:Al ratio and Fe loading

Various weight loading Fe-ZSM-5 catalysts were prepared by chemical vapour impregnation, using both 23 and 30 Si:Al ratio, and calcined at 550 °C in static air for 3 hours at 10 °C min^{-1}. Initially 0.4 wt. % and 1.25 wt. % iron loadings were prepared and the effect of Si:Al investigated, with further 0.16 wt. % and 2.5 wt. % Fe loadings prepared and characterised to find a suitable catalyst for acid washing. 0.4 wt. % Fe catalyst was acid washed by 10 v/v% HNO_3 at 50 °C for 10 min to produce a catalysts with a final Fe weight loading of 0.16 wt. %. A 0.16 wt. % Fe catalyst prepared by CVI for comparison.

Catalysts were tested under two regimes, N_2O only (5 % N_2O, balance He) or N_2O and Propane (5 % N_2O, 5 % C_3H_8, balance He) over the temperature range of 400 – 600 °C, with a total flow of 100 ml min^{-1}, using 0.06 g catalyst.

Fe-ZSM-5 catalysts with Fe loadings of 0.4 wt. % and 1.25 wt. % and Si:Al ratios of 23 or 30 were tested for N_2O decomposition. From the data shown in Table 3.1 it is clear that the lower Si:Al ratio catalysts exhibit a higher relative activity. This is in part due to the increased amount of aluminium present within the support that enables the formation of Fe-Al sites which have been shown previously to be the active site for N_2O decomposition. [2,5,6] This in turn explains why a lower Fe:Al ratio leads to a higher activity (Table 3.1). Which is due to the increased Al content, and therefore an increased number of Fe-Al sites (α-Fe). α-Fe species can only form on Al sites, as the term refers to Fe that is coordinated to Al, therefore the more Al the more α-Fe that is possible to form. Decomposition of N_2O leads to oxidised α-Fe sites remaining on the surface of the catalyst, these sites preventing turnover of N_2O. When propane is added to the gas stream the gas acts a reductant and reduces the oxidised α-Fe increasing the TOF.[24,29–33] Higher Fe loadings also increase the activity of the catalysts, this is due to the increased number of active sites that could be present. Due to the higher activity of the Fe-ZSM-5 (23) parent zeolite catalyst, further investigation was carried out on the zeolite with this Si:Al ratio.[5]

Table 3.1. Influence of Fe:Al ratio on 0.4 wt. % Fe and 1.25 wt. % Fe-ZSM-5 for N_2O Decomposition both with and without propane present.

Catalyst	Fe:Al Ratio	N_2O conversion at 550 °C without propane (%)	N_2O conversion at 550 °C with propane (%)
0.4 wt. % Fe-ZSM-5 (23)	0.072	20	90
0.4 wt. % Fe-ZSM-5 (30)	0.092	12	81
1.25 wt. % Fe-ZSM-5 (23)	0.224	35	81
1.25 wt. % Fe-ZSM-5 (30)	0.288	29	68

Reaction Conditions: Total flow rate 100 ml min^{-1}, 0.06 g catalyst, temperature range 400-600 °C, GHSV 45000 h^{-1}, either 5 % N_2O/He or 5 % N_2O, 5 % C_3H_8 in He.

UV/Vis spectroscopy was performed on the various catalysts to understand how the Si:Al ratio effects the species of Fe present after preparation (Fig. 3.1). When Fe is supported on H-ZSM-5, the four UV-active species absorb at 200-250 nm (isolated Fe^{3+} in framework sites), 250-350 nm (isolated or oligomeric extra framework Fe species in zeolite channels), 350-450 nm (iron oxide clusters) and > 450 nm (large surface oxide species).[17,34] Fig. 3.1 illustrates the correlation between a lower Si:Al ratio and the increased density of extra-framework α-Fe due to higher relative absorbance in the region 250-350 nm.

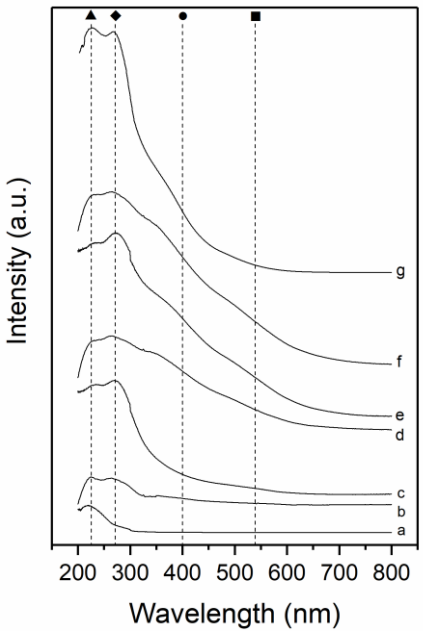

Fig. 3.1. UV/Vis spectra of a series of Fe-ZSM-5 (23 or 30) catalysts and H-ZSM-5 support. ▲- Framework Fe^{3+}, ◆ - Extra framework α-Fe species, ● - Fe_xO_y clusters, ■ - Large Fe_xO_y species. a - H-ZSM-5 (23), b – H-ZSM-5 (30), c – 0.4 wt. %Fe-ZSM-5 (23), d – 0.4 wt. % Fe-ZSM-5 (30), e – 1.25 wt. % Fe-ZSM-5 (23), f – 1.25 wt. % Fe-ZSM-5 (30), g – 2.5 wt. % Fe-ZSM-5 (23).

An additional Fe-ZSM-5 (23) catalyst with a 2.5 wt. % weight loading was prepared and compared to the 0.4 and 1.25 wt. % catalysts. Fig. 3.2 (closed symbols) shows how the conversion of N_2O of the three Fe-ZSM-5 (23) catalysts changes over the temperature range of 400 – 600 °C. The supports were tested to confirm that the supports alone are not active for the decomposition of N_2O. The increase in weight loading of Fe in Fe-ZSM-5 lead to an increase in conversion of N_2O up to 70 % over the 1.25 wt. % catalyst, compared to 40 % conversion over the 0.4 wt. % Fe-ZSM-5 catalyst. However, increasing the weight loading further to 2.5 % did not increase the conversion further (Fig. 3.2). The lower loaded 0.4 wt. % Fe catalyst showed limited activity despite the presence of active extra-framework α-Fe from analysis of the UV/Vis spectra (Fig. 3.1). It is possible that this is due to the rate limiting oxygen recombination step, after decomposition α-Fe become oxidised and inactive, with the proximity of the adsorbed oxygen species to combine and form molecular oxygen and regenerate the active site not close enough, therefore, effectively leaving the α-Fe site blocked. It is important to note that the three weight loading catalysts all achieved similar activity at lower temperatures. This is because the catalyst activity is limited by the proximity of active sites, as described previously. When the activity is low all active sites can be used with out needing to be regenerated. The theory of the active sites being blocked by oxygen could be tested by stopping the flow of N_2O and continuing to heat the catalyst. If oxygen is seen then this is generated form the removal of O_2 from the active site, the catalyst could then be cooled and N_2O added back into the stream and a higher conversion should be noted.

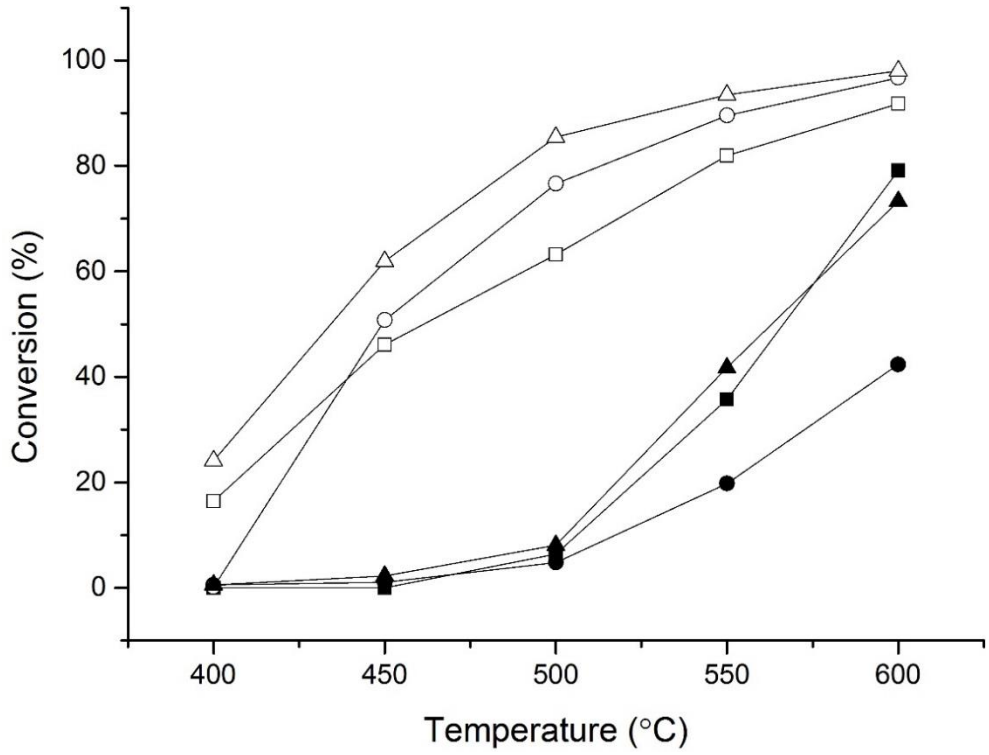

Fig. 3.2. The influence of Fe weight loading on N_2O conversion over Fe-ZSM-5 catalysts. Closed symbols: N_2O present 5 % N_2O/He, Open Symbols: N_2O + Propane present: 5 % N_2O, 5 % C_3H_8 in He, ● - 0.4 wt. % Fe-ZSM-5 (23), ■ - 1.25 wt. % Fe-ZSM-5 (23), ▲ - 2.5 wt. % Fe-ZSM-5 (23). Conditions; total flow rate 100 ml min^{-1}, 0.06g catalyst, temperature range 200-600 °C, GHSV 45000 h^{-1}.

Higher loadings of Fe lead to a higher proportion of active framework and extra-framework species. In the N_2O only reactions, this increased density of active sites leads to an increase in the rate of oxygen recombination and therefore a higher N_2O conversion due to the regeneration of active sites. UV/Vis spectroscopy (Fig. 3.1.) shows that there are number of appreciable Fe species present in the high loading catalysts, especially noting the high proportion of FeO_x nano-particle and cluster species, which are not active for N_2O decomposition,[3,25,35] indicating that not all Fe present is utilised for the reaction. Therefore, while a significant proportion of Fe is not active, there is a high concentration of active α-Fe that can allow oxygen recombination and efficient, high N_2O conversion.

The presence of a reductant such as propane shifts the N_2O decomposition activity to 400 – 450 °C from a much higher temperature of > 600 °C (Fig. 3.2. open symbols). Propane is acting as a reductant [5,8,10,36,37] by removing any remaining oxygen that blocks the α-Fe active sites, and lowers the rate of N_2O decomposition. Thereby, oxygen recombination is the rate-limiting step in the reaction. Propane

activates the oxidised α-Fe sites forming CO and CO_2 in the process, this regeneration cycle allows the reaction to proceed.[31,32,38–40] At low temperatures (< 450 °C) minor quantities of propene (90 % selectivity at < 6 % conversion) are produced by oxidative dehydrogenation of propane alongside some ethene and ethane via a cracking mechanism. However, at higher temperatures the selectivity shifts exclusively to combustion products such as CO and CO_2.

XPS was performed on the series of Fe-ZSM-5 catalysts. Typically, metal oxide O 1s binding energies are around 529 – 530 eV, this corresponds to the Fe-O fitting seen at 529.9 eV in Fig. 3.3. [41] Typically Al-O and Si-O binding energies are seen around 531 and 532.9 eV respectively. [41–43] This relates to the fitting at 532.5 eV, this is a combination of both Al-O and Si-O bonding as found in the ZSM-5 framework.[44–46] With more Si present in the zeolite framework, the binding energy is shifted to a higher value compared to Al-O to represent the distribution of the framework. This is more evident in the O 1s XPS spectrum of the H-ZSM-5 zeolites; in the (23) zeolite there is more Al present than in the (30) zeolite and therefore the binding energy is shifted closer to that of Al-O than Si-O. In the case of Fe-O species, the higher the Fe weight loading the more Fe-O seen in the XPS spectra. This is due to the increased % of bulk Fe-O found within the catalyst as confirmed by UV/Vis spectroscopy, this is especially true in the 1.25 wt. % Fe-ZSM-5 (23) and (30) and the 2.5 wt. % Fe-ZSM-5 (23) catalysts.

Comparing the reaction data (Fig. 3.2.), UV/Vis spectroscopy (Fig. 3.1.), and XPS oxygen region (Fig. 3.3.), it is possible to observe that the more active catalyst have a higher proportion of framework and extra framework α-Fe species. In the case of the 0.4 wt. % Fe-ZSM-5 catalyst, UV/Vis spectroscopy shows a major absorbance in the region that correlates to framework and extra framework α-Fe species, with only a small absorbance due to FeO_x nanoparticles and bulk species. XPS of the O region confirms the limited presence of these species. When considering the poor activity of the 1.25 wt. % Fe-ZSM-5 catalyst, it is possible to connect this to the presence of FeO_x nanoparticles and bulk species: UV/Vis shows a large absorbance due to these species, and XPS shows a large split in the oxygen environment, with a large response due to Fe-O_x compared to lower loadings.

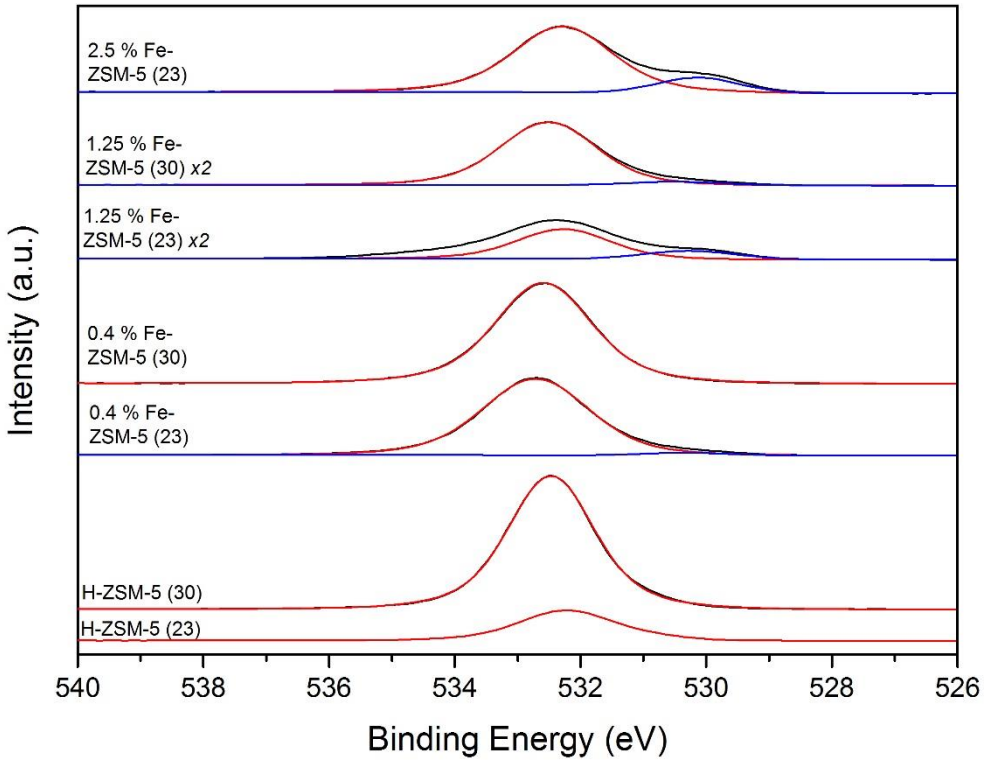

Fig. 3.3. XPS data of the O 1s region of H-ZSM-5 (23) and (30) and various Fe-ZSM-5 (23) and (30) catalysts. Legend: Red – O-ZSM-5 fitting, Blue – Fe-Ox fittings.

3.5 Acid Washing Fe-ZSM-5 catalysts

Peneau *et al.* showed that, by using dilute HNO_3, it is possible to remove excess iron and spectator species from the catalyst; the group investigated the effect of acid washing on the selective oxidation of ethane by H_2O_2.[18] They showed it was possible to increase both the the catalytic activity and stability of the catalysts by acid washing for short periods of time. The 0.4 wt. % Fe-ZSM-5 (23) catalyst was selected for acid washing due to the presence of extra-framework α-Fe species and minor levels of spectator Fe_xO_y nano-particulates and clusters. Furthermore, previous work with acid washing in the group has shown it is difficult to distinguish between the Fe species present at higher weight loadings.[47,48] For the calcined catalyst, post-acid washing ICP-OES analysis showed a reduction in the Fe loading to 0.16 wt. % compared to 0.4 wt. % of the parent material.

Fig. 3.4a demonstrates the activity of the as prepared parent catalyst, the acid washed catalyst, a 0.16 wt. % Fe-ZSM-5 (prepared by CVI for comparison to the AW catalyst), and the analogous H-ZSM-5 supports. The supports were tested to confirm that the supports alone are not active for the decomposition of N_2O. The

parent catalyst [0.4 wt. % Fe-ZSM-5 (23)] has a conversion of 40 % at 600 °C, however, when comparing this to the acid washed catalyst the conversion at 600 °C was lower, at 25 %. It is thought that this difference in activity is due to the removal of framework Fe^{3+} ions, which are extracted and deposited on the surface of the catalyst as nanoparticles of FeO_x. This is complemented by UV/Vis spectroscopy (Fig. 3.5), which shows there is a decrease in intensity at 250 nm due to extra-framework Fe and an increase in intensity at 350 nm due to FeO_x species. In the low loaded 0.16 wt. % Fe-ZSM-5 (23) catalyst, UV/Vis spectroscopy shows that only framework Fe^{3+} and extra-framework α-Fe species of Fe are present. The high intensity of active sites (frame work and extra-framework α-Fe species) should produce a catalyst that has a high activity, however, this is not the case. The low loading and high dispersion of Fe means that the proximity of Fe species to each other is very low; the proximity is crucial to achieve high activity in N_2O decomposition. [49–51] When propane is present in the gas feed (Fig. 3.4b) the proximity of the active sites is not as closely linked to the activity, as propane can remove oxygen to form CO_x and regenerate the Fe active site in the process.

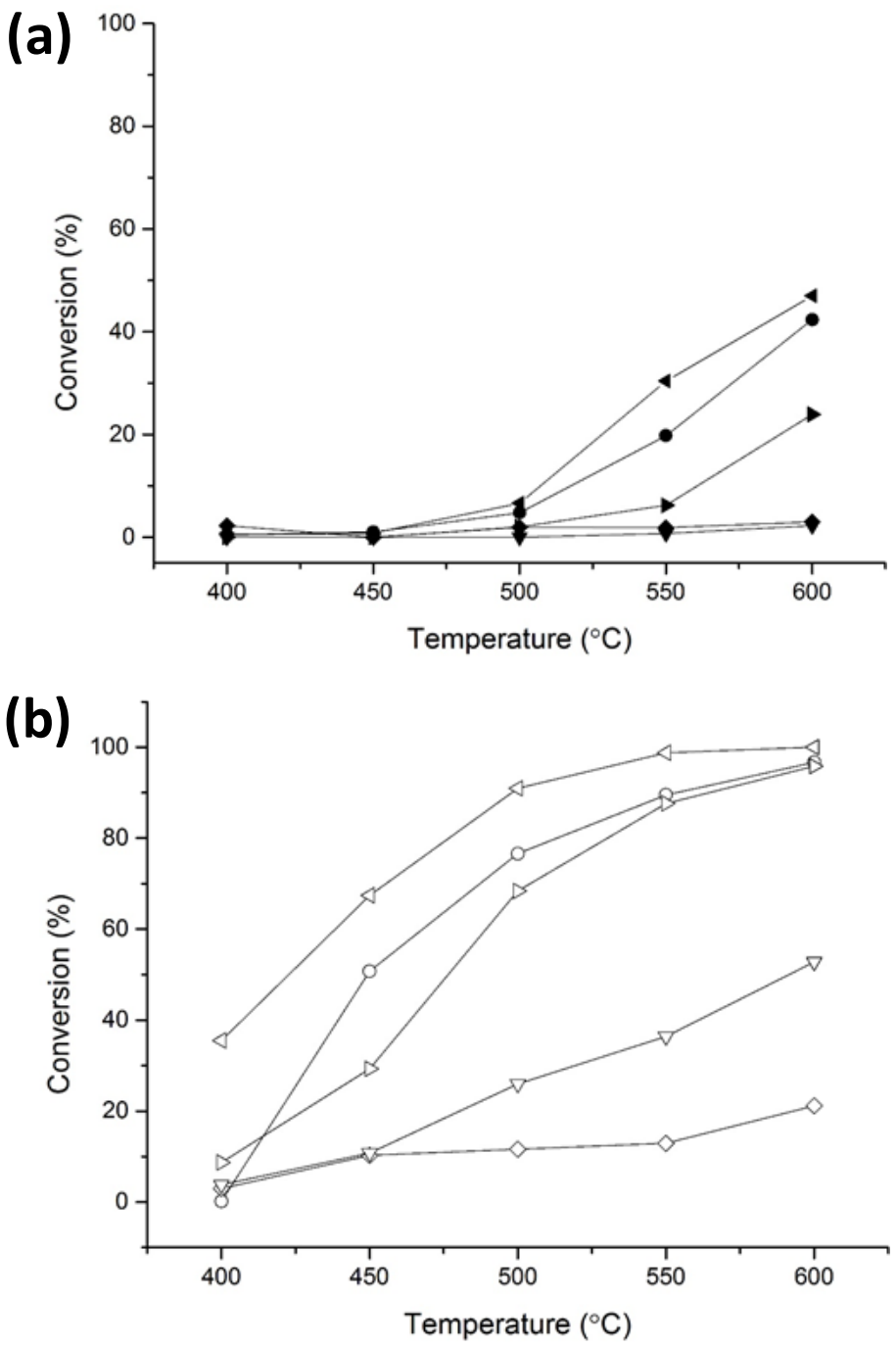

Fig. 3.4. Influence of Fe loading and acid washing over Fe-ZSM-5 catalysts for N_2O conversion; ◀ - 0.16 wt. % Fe-ZSM-5 (23), ● - 0.4 wt. % Fe-ZSM-5 (23), ▶ - 0.4 wt. % Fe-ZSM-5 (23) Acid washed, ◆ - H-ZSM-5 (23), ▼ - H-ZSM-5 (23) Acid washed. (a) Closed symbols: Conditions; 5 % N_2O/He, total flow rate 100 ml min^{-1}, 0.06g catalyst, temperature range 400-600 °C, GHSV 45000 h^{-1}.
(b) Open symbols: Conditions; 5 % N_2O, 5 % C_3H_8 in He total flow rate 100 ml min^{-1}, 0.06g catalyst, temperature range 400-600 °C, GHSV 45000 h^{-1}.

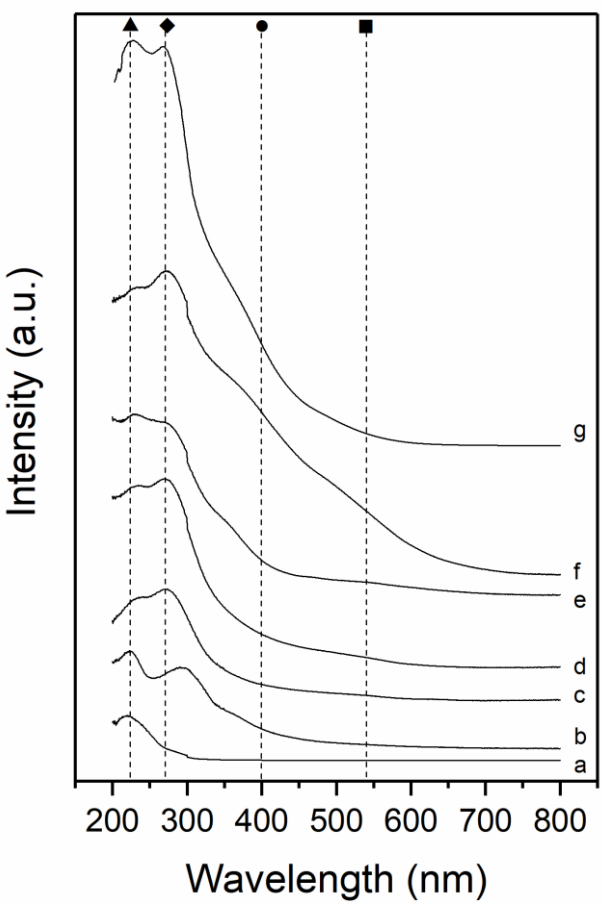

Fig. 3.5. UV/Vis spectra of a series of Fe-ZSM-5 (23) catalysts and H-ZSM-5 support. ▲- Framework Fe^{3+}, ◆ - Extra framework α-Fe species, ● - Fe_xO_y clusters, ■ - Large Fe_xO_y species. a - H-ZSM-5 (23), b – H-ZSM-5 (23) AW, c - 0.16 wt. % Fe-ZSM-5 (23), d – 0.4 wt. % Fe-ZSM-5 (23), e – 0.4 wt. % Fe-ZSM-5 (23) AW, f – 1.25 wt. % Fe-ZSM-5 (23), g – 2.5 wt. % Fe-ZSM-5 (23)

UV/Vis spectroscopy enabled the influence of Fe loading on N_2O decomposition with and without propane to be investigated further. In the parent zeolite H-ZSM-5 (23), UV/Vis shows an absorbance at 220 nm (Fig. 3.5.) which indicates that framework Fe^{3+} species are present, these are likely to be impurities from the manufacturing process.[52] UV/Vis spectroscopy shows that during acid washing of H-ZSM-5 (23) the framework Fe^{3+} species are re-dispersed with extra framework Fe species now present in the support. The absorbance at 300 nm has increased in intensity, meaning more extra framework Fe species present. Based on the absorbance at 250 and 280 nm, the 0.16 wt. % Fe-ZSM-5 has both framework and extra-framework Fe ions, whereas both the 1.25 wt. % and 2.5 wt. % Fe-ZSM-5 catalysts have all species of Fe present with absorbances at 250 nm (framework), 280 nm (extra-framework Fe), 400 nm (FeO_x nanoparticles) and 450 nm (large FeO_x clusters). The presence of FeO_x species are confirmed by studying the oxygen region

in XPS. The UV/Vis spectra of 1.25 wt. % and 2.5 wt. % show the four different species (Fig. 3.5.); in the 0.4 wt. % Fe-ZSM-5 catalyst there are three species of Fe present: framework Fe^{3+}, extra-framework α-Fe and large FeO_x clusters. After acid washing, the iron has been re-distributed (the same as the acid washed support), with now four species of Fe present. The most important change however is the drop-in intensity of the absorbance due to the extra-framework α-Fe species, these have been extracted and deposited as FeO_x nanoparticles and clusters.

Further characterisation with XPS (Table 3.2) and surface area analysis (Table 3.3) was performed on a selection of catalysts. XPS measurements revealed the drastic loss of Fe from the surface of the catalyst following acid washing, with the atomic % of Fe falling from 2.02 to 0.28 %, which was accompanied by a large loss in intensity of the Fe peak (Fig. 3.6). A decrease in the surface to bulk Fe ratio was observed using XPS and ICP-OES, from 5.05 for the 0.4 wt. % Fe-ZSM-5 (23) catalyst to 1.75 after acid washing. This confirmed that Fe was preferentially removed from the surface of the catalyst rather than from the micro-porous channels. The Fe 2p XPS binding energy for both the 0.4 wt. % Fe-ZSM-5 (23) calcined and acid washed was 711 eV, with a satellite binding energy of 719 eV, that indicates Fe^{3+} species are present.[53,54] Once Fe has been added to the zeolite support, the binding energy of both Al and Si shift to a higher value. With Al moving from 102.9 eV in H-ZSM-5 to 103.4 eV in the Fe catalysts, and Si shifting from 74.1 eV to 74.9 eV. The shift in binding energy of the constituent zeolite framework elements confirms the presence of framework Fe^{3+} species and that Fe has substituted into the zeolite lattice.[55–57]

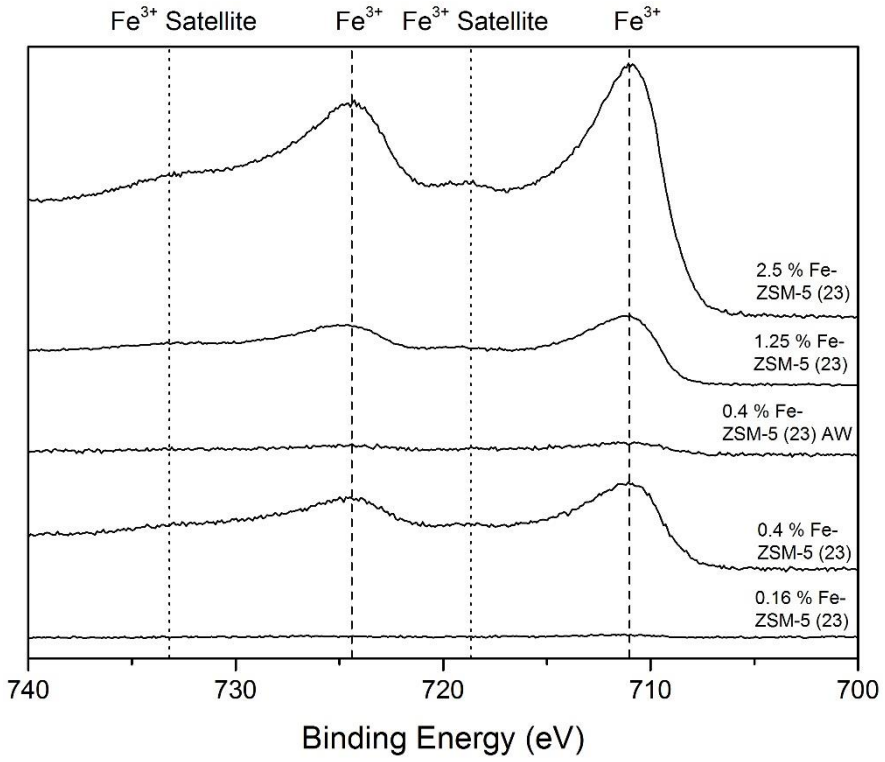

Fig. 3.6. XPS data of the Fe region of various Fe-ZSM-5 (23) catalysts, including calcined and acid washed catalysts.

Table 3.2. Surface composition, Fe binding energies of a series of Fe-ZSM-5 (23) + (30) catalysts and H-ZSM-5 (23) + (30) supports as reported by XPS analysis.

Catalyst	**Al 2p (at%)**	**O 1s (at%)**	**Si 2p (at%)**	**Fe 3p (at%)**	**Al Binding energy (eV)**	**Si Binding Energy (eV)**	**Fe Binding energy (eV)**	**Fe satellite Binding energy (eV)**
H-ZSM-5 (23)	3.33	62.77	33.90	-	102.9	74.1	-	-
H-ZSM-5 (23) AW	1.96	70.02	28.02	-	103.6	75.3	-	-
0.4 wt. % Fe-ZSM-5 (23)	2.58	63.36	32.13	1.91	103.4	74.9	711.2	719.0
0.4 wt. % Fe-ZSM-5 (23) AW	2.72	63.20	33.70	0.39	103.5	74.7	711.0	719.0
0.16 wt. % Fe-ZSM-5 (23)	2.60	69.70	27.30	0.41	103.5	74.7	711.8	-
1.25 wt. % Fe-ZSM-5 (23)	2.36	56.88	28.44	12.32	103.6	75.0	711.2	718.9
2.5 wt. % Fe-ZSM-5 (23)	3.21	61.32	27.38	8.09	102.9	74.7	711.1	718.9
H-ZSM-5 (30)	1.91	63.12	34.97	-	103.0	74.3	-	-
0.4 wt. % Fe-ZSM-5 (30)	1.82	63.27	34.39	0.52	103.3	74.8	710.3	-
1.25 wt. % Fe-ZSM-5 (30)	1.44	68.66	26.52	3.37	103.5	74.5	711.3	719.0

Surface area measurements were performed on all catalysts. For the H-ZSM-5 (23) catalysts the surface area remained constant at around 430 $m^2\ g^{-1}$, and for the H-ZSM-5 (30) catalysts remained at around 350 $m^2\ g^{-1}$ after iron loading. The micropore volume of H-ZSM-5 (23) was calculated to be 0.167 $cm^3\ g^{-1}$, which varies slightly when iron is added (± 0.022 $cm^3\ g^{-1}$) (Table 3.3). However, the micropore volume does not greatly change after acid washing has been performed (± 0.005 $cm^3\ g^{-1}$). The consistency of the surface area and micropore volume during catalyst preparation, calcination and acid washing suggests that H-ZSM-5 is stable under pre-treatment conditions.

Table 3.3. Surface area and micropore volume of a series of Fe-ZSM-5 (23) + (30) catalysts and H-ZSM-5 (23) + (30) supports.

Catalyst	**Surface Area (m^2 g^{-1})**	**Micropore Volume (cm^3 g^{-1})**
H-ZSM-5 (23)	423	0.167
0.4 wt. % Fe-ZSM-5 (23)	437	0.169
0.4 wt. % Fe-ZSM-5 (23) AW	428	0.164
0.16 wt. % Fe-ZSM-5 (23)	402	0.152
1.25 wt. % Fe-ZSM-5 (23)	379	0.145
2.5 wt. % Fe-ZSM-5 (23)	401	0.152
H-ZSM-5 (30)	345	0.129
0.4 wt. % Fe-ZSM-5 (30)	352	0.133
1.25 wt. % Fe-ZSM-5 (30)	375	0.149

Degas conditions – 9 h at 250 °C prior to analysis.

It was not possible to see any Fe reflections in the XRD patterns of Fe-ZSM-5 (23) catalysts (Fig. 3.7), due to the detection limit on small particles being less than 5 nm, which indicates the all Fe present is < 5 nm in size. This is in line with previous characterisation data, in which we see only framework and extra-framework species and some nanoparticles of FeO_x, with very few bulk species seen. However, there are notable changes in the spectrum, such as the changes in intensity of the (011) and (200) reflections at 7.94 ° and 8.90 °. These intense low 2θ reflections tell us a great deal of information about the amount of aluminium present: higher Al content will lead to higher intensity of reflections at these low 2θ values.[58–60] Fig. 3.7 illustrates the decrease in intensity of these reflections after acid washing indicating that some Al has been removed during this process.

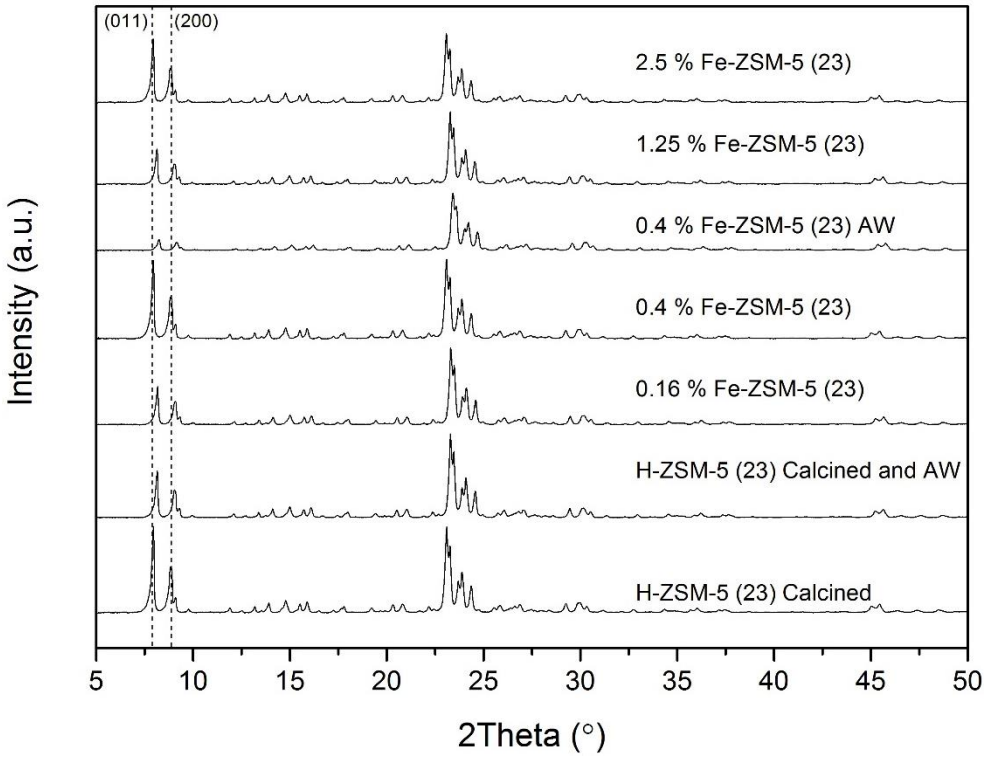

Fig. 3.7. XRD pattern of H-ZSM-5 (23) and various Fe-ZSM-5 (23) catalysts.

It is extremely difficult to resolve the active Fe species, therefore turnover frequency (TOF) over the catalysts was calculated for N_2O decomposition (Fig. 3.9a) using the total moles of Fe present in the catalyst using Eq. 2. The decision to use total moles was taken after trying to resolve the active species in UV/Vis spectroscopy (Fig. 3.8). Deconvoluting these species is not possible due to the degree of overlap in the absorbance profile of the species present, and the subjective nature of fitting peaks to broad spectrums, as shown in Fig. 3.8. Following on from the subjective nature of the fittings it is also not possible to quantitatively define the area of each fitting as the UV/Vis spectroscopy was not performed using the Kubelka Munk model.[61] Hence total Fe moles was used for the TOF calculation as described in Eq. 2.

$$Turnover\ Frequency\ (TOF) = \frac{mol\ of\ N_2O\ converted\ per\ second}{total\ mol\ of\ Fe\ from\ synthesis} \qquad \text{(Eq. 2)}$$

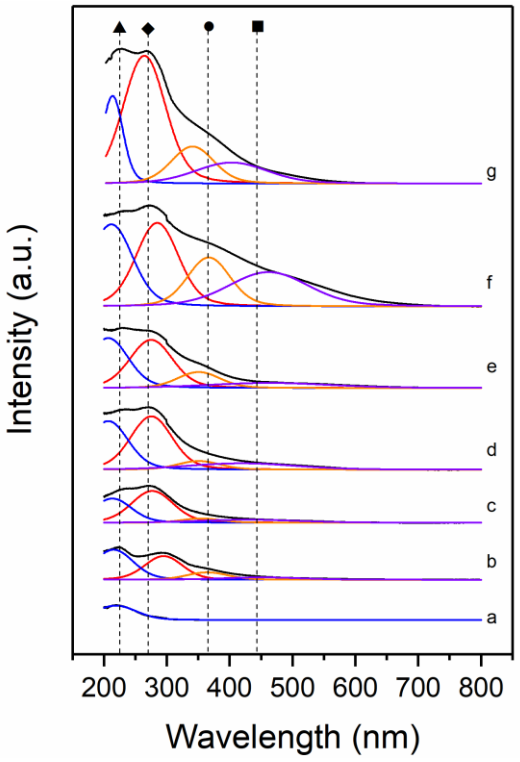

Fig. 3.8. UV-vis spectra of a series of Fe-ZSM-5 (23) catalysts and H-ZSM-5 support. ▲- Framework Fe^{3+} (blue), ◆ - Extra framework species (red), ● - FeO_x clusters (orange), ■ - Large FeO_x species (purple). a - H-ZSM-5 (23), b – H-ZSM-5 (23) AW, c - 0.16 wt. %Fe-ZSM-5 (23), d – 0.4 wt. % Fe-ZSM-5 (23), e – 0.4 wt. % Fe-ZSM-5 (23) AW, f – 1.25 wt. % Fe-ZSM-5 (23), g – 2.5 wt. % Fe-ZSM-5 (23).

The 0.16 wt. % Fe-ZSM-5 (23) catalyst achieved a TOF of *ca.* 3.99 s^{-1} at 600 °C. The TOF of the acid washed support H-ZSM-5 (23) at 600 °C is an order of magnitude greater than the Fe based catalysts when propane is present (Fig. 3.9b). Despite the N_2O conversion being half that of the Fe based catalyst (52 % at 600 °C) the amount of iron present is only trace (245 ppm) which is located in the framework positions. Therefore, the parent zeolite has an extremely high TOF due to the ppm of Fe present, however, a very low yield of nitrogen was observed. It can be reasoned that the acid washed support shows activity due to the redistribution of iron through acid washing from the framework position to extra frame-work α-Fe, which are the active species for N_2O decomposition.[19,20,25] When comparing the TOF of the fresh and acid washed Fe catalyst, the TOF increased from 0.69 s^{-1} to 0.94 s^{-1} at 600 °C. Though, when comparing the same catalysts when propane is present in the gas feed the difference in activity is less significant, with both catalysts achieving 95 % N_2O conversion at 550 °C (Fig. 3.9b). The TOF of the acid washed catalyst is 2 and a half times that of the calcined catalyst (Fig. 3.9b). However, the

TOF over the low loaded 0.16 wt. % Fe-ZSM-5 (23) catalyst is *ca*. 8.5 s^{-1} at 550 °C when propane is present in the gas feed. Compared to literature examples this catalyst out performs others; Park *et al*. reported a TOF of 1.8 s^{-1} for N_2O decomposition at 550 °C using 1.96 wt. % Fe-ZSM-5 (27).[62] Compared to the TOF achieved by the low loaded catalyst of 2.59 s^{-1} at similar conditions and the same temperature, this demonstrates the superior activity of the low loaded catalyst when propane is present.

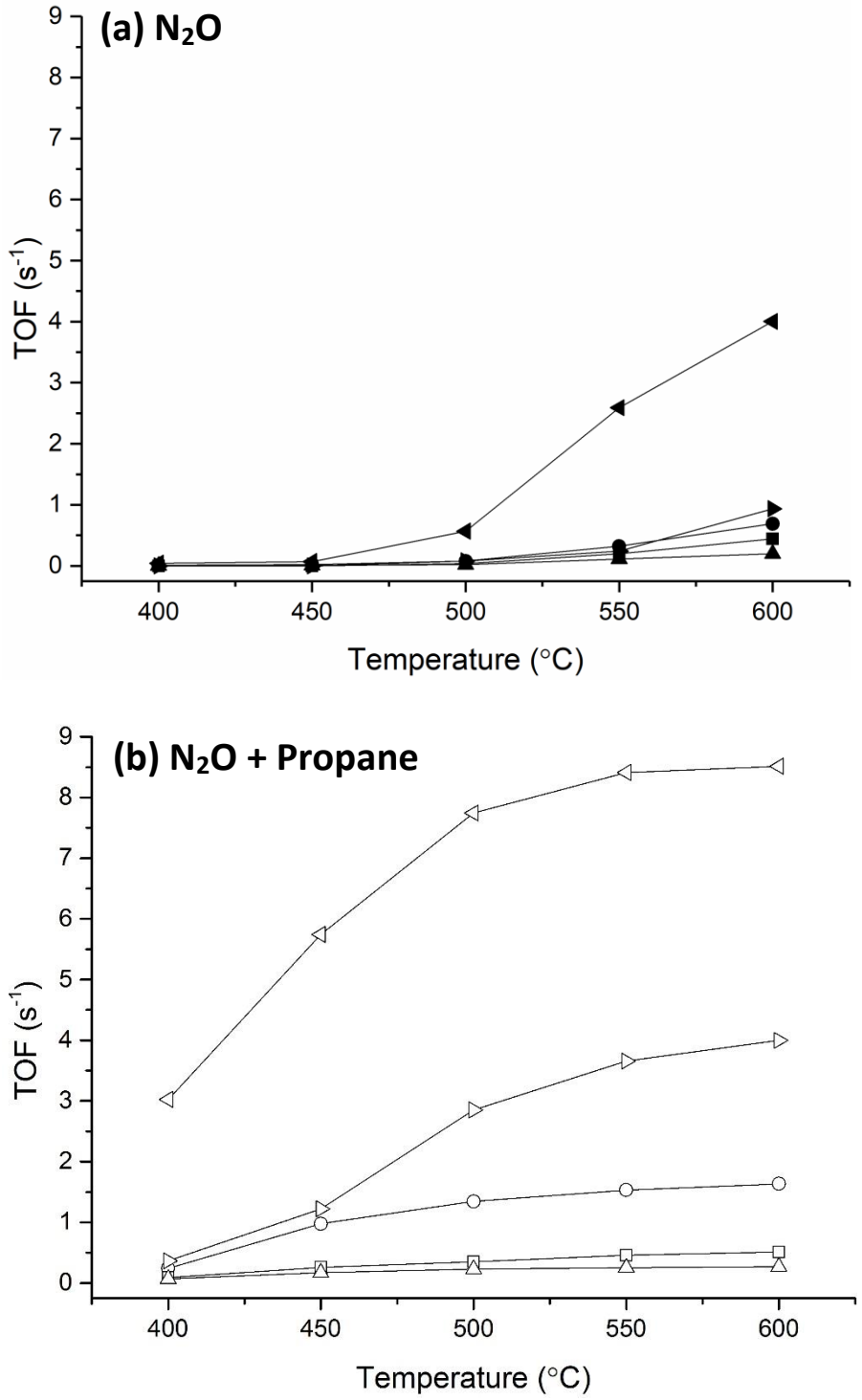

Fig. 3.9. TOF of N_2O decomposition over a series of Fe-ZSM-5 catalysts that have been calcined or acid washed. ◀ - 0.16 wt. % Fe-ZSM-5 (23), ● - 0.4 wt. % Fe-ZSM-5 (23), ■ - 1.25 wt. % Fe-ZSM-5 (23), ▲ - 2.5 wt. % Fe-ZSM-5 (23) ▶ - 0.4 wt. % Fe-ZSM-5 (23) AW.
(a) Closed symbols, Conditions; 5 % N_2O/He, total flow rate 100 ml min^{-1}, 0.06g catalyst, temperature range 400-600 °C, GHSV 45000 h^{-1}.
(b) Open symbols, Conditions; 5 % N_2O, 5 % C_3H_8 in He, total flow rate 100 ml min^{-1}, 0.06g catalyst, temperature range 400-600 °C, GHSV 45000 h^{-1}.

3.6 Conclusions

When prepared by CVI, low loaded Fe-ZSM-5 (23) catalysts have only two species of Fe present, framework Fe^{3+} and isolated extra framework α-Fe, as shown by UV/Vis spectroscopy. When higher loadings are prepared by this method, there are two extra species of Fe present, FeO_x nanoparticles and large clusters, these are not active species for the decomposition of N_2O and are, therefore, not desirable. Here it is shown that framework and extra-framework α-Fe species are active for the decomposition of N_2O and lead to high conversions when a reductant such as propane is present. For example 0.16 wt. % Fe-ZSM-5 (23) has only the two active species of Fe present, and out performs all other catalysts even though the loading of Fe is very low.

However, when the reductant is not present, the activity of the catalysts are limited by the slow desorption of oxygen that occurs when the Fe species are highly dispersed and oxygen recombination is inhibited. This oxygen recombination and desorption becomes the rate limiting step. At higher weight loadings and with only N_2O present in the gas feed, the activity of the catalysts increase as the density of the active sites increases, increasing the rate of molecular oxygen recombination and desorption. This is visible in the higher weight loading catalysts with 1.25 wt. % Fe-ZSM-5 (23) and 2.5 wt. % Fe-ZSM-5 (23) out performing that of the 0.4 wt. % Fe-ZSM-5 (23) for N_2O decomposition. However, as soon as a reductant is added to the gas feed the catalytic activity is similar at 600 °C between the three weight loadings, as shown in Fig. 3.2. As described, this is due to the dispersion of the active sites and the limiting effect this has on the oxygen recombination, which is the rate determining step; this effect is removed when propane is added as a reductant to the feed as this cleaves any oxygen atoms and reduces the active site ready for another incoming N_2O molecule.

Initially literature suggested that it would be possible to selectively remove FeO_x nano-particles and clusters from the surface of the catalyst by performing an acid washing pre-treatment step. However, when acid washing is performed it is not possible to remove FeO_x from the surface of the catalyst but instead Fe is extracted from pores in the active extra-framework positions and deposited on the surface, which leads to a decrease in conversion but an increase in TOF. The decrease in conversion is due to the removal of active α-Fe species, whereas the increase in

TOF is due to the removal of around 60 % of the weight loading of Fe. Although acid washing did not remove iron as predicted, it did mean that a catalyst with the same very low weight loading was prepared by chemical vapour impregnation. This low loading catalyst (0.16 wt. % Fe) has only the active species of Fe present and is the most active catalyst. The TOF for this catalyst (8.5 s^{-1}) outperforms that of all other catalysts in the series due to the extremely low Fe weight loading and very high activity. Park *et al*. reported a TOF of 1.8 s^{-1} for N_2O decomposition at 550 °C using 1.96 wt. % Fe-ZSM-5 (27).[62] Compared to this catalyst, the TOF achieved by the low loaded catalyst is 2.59 s^{-1} more active at similar conditions and the same temperature, therefore demonstrating the superior activity of the low loaded catalyst when propane is present.

3.7 Future work

Literature shows that steaming pre-treatments can be used to extract Fe from the pores and into the extra-framework sites,[63–67] which would be interesting to study in future work. The extraction of Fe from pores and into the extra-framework sites should lead to an increase in conversion as it has been shown that extra-framework α-Fe sites are active for N_2O decomposition. It would be interesting to see the lowest weight loading of Fe capable of N_2O decomposition and whether either the chemical vapour impregnation preparation method and the steaming pre-treatment would be able to prepare a catalyst with only α-Fe present. Characterisation of the used catalysts could lead to the further identification of the active site and give a better understanding of the catalyst. Another method to confirm that the active sites are in fact α-Fe and formed on the Al sites in the ZSM-5 framework would be to prepare the same weight loading catalyst on a silicate support which has no Al present, and should therefore not be able to form α-Fe and be an inactive catalyst. Following on from this theory, it would be interesting to look at even lower SiAl ratio ZSM-5 supports. These would contain a higher percentage of Al atoms and would further enable the formation of the active α-Fe species, producing a better catalyst.

3.8 Comments

Figures in this chapter have been reproduced with permission from Springer. [68]

3.9 References

1 M. I. Konsolakis, *ACS Catal.*, 2015, **5**, 6397–6421.

2 M. Rauscher, K. Kesore, R. Mönnig, W. Schwieger, A. Tißler and T. Turek, *Appl. Catal. A Gen.*, 1999, **184**, 249–256.

3 B. M. Abu-Zied, W. Schwieger and A. Unger, *Appl. Catal. B Environ.*, 2008, **84**, 277–288.

4 S. Sklenak, P. C. Andrikopoulos, B. Boekfa, B. Jansang, J. Nováková, L. Benco, T. Bucko, J. Hafner, J. Ddeek and Z. Sobalík, *J. Catal.*, 2010, **272**, 262–274.

5 H. Abdulhamid, E. Fridell and M. Skoglundh, *Top. Catal.*, 2004, **30/31**, 161–168.

6 I. Melián-Cabrera, E. R. H. van Eck, S. Espinosa, S. Siles-Quesada, L. Falco, A. P. M. Kentgens, F. Kapteijn and J. A. Moulijn, *Appl. Catal. B Environ.*, 2017, **203**, 218–226.

7 H. Ohtsuka, T. Tabata, O. Okada, L. M. F. Sabatino and G. Bellussi, *Catal. Letters*, 1997, **44**, 265–270.

8 H. Ohtsuka, T. Tabata, O. Okada, L. M. . Sabatino and G. Bellussi, *Catal. Today*, 1998, **42**, 45–50.

9 R. W. Van Den Brink, S. Booneveld, M. J. F. M. Verhaak and F. A. De Bruijn, *Catal. Today*, 2002, **75**, 227–232.

10 G. Centi and F. Vazzana, *Catal. Today*, 1999, **53**, 683–693.

11 G. Djéga-Mariadassou, F. Fajardie, J. F. Tempère, J. M. Manoli, O. Touret and G. Blanchard, *J. Mol. Catal. A Chem.*, 2000, **161**, 179–189.

12 L. He, L. C. Wang, H. Sun, J. Ni, Y. Cao, Y. He and K. N. Fan, *Angew. Chemie - Int. Ed.*, 2009, **48**, 9538–9541.

13 K. Teramura, T. Tanaka, H. Ishikawa, Y. Kohno and T. Funabiki, *J. Phys. Chem. B*, 2004, **108**, 346–354.

14 K. Yogo, M. Ihara, I. Terasaki and E. Kikuchi, *Chem. Lett.*, 1993, **22**, 229–232.

15 R. Burch and P. K. Loader, *Appl. Catal. B Environ.*, 1994, **5**, 149–164.

16 A. Ates, C. Hardacre and A. Goguet, *Appl. Catal. A Gen.*, 2012, **441**–**442**, 30–41.

17 J. Pérez-Ramírez, J. C. Groen, A. Brückner, M. S. Kumar, U. Bentrup, M. N. Debbagh and L. A. Villaescusa, *J. Catal.*, 2005, **232**, 318–334.

18 V. Peneau, R. D. Armstrong, G. Shaw, J. Xu, R. L. Jenkins, D. J. Morgan, N. Dimitratos, S. H. Taylor, H. W. Zanthoff, S. Peitz, G. Stochniol, Q. He, C. J. Kiely and G. J. Hutchings, *ChemCatChem*, 2017, **9**, 642–650.

19 K. Sun, H. Zhang, H. Xia, Y. Lian, Y. Li, Z. Feng, P. Ying and C. Li, *Chem. Commun.*, 2004, 2480–2481.

20 E. J. M. Hensen, Q. Zhu, M. M. R. M. Hendrix, A. R. Overweg, P. J. Kooyman, M. V. Sychev and R. A. Van Santen, *J. Catal.*, 2004, **221**, 569–583.

21 V. I. Sobolev, G. I. Panov, A. S. Kharitonov, V. N. Romannikov, A. M. Volodin and K. G. Ione, *J. Catal.*, 1993, **139**, 435–443.

22 G. I. Panov, A. S. Kharitonov and V. I. Sobolev, *Appl. Catal. A, Gen.*, 1993, **98**, 1–20.

23 G. I. Panov, V. I. Sobolev and A. S. Kharitonov, *J. Mol. Catal.*, 1990, **61**, 85–97.

24 G. D. Pirngruber, *J. Catal.*, 2003, **219**, 456–463.

25 J. Pérez-Ramírez, F. Kapteijn and A. Brückner, *J. Catal.*, 2003, **218**, 234–238.

26 G. I. Panov, E. V. Starokon, L. V. Pirutko, E. A. Paukshtis and V. N. Parmon, *J. Catal.*, 2008, **254**, 110–120.

27 M. V. Parfenov, E. V. Starokon, L. V. Pirutko and G. I. Panov, *J. Catal.*, 2014, **318**, 14–21.

28 Y. K. Chow, N. F. Dummer, J. H. Carter, C. Williams, G. Shaw, D. J. Willock, S. H. Taylor, S. Yacob, R. J. Meyer, M. M. Bhasin and G. J. Hutchings, *Catal. Sci. Technol.*, 2017, 154–163.

29 H. Guesmi, D. Berthomieu and L. Kiwi-Minsker, *J. Phys. Chem. C*, 2008, **112**, 20319–20328.

30 C. Sang, B. H. Kim and C. R. F. Lund, *J. Phys. Chem. B*, 2005, **109**, 2295–2301.

31 N. Hansen, A. Heyden, A. T. Bell and F. J. Keil, *J. Phys. Chem. C*, 2007, **111**, 2092–2101.

32 B. R.Wood, J. A. Reimer and A. T. Bell, *J. Catal.*, 2002, **209**, 151–158.

33 K. Sun, H. Xia, E. Hensen, R. van Santen and C. Li, *J. Catal.*, 2006, **238**, 186–195.

34 M. S. Kumar, J. Perez-Ramirez, M. N. Debbagh, B. Smarsly, U. Bentrup and A. Bruckner, *Appl. Catal. B Environ.*, 2006, **62**, 244–254.

35 J. Pérez-Ramírez, F. Kapteijn, G. Mul and J. a. Moulijn, *Chem. Commun.*, 2001, 693–694.

36 H. Ohtsuka, T. Tabata, O. Okada, L. M. F. Sabatino and G. Bellussi, 1997, **44**.

37 R. W. Van Den Brink, S. Booneveld, M. J. F. M. Verhaak and F. A. De Bruijn, in *Catalysis Today*, 2002, vol. 75, pp. 227–232.

38 C. Sang, B. H. Kim and C. R. F. Lund, *J. Phys. Chem. B*, 2005, **109**, 2295–2301.

39 D. A. Bulushev, L. Kiwi-minsker and A. Renken, *Ind. Eng. Chem. Res.*, 2004, **211**, 2004.

40 H. Guesmi, D. Berthomieu and L. Kiwi-Minsker, *J. Phys. Chem. C*, 2008, **112**, 20319–20328.

41 J. C. Dupin, D. Gonbeau, P. Vinatier and A. Levasseur, *Phys. Chem. Chem. Phys.*, 2000, **2**, 1319–1324.

42 A. Y. Stakheev, E. S. Shpiro and J. Apijok, *J. Phys. Chem.*, 1993, **97**, 5668–5672.

43 J. van den Brand, P. C. Snijders, W. G. Sloof, H. Terryn and J. H. W. de Wit, *J. Phys. Chem. B*, 2004, **108**, 6017–6024.

44 R. B. Borade, A. Adnot and S. Kaliaguine, *Zeolites*, 1991, **11**, 710–719.

45 R. B. Borade, *Zeolites*, 1987, **7**, 398–403.

46 J. M. Stencel, J. R. Diehl, L. J. Douglas, C. A. Spitler, J. E. Crawford and G. A. Melson, *Colloids and Surfaces*, 1982, **4**, 305–329.

47 Y. K. Chow, N. F. Dummer, J. H. Carter, R. J. Meyer, R. D. Armstrong, C.

Williams, G. Shaw, S. Yacob, M. M. Bhasin, D. J. Willock, S. H. Taylor and G. J. Hutchings, *ChemPhysChem*, 2018, **19**, 402–411.

48 J. Xu, R. D. Armstrong, G. Shaw, N. F. Dummer, S. J. Freakley, S. H. Taylor and G. J. Hutchings, *Catal. Today*, 2016, **270**, 93–100.

49 D. A. Bulushev, L. Kiwi-Minsker and A. Renken, *J. Catal.*, 2004, **222**, 389–396.

50 L. Kiwi-Minsker, D. A. Bulushev, A. Renken and P. Prechtl, *Ind. Eng. Chem. Res.*, 2007, **46**, 4178–4185.

51 J. Pérez-Ramírez, F. Kapteijn, G. Mul and J. A. Moulijn, *J. Catal.*, 2002, **208**, 211–223.

52 C. Hammond, M. M. Forde, M. H. Ab Rahim, A. Thetford, Q. He, R. L. Jenkins, N. Dimitratos, J. A. Lopez-Sanchez, N. F. Dummer, D. M. Murphy, A. F. Carley, S. H. Taylor, D. J. Willock, E. E. Stangland, J. Kang, H. Hagen, C. J. Kiely and G. J. Hutchings, *Angew. Chemie - Int. Ed.*, 2012, **51**, 5129–5133.

53 M. C. Biesinger, B. P. Payne, A. P. Grosvenor, L. W. M. Lau, A. R. Gerson and R. S. C. Smart, *Appl. Surf. Sci.*, 2011, **257**, 2717–2730.

54 P. C. J. Graat and M. A. J. Somers, *Appl. Surf. Sci.*, 1996, **100**–**101**, 36–40.

55 S. Södergren, H. Siegbahn, H. Rensmo, H. Lindström, A. Hagfeldt and S.-E. Lindquist, *J. Phys. Chem. B*, 1997, **101**, 3087–3090.

56 W. Chen, Q. Xu, Y. S. Hu, L. Q. Mai and Q. Y. Zhu, *J. Mater. Chem.*, 2002, **12**, 1926–1929.

57 A. Y. Stakheev, E. S. Shpiro and J. Apijok, *J. Phys. Chem.*, 1993, **97**, 5668–5672.

58 A. S. Al-Dughaither and H. de Lasa, *Ind. Eng. Chem. Res.*, 2014, **53**, 15303–15316.

59 Y. T. Kim, K. D. Jung and E. D. Park, *Appl. Catal. B Environ.*, 2011, **107**, 177–187.

60 M. M. J. Treacy and J. B. Higgins, *Collection of Simulated XRD Powder Patterns for Zeolites*, Elsevier, 4th edn., 2001.

61 J. H. Nobbs, *Rev. Prog. Color. Relat. Top.*, 1985, **15**, 66–75.

62 J. H. Park, J. H. Choung, I. S. Nam and S. W. Ham, *Appl. Catal. B Environ.*, 2008, **78**, 342–354.

63 K. Sun, H. Zhang, H. Xia, Y. Lian, Y. Li, Z. Feng, P. Ying and C. Li, *Chem. Commun.*, 2004, **216**, 2480–2481.

64 K. A. Dubkov, N. S. Ovanesyan, A. A. Shteinman, E. V. Starokon and G. I. Panov, *J. Catal.*, 2002, **207**, 341–352.

65 A. Ribera, I. W. C. E. Arends, S. De Vries, J. Pérez-Ramírez and R. A. Sheldon, *J. Catal.*, 2000, **195**, 287–297.

66 G. I. Panov, A. K. Uriarte, M. A. Rodkin and V. I. Sobolev, *Catal. Today*, 1998, **41**, 365–385.

67 Q. Zhu, E. J. Hensen, B. L. Mojet, J. H. van Wolput and R. A. van Santen, *Chem Commun*, 2002, 1232–1233.

68 N. Richards, E. Nowicka, J. H. Carter, D. J. Morgan, N. F. Dummer, S. Golunski and G. J. Hutchings, *Top. Catal.*, 2018, **61**, 1983–1992.

4 The effect of particle size on Pd-Al_2O_3 catalysts for N_2O decomposition.

4.1 Abstract

The preparation of efficient supported metal catalysts is of great importance in heterogeneous catalysis and the consequences of many synthesis variables are not fully understood. The catalytic activity of palladium supported on gamma alumina (Pd-γAl_2O_3) was found to be highly dependent on reaction cycles and catalyst preparation methodology for N_2O decomposition. Analysis of a series of 2.6 wt. % Pd-Al_2O_3 catalysts revealed the presence of physisorbed water on the support prior to metal deposition. *In-situ* XRD measurements showed that the thermal stability of Pd nanoparticles was enhanced if water was removed prior to metal deposition. The activity and stability of the catalysts following Pd deposition were greatly influenced by the point of zero charge of the support and the presence of water species on the surface of the support. Additionally, the presence of chloride species on the catalyst surface were identified as inhibiting the catalytic activity, with multiple reaction cycles shown to remove these species and a subsequent increase in activity observed (10.3 mol_{N2O} h^{-1} kg_{cat}^{-1} at 550 °C in the first use, increased to 28.7 mol_{N2O} h^{-1} kg_{cat}^{-1} in the 4th use at the same temperature). Although Pd dispersion was partly predictive of catalytic activity, the removal of surface water by calcining the support before palladium deposition resulted in improved activity. Comparison catalysts were prepared using a deposition technique that has been shown previously to control particle size; however, this requires an increased concentration of Cl ions, therefore, resulting in increased Pd-Cl species in the final catalyst. This increase in Pd-Cl species should hinder the catalytic activity but interestingly, this is not the case due to the fine control of particle size leading to a more positive effect on the decomposition rate.

4.2 Keywords

Nitrous Oxide Decomposition, Particle Size, CO Chemisorption, HAADF-STEM, Pd-Al_2O_3.

4.3 Introduction

Pd-Al_2O_3 catalysts have not been extensively studied in literature for the decomposition of N_2O into N_2 and O_2, [1–5] however similar catalytic systems have been demonstrated to exhibit high activity and stability in other applications. [6–11] Pekridis *et al.* reported a T_{100} (i.e. the temperature to reach 100 % conversion) of 425 °C using a 2 wt. % Pd-Al_2O_3 catalyst prepared by wet-impregnation. The group also showed that the addition of propane to the gas feed lowered the T_{100} to 400 °C. [1] As described previously, the rate limiting step in the decomposition of N_2O is typically the recombination of oxygen to form O_2. [12–18] Therefore, propane acts as reductant that can facilitate the abstraction of oxygen from the oxidised active site, significantly increasing the observed rate of N_2O decomposition at lower temperatures. [1,2] Christoforou *et al.* reported that 72 % conversion was possible using 2 wt. % Pd-Al_2O_3 at 600 °C, but the addition of propane to the feed lowers this temperature by over 200 °C with 100 % N_2O conversion. [2] Doi *et al.* utilised a higher weight loading of 5 % with only 60 ppm N_2O in the gas stream, and showed that it was possible to decompose this low concentration at 300 °C; however, air was used as the balance gas in this reaction and it has been shown since that the addition of oxygen to the feed increases the activity. [5] It is important to note that in most cases the addition of oxygen to the gas feed limits the conversion of N_2O, because the oxygen present oxidises the active site of the catalysts. [1,19,20]

Tateishi *et al.* also demonstrated that a higher weight loading was also active for this reaction with a commercial 5 wt.% Pd-Al_2O_3 catalyst achieving 100 % conversion at 320 °C, though the catalyst prepared in house by the group by wet impregnation required 500 °C to achieve the same conversion under the same conditions. [4] Pekridis *et. al.* prepared a 2 wt. % Pd-Al_2O_3 catalyst and achieved 90 % compared to 95 % when propane is present at 350 °C, however when comparing the Pd:N_2O molar ratio Pekridis had a ratio of 1:0.23 compared to the research in

this chapter at 1:3.80, therefore, the catalysts in this chapter outperform the previous literature catalyst. [1]

This work investigates the importance of surface species and particle size on Pd-Al_2O_3 catalysts for the decomposition of N_2O in the presence and absence of a reductant, propane. The effect of removal of surface species such as water and chloride ions have been investigated by different pre-treatments and support pre-treatments. In addition to comparing how activity changes based on these pre-treatments, these have been evaluated for the control the particle size and consequently, catalyst activity. Through pre-treatment of the catalyst support prior to metal deposition, catalytic activity significantly increased, resulting in a decrease of the T_{100} from 550 °C to 400 °C. Pd-Al_2O_3 catalysts show promise for N_2O decomposition when a reductant (such as propane) is added to the gas feed and show high stability over extended periods of time. [1]

4.4 Effect of reaction cycle on catalytic activity

A blank reaction was performed with only quartz wool and no catalyst. No conversion of N_2O was measured over the temperature range of 300 – 600 °C, indicating the reactor was not active over the temperature range of interest (Table 4.1 Entry 1). Decomposition of N_2O was studied using 2.6 wt. % Pd-Al_2O_3 prepared by wet impregnation, with a pre-treatment (1 h at 600 °C, 13 % O_2, 87 mL min^{-1}) over the temperature range 300 – 600 °C. The fresh catalyst (Table 4.1 entry 2) was able to convert at a rate of 10.3 mol_{N2O} h^{-1} kg_{cat}^{-1} at 550 °C, while the catalyst by Tzitzious *et al*. converted at a rate of 20.9 mol_{N2O} h^{-1} kg_{cat}^{-1} at the same temperature.[21]

Table 4.1. The effect of multiple reaction cycles or heat treatments on N_2O conversion over 2.6 wt. % Pd-Al_2O_3 catalysts.

Entry	Catalyst (2.6 wt. % Pd-Al_2O_3)	T_{50}[a] (°C)	Conversion at 550 °C (%)	Decomposition Rate at 550 °C (mol_{N2O} h^{-1} kg_{cat}^{-1})
1	Blank	-	0	0
2	Fresh	577	24	10.3
3	2R	565	39	16.7
4	3R	542	56	24.0
5	4R	527	67	28.7
6	5R	540	57	24.4
7	5HT	584	22	9.4

[a] the temperature at 50 % N_2O conversion; R – Reaction cycle

Large quantities of N_2O are produced in the tail gases of industrial processes such as the production of nitric acid and therefore catalysts have been designed to convert this into less destructive non-greenhouse gases. With stability being a key factor in industrial use, catalyst re-use was studied as an indicator as to how the catalysts would behave in start-up-shut down procedures. To investigate stability of the catalyst, the catalyst was reused with a pre-treatment between each use, which showed an increase in N_2O conversion with each use, up to the fourth use (Table 4.1 entries 3-5). After the second reaction cycle the decomposition rate increased from 16.7 to 24.0 mol_{N2O} h^{-1} kg_{cat}^{-1}, this increased to a maximum at the 4th use (**4R**) of 28.7 mol_{N2O} h^{-1} kg_{cat}^{-1}. The fifth cycle saw a decrease in the decomposition rate to 24.4 mol_{N2O} h^{-1} kg_{cat}^{-1}. The observed increase in activity after multiple uses was investigated by replicating the five heat treatment cycles *ex situ*, i.e. in a furnace (flowing air at 600 °C for 1 h) to simulate reaction conditions and potentially remove the remaining chloride species. The activity of this catalyst (denoted **5HT**) did not compare to that of the multiple use catalyst (Fig. 4.1), but was comparable to the fresh catalyst. The decomposition rate at 550 °C was 9.4 mol_{N2O} h^{-1} kg_{cat}^{-1}.

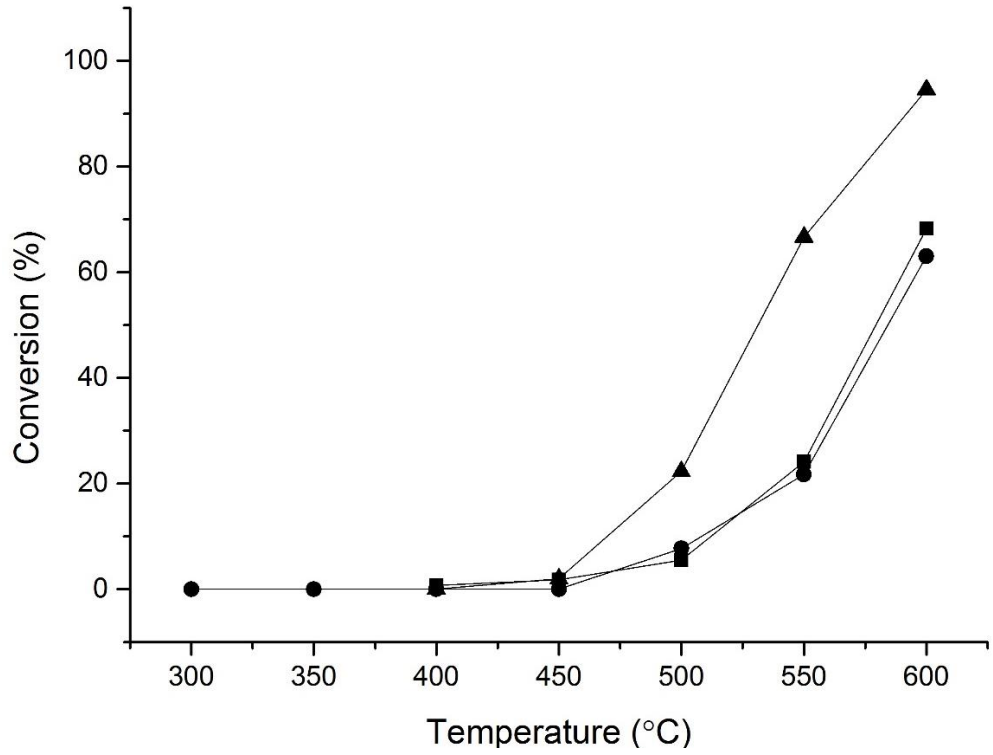

Fig. 4.1. The effect of multiple uses or heat treatments on N_2O decomposition using a 2.6 wt. % Pd-Al_2O_3 catalyst. Reaction Conditions: 1 % N_2O/He total flow 100 mL min^{-1}, GHSV: 76690 h^{-1} Legend: ■ - 2.6 wt. % Pd-Al_2O_3 Fresh, ● - 2.6 wt. % Pd-Al_2O_3 **5HT**, ▲- 2.6 wt. % Pd-Al_2O_3 **5R**.

The Pd-Al_2O_3 catalysts were characterised to understand the origin in the difference in activity. The samples of interest were the fresh 2.6 wt. % Pd-Al_2O_3 catalyst, the catalyst after five reaction cycles (**5R**) and the catalyst after five heat-treatments in the furnace (**5HT**). Fig. 4.2 shows the XRD patterns; the support exhibits only alumina reflections, as does the fresh 2.6 wt. % Pd-Al_2O_3 catalyst with these assigned as γ-Al_2O_3 (3 1 1) 2θ = 37.1 °, (4 0 0) 2θ = 46.0 ° and (4 4 0) 2θ = 66.6 °. [22] In contrast, the 5R and 5HT catalysts exhibited reflections due to Pd. These reflections were assigned as PdO (1 0 1) 2θ = 33.855 °, PdO (3 1 1) 2θ = 54.900 ° and PdO (2 1 1) 2θ = 71.485 °. [23] A Pd^0 reflection was observed at Pd (1 1 1) 2θ = 42.034 °. [24] There is no reflection present for metallic Pd in the fresh catalyst, this indicates that the particle size of Pd is below the nanoparticle detection limit, around 5 nm, or not present. In contrast, the **5R** and **5HT** catalysts exhibited reflections due to Pd as PdO (1 0 1) 2θ = 33.855 °, PdO (3 1 1) 2θ = 54.900 ° and PdO (2 1 1) 2θ = 71.485 °. [23] A Pd^0 reflection was observed at Pd (1 1 1) 2θ = 42.034 ° [24]. In the used (**4R** and **5R**) and **5HT** catalysts there are reflections present due to both PdO and Pd, this presence of reflections suggests that Pd nanoparticles have sintered as the particles are now observable by XRD.

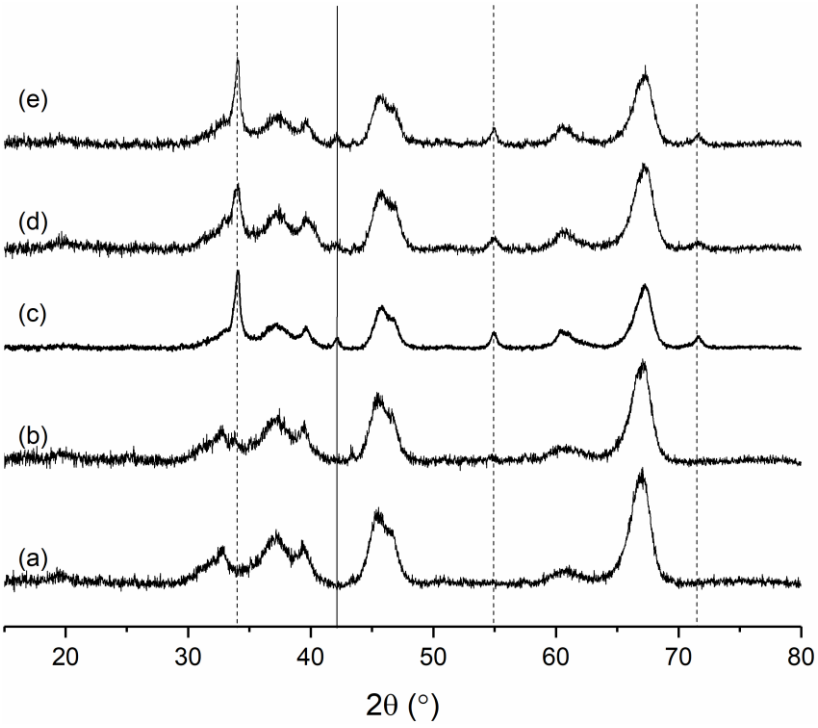

Fig. 4.2. XRD data for 2.6 wt. % Pd-Al_2O_3 and γ-Al_2O_3 Legend: (a) – Al_2O_3, (b) 2.6 wt. % Pd-Al_2O_3 Fresh, (c) 2.6 wt. % Pd-Al_2O_3 4R, (d) 2.6 wt. % Pd-Al_2O_3 5R, (e) 2.6 wt. % Pd-Al_2O_3 5HT, dashed line – PdO, solid line – Pd. [22,23]

The improvement in activity on repeated uses may have been caused by the removal of residual Cl species that has been reported to poison the catalyst. [25] This would be achieved over the reaction cycles through a process of converting any remaining Pd-Cl species to PdO. X-Ray photoelectron spectroscopy (XPS) was used to investigate the surface composition and oxidation state of Pd in more detail. Most literature Pd XPS spectra consist of two peaks at 336.8 eV and 334.9 eV, with the peak at 336.8 eV ascribed to PdO-Al_2O_3 as previously reported by Batista *et al.* [26] while the peak at 334.9 eV was attributed to Pd^0 on Al_2O_3. [27,28] Depending on catalyst preparation techniques, Pd-Cl species can also be present in the spectrum and correspond to the peaks at 338.2 eV.[29] Each Pd species will have two peaks assigned to it due to the spin orbit splitting value of 5.3 eV.[30,31] For example Pd^{2+} (Pd 3d 5/2) has a major peak at *ca.* 336.8 eV whilst the second peak (Pd 3d 3/2) at *ca.* 342.1 eV. [30,31]. All catalysts show only PdO and Pd-Cl species and the concentration of these species was observed to change as the catalyst was subjected to reaction conditions. Specifically, the proportion of Pd-Cl species decreased while PdO species increased, overall. The **5R** catalyst shows an increase in PdCl species over the **4R** catalysts. This is not because the catalyst has gained Cl, but because the % Pd present has decreased meaning more of the surface of the Pd is in the form PdCl as sintering has taken place (Table 4.2). When the catalyst was heated in the furnace (**5HT**) almost all the PdCl species were removed (Fig. 4.3), however, the catalytic activity is not improved above that of the fresh catalyst. When the catalyst is used/heated multiple times the % of Pd-Cl decreases, this is accompanied by a decrease in the intensity of Cl in the Cl 2p region (not shown). As the number of heat treatments increases the surface concentration of total Pd % decreases (Table 4.2), this indicates that the % of Pd at the surface has decreased, which can indicate Pd sintering or agglomeration has taken place. This is seen dramatically between the **4R** and **5R** catalysts with the at.% of Pd dropping from 0.40 to 0.11 %. As described, this is due to the decrease in the surface of Pd available for analysis due to sintering or agglomeration.

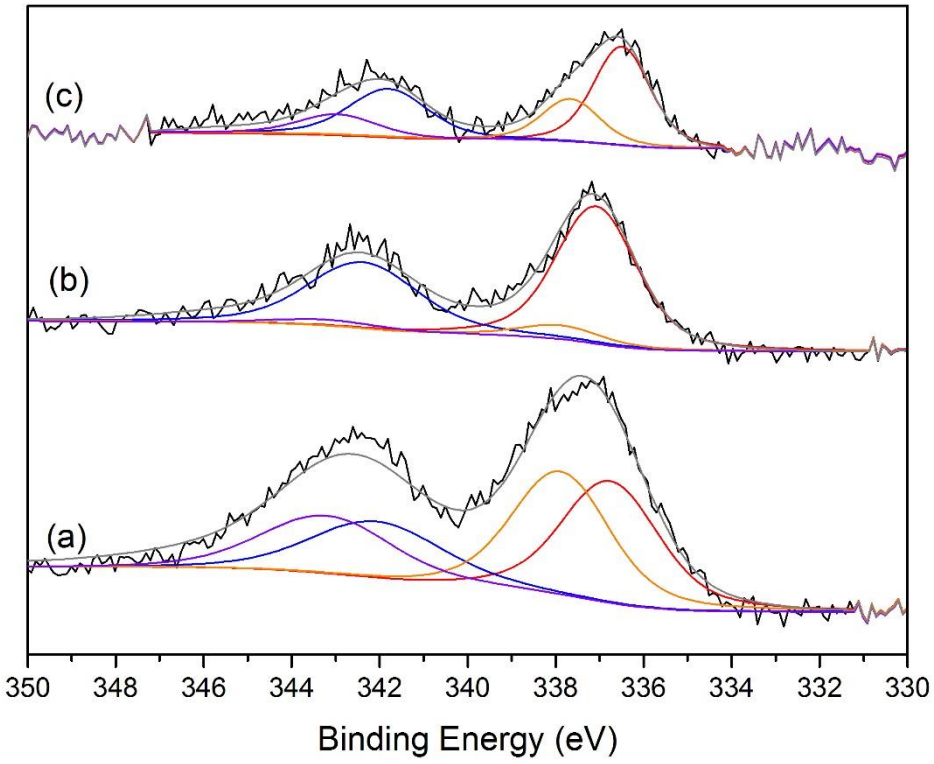

Fig. 4.3. XPS spectra for various 2.6 wt. % Pd-Al_2O_3 catalysts. Each spectra is fitted with two peaks corresponding to PdO and Pd-Cl species. Legend: Red and Blue – PdO, Orange and Purple – PdCl. 2.6 wt.% Pd-Al_2O_3 (a) Fresh, (b) 5HT, (c) 5R.

Table 4.2. Surface composition of Pd-Al_2O_3 catalysts as reported by XPS analysis.

Catalyst	**Pd 3d (at.%)**	**% of PdO (337 eV) (%)** [26]	**% of PdCl (339 eV) (%)** [29]
2.6 wt. % Pd-γAl_2O_3 Fresh	0.46	50	50
2.6 wt. % Pd-γAl_2O_3 **4R**	0.40	78	22
2.6 wt. % Pd-γAl_2O_3 **5R**	0.11	72.7	27.3
2.6 wt. % Pd-γAl_2O_3 **5HT**	0.25	92	8

The XRD patterns indicate that with increased reaction cycles and heat treatments Pd sintering took place. Furthermore, XPS measurements indicated that in addition to sintering the population of Pd-Cl species decreased across the samples. However, the N_2O decomposition activity of the **4R** sample when compared to the **5HT** sample is suggestive of another factor not examinable by XPS or XRD, such as particle size. Therefore, HAADF-STEM was performed on the samples to provide a greater insight into the particle size changes suggested by XRD and XPS. Comparison of fresh **5R** and **5HT** 2.6 wt. % Pd-Al_2O_3 samples by electron microscopy are shown in Fig. 4.4. The fresh catalyst possesses Pd particles in the range of 1-5 nm (Fig. 4.4a). Large Pd particles (> 10 nm) of PdO are present after five reaction

cycles (Fig. 4.4b), however, small particles persist. These large particles were not present in the fresh catalyst and are, therefore, consistent with analysis of the XRD and XPS results. That is PdO particles have sintered to form large nano-particles greater than 10 nm, which do not appear to be contributing to the activity of the catalyst. Liu *et al*. showed that sintering is a common mechanism by which metal surface area and dispersion decreases.[32,33] In the **5HT** sample, HAADF-STEM shows that there are a range of particle sizes visible with both large particles (> 5 nm) and small (< 2 nm) present. In general, the presence of the large nanoparticles indicates that during the heat treatments sintering occurred and despite the removal of Cl^- ions an increase in activity was not realised, due to the concomitant the loss of metal surface area. The increase in activity of the Fresh catalyst with multiple use is due to incremental removal of Cl^- ions, with a slight drop in activity seen after the 4th cycle (**4R**) as the effect of the removal of Cl is negated by the formation of larger Pd nano-particles, as seen by HAADF-STEM in the **5R** sample. Representative particle size distributions could not be constructed due the presence of non-spherical agglomerates of nano-particles that would produce a statistically irrelevant distribution.

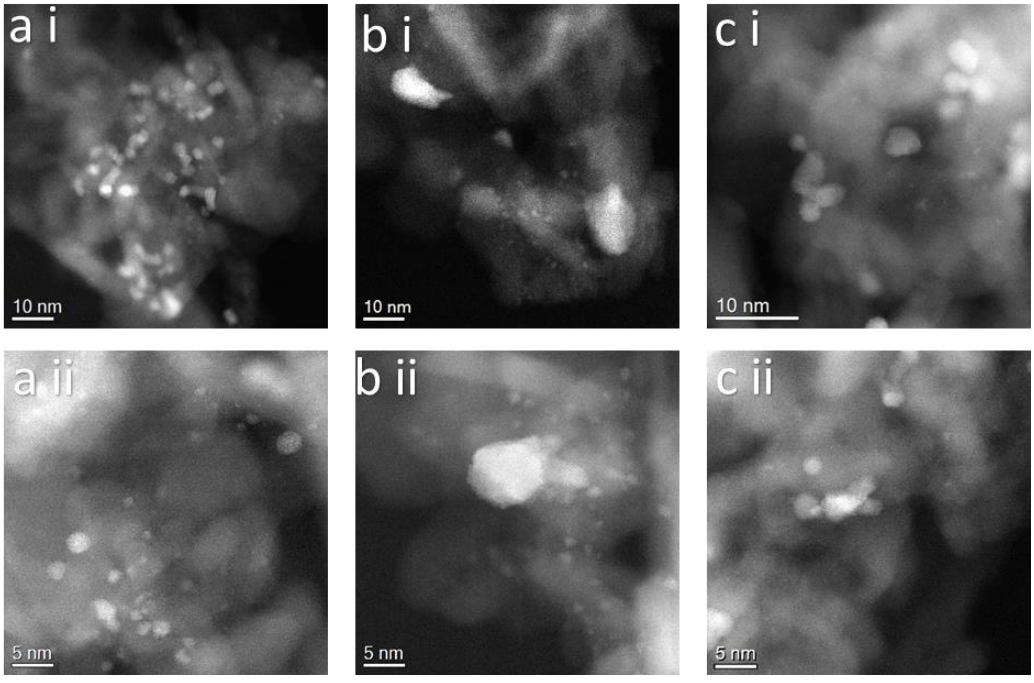

Fig. 4.4. HAADF-STEM images of 2.6 wt. % Pd-Al_2O_3 Fresh (a), 5R (b), and 5 HT (c) acquired by Qian He at Lehigh University using a JEOL ARM 200CF AC-STEM instrument.

The Fresh Pd catalyst prepared by impregnation was tested for N_2O decomposition, and when used multiple times the activity increased. XPS showed that the majority of Cl species that remain from the catalyst preparation were removed and HAADF-STEM indicated that there was an increase in small, well dispersed nano-particles. To replicate the removal of any chlorine species that remained on the catalyst, a heat-treatment cycle was employed. The activity was the same as seen previously in the fresh catalyst. Even though almost all Cl species had been removed during the heat treatments, the STEM images indicate that sintering has taken place as there are only a small number of small nano-particles present in the 5HT sample, with mainly large nano-particles (> 5 nm) seen. Therefore the increase in activity that is expected from the removal of Cl species is not observed, due to the decrease in metal surface area available for reaction.

4.5 Effect of support calcination on catalytic activity.

Initial results suggest that alongside the presence of Cl^-, the size of the Pd particles strongly contribute to the rate of N_2O decomposition. To achieve similar levels of activity as with the 5th reaction cycle 2.6 wt. % Pd-Al_2O_3 catalyst without carrying out multiple catalyst tests the support was calcined before catalyst preparation (denoted as **SC**). As Al_2O_3 is a hygroscopic, it was hypothesised that the removal of surface water species and carbonates (XPS C 1s region showed peak at 289.7 eV) could enhance the dispersion of Pd, as these species may block Al_2O_3 pores. [34,35] A 2.6 wt. % Pd-Al_2O_3 catalyst was prepared by wet impregnation using γ-Al_2O_3 that had been calcined in flowing air at 600 °C at 10 °C min^{-1} for 4 h. The removal of water during the calcination, as shown by SS MAS NMR (Fig. 4.8), lead to a change in the point of zero charge of the γ-Al_2O_3, from PZC = 8.43 for the untreated support, with this changing to 8.04 after calcination (Fig. 4.5 and Fig. 4.6). The R^2 values of both polynomial fittings show good fittings to the data, the fresh PZC curve has a R^2 of 0.97902, whilst the calcined PZC curve has a R^2 value of 0.98854. The pH of the PdCl solution used to prepare the catalysts was recorded to be pH 1, with the species of Pd confirmed as $PdCl_3(H_2O)^-$ by Raman spectroscopy (Fig. 4.7). Both peaks can be assigned to Pd-Cl stretches, the symmetric stretch at 296 cm^{-1} and 342 cm^{-1} due to out of phase mode of Pd-Cl. [36] When the pH of the solution is lower than

that of the PZC, the surface will be protonated and will strongly interact with anions [37,38] therefore the decrease in PZC of the calcined catalyst will mean the surface is less positively-charged during the catalyst preparation. This modification in surface charge may be beneficial for the dispersion of the Pd nanoparticles on the support, as is the case for the preparation of gold catalysts by deposition-precipitation.[39] Therefore the 2 wt. % Pd-Al_2O_3 **SC** would be expected to have a better dispersion than the palladium supported on the untreated support. An accurate Pd weight loading on both the fresh and **SC** Pd-Al_2O_3 catalysts was performed with ICP-OES, both catalysts had a 2.61 wt. % Pd loading.

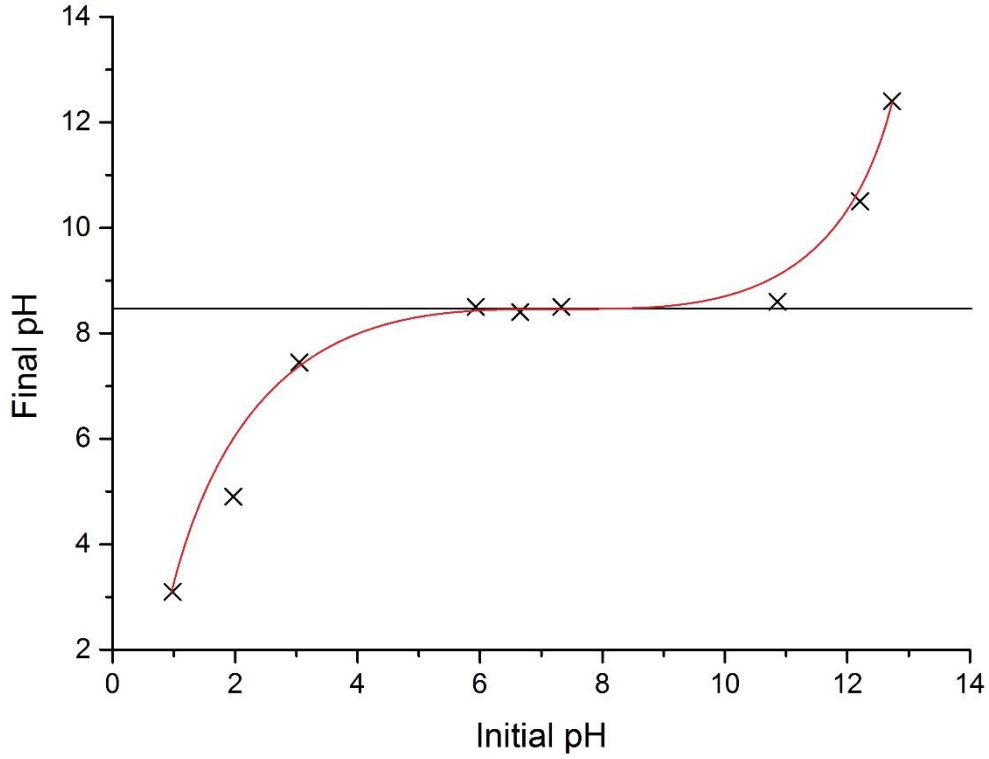

Fig. 4.5. Calculation of Point of Zero Charge (PZC) for untreated Al_2O_3. R^2 = 0.97902

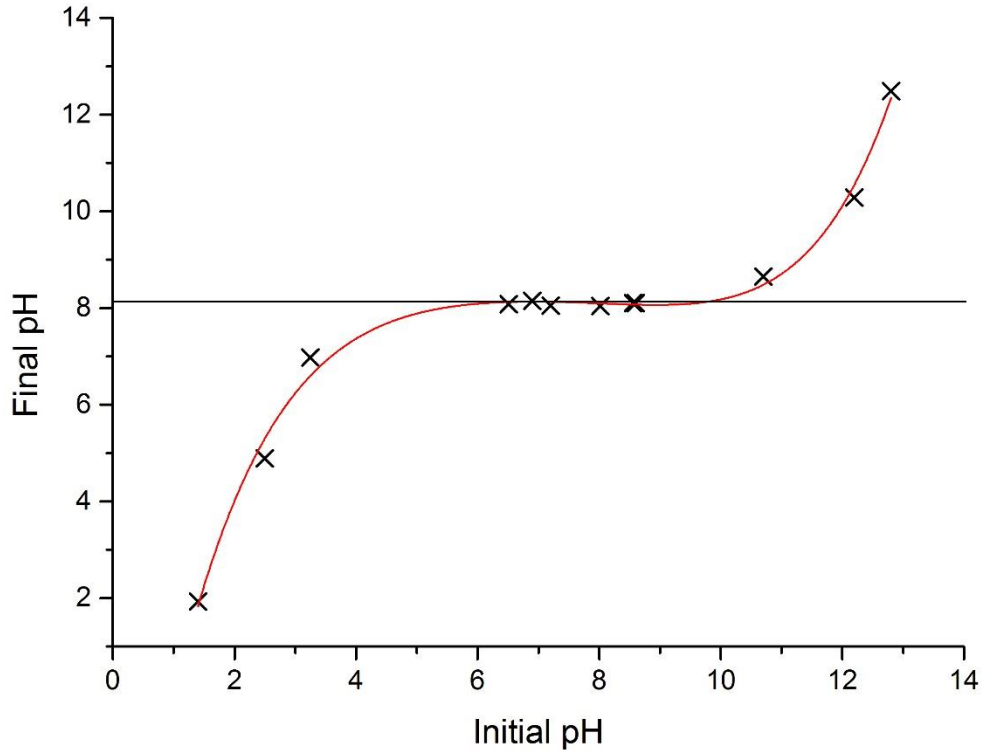

Fig. 4.6. Calculation of Point of Zero Charge (PZC) for calcined Al_2O_3. R^2 = 0.98854

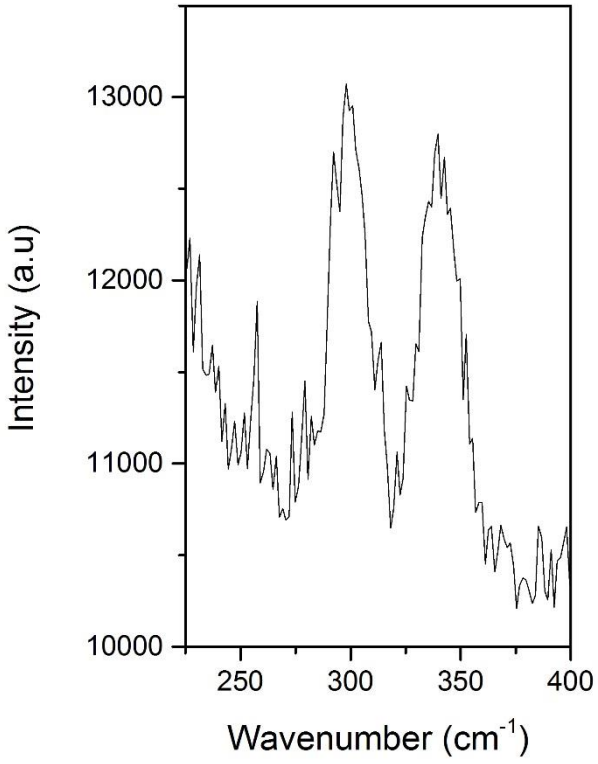

Fig. 4.7. Raman Spectra of $PdCl_2$ solution using a 514 nm laser at 100 % power and 100 scans.

The properties of the untreated, as received Al_2O_3 and calcined Al_2O_3 support were investigated using solid state magic angle spinning (MAS) ^{1}H NMR (Fig. 4.8). Both spectra contain a single broad peak that is associated to the protons of physisorbed water. The difference in broadness is related to the quantity of water absorbed on the surface of the support. There are more physisorbed water molecules in the fresh sample than the calcined sample even though these are present in both. Both spectra have a large resonance at 4.6 ppm that corresponds to hydrogen bonded water on the Al_2O_3 surface. The untreated Al_2O_3 spectra has a shoulder present that is not present in the calcined sample; this shoulder at 1.2 ppm is due to the presence of non-hydrogen bonded physisorbed water.[40,41] In this spectra there is also a slight shoulder at 7 ppm; this resonance is due to Brønsted acid sites that are produced when water adsorbs onto a Lewis acidic site.[42] The lack of the two shoulder resonances indicates that water was removed during the calcination treatment.

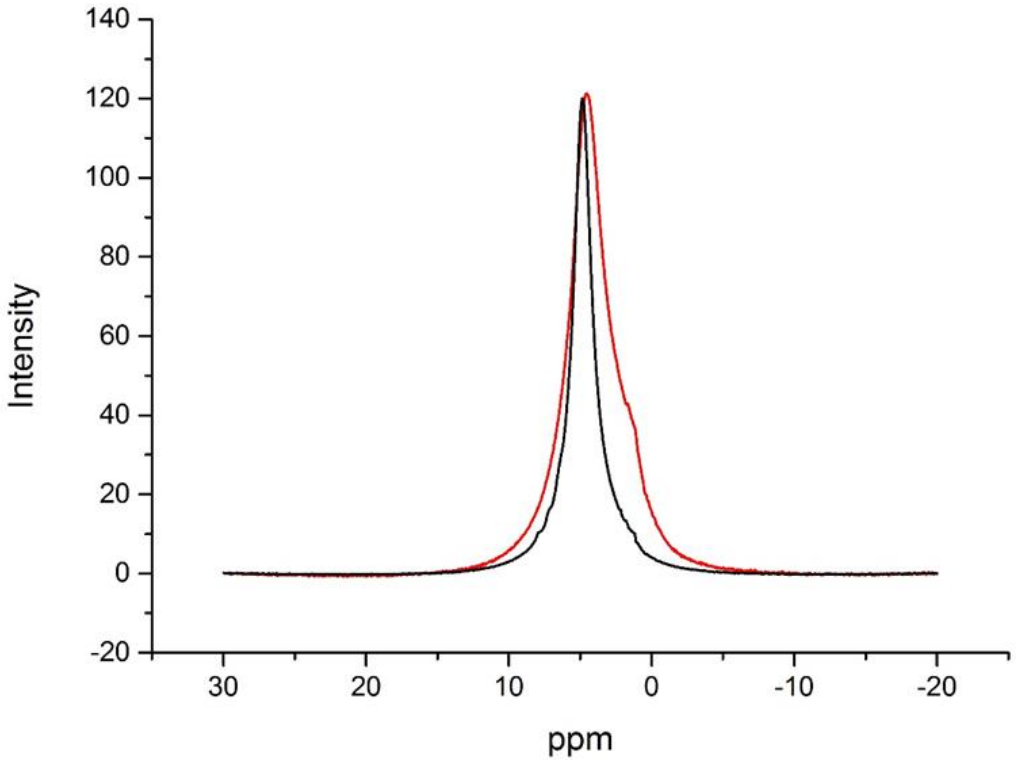

Fig. 4.8. Solid-state ^{1}H NMR spectrum of Al_2O_3 untreated (red) and calcined (black)

TGA of both the untreated and the calcined Al_2O_3 show a gradual decrease in mass loss over the temperature range tested for both the fresh and the calcined Al_2O_3 (Fig. 4.9). The mass loss is due to the removal of water, in the case of the untreated Al_2O_3 both chemisorbed and physisorbed water. In the case of the calcined Al_2O_3,

only chemisorbed water was removed. The calcined Al_2O_3 loses more mass due to the fact that water was removed from the surface during the calcination, leaving an extremely clean surface but, as alumina is hygroscopic, it absorbs water from the atmosphere, with more absorbed now that the surface is clean, due to the increased lability of the surface. The fresh sample loses 0.62 mg (10.91 mg starting weight) after exposure to 800 °C, whereas the calcined Al_2O_3 loses 0.71 mg (10.53 mg starting weight) after the same treatment.

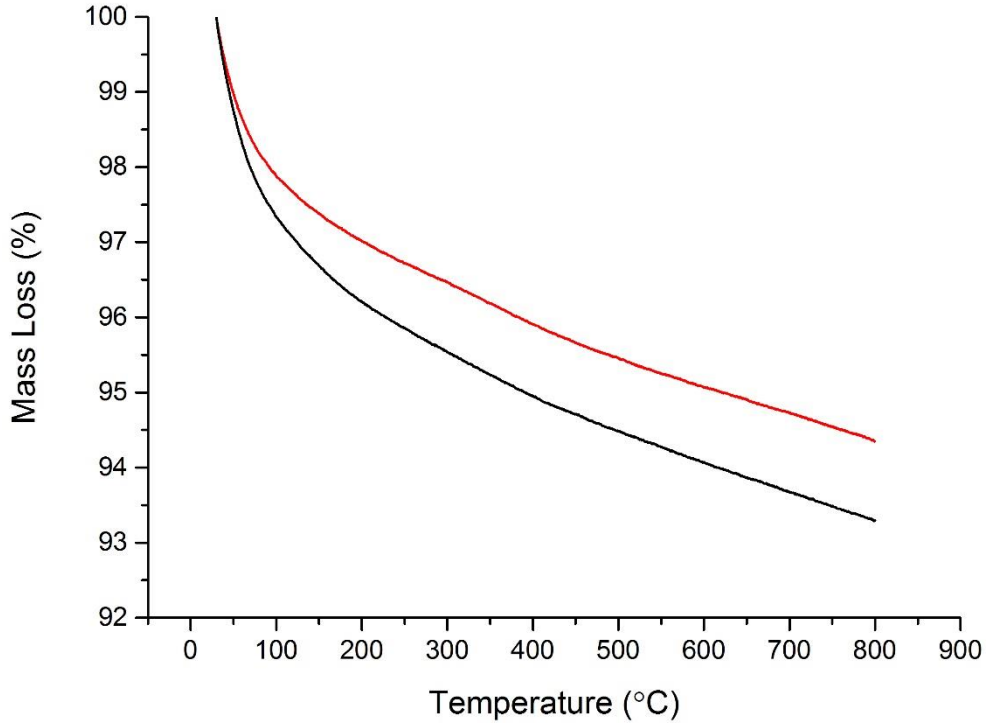

Fig. 4.9. TGA showing the mass loss over the temperature range of 800 °C of both fresh (red) and calcined Al_2O_3 (black) in nitrogen, heated at 10 °C min^{-1}.

A TGA of reaction conditions was performed on both the fresh and **SC** catalyst to monitor the weight loss during the reaction, the profile is as described below:

1. A. Reaction pre-treatment in air to 200 °C,
1. B. Second part of pre-treatment, 200-600 °C and hold for 1 hour.
2. Cool from 600 °C to 50 °C.
3. Change gas from Air to 1% N_2O/N_2 and hold for 1 hour at 50 °C.
4. A. Heat to 400 °C and hold for 1 hour,
4. B. Increase temperature at 50 °C intervals and hold at each temperature for 1 hour.

Both catalysts show mass loss in the first and 4th steps of the profile, whilst mass gain is seen in steps 2 and 3. Fig. 4.10 shows the difference between the two catalysts, most differences are seen in the pre-treatment step, with the **SC** catalyst

loosing *ca.* 6 % in the first step compared to *ca.* 10 % with the fresh support. The fresh catalyst also gains more weight when the gas is changed to 1 % N_2O/N_2 (step 3) compared to the **SC** catalyst. The reaction profile in step 4 is very similar in both cases. From this we can determine that the weight loss during the 1st step is due to the removal of water bound to the Al_2O_3. This first step is not as drastic in the **SC** catalyst because the water is removed during the support calcination before catalyst preparation, with any physisorbed water that may have reabsorbed removed in the calcination step after metal loading.

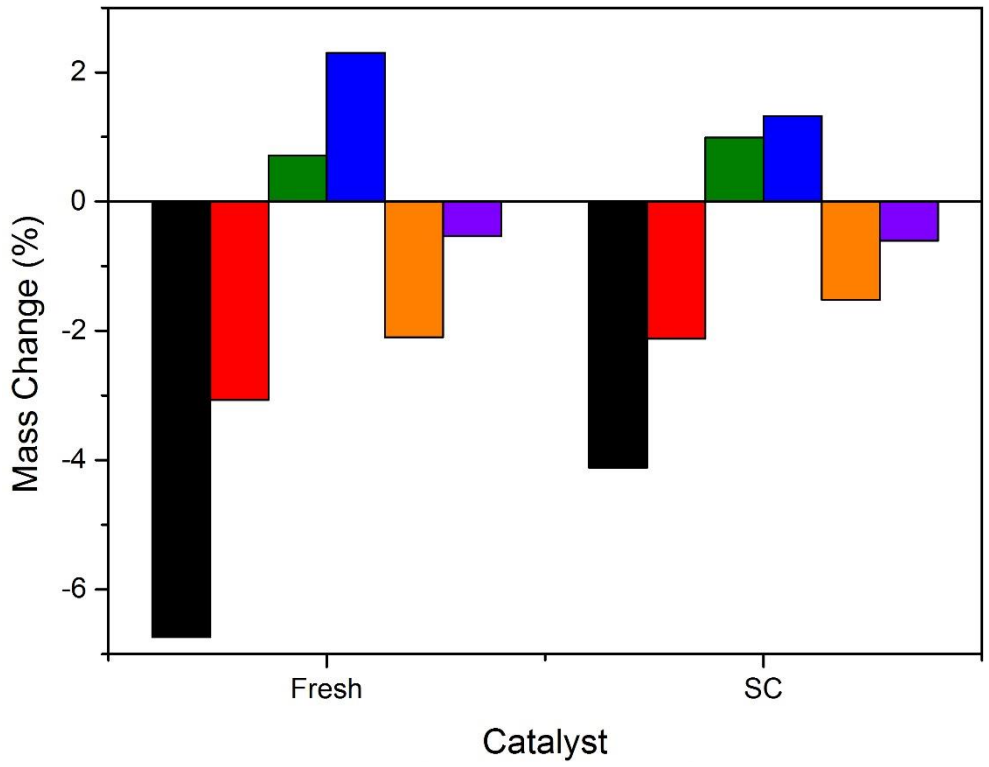

Fig. 4.10. Graph showing weight change for 2 wt.% Pd-Al_2O_3 Fresh and **SC** per step of the reaction shown the TGA's above. Legend: Black – Step 1 a < 200 °C, Red – Step 1 b: 200 - 600 °C, Green - Step 2, Blue – Step 3, Orange – Step 4a < 400 °C, Purple – Step 4b: 400 - 600 °C.

HAADF-STEM shows similar Pd nanostructures present in the fresh and **SC** catalysts with nanoparticles and clusters present in both samples (Fig. 4.11). However, HAADF-STEM indicates that in the **SC** catalyst there are an increased quantity of small nanoparticles than in the fresh catalyst (Fig. 4.11). The HAADF-STEM of the **SC** catalyst has many nanoparticles less than 1 nm and some nanoparticles in the range of 3 – 8 nm. When compared to the used catalyst, there are significantly more smaller nanoparticles present in the **SC** catalyst, for example in the images in Fig.

4.4.a there are no nanoparticles that are sub 1 nm, whereas these are easily identifiable in the **SC** catalyst Fig. 4.11b.

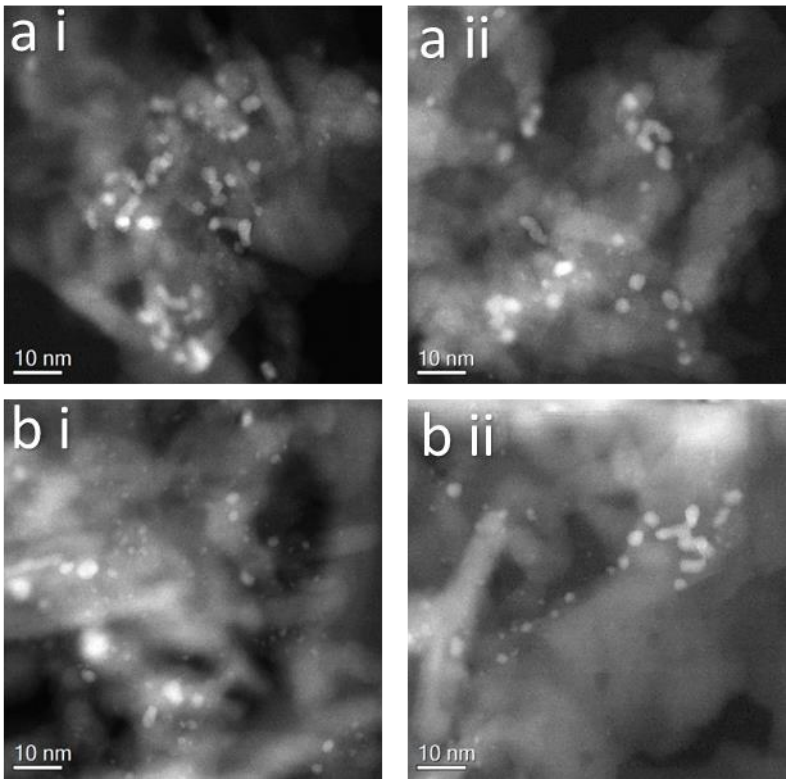

Fig. 4.11. HADDF-STEM images of 2.6 wt. % Pd-Al_2O_3 Fresh (a) and Support calcined (**SC**) (b) acquired by Qian He at Lehigh University using a JEOL ARM 200CF AC-STEM instrument.

The **SC** catalyst was evaluated for N_2O decomposition and compared to the fresh and **5R** catalysts (Fig. 4.12). The T_{50} obtained over the **SC** catalyst was found to be 561 °C and compared to the values of 577 and 540 °C over the fresh and **5R** catalysts. The support pre-treatment step has increased the N_2O decomposition rate to 15.9 mol_{N2O} h^{-1} kg_{cat}^{-1} at 550 °C and is indicative of the formation of a higher density of active small Pd nano-particles. Performing a comparable reaction cycle with the **SC** catalyst resulted in a modest increase of the decomposition rate to 18.8 mol_{N2O} h^{-1} kg_{cat}^{-1} at 550 °C and a decrease of the T_{50} to 556 °C over the fifth use catalyst (**SC 5R**). The modest improvement in the decomposition rate suggests that the PdCl population has decreased as with the **5R** sample.

Propane acts as reductant that can facilitate the abstraction of oxygen from the oxidised active site, significantly increasing the observed rate of N_2O decomposition at lower temperatures. [1,2,12–18] Here the presence of propane lowers the temperature required by almost 200 °C. Reactions were carried out with the

addition of propane in the gas feed (1 %). The dramatic increase in decomposition activity is observed with all catalysts but is most noticeable with the **SC** catalyst: with N_2O only, 95 % conversion is achieved at 600 °C; in the presence of propane 95 % conversion is achieved at 350 °C.

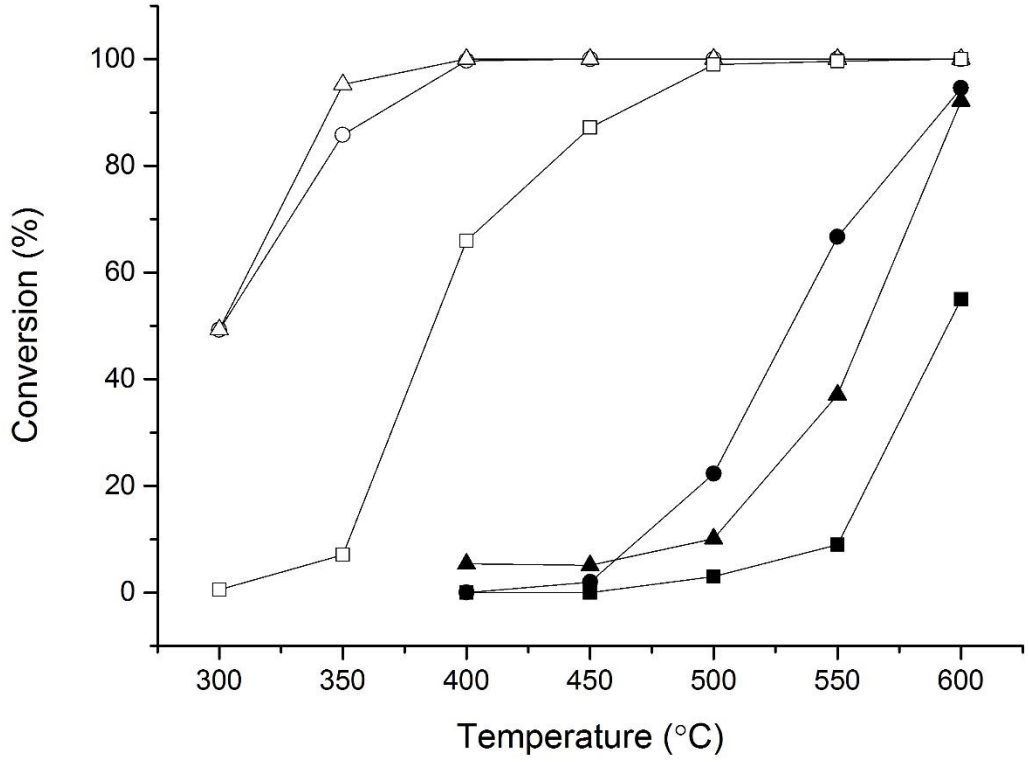

Fig. 4.12. The effect on N_2O conversion of heat treatments on 2.6 wt. % Pd-Al_2O_3. Reaction Conditions: total flow 100 mL min^{-1}, GHSV: 76690 h^{-1} 300 - 600 °C, Closed symbols: 1 % N_2O/He, Open symbols: 1 % N_2O/1 % C_3H_8/He. Legend: ■ - 2.6 wt. % Pd-Al_2O_3 Fresh, ● - 2.6 wt. % Pd-Al_2O_3 5R, ▲- 2.6 wt. % Pd-Al_2O_3 **SC**.

ICP-OES was performed to determine an accurate Pd weight loading on both the fresh and **SC** 2.6 wt. % Pd-Al_2O_3 catalyst. Analysis showed both catalysts have a 2.61 wt. % Pd loading. Therefore, the change in activity is not considered to be due to a difference in Pd loading.

The superior dispersion of Pd on the **SC** catalyst, as evidenced by HAADF-STEM, implies that the anchoring of Pd is stronger on the calcined support. To examine directly the stability of the Pd species on the surface of the Al_2O_3, *in situ* XRD was performed. The *in-situ* XRD profiles of 2.6 wt. % Pd-Al_2O_3 and **SC** catalysts are illustrated in Fig 4.13.a and b respectively. The samples were heated in 1 % N_2O/N_2 and cooled in N_2 at 50 °C intervals. The *in situ* XRD patterns of 2.6 wt. % Pd-Al_2O_3 shows that small PdO reflections were present at 500 °C, with the intensity of the

PdO reflections not increasing past 550 °C, with Pd^0 reflections forming at the same temperatures. In the **SC** catalyst PdO and Pd reflections were not visible until at least 600 °C. The difference in temperature required to observe reflections corresponding to nanoparticles of PdO and Pd indicates that the Pd nanoparticles are more strongly anchored to the calcined Al_2O_3 than the untreated support.

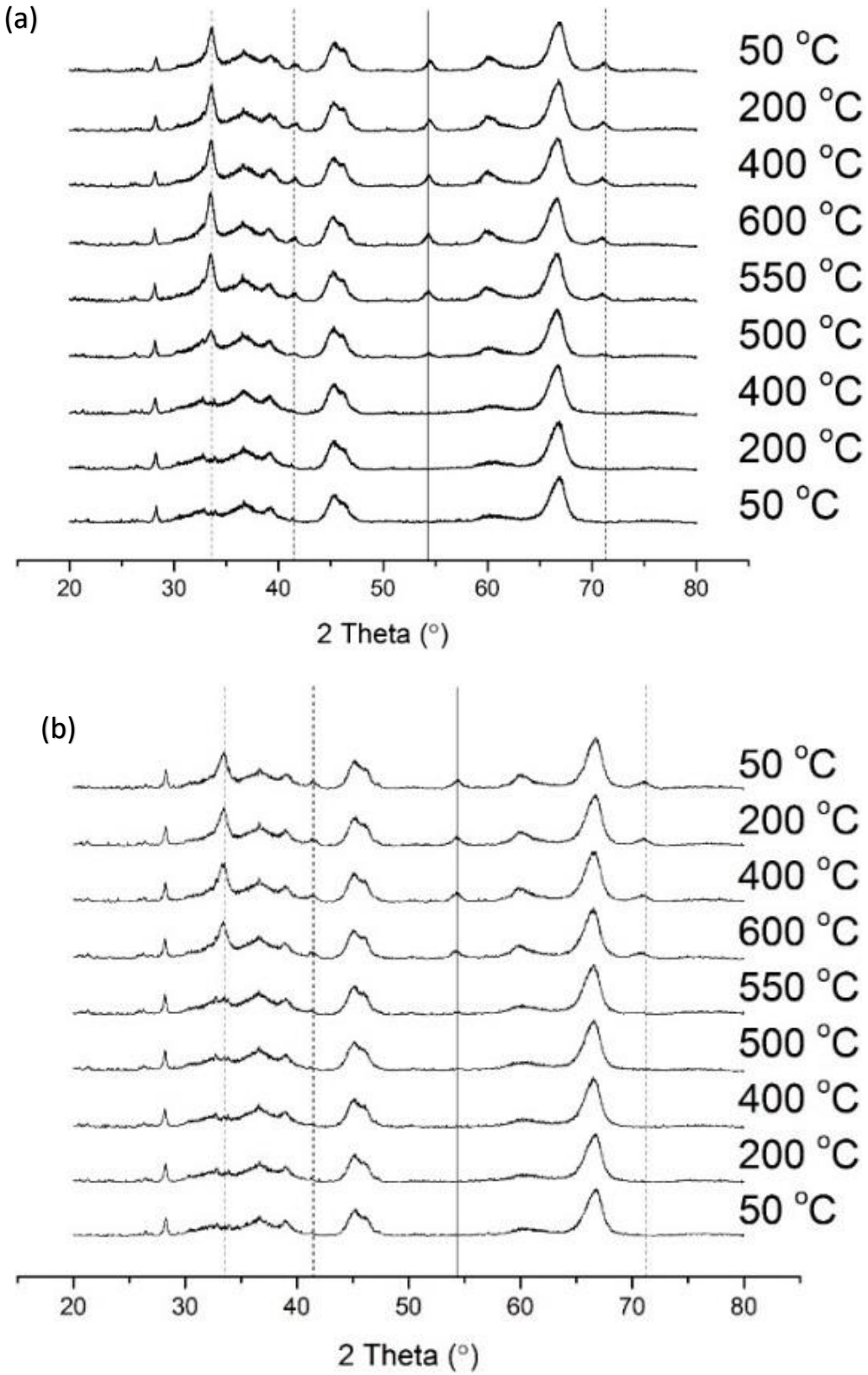

Fig. 4.13. *In-situ* XRD of (a) 2.6 wt. % Pd-Al_2O_3 Fresh and (b) 2.6 wt. % Pd-Al_2O_3 **SC** heated in 1 % N_2O/N_2 and cooled in N_2 at 50 °C intervals. Legend: Solid Line Pd, Dashed line PdO.

The average particle size of the Pd present on the surface were further investigated with CO chemisorption of the fresh and **SC** catalysts. It is assumed that all Pd particles are hemispherical and that one CO molecule will bind to one Pd atom: we acknowledge that STEM has shown this is not the case but this will give an average particle size and metal surface area. Metal nanoparticle dispersion increased modestly from 24.7 % to 27.5 % with the fresh to the **SC** catalyst (Table 4.3). The average particle size of Pd particles in the **SC** catalyst decreased when compared to the fresh catalyst. This decrease in average particle size indicated that the nanoparticles found on the **SC** catalyst are smaller and further support the inference that smaller particles are more active than larger particles for N_2O decomposition. This is due to the smaller particles having a larger surface area per gram of metal and this small change in particle size facilitates an increased decomposition reaction rate through the increased surface area available.

Table 4.3. Dispersion and metal surface area as calculated by CO Chemisorption on 2.6 wt. % Pd-Al_2O_3 fresh and SC.

Catalyst	**Metal Surface Area (m^2 g^{-1})**	**Avg. crystallite size (nm)**	**Dispersion (%)**
2.6 wt. % Pd-Al_2O_3 Fresh	2.9	1.51	24.7
2.6 wt. % Pd-Al_2O_3 **SC**	3.2	1.36	27.5

4.6 How the control of particle size by modified impregnation catalyst preparation technique effects catalytic activity

The catalytic activity for N_2O decomposition when propane is present over the fresh and **SC** catalysts is markedly different (Fig. 4.12). To investigate the effect of particle size, the catalysts were re-prepared using a modified impregnation (**MI**) technique which has been shown previously to produce catalysts with a very narrow particle size distribution.[43]

Palladium was deposited with the MI technique on a calcined alumina and an as-received alumina and examined by XPS, XRD, CO chemisorption and HAADF-STEM. The Pd loading of the MI prepared catalysts was analysed by ICP-OES and was found to be lower (2.1 wt.%) than the traditionally prepared impregnation catalysts (2.6

wt. %). The materials were examined by CO chemisorption (Table 4.4) and revealed that the average Pd particle size, 1.25 and 1.28 nm was smaller than the analogue impregnation catalysts displayed in Table 4.3. However, the metal surface area was found to be lower and can be assigned to the lower Pd loading of the **MI** catalysts. When comparing the XRD patterns of 2.1 wt. % Pd-Al_2O_3 **MI** catalysts, it is clear that there are no Pd or PdO reflections (Fig. 4.14). This indicates that the Pd species are smaller than the detection limit of XRD, which is consistent with the CO chemisorption data.

Table 4.4. Dispersion and metal surface area as calculated by CO Chemisorption on 2.1 wt. % Pd-Al_2O_3 fresh and **SC** prepared by modified impregnation.

Catalyst	Metal Surface Area (m^2 g^{-1})	Avg. particle size (nm)	Dispersion (%)
2.1 wt.% Pd-Al_2O_3 Fresh **MI**	2.8	1.25	29.8
2.1 wt.% Pd-Al_2O_3 **SC MI**	2.7	1.28	29.3

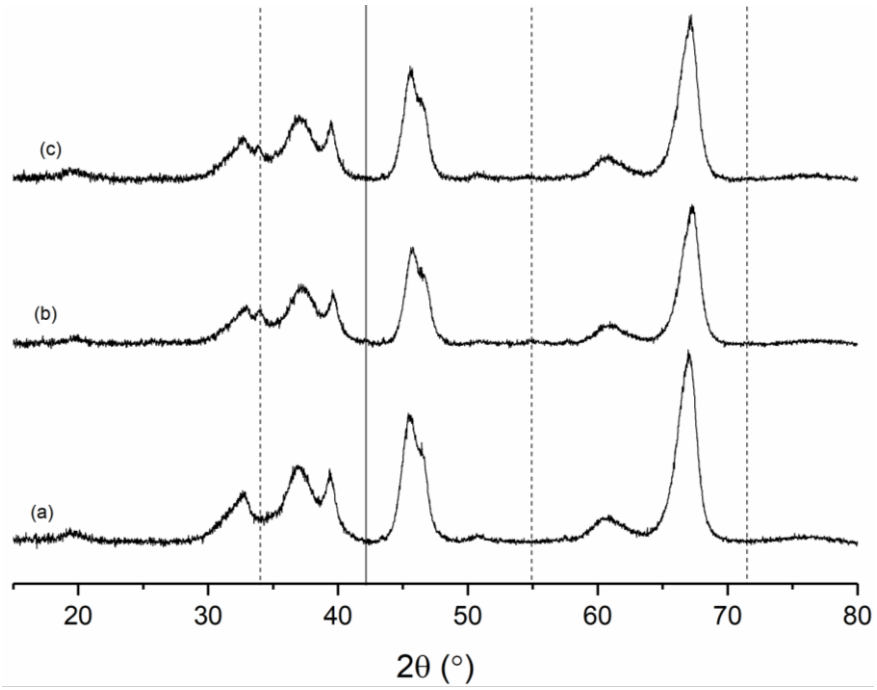

Fig. 4.14. XRD data for a - γ-Al_2O_3 calcined, b – 2.1 wt. % Pd-Al_2O_3 **MI** and c – 2.1 wt. % Pd-Al_2O_3 **SC MI**. Legend dashed line – PdO, solid line – Pd^0.

The modified impregnation technique requires an excess of HCl to be added during the preparation. This facilitates the deposition of Pd and the subsequently observed metal particle control, through altering the support PZC and inducing an increased interaction between the Pd precursor and the support. Characterisation by XPS shows a high ratio of PdO to PdCl in the modified impregnation catalysts. For both the un-calcined support catalyst (2.1 wt. % Pd-Al_2O_3 Fresh **MI**) and the calcined

support catalyst (2.1 wt. % Pd-Al_2O_3 **SC MI**), there is an elevated population of Pd-Cl species compared to PdO species, despite undergoing calcination (Fig. 4.15 and Table 4.5). In contrast, when comparing the ratio of PdO to PdCl species for the 2.6 wt. % Pd-Al_2O_3 **SC** catalyst, more PdO is present than PdCl.

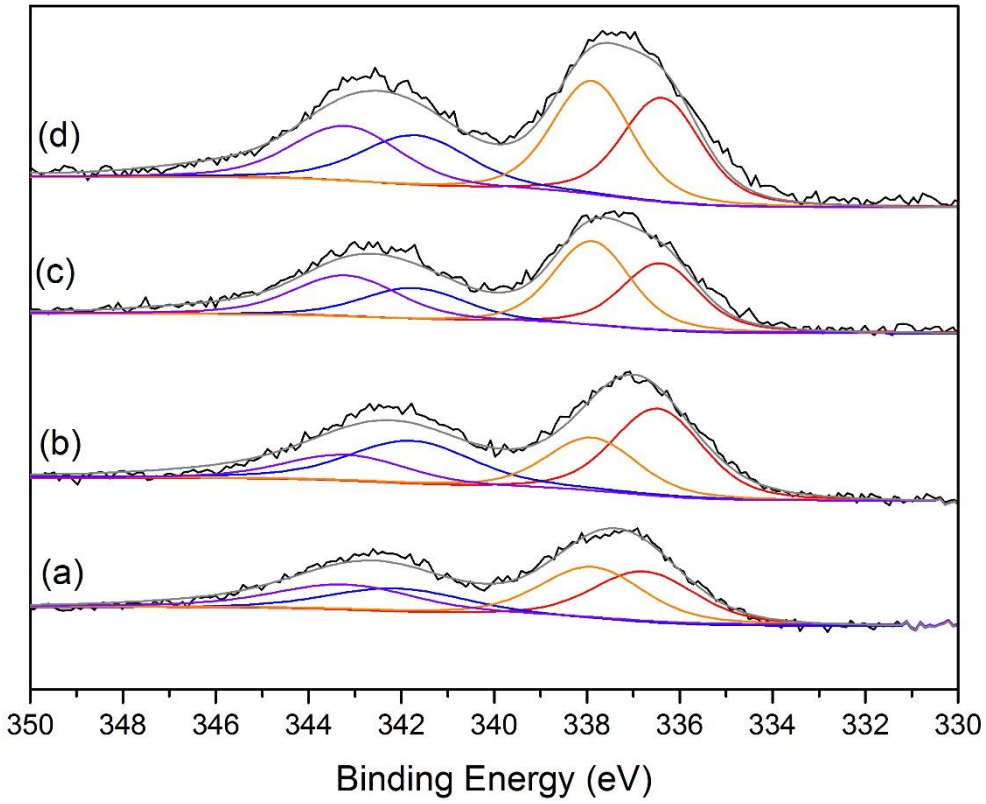

Fig. 4.15. XPS spectra for fresh and **SC** Pd-Al_2O_3 catalysts prepared by impregnation (2.6 wt. % Pd) or Modified Impregnation (2.1 wt. % Pd). Legend: (a) Fresh, (b) **SC**, (c) **MI**, (d) **MI SC**. Each spectra is fitted with two peaks corresponding to PdO and PdCl species. Legend: Red and Blue – PdO, Orange and Purple – PdCl.

Table 4.5. Surface composition of Pd-Al_2O_3 catalysts as reported by XPS analysis

Catalyst	**Pd 3d (at.%)**	**% of PdO (337 eV) (%)**	**% of PdCl (339 eV) (%)**
2.6 wt. % Pd-Al_2O_3 **SC**	0.48	62.3	37.7
2.1 wt. % Pd-Al_2O_3 Fresh **MI**	0.39	43.5	56.5
2.1 wt. % Pd-Al_2O_3 **SC MI**	0.42	47.6	52.3

The 2.1 wt.% Pd/Al_2O_3 **MI** and 2.1 wt.% Pd/Al_2O_3 **SC MI** catalysts were tested for N_2O decomposition with and without propane present and compared to the equivalent impregnation catalysts (Fig. 4.16.a and b). When only N_2O is present in the gas feed there is still minor difference in activity, with the **SC MI** catalyst modestly outperforming, that of the fresh **MI** catalyst (Fig. 4.16**Error! Reference**

source not found..a). The **MI** catalysts outperform the corresponding impregnation catalysts, and further support the supposition that the N_2O decomposition reaction is sensitive to the active surface composition and structure. This reactivity can be attributed to the increased dispersion of smaller and more active metal particles available for N_2O decomposition to occur, based on the results from CO Chemisorption (Table 4.4). However, the increased Cl^- on the surface of the **MI** catalysts restricts the activity to only the minor improvement observed. The T_{50} obtained over the **MI** catalyst was found to be 576 °C and compared to the values of 547 °C over the **MI SC** catalyst. Therefore, the support pre-treatment step has increased the N_2O decomposition rate from 16.3 mol_{N2O} h^{-1} kg_{cat}^{-1} to 21.9 mol_{N2O} h^{-1} kg_{cat}^{-1} at 550 °C.

When propane was added to the reaction mixture the effect of calcining the support prior to Pd deposition was negated (Fig. 4.16b). The activity of the **MI** catalysts was lower, at *ca*. 78 % N_2O conversion compared to that of the **SC** catalyst, but higher than that of the fresh supported Al_2O_3 catalyst at 350 °C, compared to 96 % for **SC** and 7 % for the fresh catalyst (Fig. 4.16a). The activity of both **MI** catalysts was comparable: the decomposition rate was *ca*. 30 mol_{N2O} h^{-1} kg_{cat}^{-1} at 350 °C with propane present. It is possible that residual chlorine species may inhibit the reaction as observed with the catalysts that underwent increasing reaction cycles. However, it is clear that the influence of calcining the support prior to metal impregnation is negated with the **MI** catalysts for this reaction with propane.

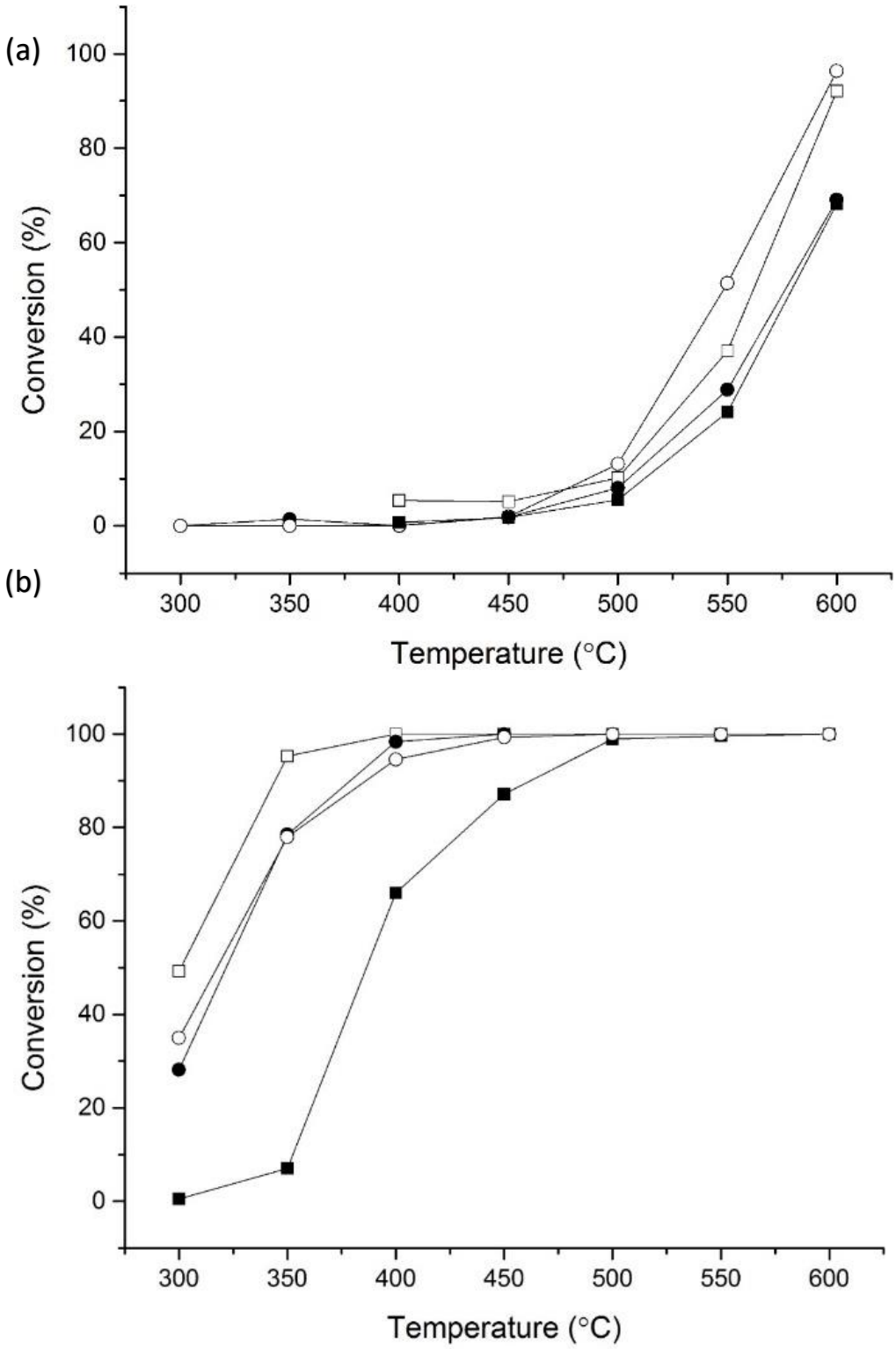

Fig. 4.16. The effect on N_2O conversion of catalyst preparation over Pd-Al_2O_3 Fresh (filled symbols) and **SC** catalysts (open symbols): ■ - 2.6 wt.% Pd Fresh, □ - 2.6 wt.% Pd **SC**, ● - 2.1 wt.% Pd **MI**, ○ - 2.1 wt.% Pd **SC MI**. Reaction conditions; (a), 1 % N_2O/He, total flow 100 ml min^{-1}, GHSV: 75900 h^{-1}, (b), 1 % N_2O/1 % C_3H_8/He, total flow 100 ml min^{-1}, GHSV: 75900 h^{-1}.

HAADF-STEM images of the fresh **MI** catalyst (Fig. 4.17a) and the post-reaction **MI** catalyst (Fig. 4.17b) show small, uniform particles that sinter after use. The particles that are present on the fresh **MI** catalyst are sub 2 nm, with only a few particles larger than 2 nm. After one reaction cycle, the some particles present were measured to be *ca*. 5 nm, indicating that Pd sintering has taken place. We consider that although the modified impregnation technique does provide increased control over the metal nano-particle size, it does not control the metal-support interaction. In theory, the modified impregnation solution is more acidic due to the presence of HCl so the surface of the support is more positively charged. The consequence of this should be a stronger interaction between the precursor and the support, resulting in an increased metal dispersion compared to a conventional impregnation technique. However, as the support is not calcined it can be hypothesised that the interaction between the smaller particles produced by MI and the support may not be sufficiently strong due, to the presence of water that can diminish the strength at which the Pd can anchor to the support and consequently lead to sintering.

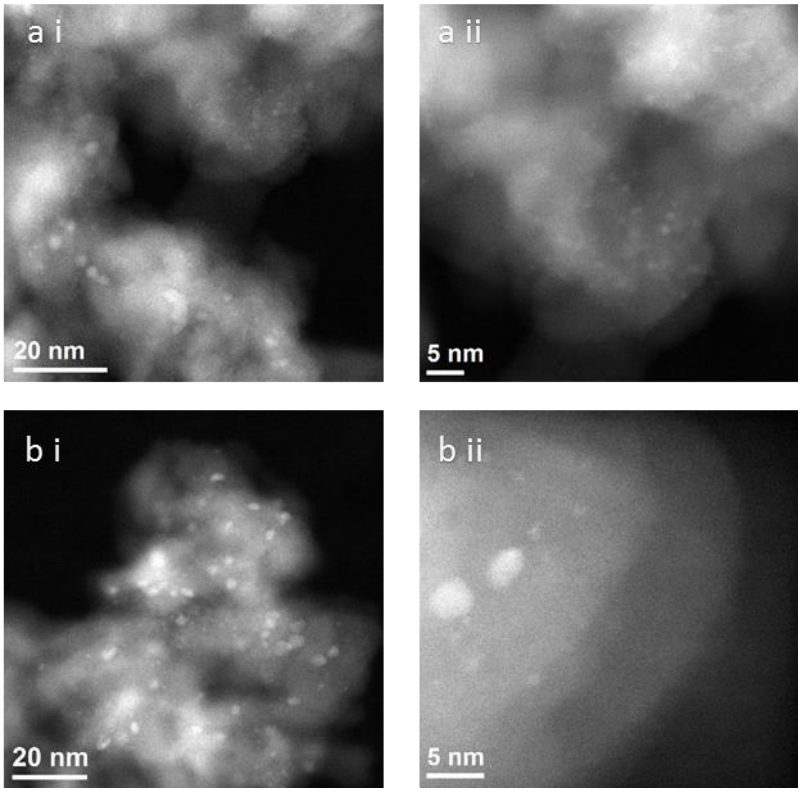

Fig. 4.17. HAADF-STEM images of 2.1 wt. % Pd-Al_2O_3 **MI** (a) **MI** fresh, (b) catalyst following one reaction cycle (**MI 1R)** acquired by Qian He at Lehigh University and Diamond Light Source using a JEOL ARM 200CF AC-STEM instrument.

The reactivity data highlights the structural sensitivity of the active site and how important the relationship between Pd dispersion and presence of PdCl is. The increase in Pd dispersion resulted in an increase in activity as seen when the support is calcined before catalyst preparation. However, removal of Cl^- from the catalyst surface as with the catalysts that have undergone four or five reaction cycles can lead to an improvement in activity despite the onset of Pd sintering and reduced Pd dispersion. Further activity gains can be observed through careful control of the Pd dispersion, through the MI technique, despite a high density of PdCl. Therefore, the balance between a high Pd dispersion and the presence of PdCl appears to favour the former.

4.7 Conclusions

The effect of heat treatment conditions on 2.6 wt. % Pd-Al_2O_3 catalysts have been investigated for the catalytic decomposition of N_2O into N_2 and O_2 in the absence and presence of a reducing agent (C_3H_8). It was found that the use of several reaction cycles increases the conversion of N_2O from 58 % to 96 % at 600 °C. These multiple use catalysts also show improved stability on-stream. It has also been demonstrated that by calcining the support before catalyst preparation, similar conversions as the multiple use catalyst can be achieved in the first cycle of the support calcined catalyst. This enables high activity to be achieved on initial use rather than on the 5^{th} cycle of use (**5R**). It is suggested that this is due to the removal of water species lowering the PZC of the support, which indicates a reduced interaction between the Pd ion and the support surface, leading to the formation of smaller nanoparticles. When a reductant is present, the temperature at which 100 % conversion is observed is shifted from 550 °C to 350 °C. The presence of the reductant enhances the decomposition of N_2O to N_2, however a limited amount of O_2 is measured, suggesting that the reductant was acting as a scavenger of oxygen to form cracked, oxidation products and water. When the support was calcined before catalyst preparation, the resultant catalyst was formed of small Pd nanoparticles. Reaction data indicates that small nanoparticles are the more active species, as when the particle size is controlled by using a modified impregnation preparation method the activity of both catalysts is the same, therefore further adding credit to the theory that the particle size, and subsequently dispersion, control the activity of a Pd-Al_2O_3 catalysts for N_2O decomposition.

4.8 Future Work

The effect of PZC and metal interaction can be studied further by using a range of reducible and non-reducible supports such as MgO, SiO_2 (irreducible) and CeO_2, TiO_2 (reducible).[44] The investigation of the interaction of the metal and support at different PZC can lead to the formation of a new preparation method that controls the deposition of metal and subsequently particle size. As particle size is normally an influential controlling factor in the activity of catalysts, the creation of a new preparation method that can control this would be relevant to all in the field.

Following on from the discussion on the effect of the presence of Cl ions, there are preparation methods that can be used that do not require a Cl precursor to be used, such as Chemical Vapour Impregnation (CVI). This preparation method utilises a $Pd(acac)_2$ precursor and is also solvent free, meaning no additional water species are present to hinder the deposition of metal nanoparticles. This can give an indication as to the effect that both the solvent and the Cl species are having on the conversion of N_2O.

4.9 References

1 G. Pekridis, C. Athanasiou, M. Konsolakis, I. V. Yentekakis and G. E. Marnellos, *Top. Catal.*, 2009, **52**, 1880–1887.

2 S. C. Christoforou, E. A. Efthimiadis and I. A. Vasalos, *Catal. Letters*, 2002, **79**, 137–147.

3 M. Machida, T. Watanabe, S. Ikeda and T. Kijima, *Catal. Commun.*, 2002, **3**, 233–238.

4 Y. Tateishi, T. Tsuneyuki, H. Furukawa, S. Kagawa, I. Moriguchi, Y. Kanmura and Y. Teraoka, *Catal. Today*, 2008, **139**, 59–63.

5 K. Doi, Y. Y. Wu, R. Takeda, A. Matsunami, N. Arai, T. Tagawa and S. Goto, *Appl. Catal. B Environ.*, 2001, **35**, 43–51.

6 K. Zorn, S. Giorgio, E. Halwax, C. R. Henry, H. Gronbeck and G. Rupprechter, *J. Phys. Chem. C*, 2011, **115**, 1103–1111.

7 T. Maillet, C. Solleau, J. Barbier and D. Duprez, *Appl. Catal. B Environ.*, 1997,

14, 85–95.

8 A. S. Ivanova, E. M. Slavinskaya, R. V. Gulyaev, V. I. Zaikovskii, O. A. Stonkus, I. G. Danilova, L. M. Plyasova, I. A. Polukhina and A. I. Boronin, *Appl. Catal. B Environ.*, 2010, **97**, 57–71.

9 D. Roth, P. Gélin, A. Kaddouri, E. Garbowski, M. Primet and E. Tena, *Catal. Today*, 2006, **112**, 134–138.

10 D. Gao, C. Zhang, S. Wang, Z. Yuan and S. Wang, *Catal. Commun.*, 2008, **9**, 2583–2587.

11 J. Lu, B. Fu, M. C. Kung, G. Xiao, J. W. Elam, H. H. Kung and P. C. Stair, *Science*, 2012, **335**, 1205–1208.

12 H. Guesmi, D. Berthomieu and L. Kiwi-Minsker, *J. Phys. Chem. C*, 2008, **112**, 20319–20328.

13 C. Sang, B. H. Kim and C. R. F. Lund, *J. Phys. Chem. B*, 2005, **109**, 2295–2301.

14 N. Hansen, A. Heyden, A. T. Bell and F. J. Keil, *J. Phys. Chem. C*, 2007, **111**, 2092–2101.

15 D. A. Bulushev, L. Kiwi-minsker and A. Renken, *Ind. Eng. Chem. Res.*, 2004, **211**, 2004.

16 K. Sun, H. Xia, E. Hensen, R. van Santen and C. Li, *J. Catal.*, 2006, **238**, 186–195.

17 G. D. Pirngruber, *J. Catal.*, 2003, **219**, 456–463.

18 B. R.Wood, J. A. Reimer and A. T. Bell, *J. Catal.*, 2002, **209**, 151–158.

19 S. Parres-Esclapez, M. J. Illan-Gomez, C. S. M. de Lecea and A. Bueno-Lopez, *Appl. Catal. B Environ.*, 2010, **96**, 370–378.

20 M. Konsolakis, I. V. Yentekakis, G. Pekridis, N. Kaklidis, A. C. Psarras and G. E. Marnellos, *Appl. Catal. B Environ.*, 2013, **138**–**139**, 191–198.

21 V. K. Tzitzios and V. Georgakilas, *Chemosphere*, 2005, **59**, 887–891.

22 F. Hu, X. Wu, Y. Wang and X. Lai, *RSC Adv.*, 2015, **5**, 54053–54058.

23 B. Ngamsom, N. Bogdanchikova, M. A. Borja and P. Praserthdam, *Catal.*

Commun., 2004, **5**, 243–248.

24 Y. Ning, Z. Yang and H. Zhao, *Platin. Met. Rev.*, 1996, **40**, 80–87.

25 P. Marécot, A. Fakche, B. Kellali, G. Mabilon, P. Prigent and J. Barbier, *Applied Catal. B, Environ.*, 1994, **3**, 283–294.

26 J. Batista, A. Pintar, D. Mandrino, M. Jenko and V. Martin, *Appl. Catal. A Gen.*, 2001, **206**, 113–124.

27 J. Z. Shyu, K. Otto, W. L. H. Watkins, G. W. Graham, R. K. Belitz and H. S. Gandhi, *J. Catal.*, 1988, **114**, 23–33.

28 L. Liu, F. Zhou, L. Wang, X. Qi, F. Shi and Y. Deng, *J. Catal.*, 2010, **274**, 1–10.

29 A. Tressaud, S. Khairoun, H. Touhara and N. Watanabe, *Zeitschrift Anorg. und Allg. Chemie*, 1986, **540**, 291–299.

30 J. C. Zhou, C. M. Soto, M.-S. Chen, M. A. Bruckman, M. H. Moore, E. Barry, B. R. Ratna, P. E. Pehrsson, B. R. Spies and T. S. Confer, *J. Nanobiotechnol.*, 2012, **10**, 18.

31 M. C. Militello and S. J. Simko, *Surf. Sci.*, 1997, **3**, 402–409.

32 R. J. Liu, P. A. Crozier, C. M. Smith, D. A. Hucul, J. Blackson and G. Salaita, *Appl. Catal. A Gen.*, 2005, **282**, 111–121.

33 J. J. Chen and E. Ruckenstein, *J. Catal.*, 1981, **69**, 254–273.

34 W. Chen, Y. Ding, X. Song, T. Wang and H. Luo, *Appl. Catal. A Gen.*, 2011, **407**, 231–237.

35 N. Yao, J. Chen, J. Zhang and J. Zhang, *Catal. Commun.*, 2008, **9**, 1510–1516.

36 C. Drew Tait, D. R. Janecky and P. S. Z. Rogers, *Geochim. Cosmochim. Acta*, 1991, **55**, 1253–1264.

37 J. Park and J. R. Regalbuto, *J. Colloid Interf. Sci.*, 1995, **175**, 239–252.

38 K. P. De Jong, *Synthesis of Solid Catalysts*, Wiley-VCH Verlag GmbH & Co. KGaA, 1st edn., 2009, vol. 39.

39 P. Munnik, P. E. De Jongh and K. P. De Jong, *Chem. Rev.*, 2015, **115**, 6687–6718.

40 C. E. Bronnimann, I. ssuer Chuang, B. L. Hawkins and G. E. Maciel, *J. Am. Chem. Soc.*, 1987, **109**, 1562–1564.

41 E. C. Decanio, J. C. Edwards and J. W. Bruno, *J. Catal.*, 1994, 148, 76–83.

42 M. Hunger, D. Freude, H. Pfeifer, H. Bremer, M. Jank and K. P. Wendlandt, *Chem. Phys. Lett.*, 1983, **100**, 29–33.

43 M. Morad, M. Sankar, E. Cao, E. Nowicka, T. E. Davies, P. J. Miedziak, D. J. Morgan, D. W. Knight, D. Bethell, A. Gavriilidis and G. J. Hutchings, *Catal. Sci. Technol.*, 2014, **4**, 3120–3128.

44 A. R. Puigdollers, P. Schlexer, S. Tosoni and G. Pacchioni, *ACS Catal.*, 2017, **7**, 6493–6513.

5 Effect of lattice oxygen species and surface area of Perovskites on N_2O decomposition.

5.1 Abstract

Perovskites have been prepared by various methods and tested for N_2O decomposition. Initially, a citric acid preparation was utilised with altering of A and B ratios in order to increase phase purity. Following this, the catalysts were re-prepared by the SAS technique to produce perovskites with a higher surface area. The materials were also prepared by the oxalic acid precipitation method for comparison. It has been shown that, by altering the A and B ratios, it is possible to reduce the temperature required to produce a pure phase perovskite. The low temperature is crucial to form a perovskite with a higher surface area, which has implications when studying reactions such as N_2O decomposition, which has been shown to have a high dependency on surface area.[1–4] The use of different preparation methods also enables the production of perovskites with varying oxygen species, as determined by XPS and O_2-TPD. This work has confirmed the importance of lattice oxygen species that have high oxygen mobility for the decomposition of N_2O. Lattice oxygen has been shown to be crucial as the rate limiting step in the decomposition of N_2O, as the formation of molecular oxygen is limited by surface adsorbed O species being within a distance at which recombination is possible. An abundance of mobile lattice oxygen therefore aids recombination and facilitates the regeneration of active sites for N_2O decomposition. Two perovskite catalysts have been the focus of this work, $La_{0.75}Sr_{0.25}Co_{0.81}Fe_{0.19}O_x$ (LSCF) and $Pr_{0.75}Ba_{0.25}CoO_x$ (PBC). The LSCF catalyst follows the trend that an increase in the amount of lattice oxygen present (predicted by XPS) results in a higher activity, with the most active and lattice oxygen rich catalyst resulting from the citric acid preparation method. The PBC catalyst differed from

the above trend, as the most active catalyst did not have the highest percentage of lattice oxygen shown by XPS; however, activity was correlated with an increase in amount of mobile oxygen species. In this case, the SAS precipitation preparation method produced a catalyst with mobile oxygen species and a high surface area. The LSCF catalyst prepared by citric acid achieved 85 % conversion of N_2O at 500 °C, and the PBC catalyst prepared by SAS converted 95 % N_2O at 500 °C, with both showing stability over a 24 hour period under reaction conditions at 450 °C.

5.2 Introduction

Perovskites are a class of materials represented by the formula ABO_3, with the A site generally being a large, often rare earth element such as La. The B site is generally a smaller transition metal element such as Co or Fe. The substitution of elements into the A or B site leads to the formation of abnormal valencies on the B site cation, which results in oxygen vacancies, Sr or Ce are often used for A site substitution.[2]

Perovskites are known for their low cost and high structural and thermal stability, which usually arises due to the high temperatures required during preparation to form the perovskite phase.[5–9] This high temperature preparation leads to low specific surface areas, typically less than 10 $m^2 g^{-1}$.[2,5,10–13] Perovskites are also known for their oxygen mobility and oxygen storage capacity, with oxygen mobility contributing greatly to their high catalytic activity for N_2O decomposition.[14–17] The most notable perovskite catalysts for N_2O decomposition are given in Table 5.1.

Table 5.1. Table showing the most relevant perovskite systems for N_2O decomposition.

Catalyst	Conditions	Conversion	Reference
$LaCoO_3$	0.5 % N_2O, He, WHSV = 120 000 mL g^{-1} h^{-1}	100 % at 550 °C 50 % at 455 °C	[18]
$Pr_{0.8}Ba_{0.2}MnO_3$	0.5 g, 0.5 % N_2O, He balance. GHSV = 7500 h^{-1}	100 % at 550 °C 50 % at 442 °C	[19]
$La_{0.7}Ba_{0.3}Mn_{0.8}In_{0.2}O_3$	10 % N_2O in He, 20 ml min^{-1} W/F = 3.0 g s cm^{-3}	92 % at 500 °C 50 % at 443 °C	[20]
$La_{0.75}Sr_{0.25}MnO_3$	0.15 % N_2O GHSV = 30 800 h^{-1}	50 % at 725 °C	[21,22]
$La_{0.4}Sr_{0.6}FeO_3$	0.15 % N_2 GHSV = 30 800 h^{-1}	50 % at 815 °C	[23]

5.3 Preparation of perovskite catalysts by citric acid

Perovskites were prepared using the citrate preparation method as described in Chapter 2.2.7, dried overnight and then heat treated in a chamber furnace at 400 or 550 °C depending when the last major mass loss was observed on the TGA profile. Following this, the materials were calcined at an appropriate temperature defined by *in situ* XRD to produce the following pure phase perovskites:

- $Ba_{0.5}Pr_{0.5}CoO_x$ (BPC)
- $SrCo_{0.81}Fe_{0.19}O_x$ (SCF)
- $La_{0.75}Sr_{0.25}CoO_x$ (LSC)

All catalysts in this section were prepared using citric acid and a mixture of metal nitrates. The combined decomposition of citric acid and metal nitrates can lead to a runaway exothermic reaction and ultimately an explosion if the heat treatment is not controlled. Therefore, it is crucial to perform TGA of the catalysts before heat treatments are performed to optimise conditions. The TGA of the precursors can give an indication of the temperature of decomposition. For example, in the TGA of citric acid there is one major weight loss at 240 °C shown below (Fig. 5.1).

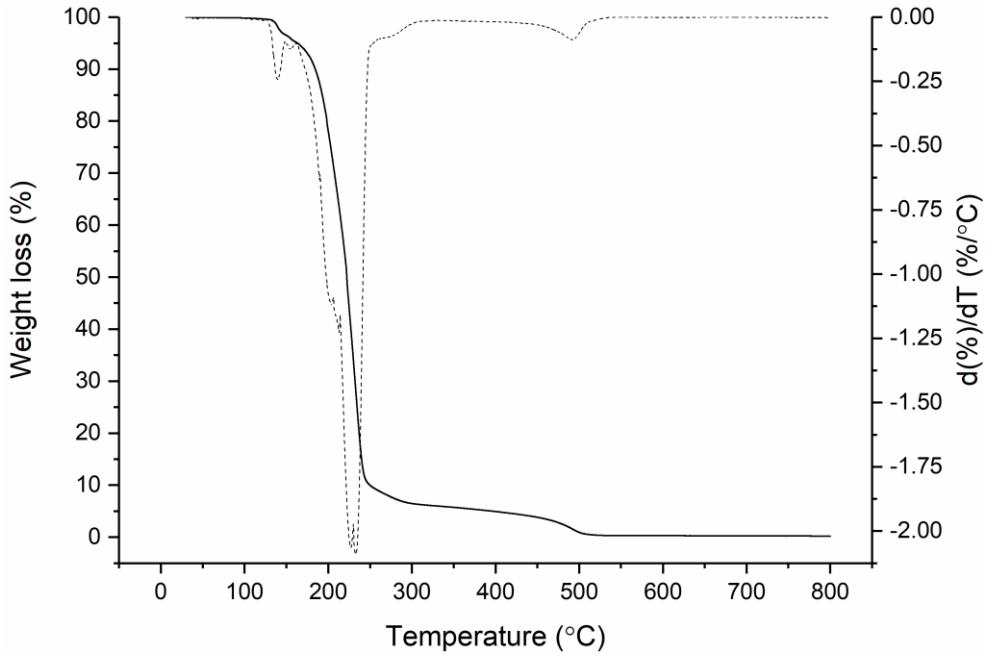

Fig. 5.1 TGA of Citric Acid up to 900 °C at 5 °C min^{-1} in air at 50 ml min^{-1}.

The TGA profile of LSC (Fig. 5.2) shows a major weight loss at 170 °C due to decomposition of the citric acid and La nitrate, followed by further weight losses at 300 °C due to a combination of La and Co nitrate decomposition with a final mass loss event seen at 600 °C due to the decomposition of Sr nitrate. This is known by performing TGA's of the individual precursors. To successfully form the pure phase perovskite, the catalyst was heat-treated to a high temperature determined by *in situ* XRD. To perform an *in situ* XRD, the sample must be packed into a sample holder. It is crucial that when the sample is heated the sample remains flat and the holder fully filled; therefore, the catalysts must be pre-treated to limit mass loss when the *in situ* XRD is performed. For the LSC catalyst a temperature of 400 °C was chosen as all major mass loss events had occurred below this point (Fig. 5.2). Importantly, all pre-treatments were performed at 1 °C min^{-1} in a chamber oven, and held at the maximum temperature for 2 hours to ensure that the exothermic reaction was controlled and the heat-treatment was performed safely.

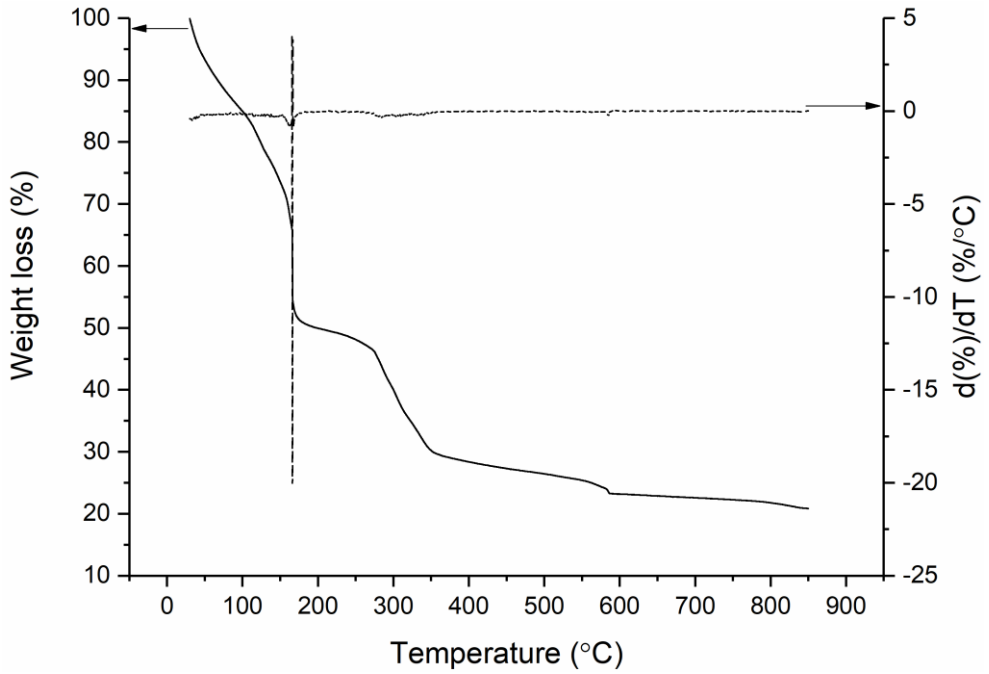

Fig. 5.2 TGA of $La_{0.75}Sr_{0.25}CoO_x$ up to 850 °C at 5 °C min^{-1} in air at 50 ml min^{-1}.

The same TGA process described previously was also performed for BPC (Fig. 5.3) and SCF (Fig. 5.4) catalysts. Both show a mass loss below 200 °C that can be associated to the decomposition of citric acid into CO_2. In BPC (Fig. 5.3) there is another mass loss at 300 °C that is due to the decomposition of Co nitrate and Ba nitrate, followed by a minor mass loss at 580 °C due to the decomposition of Pr nitrate. Therefore, a pre-treatment temperature of 400 °C was selected for this catalyst. The SCF sample (Fig. 5.4) exhibited mass losses in two events up to 350 °C and are due to the decomposition of Co and Fe nitrates, with the final mass loss event due to the decomposition of Sr nitrate. For this catalyst a pre-treatment temperature of 550 °C was selected.

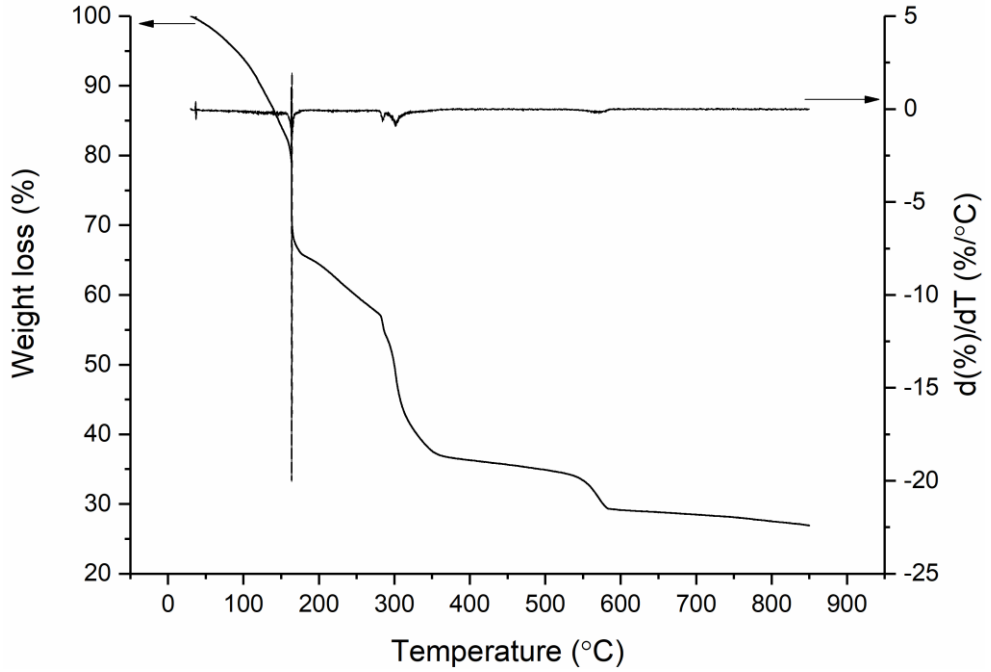

Fig. 5.3. TGA of $Ba_{0.5}Pr_{0.5}CoO_x$ up to 850 °C at 5 °C min^{-1} in air at 50 ml min^{-1}.

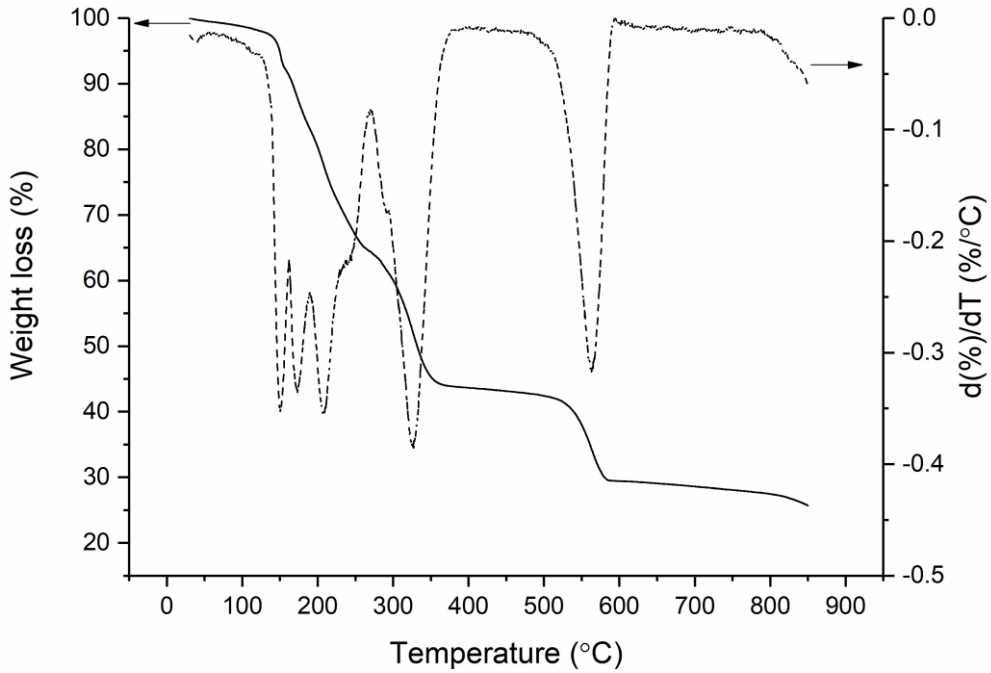

Fig. 5.4. TGA of $SrCo_{0.81}Fe_{0.19}O_x$ up to 850 °C at 5 °C min^{-1} in air at 50 ml min^{-1}.

Following the appropriate pre-treatments, *In situ* XRD was performed to determine the lowest temperature at which a phase pure perovskite was formed. The *in situ* XRD profile described in chapter 2.3.2 was used.

The *in situ* XRD of LSC (Fig. 5.5) shows the profiles from 550 to 850 °C, with a perovskite structure seen in all spectra; however, the purity increases with

temperature, the reflections increase in intensity as the temperature increases, indicating that the catalyst is becoming more crystalline. The impurities decrease as temperature increases, the reflections become narrower and more defined. The highest phase purity of 98 % was achieved at 850 °C, therefore this was selected as a suitable calcination temperature. This was also deemed suitable from the TGA profile (Fig. 5.2) as all major mass loss events had occurred prior to this.

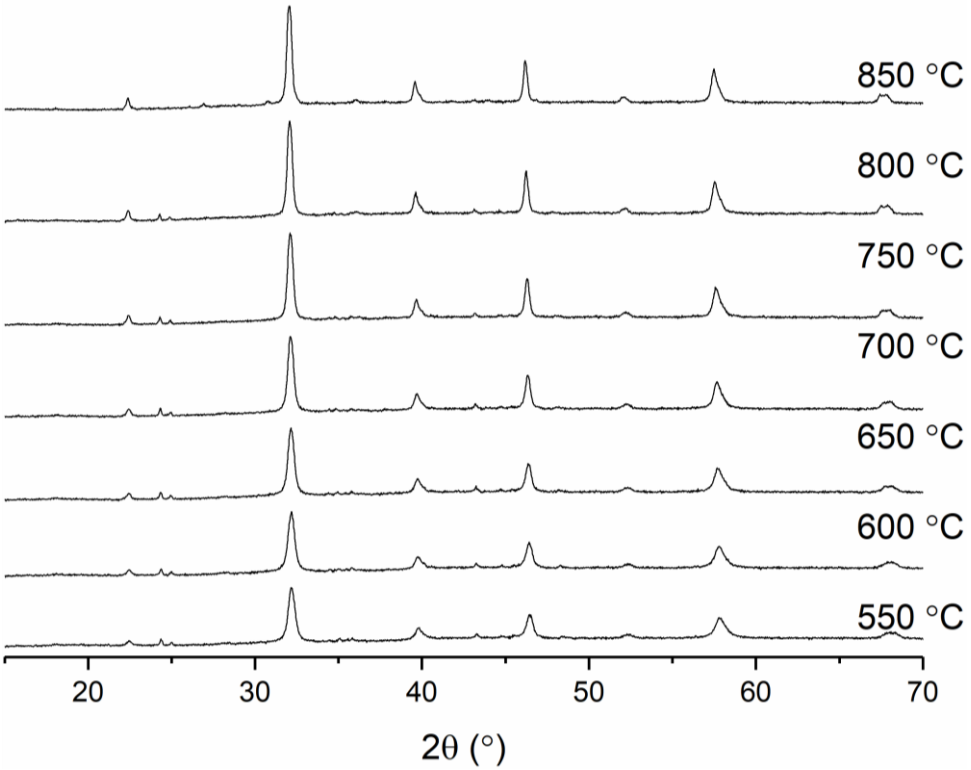

Fig. 5.5. *In situ* XRD of $La_{0.75}Sr_{0.25}CoO_x$ treated to 400 °C prior to analysis heated from 550 °C to 850 °C in air (25 ml min^{-1}).

From the *in situ* XRD profile of BPC (Fig. 5.6) it is possible to see the formation and growth of the principal perovskite phase reflection at 34 ° as the temperature increases from 550 to 850 °C. Some of the reflections that are seen in the 550 °C spectra (impure) are still present in the 850 °C spectra (24 °, 37 °, 46.5 °). At 850 °C the purity of the perovskite was low with two perovskite phases seen. Therefore, a higher calcination temperature of 900 °C was selected, resulting in a purity of 77 %. This the maximum temperature that the equipment that we have access to can be safely used at. The two phases are still seen even after the high calcination temperature indicating that there may be phase separation occurring in the catalyst during heat treatment.

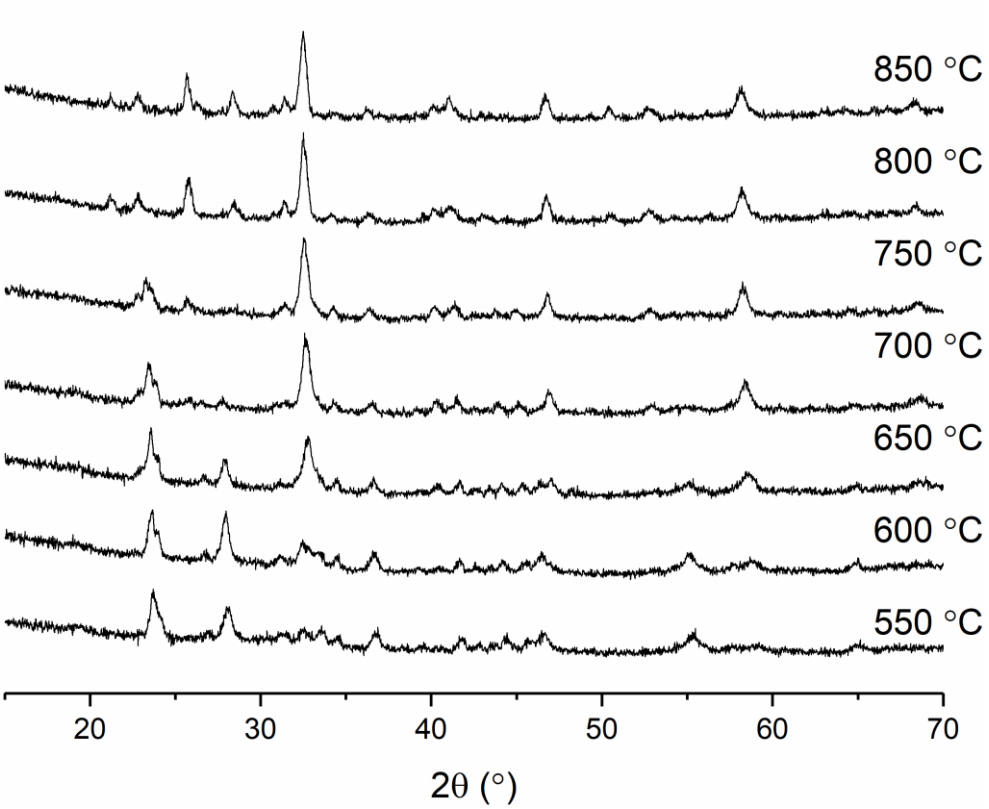

Fig. 5.6 *In situ* XRD of $Ba_{0.5}Pr_{0.5}CoO_x$ treated to 400 °C prior to analysis heated from 550 °C to 850 °C in air (25 ml min^{-1}).

The *in situ* XRD of SCF given in Fig. 5.7 shows the profiles from 550 to 850 °C. Here, small differences are observed as the temperature increases from 550 to 800 °C, with shrinking of the reflections present at 24, 26 and 36.5 °. This is paired with the formation of new reflections, most notably at 32 and 27 °, that are present in the final material at 850 °C. As with BPC, a pure phase SCF perovskite is not formed at 850 °C, with a Co_3O_4 phase seen. Therefore, a higher calcination temperature of 900 °C was required (again the maximum temp possible of the furnaces), resulting in a purity of 81 %.

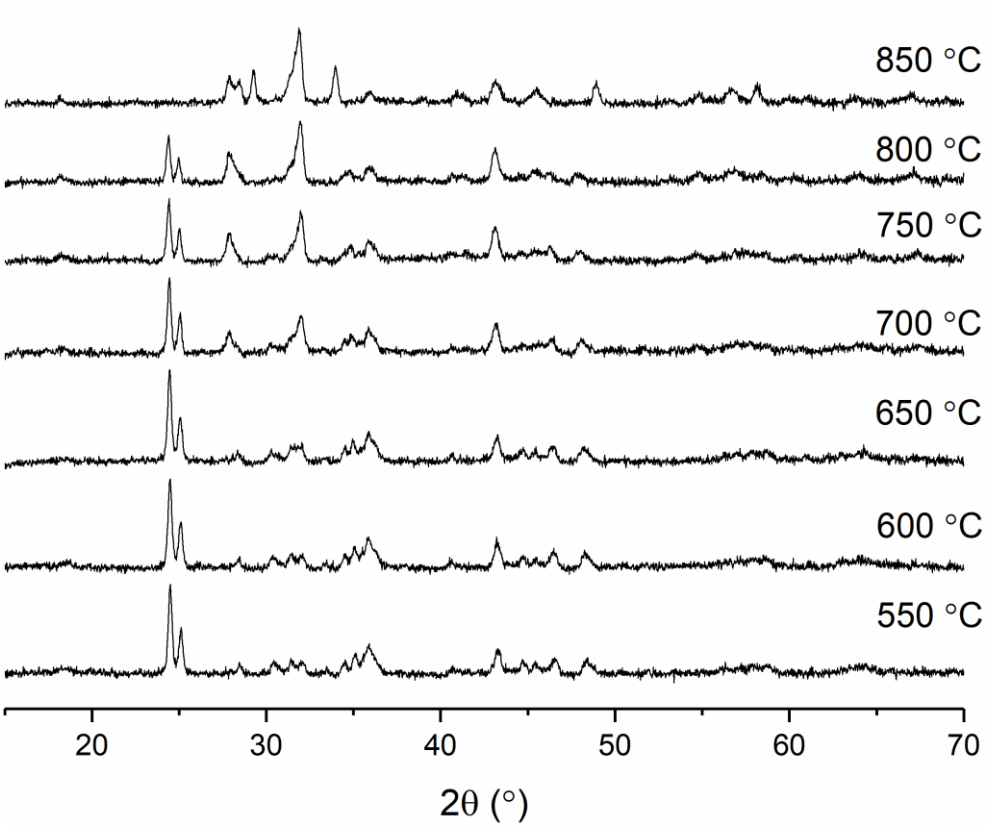

Fig. 5.7. *In situ* XRD of $SrCo_{0.81}Fe_{0.19}O_x$ treated to 400 °C prior to analysis heated from 550 °C to 850 °C in air (25 ml min^{-1}).

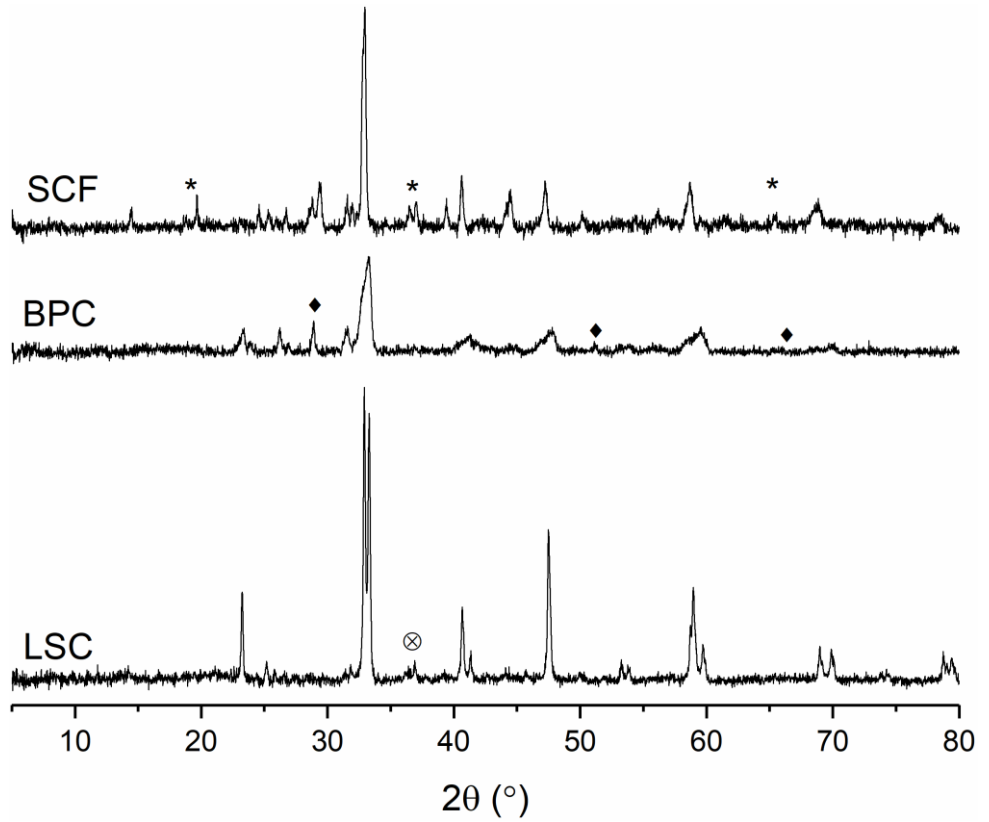

Fig. 5.8. XRD comparison of final calcined perovskite structures. * - Co_3O_4 impurities. ⊗ - CoO impurity, ♦ - $BaPrO_3$ impurity. All other reflections are perovskite phase.

The XRD of the final perovskites (Fig. 5.8) highlights the differences in obtained phase purity, with the more crystalline structures possessing the highest purity in the order LSC > SCF > BPC. Table 5.2 contains the surface area data for these catalysts, with LSC having the highest (15 m^2g^{-1}), likely a result of a lower calcination temperature. As described earlier, higher calcination temperatures can lead to lower surface areas. This is apparent with BPC and SCF catalysts, both of which were calcined at 900 °C, and have surface areas of 3 and 7 m^2g^{-1} respectively. When comparing both purity and surface area to catalytic decomposition of N_2O, it appears that both factors correlate with activity (Table 5.2). The purest and highest surface area catalyst (LSC) results in the most active, with the temperature required for 50 % conversion of N_2O (T_{50}) being 468 °C (Fig. 5.10). Based on the activity of the other two catalysts (PBC, T_{50} 527 °C and SCF, T_{50} 585 °C), the data indicates that the purity is one of the controlling factors as the second most pure catalyst is the second most active. However, the low surface area of these catalysts means that the expected effect of high surface area results in a high activity may not necessarily be true in this set of catalysts, and cannot be confirmed until it is possible to produce such catalysts.

Table 5.2. Composition determined by MP-AES, Surface area, phase purity and the temperature required for 50 % conversion (T_{50}).

Catalyst	**Composition determined by MP-AES**	**Perovskite Phase Purity (%)[a]**	**Surface area ($m^2 g^{-1}$)**	**T_{50} (°C)**	**Lattice O (%)[b]**
LSC	$La_{0.8}Sr_{0.4}CoO_{3.9}$	98	15	468	42.5
BPC	$Ba_{0.6}Pr_{0.6}CoO_{4.5}$	77	3	527	33.0
SCF	$Sr_{1.5}CoFe_{0.2}O_5$	81	7	585	1.5

[a] Perovskite phase purity calculated using XRD diffraction pattern and the ratio between the single perovskite phase and any impurities.
[b] Lattice oxygen calculated by the ratio of lattice oxygen species to the sum of molecular water, hydroxyl species, transition metal lattice oxygen as derived from XPS measurements.

Analysis of the O 1s region in XPS gives an indication of the species of oxygen present on the surface of the catalyst. There are four notable oxygen species; lattice oxygen O^{2-} which is seen at around 528.6 eV,[24–27] lattice oxygen species due to transition metal species at *ca.* 529.5 eV (Co or Fe),[28–31] hydroxyl species OH^- at 531 eV,[32] and finally surface adsorbed molecular water at 533 eV.[33–44] The water is trapped within the lattice, rather than being physisorbed on the surface as this would be removed when under the ultra-high vacuum conditions required for XPS.

Lattice oxygen is also referred to as β oxygen, with oxygen vacancies being referred to as α oxygen. The oxygen region of the spectra of both BPC and LSC show all four species of oxygen as being present. Most notably a large percentage of lattice oxygen species are present in both, with 43 % in the LSC catalyst and 33 % in BPC, with the rest of the percentage made up from lattice oxygen from transition metal species and hydroxyl species. It is important to note that the least active catalyst in this series (SCF) has very limited lattice oxygen present in the XPS spectra (Table 5.2), and generally as the lattice oxygen species concentration increase the activity also increases (remembering the influence of other factors such as surface area, oxygen vacancies and mobility). The surface does not contain these lattice oxygen species, instead the carbon region indicates that the surface contains a thin layer of carbonate species that could have formed when Sr came into contact with the atmosphere.[45] There is a large peak at 531 eV in the O 1s spectra that can either be a contribution from OH^- or CO_3^- species, in this case it is from carbonate species, confirmed by the carbon spectra. The Sr carbonate species is hygroscopic, as shown by the large peak assigned to molecular water on the surface at 533 eV, *ca*. 14 % of the O 1s spectra. Notably, the oxide of Sr is found at a slightly lower binding energy than other elements, with a response seen at 527 eV.[46–49] The lack of lattice oxygen observed may be a result of the surface sensitive nature of XPS with an analysis depth of *ca*. 8-10 nm. Therefore, an abundance of lattice oxygen in the bulk will not be represented.

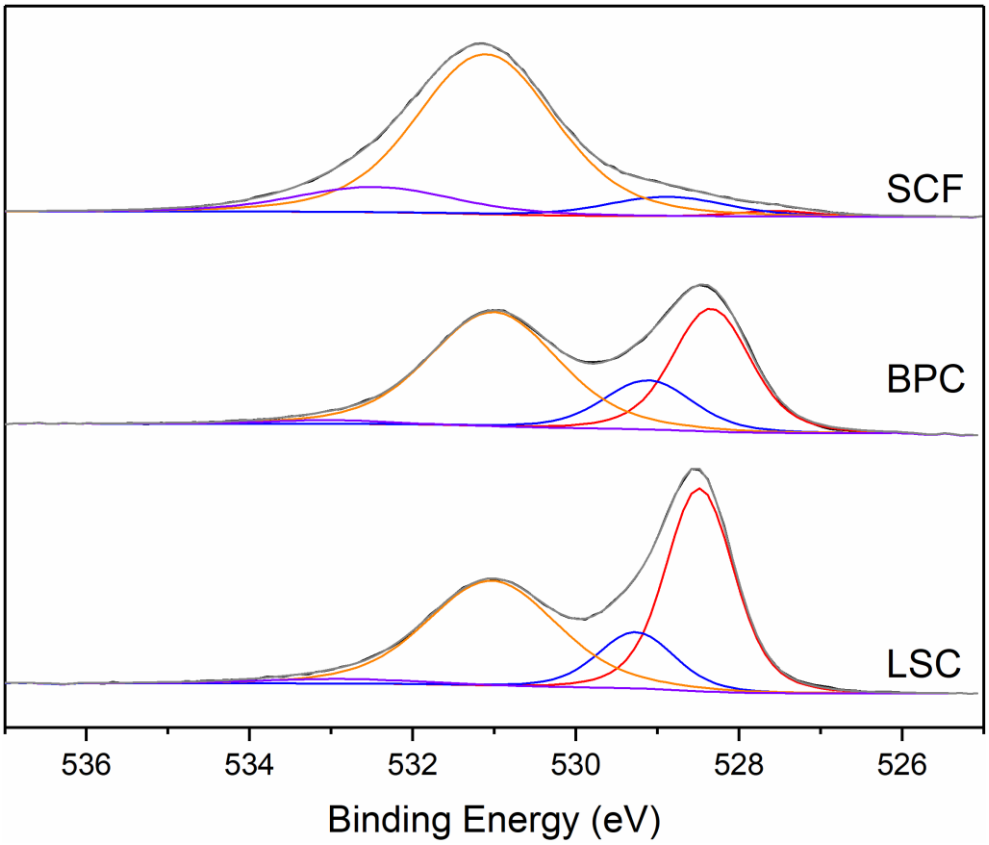

Fig. 5.9. XPS O 1s region of LSC, BPC and SCF catalysts. Fittings: Red – lattice O^{2-}, Blue – lattice O^{2-} transition metal, Orange – hydroxyl species OH^- and Purple – molecular water on surface.

The lower activity of the LSC catalyst indicates that lattice oxygen species are crucial for the decomposition of N_2O (Fig. 5.10). This is due to N_2O adsorption taking place at a vacant site, such as a coordinatively unsaturated metal, followed by decomposition and release of N_2, with adsorbed O. The rate-limiting step of this reaction is the recombination of oxygen, therefore, a high lattice oxygen concentration with sufficient mobility can aid this reaction step and produce a more active catalyst. In the case of SCF, the lack of lattice oxygen indicates that the mobile oxygen from N_2O saturates the deficient sites and does not facilitate oxygen recombination at low temperatures, with temperatures greater than 600 °C required for oxygen recombination.

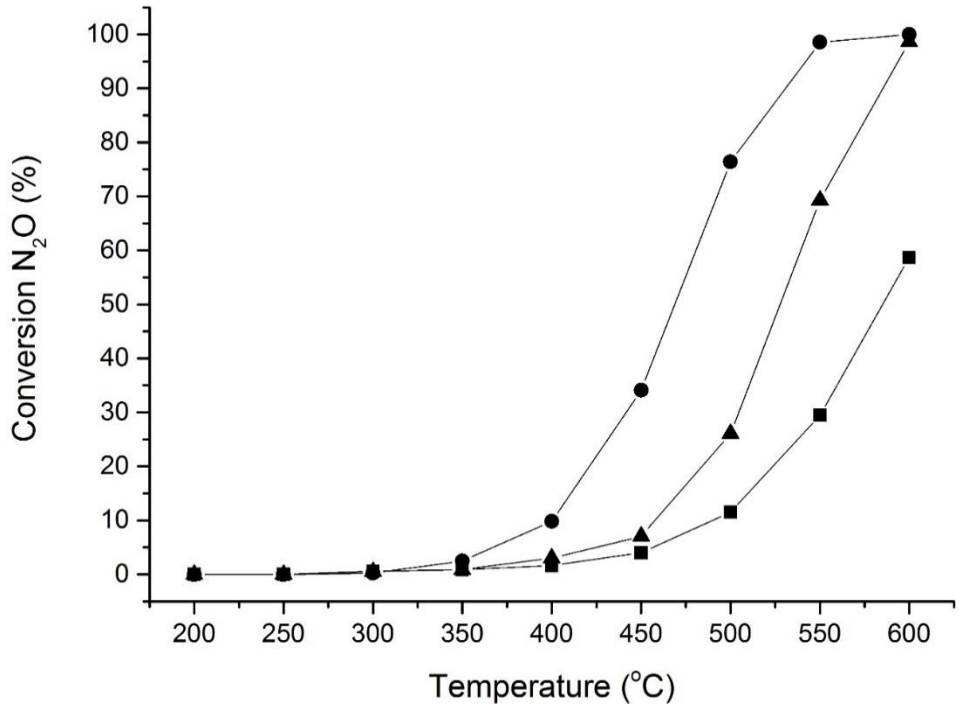

Fig. 5.10. Graph showing N_2O decomposition using perovskite based catalysts. Reaction Conditions: 1 % N_2O/He, total flow 100 ml min^{-1}, GHSV: 60000 h^{-1}. Legend: ■ - SCF, ● - LSC, ▲ - BPC.

Based on the reaction data shown in Fig. 5.10, it is apparent that a higher surface area, phase purity and lattice oxygen concentration correlate with a more active catalyst. Therefore, two perovskites with different metal ratios, that had shown promise at producing a higher purity perovskite, were prepared to increase the purity in an attempt to increase the activity.

5.4 Increased purity perovskite catalysts prepared by citric acid

In section 5.3, it was found that using a theoretical A-site metal ratio of 3:1 gave a high phase purity in the LSC catalyst. In an attempt to improve the phase purity of the other catalysts, this ratio was subsequently adopted in the preparation. Despite the Fe containing catalyst showing low activity (SCF), Fe was incorporated into the B site of the most active catalyst (LSC), due to a literature precedent for active Fe catalysts.[1,23,50,51] This produced a mixed A and B site perovskite referred to as (LSCF). All catalysts were prepared by citric acid preparation as described previously. Based on previous experience the samples were treated in a chamber oven at 200 °C (1°C

min^{-1}, 2 hours) and calcined at 500 °C (1 °C min^{-1}, 3 hours) before *in situ* XRD was used to determine the final calcination temperature.

The perovskite prepared were as follows:

- $La_{0.75}Sr_{0.25}Co_{0.81}Fe_{0.19}O_x$ (LSCF)
- $Pr_{0.75}Ba_{0.25}CoO_x$ (PBC)

In situ XRD was performed on PBC (Fig. 5.11) and LSCF (Fig. 5.12) from 550 to 850 °C, and in both cases the pure phase perovskite was formed at 550 °C, which is remarkably low. After cooling to 25 °C there is a shift in the reflections for the PBC catalyst (Fig. 5.11). In the case of LSCF (Fig. 5.12) there is a visible split in the reflections after cooling, most notably at 22.5 °. When the perovskites are subject to heating conditions further mass loss of catalysts precursors of around 20 % is expected, which can cause the sample to physically contract, reducing the sample volume and disrupt the XRD path, causing a shift or split in reflections seen. Secondly this could be due to the formation of different phase during the cooling process. However, as the catalysts does not need to be heated to 850 °C, this was not subjected to further investigation. Powder XRD measurements were taken after calcination at 550 °C on both catalysts to confirm the phase present.

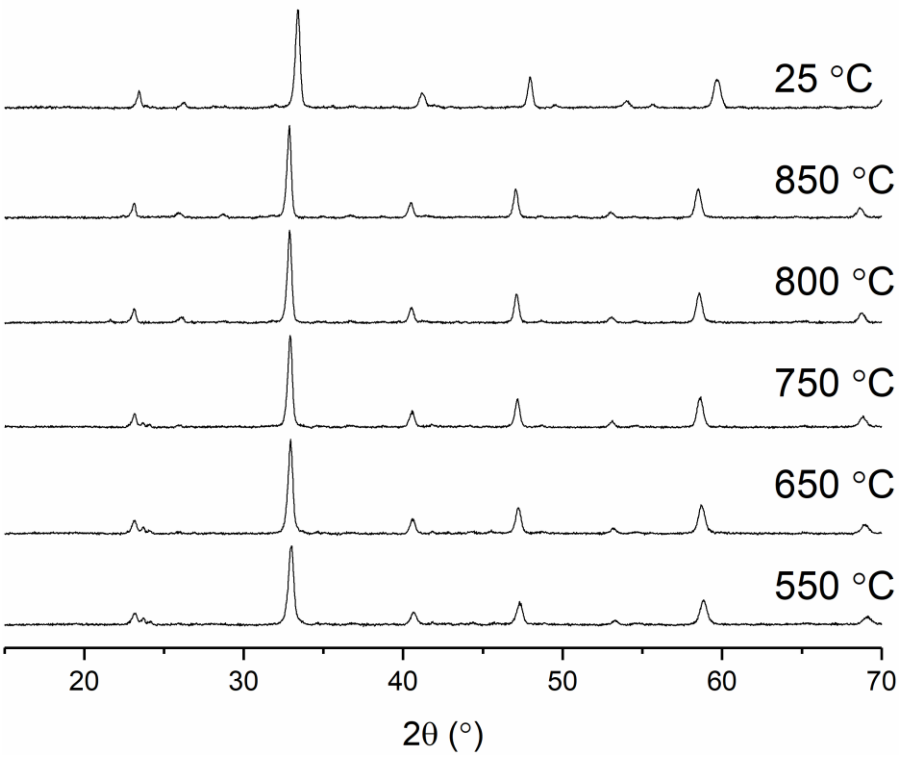

Fig. 5.11. *In situ* XRD of $Pr_{0.75}Ba_{0.25}CoO_x$ treated to 500 °C prior to analysis heated from 550 °C to 850 °C in air (5 ml min^{-1}).

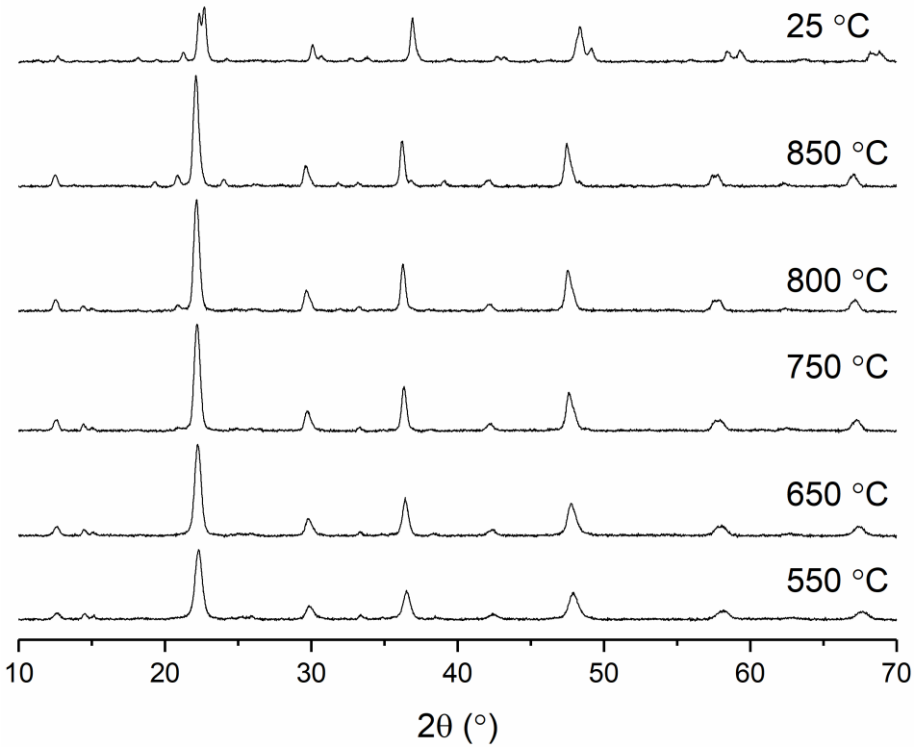

Fig. 5.12. *In situ* XRD of $La_{0.75}Sr_{0.25}Co_{0.81}Fe_{0.19}O_x$ treated to 500 °C prior to analysis heated from 550 °C to 850 °C in air (5 ml min^{-1}).

As the temperature required to form a pure phase indicated by *in situ* XRD for both PBC and LSCF was very low, a TGA was performed to confirm that no further mass loss events occur after this temperature, as this would indicate that a pure phase perovskite had not been formed. In the case of PBC (Fig. 5.13) the last major mass loss occurred at 570 °C, indicating that the pure phase can form after being held at 550 °C for an extended period of time. The major mass loss events occur at 170 °C (citric acid decomposition), 300 °C (Co and Ba nitrates decomposition) followed by the final decomposition at 570 °C (Pr nitrate).

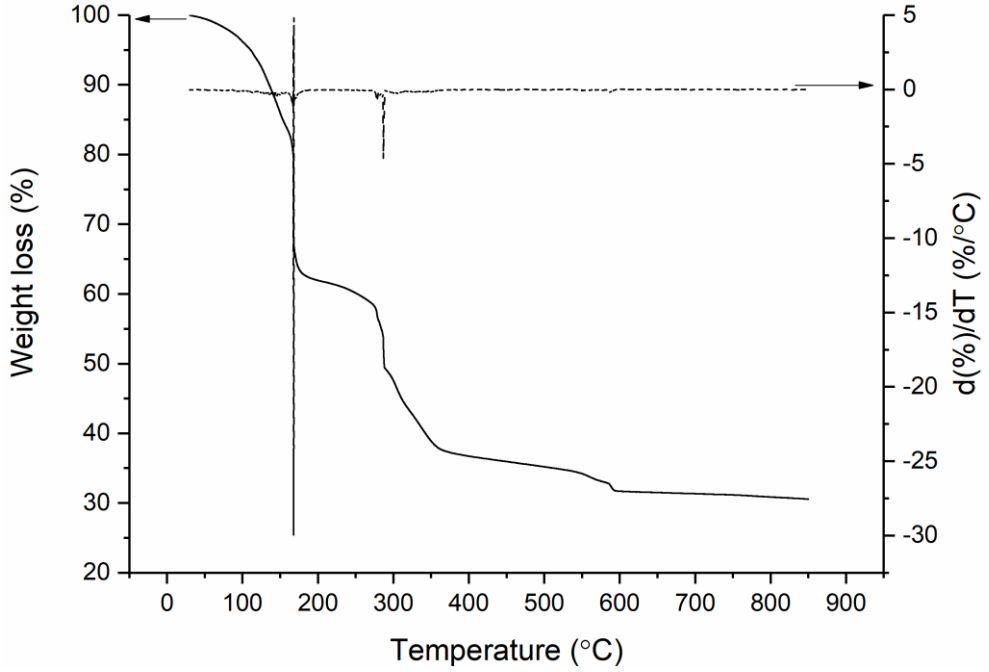

Fig. 5.13. TGA of $Pr_{0.75}Ba_{0.25}CoO_x$ up to 850 °C at 5 °C min^{-1} in air at 50 ml min^{-1}.

In relation to LSCF (Fig. 5.14), the last major mass loss occurred a 580 °C, indicating that the pure phase can form at 550 °C, when held at 550 °C for 3 hours. The major mass loss events occur at 160 °C (citric acid, La and Fe nitrate decomposition), 300 °C (Co nitrate decomposition) followed by the final decomposition at 580 °C (Sr nitrate).

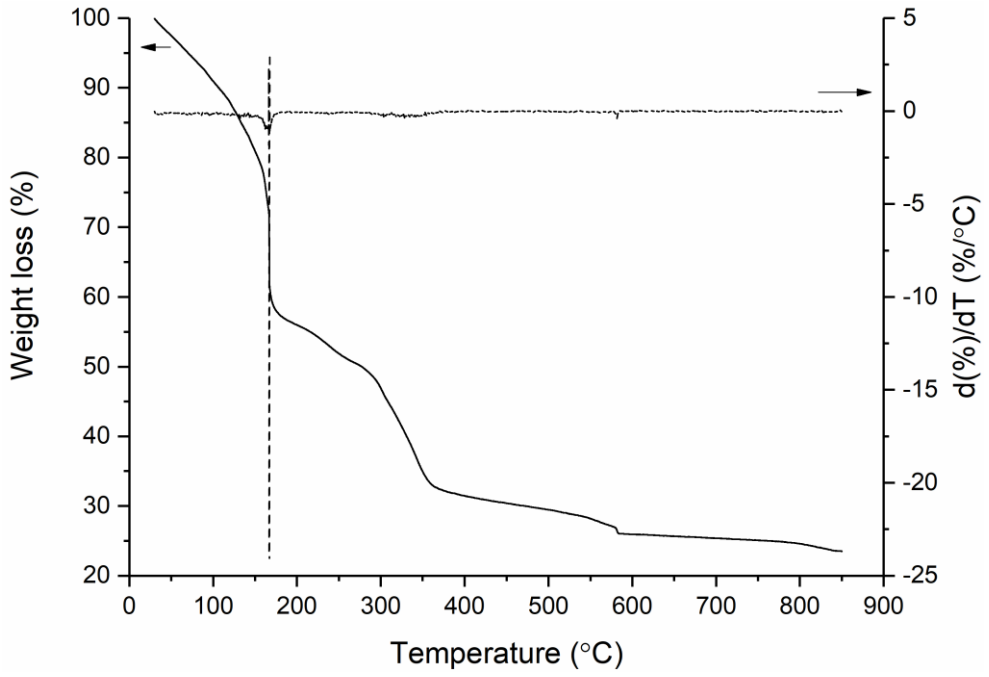

Fig. 5.14. TGA of $La_{0.75}Sr_{0.25}Co_{0.81}Fe_{0.19}O_x$ up to 850 °C at 5 °C min^{-1} in air at 50 ml min^{-1}.

Powder XRD of the final catalysts was performed to confirm the phase present. In the case of PBC (Fig. 5.15), a pure phase forms at 550 °C. Further experiments were conducted to assess whether the second pre-treatment at 500 °C is required. The catalyst was prepared without this step and XRD was subsequently performed. It is possible to see from the XRD reflections that no change is noted, and therefore the second step is not necessary as a phase purity of 100 % is achieved regardless of whether the pre-treatment step was performed. Similarly, for the LSCF catalyst (Fig. 5.16) the second pre-treatment at 500 °C was deemed unnecessary, as the same phase forms when this step is omitted. In both cases, a cubic structure is noted by XRD, with all reflections assigned to the cubic structure, in the phase present.

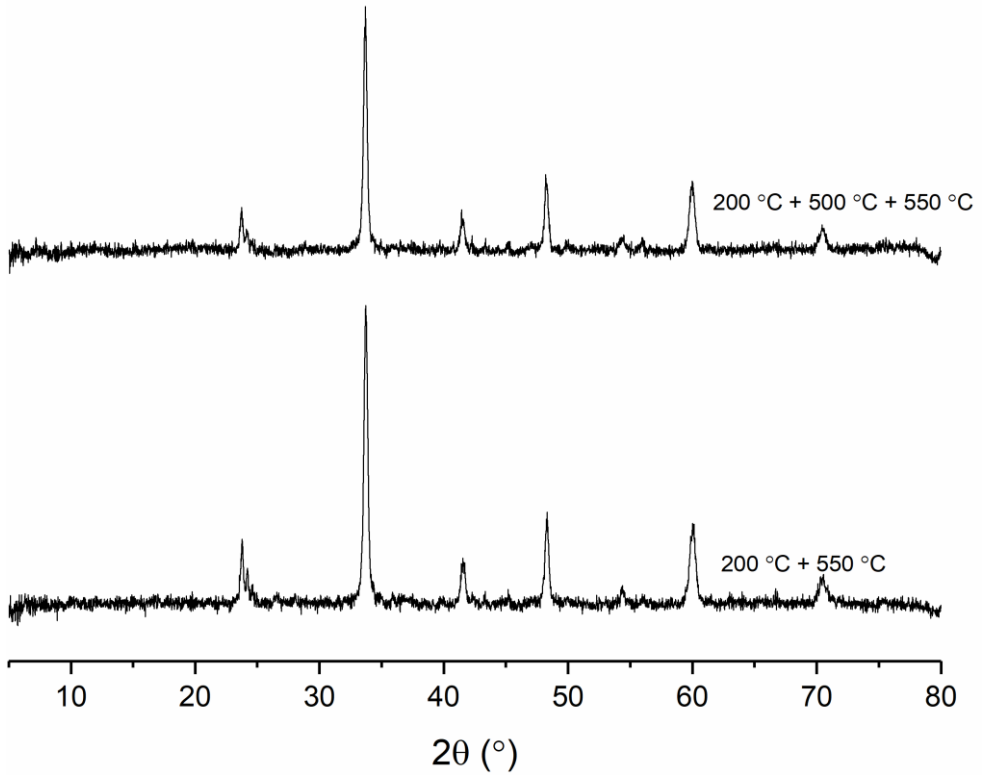

Fig. 5.15. XRD comparison of effect of intermediate pre-treatment at 500 °C on phase purity of $Pr_{0.75}Ba_{0.25}CoO_x$. Temperatures in the labels are the pre-treatment temperatures.

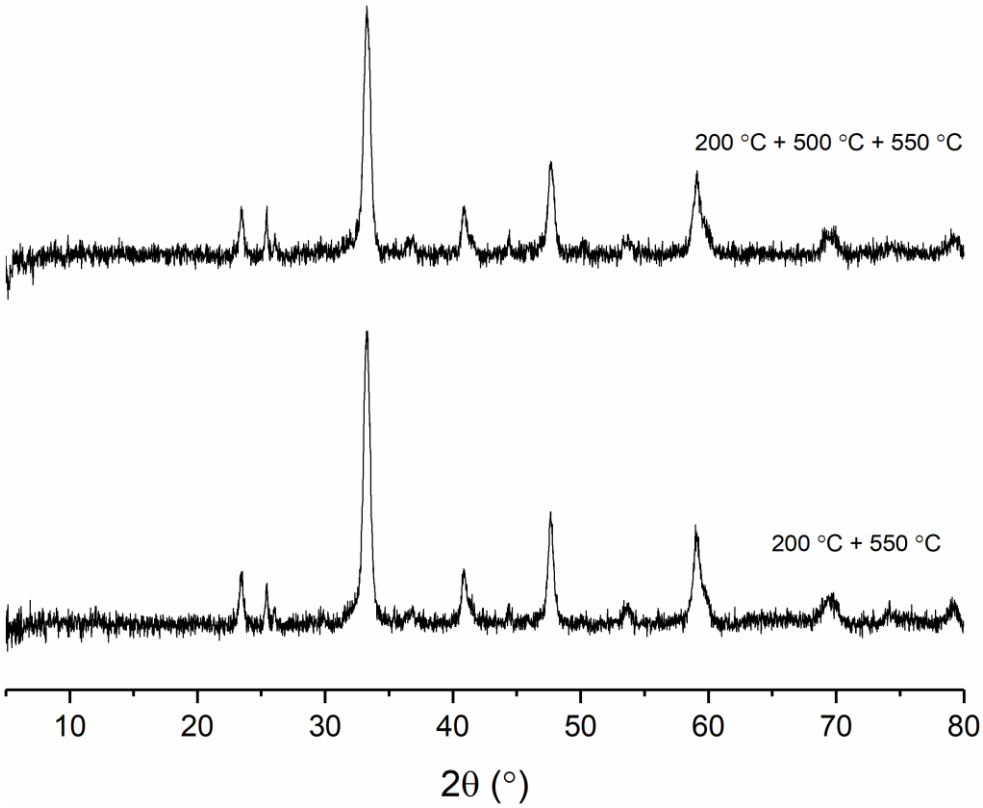

Fig. 5.16. XRD comparison of effect of intermediate pre-treatment at 500 °C on phase purity of $La_{0.75}Sr_{0.25}Co_{0.81}Fe_{0.19}O_x$. Temperatures in the labels are the pre-treatment temperatures.

In addition to phase purity and relatively high surface area, the oxygen species present in the catalyst have shown to be an important influence in the activity of the catalyst for N_2O decomposition. Therefore, through analysis of the O 1s region in the XPS of PBC and LSCF (Fig. 5.17) it is possible to predict the activity. The high percentage of lattice oxygen present at the surface in LSCF could suggest a high oxygen mobility due to the increased concentration of lattice oxygen species and therefore an increased activity compared to LSC and SCF. The PBC catalyst contains less amounts of lanthanide lattice oxygen species to the previously studied BPC, but comparable lattice oxygen when both the lanthanide and transitional lattice oxygen species are combined, 38 % in BPC and 39 % in PBC. Therefore, based on the increase in purity and similar lattice O^{2-} the catalyst was predicted to be slightly better than the first-generation catalyst. An increased purity should lead to a more active catalyst as all active metal is incorporated into the active structure, rather than being present as an inactive impurity.

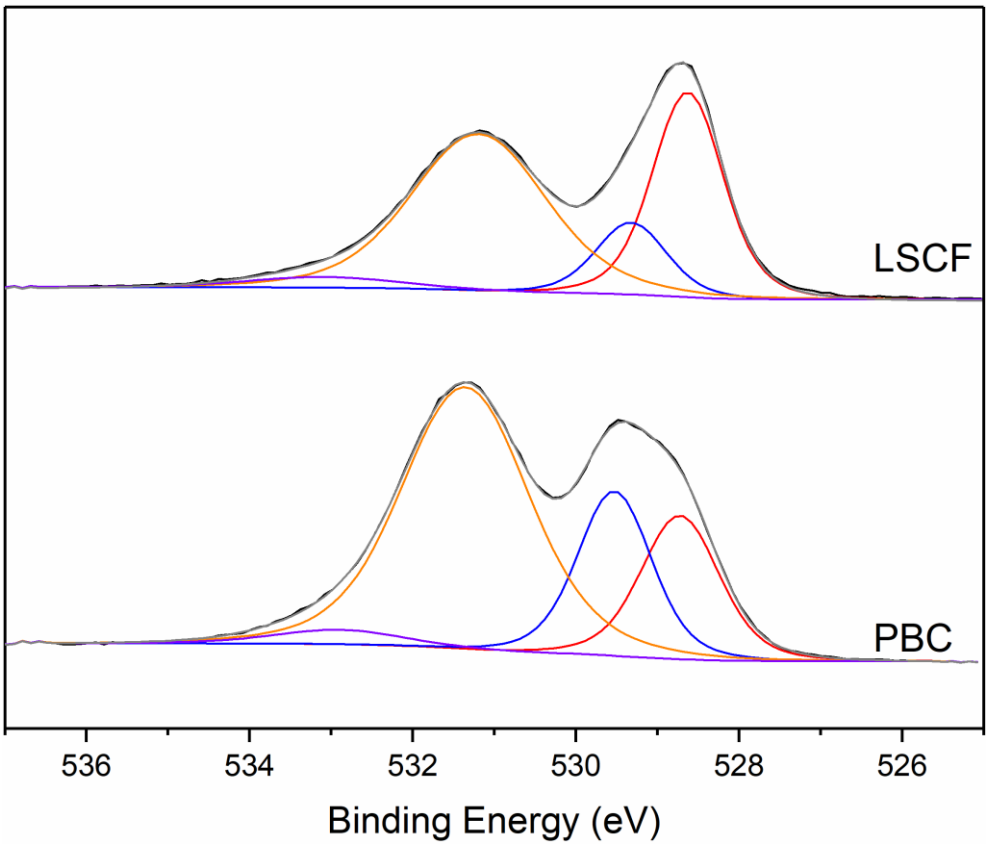

Fig. 5.17. XPS O 1s region of PBC and LSCF catalysts prepared by citric acid decomposition. Fittings: Red – lattice O^{2-}, Blue – lattice O^{2-} transition metal, Orange – hydroxyl species OH^- and Purple – molecular water on surface.

When comparing the N_2O conversion of the second-generation catalysts to the first, both outperform the preceding catalysts. Fig. 5.18 shows the catalytic activity, with N_2O conversion over BPC increasing from 7 % at 450 °C to 58 % over the PBC catalyst (T_{50} decreases from 527 °C, to 445 °C). These catalytic activity results illustrated in Table 5.3 suggest that the increase in phase purity and the presence of lattice oxygen has led to a higher activity. The low surface area may further hinder the activity of the PBC catalyst, despite the surface area of the catalyst being higher than seen previously, now achieving 12 m^2 g^{-1} compared to 3 m^2 g^{-1}; this is due to the low calcination temperature required to form a pure phase perovskite. The higher the heat treatment the lower the surface area, this is due to the higher surface area structure collapsing during the heating process. The structures basically crumble at higher temperatures.

LSCF also demonstrated higher activity than both the original LSC and SCF catalysts, with 62 % conversion at 450 °C (T_{50} decreased to 432 °C from 468 °C (LSC) and 585 °C (SCF)). The incorporation of Fe into the B site of the LSC catalyst allowed the use of a lower calcination temperature to form a phase pure perovskite. The surface area of the catalyst remained consistent at 15 m^2 g^{-1} without Fe (LSC), to 13 m^2 g^{-1} with Fe. By incorporating Fe, the percentage of surface lattice oxygen species remained the same, with 39 % in LSCF and 42 % in LSC, but a large increase on the 1 % seen in the SCF catalyst. As the concentration of surface lattice oxygen and the surface area have remained constant in the LSC to LSCF catalysts, this indicates that another factor is contributing to the increase in activity. One hypothesis could be that although the concentration of lattice oxygen species remains, the same the mobility of these species is different, with the more active catalyst having more mobile oxygen species, which can be confirmed by O_2 TPD experiments. As the mobile oxygen species are necessary to aid oxygen recombination during the decomposition of N_2O.

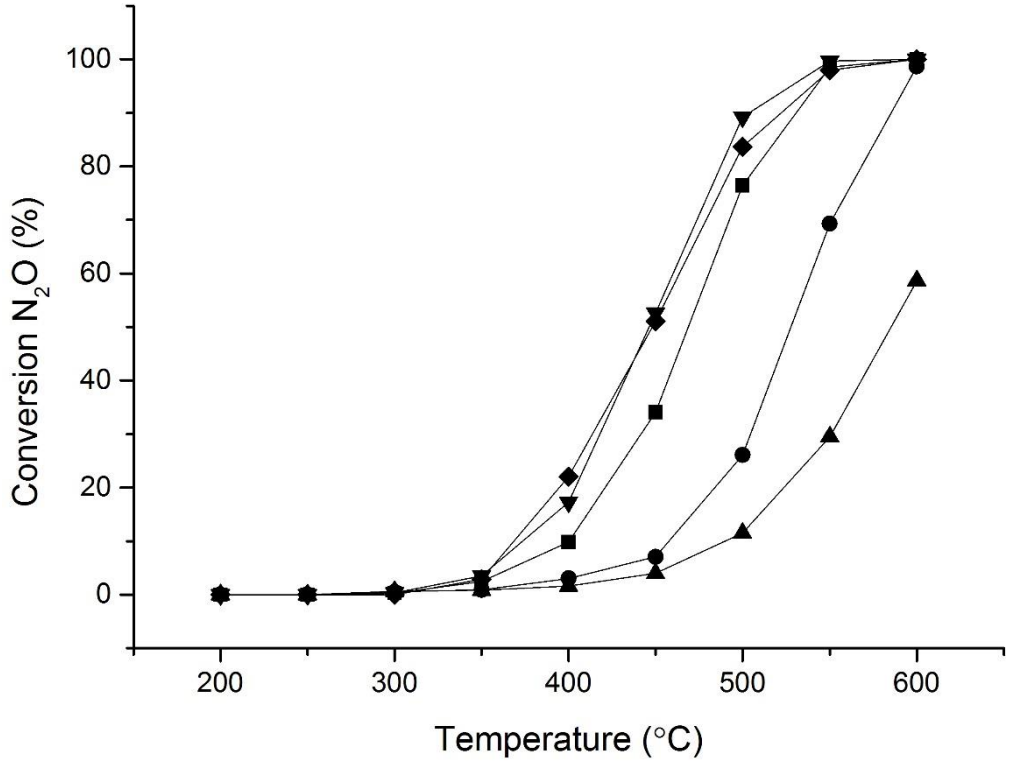

Fig. 5.18. Comparison of catalyst activity of all citric acid catalysts over the temperature range of 200 to 600 °C for N_2O Decomposition. Reaction conditions: 1 % N_2O/He, total flow 100 ml min^{-1}. Legend: ● - BPC, ■ - LSC, ▲ - SCF, ▼ - PBC 200 °C + 550 °C, ◆ - LSCF 200 °C + 550 °C.

Literature reports suggest that a high surface area will lead to an active catalyst. [1–4,52] Most attempts at increasing the surface area of perovskites have found success through supporting the perovskites on high surface area supports. Alini *et al.* supported a $CaMn_{0.6}Cu_{0.4}O_3$ perovskite on a CeO_2-ZrO_2 support, the surface area of this catalyst increased from 15 m^2 g^{-1} to 63 m^2 g^{-1}, with a 10 % perovskite loading. The N_2O conversion over the catalyst increased from 58 % to 67 % at 500 °C. The group linked both the increase in surface area and the contribution of the supports oxygen mobility to increase in activity observed.[1] However Dacquin *et al.* reported that it was possible to increase the surface area of a $LaCoO_3$ from 12 to 50 m^2 g^{-1} by changing the preparation method from templating to reactive grinding. The group stated that the highest surface area catalysts was the most active for N_2O decomposition even though the phases of perovskite present remain constant between preparation methods and that the increase in activity is down to the increases in specific surface area and the higher density of oxygen vacancies present. [51] Therefore, subsequent work focused on using a different preparation method to produce a pure phase, high surface area perovskite.

Table 5.3. Composition determined by MP-AES, surface area, phase purity and the temperature required for 50 % conversion (T_{50}).

Catalyst	Composition determined by MP-AES	Perovskite Phase Purity (%)[a]	Surface area ($m^2 g^{-1}$)	T_{50} (°C)	Lattice O (%)[b]
LSCF	$LaSr_{0.5}CoFe_{0.1}O_{5.8}$	100	13	432	34.2
PBC	$Pr_{0.8}Ba_{0.4}CoO_{5.9}$	100	12	445	19.1

[a] Perovskite phase purity calculated using XRD diffraction pattern and the ratio between the single perovskite phase and any impurities.
[b] Lattice oxygen calculated by the ratio of lattice oxygen species to the sum of molecular water, hydroxyl species, transition metal lattice oxygen as derived from XPS measurements.

5.5 Increased purity and surface area perovskite catalysts prepared by supercritical antisolvent preparation

As shown in 5.4, the purity of the perovskite can be increased by altering the ratio in the A and B sites. Furthermore, these ratios allow lower temperatures to be implemented in order to form the pure perovskite phase under calcination. These ratios were therefore utilised with different preparation methods in an attempt form higher surface area materials. High surface area perovskites are characteristically very difficult to form, with surface area typically being less than 10 $m^2 g^{-1}$. Supercritical anti-solvent (SAS) preparation was explored, as it has been shown previously to produce high surface area materials, with respect to conventional perovskite preparation methods. [53]

The perovskites prepared by supercritical anti-solvent as described in section 2.2.8 were as follows:

- $La_{0.75}Sr_{0.25}Co_{0.81}Fe_{0.19}O_x$ (LSCF SAS)
- $Pr_{0.75}Ba_{0.25}CoO_x$ (PBC SAS)

TGA was once again used to determine a suitable pre-treatment temperature as major mass loss was expected and therefore not suitable to use an untreated sample for *in situ* XRD. For LSCF SAS (Fig. 5.19) the mass loss events all take place below 600 °C. The major event at up to 100 °C is due to the loss of methanol and water, followed by the decomposition of the metal precursors between 150 and

600 °C. There are no well-defined mass loss events with La acetyl acetone (125, 200 and 520 °C), Sr acetate (230 and 475 °C), Fe acetate (80 and 285 °C) and Co acetate (90, 135, 215 and 315 °C) precursors decomposing over the range of 150 and 600 °C. Therefore 300 °C was selected as a suitable pre-treatment temperature, if the catalyst was heated to the temperature at which the final mass loss event occurred at 600 °C) then it would be possible that the phase transformation would be missed as the previous series of catalysts were a pure phase perovskite at 550 C. The pre-treatment consisted of 300 °C at 1 °C min^{-1} for 2 hours in a chamber furnace.

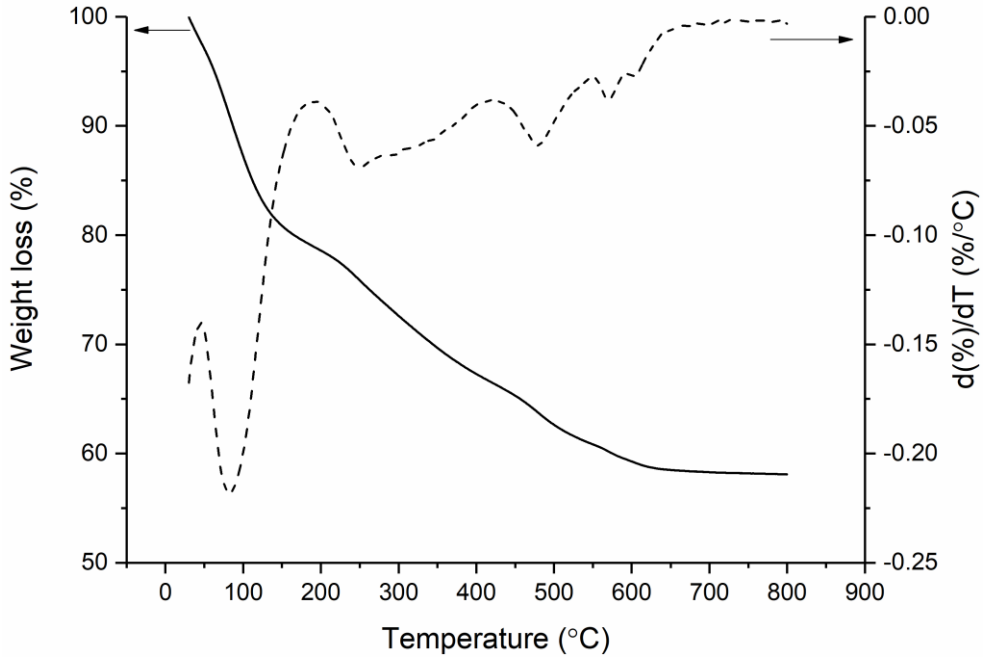

Fig. 5.19. TGA of $La_{0.75}Sr_{0.25}Co_{0.81}Fe_{0.19}O_x$ prepared by SAS up to 850 °C at 5 °C min^{-1} in flowing air at 50 ml min^{-1}.

The TGA of the PBC SAS sample (Fig. 5.20) revealed that all major loss events occurred below 650 °C. As before, a major mass loss below 100 °C due to the loss of methanol and water from the sample, followed by decomposition of the metal precursors between 150 – 640 °C. There are many mass loss events that occur over the temperature range 150- 640 °C due to the decomposition of the following precursors, Pr acetate (170, 275-380 and 560 °C), Ba acetate (225, 325, 445 and 500 °C) and Co acetate (90, 135, 215 and 315 °C). Therefore, 300 °C was selected as a suitable pre-treatment temperature, for the same reason as previously described, the pre-treatment consisted of 300 °C at 1 °C min^{-1} for 2 hours in a chamber furnace.

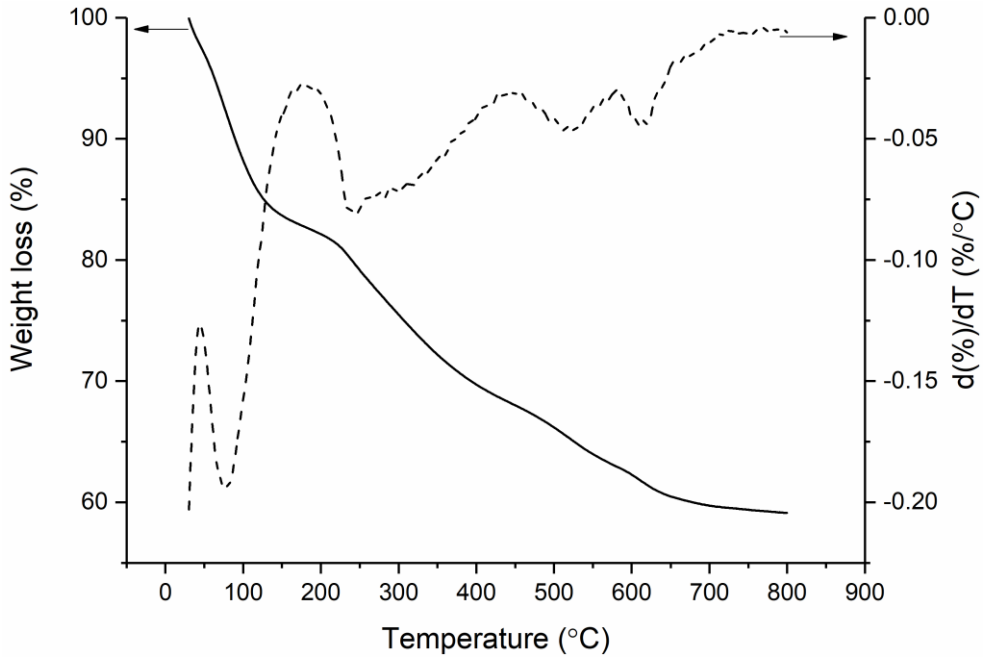

Fig. 5.20 TGA of $Pr_{0.75}Ba_{0.25}CoO_x$ prepared by SAS up to 850 °C at 5 °C min^{-1} in flowing air at 50 ml min^{-1}.

In situ XRD was performed to determine the temperature at which a pure phase perovskite is formed. For the LSCF SAS (Fig. 5.21) sample, the perovskite phase starts to form at 550 °C, although it does not fully form until 800 °C, with the purity reaching a maximum of 93 % at this temperature. Most reflections correspond to a rhombohedral structure, except the single reflection at 36 ° which corresponds to a cubic structure. A high temperature is required for calcination (800 °C), which may also lead to a low surface area perovskite. In the XRD at 50 °C, after cooling, there is a splitting of the reflections, most notably at 33 °. As described previously this could be due to the mass loss that takes place during the heating process, which results in an incorrectly filled *in situ* XRD cell and subsequently an imperfect surface on which the XRD diffraction pattern is recorded. Alternatively, it could be due to the formation of a new phase system. In this case it is likely to be the second, with a new phase formed that has a rhombohedral structure; the phase seen at 800 °C is a cubic structure, that when cooled, transforms to a rhombohedral structure. An XRD measurement was performed at room temperature after calcination at 800 °C and confirmed a single rhombohedral phase present.

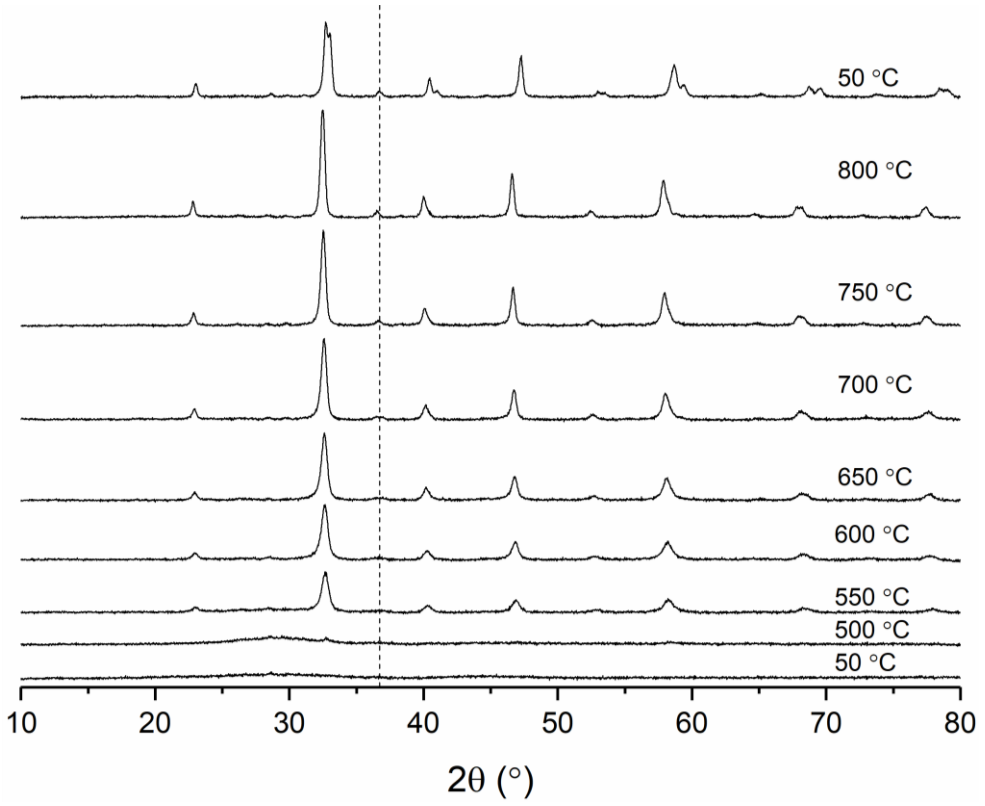

Fig. 5.21. *In situ* XRD of $La_{0.75}Sr_{0.25}Co_{0.81}Fe_{0.19}O_x$ treated to 300 °C prior to analysis heated from 550 °C to 800 °C in air (20 ml min^{-1}). Dashed line – impurity, all other reflections perovskite phase.

In the case of the PBC SAS (Fig. 5.22) sample, the perovskite phase does not start to form until 600 °C, with a 100 % pure phase forming at 700 °C. The same reflections can be observed in all spectra taken above 700 °C, this is an indication of final phase formation, the reflections are indicative of an orthorhombic structure.

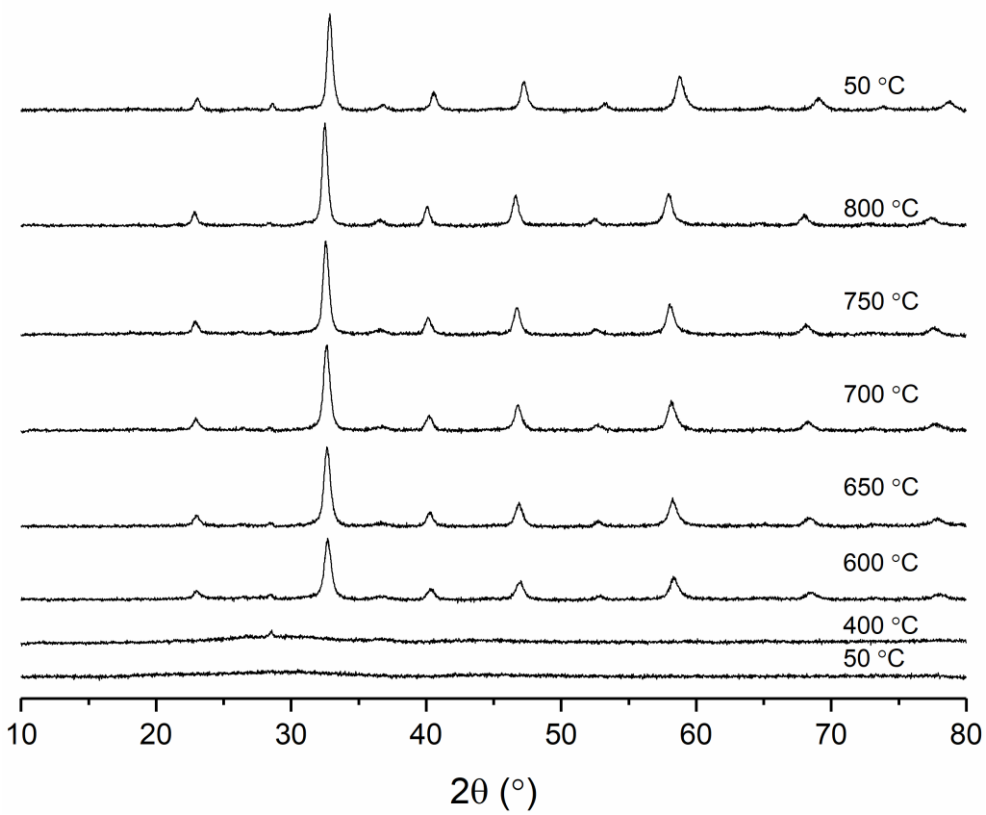

Fig. 5.22. *In situ* XRD of $Pr_{0.75}Ba_{0.25}CoO_x$ treated to 300 °C prior to analysis heated from 550 °C to 850 °C in air (20 ml min^{-1}).

The surface area of this series of catalysts was 12 and 30 m^2 g^{-1} for LSCF and PBC respectively (Table 5.4). Generally, as is the trend seen with these two catalysts, the higher calcination temperature, the lower the surface area. The PBC catalyst has increased in surface area from 12 m^2 g^{-1} to 30 m^2 g^{-1}, which corresponds to an increase in activity from 50 % at 450 °C, to 72 % at the same temperature, with a decreased in T_{50} of 35 °C to 410 °C (Fig. 5.24). The PBC SAS catalyst outperforms that of the PBC catalyst prepared by citric acid, due to the increase in surface area, as the both are high purity with the same phase present.

As the surface area of the LSCF SAS catalyst is similar to the citric acid prepared sample, a similar catalytic activity was expected. However, this was not the case as the citric acid prep LSCF catalyst achieves 85 % conversion at 500 °C, while the catalysts prepared by SAS achieved only 20 % at the same temperature (T_{50} increased from 432 to 577 °C) (Fig. 5.24). It is possible that this is due to the decrease in lattice oxygen present in the catalyst (Fig. 5.23). The lattice oxygen decreases from 39 % in the citric acid prepared catalyst to 32 % in the SAS prepared catalyst (Table 5.4). However, this change does not seem large enough for the decrease in activity that is seen. The decrease could be due to the reduction in

purity between the two catalysts: the catalyst prepared using citric acid has a purity of 100 % but the catalysts prepared by SAS has a purity of only 93 %. This is not a drastic decrease in purity compared to the decrease in activity; therefore, the decrease in activity could be indicative that the lattice oxygen species present are not as mobile as in the citric acid prepared catalyst.

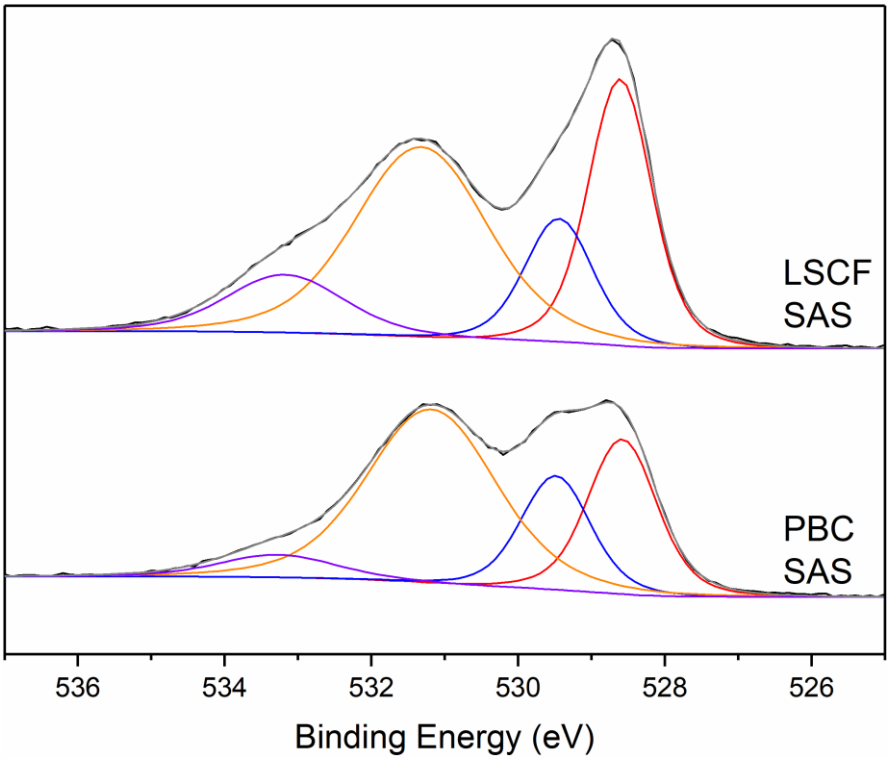

Fig. 5.23. XPS O 1s region of PBC and LSCF catalysts prepared by SAS. Fittings: Red – lattice O^{2-}, Blue – lattice O^{2-} transition metal, Orange – hydroxyl species OH^- and Purple – molecular water on surface.

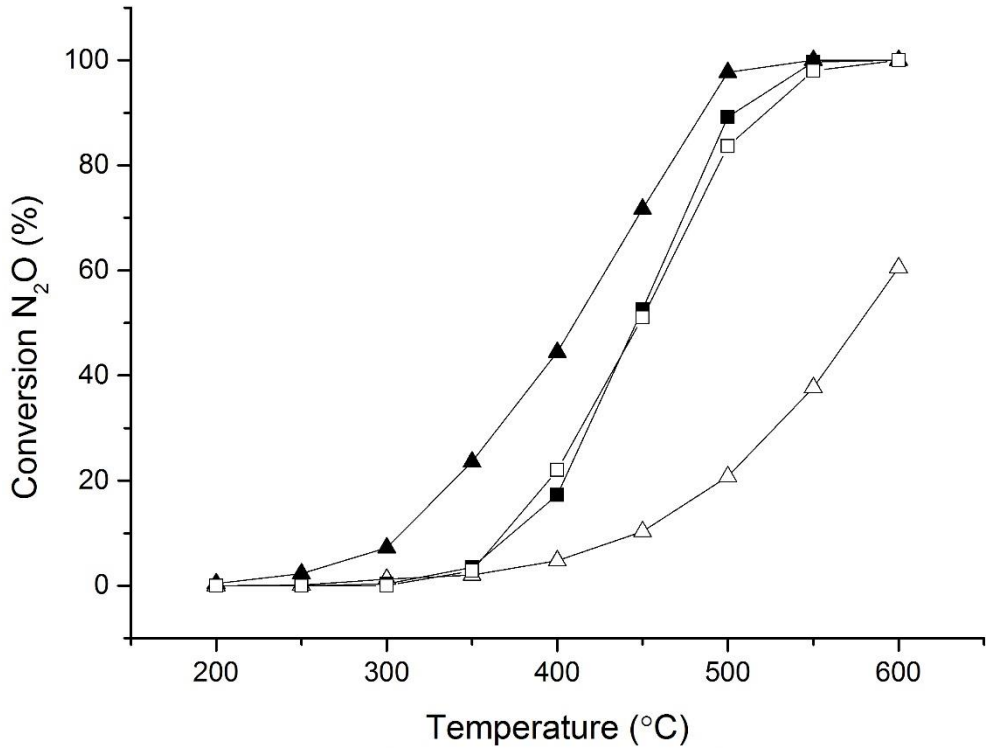

Fig. 5.24. Effect of preparation method on both $Pr_{0.75}Ba_{0.25}CoO_x$ and $La_{0.75}Sr_{0.25}Co_{0.81}Fe_{0.19}O_x$ for N_2O decomposition over the temperature range of 200 to 600 °C. Reaction conditions: 1 % N_2O/He, total flow 100 ml min^{-1}.
Legend: ■ - PBC, ▲ - PBC SAS, □ - LSCF, △ - LSCF SAS.

Table 5.4. Composition determined by MP-AES, Surface area, phase purity and the temperature required for 50 % conversion (T_{50}).

Catalyst	**Composition determined by MP-AES**	**Perovskite Phase Purity (%)[a]**	**Surface area ($m^2 g^{-1}$)**	**T_{50} (°C)**	**Lattice O (%)[b]**
LSCF SAS	$La_{0.8}Sr_{0.1}CoFe_{0.2}O_{5.2}$	93	12	577	29.5
PBC SAS	$Pr_{0.6}Ba_{0.3}CoO_{4.2}$	100	30	410	24.5

[a] Perovskite phase purity calculated using XRD diffraction pattern and the ratio between the single perovskite phase and any impurities.
[b] Lattice oxygen calculated by the ratio of lattice oxygen species to the sum of molecular water, hydroxyl species, transition metal lattice oxygen as derived from XPS measurements.

Additional work on this topic was designed to further investigate the effect of surface area, purity and lattice oxygen concentration on the activity of perovskite catalysts for N_2O decomposition. This was achieved by preparing the two most active catalysts (PBC and LSCF) by another preparation method. The following section details the effect of using an oxalic acid preparation method.

5.6 Increased purity perovskite catalysts prepared by oxalic acid precipitation method

In the previous sections (5.3, 5.4 and 5.5) it has been shown that the purity of the perovskite can be increased by altering the ratio in the A and B sites. The same ratios have been used in this section for comparison, but with different preparation methods. In this section, an oxalic acid precipitation method, described in section 2.2.7, has been used to prepare the perovskites LSCF and PBC.

The perovskite prepared were as follows:

- $La_{0.75}Sr_{0.25}Co_{0.81}Fe_{0.19}O_x$ (LSCF Oxalic)
- $Pr_{0.75}Ba_{0.25}CoO_x$ (PBC Oxalic)

As shown previously, TGA has been used to determine a suitable pre-treatment temperature as major mass loss was expected and therefore not suitable to use an untreated sample for *in situ* XRD. For LSCF Oxalic (Fig. 5.25) the mass loss events all take place below 650 °C with a substantial event around 100 °C due to the loss of oxalic acid. This is followed by the decomposition of the metal precursors between 150 and 650 °C. The most notable loss occurred at 270 °C, due to the decomposition of the Co, La and Fe precursors, with other mass loss events occurring at 200 °C, due to oxalic acid and Fe nitrate decomposition, and at 650 °C due to the decomposition of Sr nitrate. Therefore, 300 °C was selected as a suitable pre-treatment temperature even though the final mass loss event occurred at 650 °C. This is because if the catalysts was pre-treated to 650 °C, the perovskite phase may of already formed and the temperature at which this occurred at will not be known. The citric acid prepared PBC and LSCF catalysts formed pure phase perovskites at

550 °C, this would have been missed in this case. The pre-treatment is performed using a ramp rate of 1 °C min^{-1}, for 2 hours in a chamber oven.

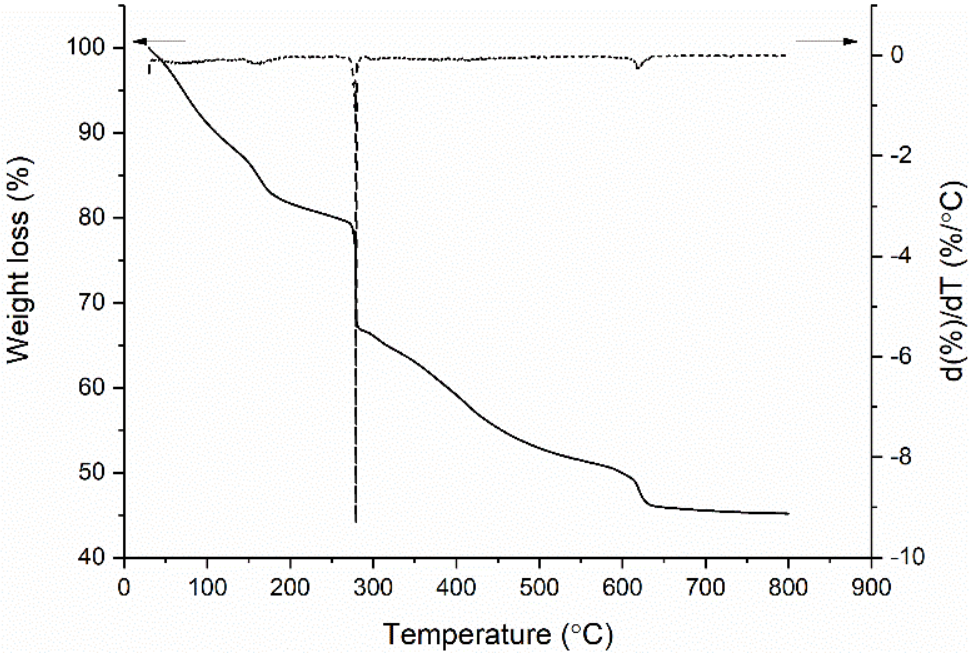

Fig. 5.25. TGA of $La_{0.75}Sr_{0.25}Co_{0.81}Fe_{0.19}O_x$ prepared by oxalic acid prep up to 850 °C at 5 °C min^{-1} in flowing air at 50 ml min^{-1}.

In the case of PBC Oxalic (Fig. 5.26), the last major event loss occurs around 600 °C. A significant mass loss below 100 °C, due to the removal of oxalic acid from the sample, is followed by decomposition of the metal precursors between 250 – 600 °C. Most notably, the major mass loss event occurred at 280 °C due to the decomposition of the Co and Pr precursors, with other mass loss events occurring at 175 °C due to oxalic acid decomposition, 350°C due to Pr nitrate and at 600 °C due to the decomposition of Ba nitrate. Therefore, as described previously, 300 °C was selected as a suitable pre-treatment temperature.

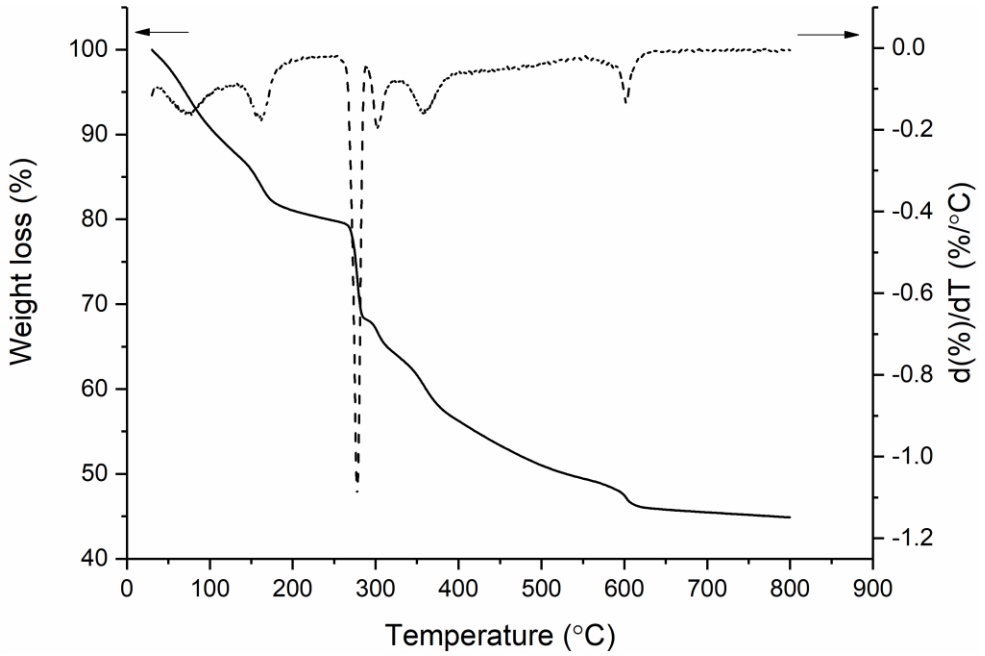

Fig. 5.26. TGA of $Pr_{0.75}Ba_{0.25}CoO_x$ prepared by oxalic acid prep up to 850 °C at 5 °C min^{-1} in flowing air at 50 ml min^{-1}.

In situ XRD was performed to determine the temperature that a pure phase perovskite can be formed. For LSCF Oxalic (Fig. 5.27), the perovskite phase starts to form at 600 °C but does not fully form until 800 °C. All reflections correspond to the formation of a 100 % pure rhombohedral phase. Therefore, a high temperature is required for calcination, suggesting that a low surface area perovskite may be formed. In the XRD diffraction pattern at 50 °C, after cooling, there is a splitting of the reflections most notably at 33 °. As described previously, this could be due to the expected mass loss that occurs during the heating process, and therefore an imperfect surface may form within the sample cell, on which a perfect XRD diffraction pattern cannot be recorded. Alternatively, it could be due to the formation of a new phase system. In this case it is likely to be the second, a new phase has formed that has a rhombohedral structure, as the phase seen at 800 °C is a cubic structure that when cooled transforms to a rhombohedral structure. An XRD measurement was performed after calcination and confirmed a single phase present, confirming the transformation from a cubic to rhombohedral structure.

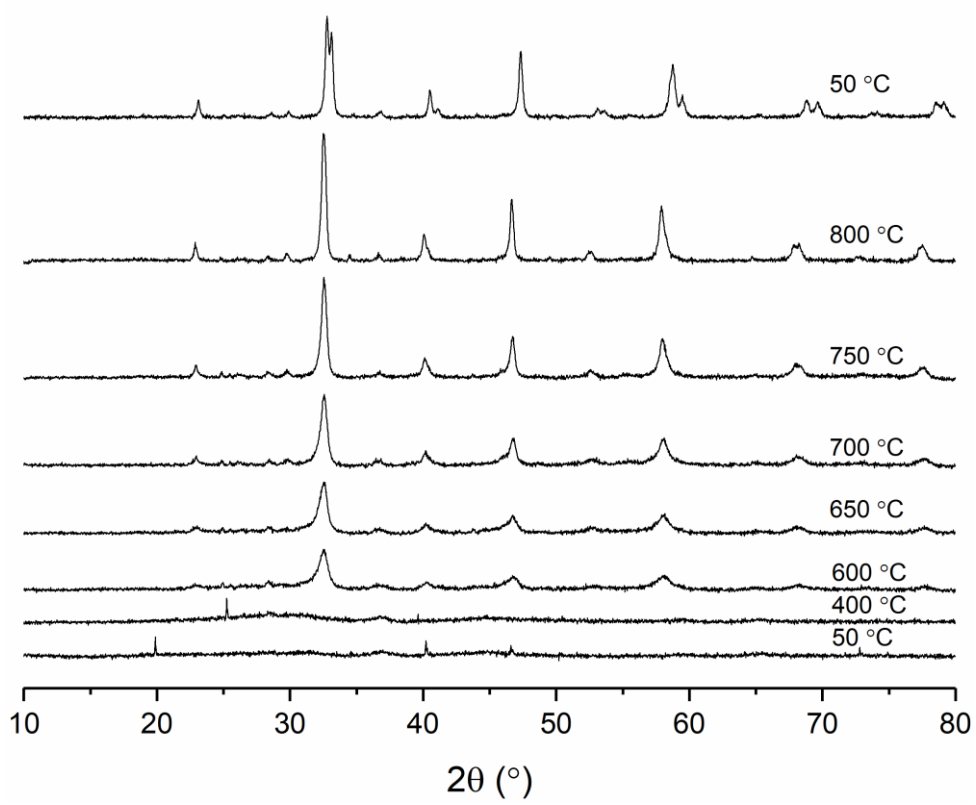

Fig. 5.27. *In situ* XRD of $La_{0.75}Sr_{0.25}Co_{0.81}Fe_{0.19}O_x$, treated to 200 °C prior to analysis, heated from 550 °C to 850 °C in air (20 ml min^{-1}).

In the case of PBC (Fig. 5.28) the perovskite phase does not start to form until 550 °C, with a pure phase forming at 700 °C. The same reflections are seen in all spectra above 700 °C, this is an indication of final phase formation. The purity of this catalyst reaches a maximum of 96 % at 700 °C, therefore, this temperature was selected for the final calcination temperature. The major reflections are indicative of a tetragonal structure, with the impurities having a cubic structure. The reflections of the impurity phase are seen at 28.7, 36.6 and 56.5 °. After cooling to 50 °C, there is a shift in the reflections, with all 2θ values increasing by +0.47 ° to +0.99 °. This is due to the contraction of the solid after heating, leaving an imperfect surface that the XRD diffraction pattern is recorded on.

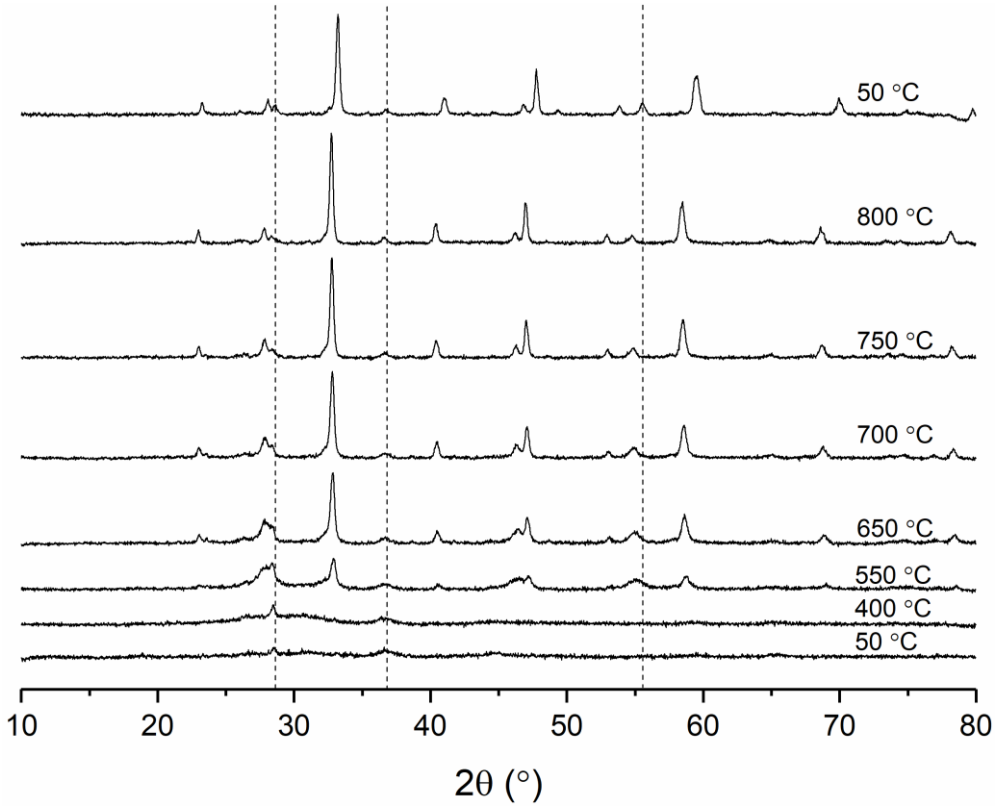

Fig. 5.28. *In situ* XRD of $Pr_{0.75}Ba_{0.25}CoO_x$, treated to 200 °C prior to analysis, heated from 550 °C to 850 °C in air (20 ml min^{-1}). Dashed line – Impurities. All other reflections perovskite phase.

As suggested previously, the oxygen species present in the perovskite may play a large part in the activity. XPS can be used to determine the oxygen species present, with four main species seen: lattice oxygen from lanthanide elements, lattice oxygen from transition metals, hydroxyl species or molecular water. [33–35,54] Molecular water is lost during the reaction due to the increase in temperature, while the hydroxyl species just block the surface of the catalysts.

In the case of LSCF (Fig. 5.29), all oxygen species are present, most notably there is a large peak associated to lattice oxygen. In addition to lattice oxygen being required, oxygen mobility has also been shown to be crucial in the decomposition of N_2O due to the requirement to recombine O to form O_2 in the rate determining step. If there is a large amount of lattice oxygen present that is mobile, this can then bind with the deposited O forming O_2 and regenerate the active site. In LSCF, 34 % of the oxygen present is in the form of lattice oxygen, similar to what is seen in the citric acid preparation, therefore the activity should be comparable. In PBC, again all oxygen species are present (Fig. 5.29), with 27 % of the oxygen present as lattice oxygen. This is the highest percentage of lattice oxygen across all the PBC catalysts

prepared by different preparation methods, and therefore this was predicted to be the most active catalysts in the series.

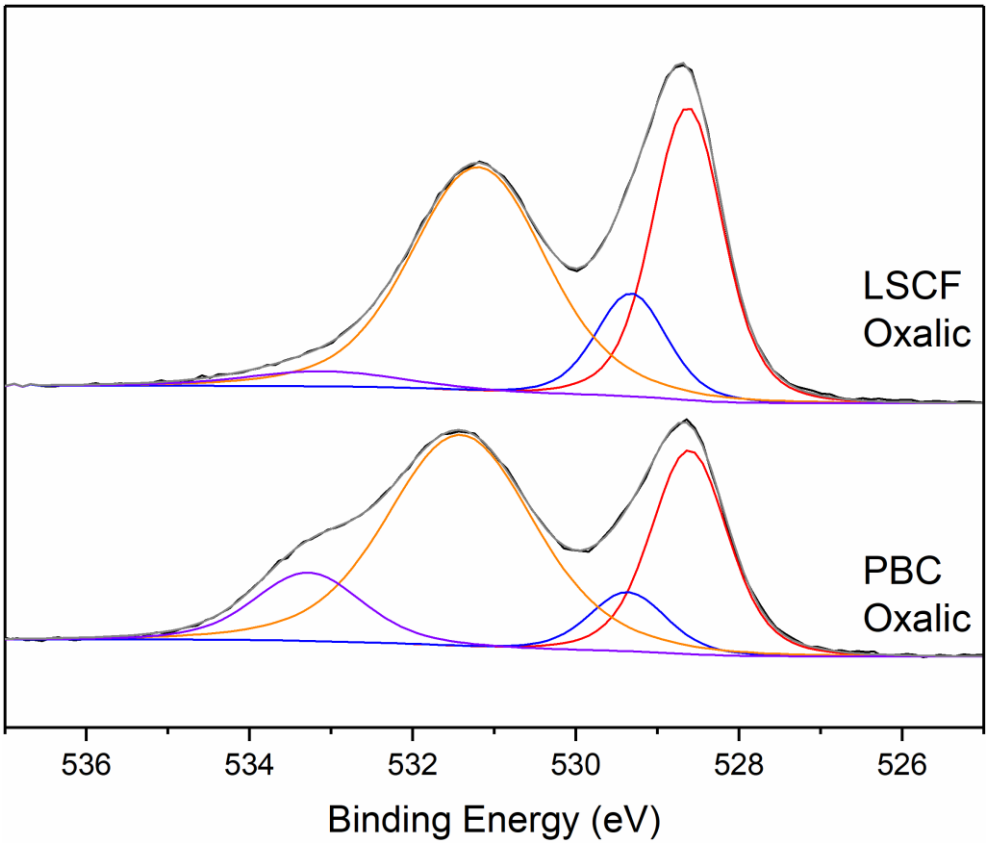

Fig. 5.29. XPS O 1s region of PBC and LSCF catalysts prepared by oxalic acid precipitation method. Fittings: Red – lattice O^{2-}, Blue – lattice O^{2-} transition metals, Orange hydroxyl species OH^-, and Purple – molecular water on surface.

The activity of the LSCF Oxalic catalyst was not as good as the citric acid prepared catalyst, with 80 % conversion achieved at 550 °C compared to the LCSF catalyst which 98 % at the same temperature (T_{50} increased from 432 to 475°C) (Fig. 5.30. a). Although both catalysts have the same percentage of lattice oxygen the mobility of the species present may be different. The oxalic acid prepared catalysts may have less mobile lattice oxygen species compared to the citric acid prepared catalyst, leading to a lower activity. The surface area of the LSCF catalysts has remained fairly consistent across preparation methods, from 12 – 14 $m^2\ g^{-1}$ (Table 5.5), indicating that for this catalyst the surface area is not as important a factor as initially thought. When the conversion is normalised by surface area (Fig. 5.30 b) there is no change in trends seen as the surface area values are all so similar.

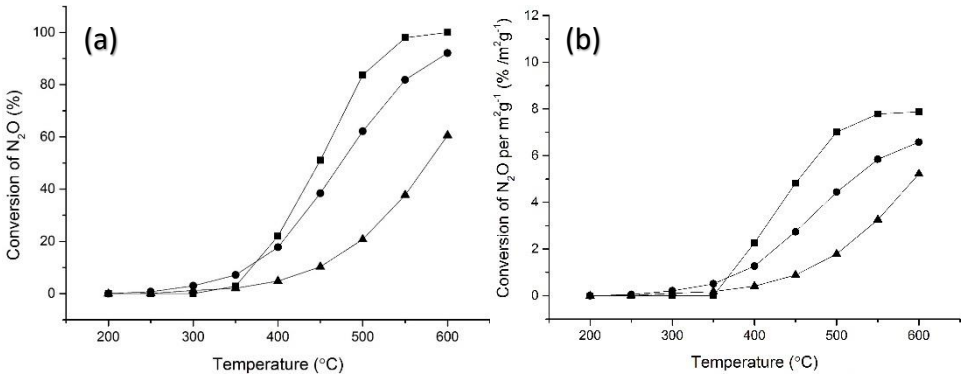

Fig. 5.30. (a) Effect of preparation method on $La_{0.75}Sr_{0.25}Co_{0.81}Fe_{0.19}O_x$ for N_2O decomposition over the temperature range of 200 to 600 °C. (b) Surface area normalised reaction data showing the effect of preparation method on $La_{0.75}Sr_{0.25}Co_{0.81}Fe_{0.19}O_x$ for N_2O decomposition over the temperature range of 200 to 600 °C. Reaction conditions: 1 % N_2O/He, total flow 100 ml min^{-1}. Legend: ■ - LSCF Citric, ▲ - LSCF SAS, ● - LSCF Oxalic.

When comparing the O_2-TPD profiles of the three catalysts it is possible to compare the mobility of the lattice oxygen present. As there is no response in the region < 700 °C meaning only β-oxygen (also referred to as lattice oxygen) is considered to be present. A greater response during the O_2-TPD indicates a higher mobility of lattice oxygen present. The lower the temperature at which a response is noted, the more mobile the oxygen species present are. [13,37,55–58] As mobility increases, the activity of the catalysts should also increase, if the mobility of the oxygen is as important as it has been described.[21,23,58,59] Fig. 5.31 displays the O_2-TPD experiments of LSCF prepared by the three preparation methods. As predicted by XPS, the SAS preparation produced the catalyst with the lowest response, with the signal forming at the highest temperature; this corresponds to lattice oxygen that is not mobile, hence producing a non-active catalyst. The catalyst is not completely inactive, due to the small signal response seen at around 700 °C that corresponds to a small amount of mobile lattice oxygen. The oxalic and citric catalysts have similar responses at 750 °C, therefore, the mobility of the lattice oxygen is similar at these temperatures hence why at low temperatures the activity of the catalysts is similar. All catalysts show no response in the O_2-TPD between 300 – 700 °C, this is the region in which α-Oxygen is present. α-Oxygen is also referred to as oxygen vacancies; this indicates that there are a very limited number of oxygen vacancies with in this series of catalysts. Oxygen vacancies are important in this reaction as it is thought that the oxygen terminal of N_2O could bind at a vacancy site and then initiate the decomposition of N_2O, as shown in Mechanism 1.

$$N_2O_{(gas)} + O_{vac} \rightarrow N_2O_{(ads)}$$

$$N_2O_{(ads)} \rightarrow N_{2\,(gas)} + O_{(ads)}$$

$$O_{(ads)} + O_{(ads)} \rightarrow O_{2\,(gas)} + 2\,O_{vac}$$

Mechanism 1. N_2O decomposition mechanism on the surface of a perovskite. Showing the use of oxygen vacancies and the importance of the mobility of lattice oxygen (O_{ads}).

If there are limited number of the oxygen vacancy sites, then the catalyst may be limited in activity. The citric acid prepared catalyst does outperform that of the oxalic catalyst as past 750 °C more lattice oxygen is desorbed and therefore more mobile and available for reaction. Here the trend in activity is related to the lattice oxygen percentage and the mobility of these species, the more mobile lattice oxygen the more active the catalyst for N_2O decomposition.

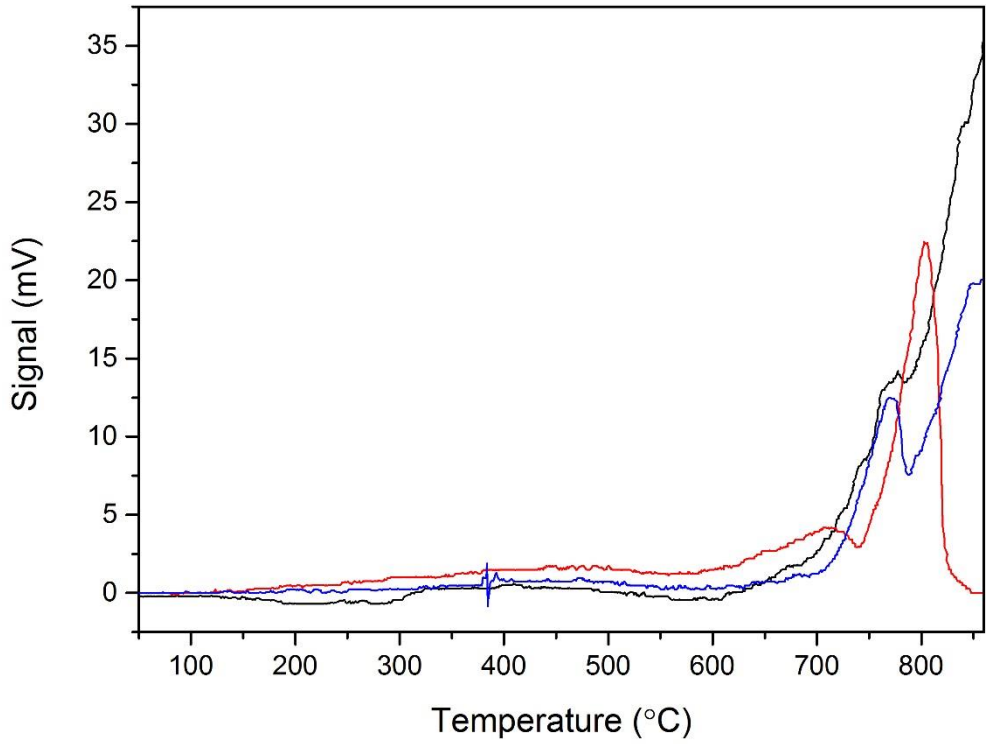

Fig. 5.31. Oxygen temperature programmed desorption (O_2-TPD) of $La_{0.75}Sr_{0.25}Co_{0.81}Fe_{0.19}O_x$ catalysts, Black - Citric prep, Red - SAS prep, Blue - Oxalic prep.

In the case of the PBC material, all preparation methods lead to the production of catalysts with very similar activity for N_2O decomposition at temperatures greater than 500 °C (Fig. 5.32 a). However, at temperatures lower than this the difference in activity is more notable: the oxalic acid catalyst achieves a T_{50} 431 °C, compared

to T_{50} 445 °C for the citric catalyst and T_{50} 410 °C for the SAS catalyst. This does not follow the trend that the more lattice oxygen the more active the catalyst for N_2O decomposition. Lattice oxygen does affect the activity, but is not the only contributing factor, with surface area playing a role. The activity in terms of lattice oxygen should follow the order, oxalic acid prep as the most active, followed by SAS and then the citric acid as the least active. However, in reality the most active catalyst is prepared by SAS precipitation method, followed by oxalic and then citric acid preparation methods. This could be linked to the surface area as the SAS catalyst has an extremely high surface area of 30 $m^2\ g^{-1}$ compared to 12 $m^2\ g^{-1}$ for the oxalic and 9 $m^2\ g^{-1}$ for the citric acid prep. Therefore, when the N_2O conversion data is normalised to surface area the oxalic acid prepared PBC catalyst out performs the other two preparation methods, even though this has the lowest percentage of lattice oxygen (Fig. 5.32 b). This is due to the catalyst having the most mobile oxygen species, as shown by O_2-TPD (Fig. 5.33). As mentioned previously there are three oxygen species that can be identified during O_2 TPD, with desorption below 300 °C indicating that chemically adsorbed O_2 is present. α-Oxygen desorbs at 300 – 700 °C which is oxygen that is present in an oxygen vacancy. Finally, at temperatures greater than 700 °C, lattice oxygen (β-O) desorbs. .[13,37,55–58] In the case of the PBC sample, the activity very closely follows the trend of the more mobile the lattice O present, the more active the catalyst. The SAS catalyst has the greatest response in the region 300 – 700 °C and therefore has the most oxygen vacancies, which are thought to be the active site based on Mechanism 1. Secondly, as shown in Fig. 5.31, the peak due to lattice oxygen for the SAS catalyst is at the lowest temperature (775 °C) and therefore has the most mobile lattice oxygen out of the three preparation methods. The oxalic catalyst has the second largest response between 300 – 750 °C, with the lattice oxygen peak at 785 °C, which results in this catalyst displaying the second highest catalytic activity. The citric acid prepared catalyst has the lowest catalytic activity as it has the least oxygen vacancies and the least mobile lattice oxygen (800 °C). As described before, a low oxygen mobility may limit oxygen recombination after N_2O has adsorbed and dissociated to N_2 and O on the surface. As the adsorbed O must combine with another O species to form O_2, if the surface species are not mobile then this step

becomes rate determining (Mechanism 1). Therefore, the most active catalyst is the catalyst with the most oxygen defects and the most mobile lattice oxygen.

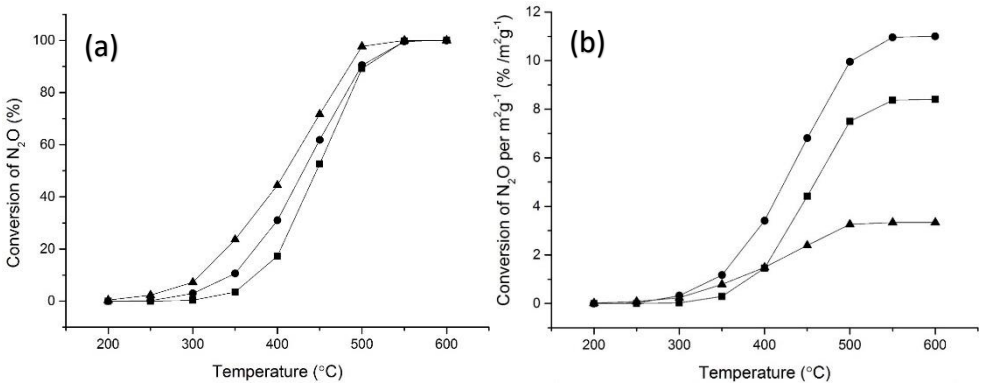

Fig. 5.32. (a) Effect of preparation method on $Pr_{0.75}Ba_{0.25}CoO_x$ for N_2O decomposition over the temperature range of 200 to 600 °C. (b) Surface area normalised reaction data showing the effect of preparation method on $Pr_{0.75}Ba_{0.25}CoO_x$ for N_2O decomposition over the temperature range of 200 to 600 °C. Reaction conditions: 1 % N_2O/He, total flow 100 ml min^{-1}. Legend: ■ - PBC Citric, ▲ - PBC SAS, ● - PBC Oxalic.

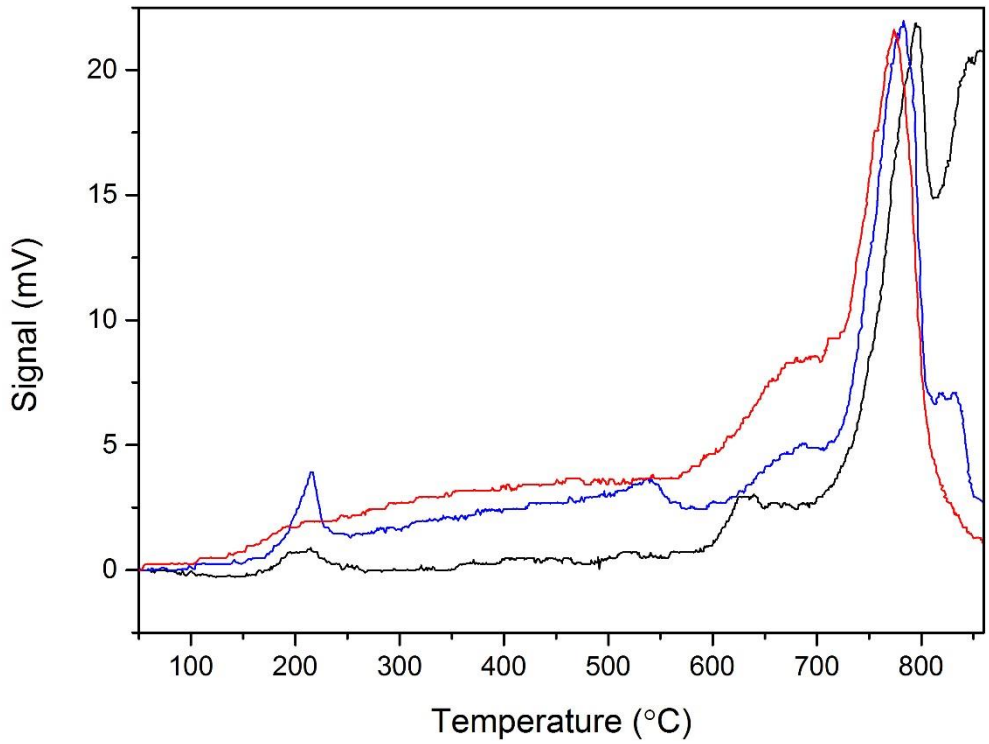

Fig. 5.33. Oxygen temperature programmed desorption (O_2-TPD) of $Pr_{0.75}Ba_{0.25}CoO_x$ catalysts, Black - Citric prep, Red - SAS prep, Blue - Oxalic prep.

Table 5.5. Composition determined by MP-AES, Surface area, phase purity and the temperature required for 50 % conversion (T_{50}).

Catalyst	Composition determined by MP-AES	Perovskite Phase Purity (%)[a]	Surface area ($m^2 g^{-1}$)	T_{50} (°C)	Lattice O (%)[b]
LSCF Oxalic	$La_1Sr_{0.3}CoFe_{0.2}O_{5.5}$	100	14	475	34.2
PBC Oxalic	$Pr_{0.8}Ba_{0.1}CoO_{4.9}$	96	9	431	26.7

[a] Perovskite phase purity calculated using XRD diffraction pattern and the ratio between the single perovskite phase and any impurities.
[b] Lattice oxygen calculated by the ratio of lattice oxygen species to the sum of molecular water, hydroxyl species, transition metal lattice oxygen as derived from XPS measurements.

Table 5.6 shows the comparison between all catalysts discussed in this Chapter. When noting the trends, it is possible to see that by changing the ratio from BPC where Ba and Pr are 50:50 in the A site to, PBC, where Pr:Ba is 75:25 in the A site, the purity increases from 77 % to 100 %, along with the T_{50} decreasing from 527 to 445 °C. Therefore, changing the ratio has improved the purity and subsequently the catalytic activity. Then, when comparing the three preparation methods for the PBC catalyst the SAS prepared catalyst, produces the catalysts with the lowest T_{50} (410 °C). There are a few factors that could be at play here: the first is the higher surface area that is achieved using the SAS preparation method, the second being the % of lattice oxygen and the mobility of such species and then the presence of oxygen vacancies with in the catalyst. Overall, the SAS preparation method produces the catalyst with the largest signal response in the α-O region (vacancies) and has the earliest onset of signal in the β-O region, indicating the most mobile lattice oxygen species and the most oxygen vacancies. Along with a relatively high surface area of 30 m^2g^{-1}, this produces the most active catalysts in the series.

The LSC and SCF perovskites elemental ratio were combined, and the purity of the perovskite phase increased from 98 and 81 % respectively to 100 %; The activity of the catalyst also increased with the T_{50} dropping from 468 and 527, respectively, to 432 °C. Again, altering the elemental ratios in the A and B site has led to the production of a pure phase catalyst with increased activity for N_2O decomposition. When comparing preparation method of the LSCF perovskite, the citric acid preparation mentioned previously produces the most active catalyst. This could be due to a number of factors, the first being that the more mobile the lattice oxygen present the more active the catalyst. With the earliest onset in the 700 – 850 °C region in the O_2-TPD being from the citric acid prepared LSCF perovskite. Secondly the difference in activity between preparation methods may be due to the different

phases of perovskite present: in both the SAS and oxalic acid prepared perovskite a rhombohedral phase is present, where as in the citric acid prepared perovskite a cubic phase is present, as shown in Fig. 5.34. Both these factors may result in the most active LSCF perovskite prepared by citric acid method.

Table 5.6. Comparison between all catalysts, preparation method, composition determined by MP-AES, surface area, phase purity and the temperature required for 50 % conversion (T_{50}).

Catalyst	**Prep method**	**Calcination Temperature (°C)**	**Composition determined by MP-AES**	**Perovskite Phase Purity (%)[a]**	**Surface area (m^2 g^{-1})**	**T_{50} (°C)**	**Lattice O (%)[b]**
LSC	Citric Acid	900	$La_{0.8}Sr_{0.4}CoO_{3.9}$	98	15	468	42.6
BPC	Citric Acid	850	$Ba_{0.6}Pr_{0.6}CoO_{4.5}$	77	3	527	33.0
SCF	Citric Acid	900	$Sr_{1.5}CoFe_{0.2}O_5$	81	7	585	1.5
LSCF	Citric Acid	550	$LaSr_{0.5}CoFe_{0.1}O_{5.8}$	100	13	432	34.2
PBC	Citric Acid	550	$Pr_{0.8}Ba_{0.4}CoO_{5.9}$	100	12	445	19.1
LSCF	SAS	800	$La_{0.8}Sr_{0.1}CoFe_{0.2}O_{5.2}$	93	12	577	29.5
PBC	SAS	700	$Pr_{0.6}Ba_{0.3}CoO_{4.2}$	100	30	410	24.5
LSCF	Oxalic	750	$La_1Sr_{0.3}CoFe_{0.2}O_{5.5}$	100	14	475	34.2
PBC	Oxalic	700	$Pr_{0.8}Ba_{0.1}CoO_{4.9}$	96	9	431	26.7

[a] Perovskite phase purity calculated using XRD diffraction pattern and the ratio between the single perovskite phase and any impurities.

[b] Lattice oxygen calculated by the ratio of lattice oxygen species to the sum of molecular water, hydroxyl species, transition metal lattice oxygen as derived from XPS measurements.

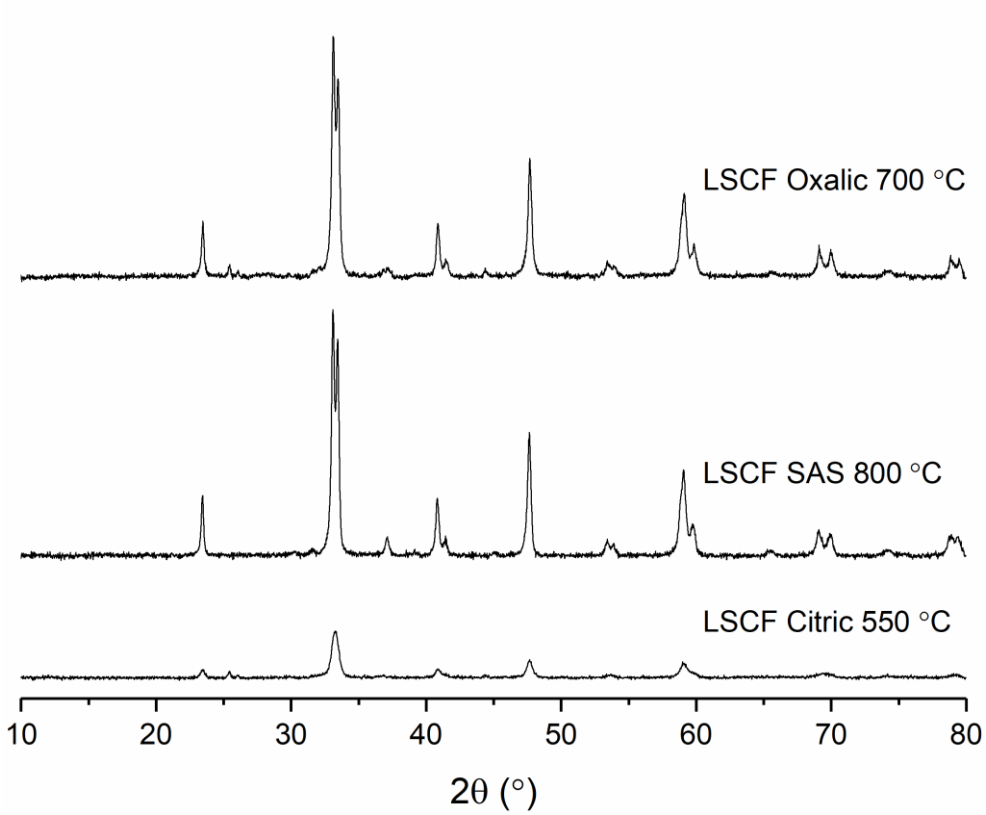

Fig. 5.34 XRD comparison of effect of preparation method on $La_{0.75}Sr_{0.25}Co_{0.81}Fe_{0.19}O_x$.

The most active catalysts from both LSCF and PBC series were tested for 24 h to give an indication of the stability of the catalysts under reaction conditions (Fig. 5.35). The citric acid prepared LCSF and SAS prepared PBC catalysts were tested. The LCSF citric catalyst has a slight induction period of *ca*. 1.5 h, but the catalyst did not lose any activity over the time period tested. The PBC SAS displayed an initial increase in activity of 10 %, which then decreased over the next 4.5 h period and eventually stabilised at around 50 % conversion. Overall, both catalysts show good stability over a 24 hour period in reaction conditions with limited activity loss observed.

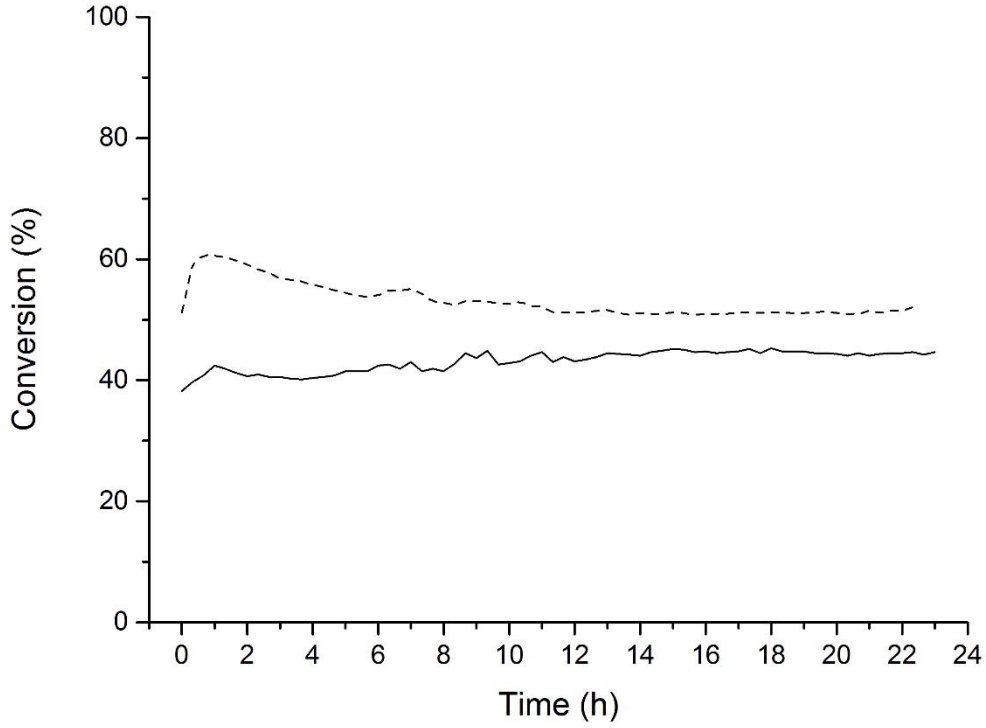

Fig. 5.35. Time online data of most active catalyst form each series for N_2O Conversion. Reaction conditions: 1 % N_2O/He, total flow 100 ml min^{-1}, 450 °C, 24 h. Legend: dashed line PBC SAS, solid line LSCF Citric.

5.7 Conclusions

The effect of A and B site ratios along with preparation method of several perovskites have been investigated for the decomposition for N_2O. It has been found that by altering the ratios of the A and B site cations makes it is possible to produce a pure phase perovskite at low temperatures, and by altering the preparation method it is possible to produce a perovskite with different oxygen species. This work has confirmed the importance of lattice oxygen species that have high oxygen mobility for the decomposition of N_2O. Mobile lattice oxygen has been shown to be crucial, as the rate-limiting step in the decomposition of N_2O is the formation of oxygen. This is limited by adsorbed O species being within a distance at which recombination is possible. However, if there is a great deal of mobile lattice oxygen present then these can aid recombination and regenerate the active site for N_2O decomposition. In the case of LSCF the activity correlates with the more mobile lattice oxygen present, the more active the catalyst. The most mobile lattice oxygen, and therefore activity, was obtained with the citric acid preparation. The PBC catalyst also followed the trend that the more mobile the lattice species

present the more active the catalyst. In the case of the PBC catalysts, there was also the presence of oxygen vacancies to compare, with more oxygen vacancies leading to a more active catalyst as these could be the active site. The most active catalyst was prepared via the SAS method, as this resulted in the highest amount of mobile lattice oxygen. When comparing to literature examples (Table 5.1) both these catalysts outperform the best literature perovskite at similar conditions, with $Pr_{0.2}Ba_{0.8}MnO_3$ achieving 50 % conversion at 442 °C, [19] whereas the catalysts tested here can convert 50 % of the N_2O at 432 °C and at 410 °C for the LSCF Citric and PBC SAS catalyst respectively.

5.8 Future Work

To further understanding the in LSCF perovskite series, the same cubic or rhombohedral phase could be prepared for all preparation methods as this will confirm whether one structure is more active than the other. This requires a low temperature calcination to form the cubic structure and a high temperature to form the rhombohedral structure.

To further understand the perovskite catalyst and how N_2O decomposition takes place, H_2-TPR should be performed to measure the reducibility of the catalysts. The reducibility of the catalysts has been shown in literature by Russo *et. al.* to be a key factor in the reaction mechanism. [4] The following mechanism is generally accepted for the decomposition of N_2O into N_2 and O_2. [2,4]

$$N_2O + * \rightarrow N_2O* \quad (1)$$

$$N_2O* \rightarrow N_2 + O* \quad (2)$$

$$2\,O* \rightarrow O_2 + 2* \quad (3)$$

$$O* + N_2O* \rightarrow O_2 + N_2 + * \quad (4)$$

Mechanism 2. Decomposition of N_2O at an oxygen vacancy on the surface of a perovskite. * = O_{vac}

In Mechanism 2, the catalyst becomes oxidised in the 2nd step and needs to be able to reduce the active site by removal of oxygen to regenerate the active site for further reactions. The reduction can take place via two routes, Eq. 3 by the Eley Rideal mechanism or by Eq. 4 which follows the principles of Langmuir

Hinshelwood. The perovskite must therefore be reducible for these steps to take place, H_2-TPR can give an indication to this. The lower the reduction temperature, the more reducible the catalyst. Russo stated that the $LaCoO_3$ catalyst tested "exhibited the highest activity as a consequence of its greater capability to be reduced at comparatively low temperature during TPR runs, a key requirement for nitrous oxide catalytic decomposition." [4] The recombination of the oxygen species can also be aided by oxygen mobility, as recombination takes place at vacancy sites and lattice oxygen is used to fill these vacancies and aid recombination, hence mobile oxygen is crucial. Therefore, the study of reduction profiles, with the most easily reduced indicating an active catalyst for N_2O decomposition.

5.9 References

1 S. Alini, F. Basile, S. Blasioli, C. Rinaldi and A. Vaccari, *Appl. Catal. B Environ.*, 2007, **70**, 323–329.

2 F. Kapteijn, J. Rodriguez-Mirasol and J. A. Moulijn, *Appl. Catal. B Environ.*, 1996, **9**, 25–64.

3 N. Labhasetwar, G. Saravanan, S. Kumar Megarajan, N. Manwar, R. Khobragade, P. Doggali and F. Grasset, *Sci. Technol. Adv. Mater.*, 2015, **16**, 036002.

4 N. Russo, D. Mescia, D. Fino, G. Saracco and V. Specchia, *Ind. Eng. Chem. Res.*, 2007, **46**, 4226–4231.

5 M. I. Konsolakis, *ACS Catal.*, 2015, **5**, 6397–6421.

6 J. Hwang, R. R. Rao, L. Giordano, Y. Katayama, Y. Yu and Y. Shao-Horn, *Science (80-.).*, 2017, **358**, 751–756.

7 R. J. H. Voorhoeve, D. W. Johnson, J. P. Remeika and P. K. Gallagher, *Science (80-.).*, 1977, **195**, 827–833.

8 M. A. Peña and J. L. G. Fierro, *Chem. Rev.*, 2001, **101**, 1981–2017.

9 G. Centi and S. Perathoner, *Microporous Mesoporous Mater.*, 2008, **107**, 3–15.

10 L. A. Isupova, G. M. Alikina, S. V Tsybulya, N. N. Boldyreva, G. N. Kryukova, I.

S. Yakovleva, V. P. Isupov and V. A. Sadykov, *Int. J. Inorg. Mater.*, 2001, **3**, 559–562.

11 J. Zhu, D. Xiao, J. Li, X. Xie, X. Yang and Y. Wu, *J. Mol. Catal. A Chem.*, 2005, **233**, 29–34.

12 J. Zhu, X. Yang, X. Xu and K. Wei, *J. Phys. Chem. C*, 2007, **111**, 1487–1490.

13 J. Zhu, Z. Zhao, D. Xiao, J. Li, X. Yang and Y. Wu, *J. Mol. Catal. A Chem.*, 2005, **238**, 35–40.

14 H. Tanaka and M. Misono, *Curr. Opin. Solid State Mater. Sci.*, 2001, **5**, 381–387.

15 L. Marchetti and L. Forni, *Appl. Catal. B Environ.*, 1998, **15**, 179–187.

16 R. J. H. Voorhoeve, J. P. Remeika and L. E. Trimble, *Ann. N. Y. Acad. Sci.*, 1976, **272**, 3–21.

17 J. Il Jung, H. Y. Jeong, J. S. Lee, M. G. Kim and J. Cho, *Angew. Chemie - Int. Ed.*, 2014, **53**, 4582–4586.

18 N. Russo, D. Mescia, D. Fino, G. Saracco and V. Specchia, *Ind. Eng. Chem. Res.*, 2007, **46**, 4226–4231.

19 S. Kumar, A. Vinu, J. Subrt, S. Bakardjieva, S. Rayalu, Y. Teraoka and N. Labhsetwar, *Catal. Today*, 2012, **198**, 125–132.

20 T. Ishihara, M. Ando, K. Sada, K. Takiishi, K. Yamada, H. Nishiguchi and Y. Takita, *J. Catal.*, 2003, **220**, 104–114.

21 D. V. Ivanov, E. M. Sadovskaya, L. G. Pinaeva and L. A. Isupova, *J. Catal.*, 2009, **267**, 5–13.

22 D. V. Ivanov, L. G. Pinaeva, L. A. Isupova, A. N. Nadeev, I. P. Prosvirin and L. S. Dovlitova, *Catal. Letters*, 2011, **141**, 322–331.

23 D. V. Ivanov, L. G. Pinaeva, L. A. Isupova, E. M. Sadovskaya, I. P. Prosvirin, E. Y. Gerasimov and I. S. Yakovleva, *Appl. Catal. A Gen.*, 2013, **457**, 42–51.

24 Thermofisher, *https://xpssimplified.com/elements/praseodymium.php*, 2019-03–19.

25 Thermofisher, *https://xpssimplified.com/elements/barium.php*, 2019-03–

19.

26 Thermofisher, *https://xpssimplified.com/elements/strontium.p*, 2019-03–19.

27 Thermofisher, *https://xpssimplified.com/elements/lanthanum.php*, 2019-03–19.

28 J. L. G. Fierro and L. G. Tejuca, *Appl. Surf. Sci.*, 1987, **27**, 453–457.

29 K. Tabata, Y. Hirano and E. Suzuki, *Appl. Catal. A Gen.*, 1998, **170**, 245–254.

30 Thermofisher, *https://xpssimplified.com/elements/iron.php*, 2019-03–19.

31 Thermofisher, *https://xpssimplified.com/elements/cobalt.php*, 2019-03–19.

32 M. A. Morris, M. O. Connell, A. K. Norman and C. F. Hu, *Catal. Today*, 1999, **47**.

33 A. Worayingyong, P. Kangvansura and S. Kityakarn, *Colloids Surfaces A Physicochem. Eng. Asp.*, 2008, **320**, 123–129.

34 Y. Zhang-Steenwinkel, J. Beckers and A. Bliek, *Appl. Catal. A Gen.*, 2002, **235**, 79–92.

35 P. Wang, L. Yao, M. Wang and W. Wu, *J. Alloys Compd.*, 2000, **311**, 53–56.

36 C. Sui, X. Niu, Z. Wang, F. Yuan and Y. Zhu, *Catal. Sci. Technol.*, 2016, **6**, 8505–8515.

37 S. Kumar, Y. Teraoka, A. G. Joshi, S. Rayalu and N. Labhsetwar, *J. Mol. Catal. A Chem.*, 2011, **348**, 42–54.

38 A. Bianconi, A. Kotani, K. Okada, R. Giorgi, A. Gargano, A. Marcelli and T. Miyahara, *Am. Phys. Soc. Phys. Rev. B*, 1988, **38**, 3433–3437.

39 P. G. Corradini, E. Antolini and J. Perez, *Phys. Chem. Chem. Phys.*, 2013, **15**, 11730–11739.

40 M. F. Sunding, K. Hadidi, S. Diplas, O. M. Løvvik, T. E. Norby and A. E. Gunnæs, *J. Electron Spectros. Relat. Phenomena*, 2011, **184**, 399–409.

41 P. Zou, M. Yao, J. Chen, Y. Peng and X. Yao, *Ceram. Int.*, 2016, **42**, 4120–4125.

42 K. Maiti, J. Fink, S. de Jong, M. Gorgoi, C. Lin, M. Raichle, V. Hinkov, M.

Lambacher, A. Erb and M. S. Golden, *Phys. Rev. B*, 2009, **80**, 165132.

43 A. Rodrigues, S. Bauer and T. Baumbach, *Ceram. Int.*, 2018, **44**, 16017–16024.

44 D. Cabrera-German, G. Gomez-Sosa and A. Herrera-Gomez, *Surf. Interface Anal.*, 2016, **48**, 252–256.

45 J. Stoch, 1991, **17**, 165–167.

46 S. Tanigawa, T. Takashima and H. Irie, *J. Mater. Sci. Chem. Eng.*, 2017, **05**, 129–141.

47 J. C. Dupin, D. Gonbeau, P. Vinatier and A. Levasseur, *Phys. Chem. Chem. Phys.*, 2000, **2**, 1319–1324.

48 P. Mack, *Spectroscopic analysis of solid oxide fuel cell material with XPS*, 2009.

49 H. Van Doveren and J. A. T. Verhoeven, *J. Electron Spectros. Relat. Phenomena*, 1980, **21**, 265–273.

50 Y. Wu, X. Ni, A. Beaurain, C. Dujardin and P. Granger, *Appl. Catal. B Environ.*, 2012, **125**, 149–157.

51 J. P. Dacquin, C. Dujardin and P. Granger, *Catal. Today*, 2008, **137**, 390–396.

52 S. Royer, D. Duprez, F. Can, X. Courtois, C. Batiot-Dupeyrat, S. Laassiri and H. Alamdari, *Chem. Rev.*, 2014, **114**, 10292–10368.

53 C. D. Evans, S. A. Kondrat, P. J. Smith, T. D. Manning, P. J. Miedziak, G. L. Brett, R. D. Armstrong, J. K. Bartley, S. H. Taylor, M. J. Rosseinsky and G. J. Hutchings, *Faraday Discuss.*, 2016, **188**, 427–450.

54 N. A. Merino, B. P. Barbero, P. Eloy and L. E. Cadús, *Appl. Surf. Sci.*, 2006, **253**, 1489–1493.

55 J. Zhu, H. Li, L. Zhong, P. Xiao, X. Xu, X. Yang, Z. Zhao and J. Li, *ACS Catal.*, 2014, **4**, 2917–2940.

56 K. L. Pan, S. J. Yu, S. Y. Yan and M. B. Chang, *J. Air Waste Manag. Assoc.*, 2014, **64**, 1260–1269.

57 Z. Zhao, X. Yang and Y. Wu, *Appl. Catal. B Environ.*, 1996, **8**, 281–297.

58 J. P. Dacquin, C. Lancelot, C. Dujardin, P. Da Costa, G. Djega-Mariadassou, P. Beaunier, S. Kaliaguine, S. Vaudreuil, S. Royer and P. Granger, *Appl. Catal. B Environ.*, 2009, **91**, 596–604.

59 C. Li, Y. Shen, S. Zhu and S. Shen, *RSC Adv.*, 2014, **4**, 29107–29119.

6 Conclusions and Future Work

6.1 N_2O and the environment

Nitrous Oxide (N_2O) is a greenhouse gas that has a devastating effect on the atmosphere, with a global warming potential of roughly 300 times that of CO_2. [1–3] With the control on the emissions not yet legislated in many cases, the use and emissions of N_2O continue to rise. The emission of N_2O from anthropogenic sources such as agriculture [4], nitric acid plants [1] and fuel combustion [4] amongst others contribute to the destruction of the ozone layer and the formation of an ozone hole above the south pole. [5,6] This leads to global warming, an increase in sea temperature and levels, causing devastating changes to the earth as we currently know it, such as land and life loss. Subsequently, as a race we need to wake up to the fact that N_2O is now one of the most threatening major polluting greenhouse gas, that should be legislated and the use of which strictly controlled.

6.2 Fe-ZSM-5 Catalysts

6.2.1 Conclusions

Iron zeolite catalysts have been used extensively for the decomposition of N_2O over the last 100 years, with Fe-ZSM-5 being the catalyst of choice. [7–10] Here, Si:Al ratio, Fe weight loading and acid washing have been investigated. The work has shown agreement with literature that low Si:Al ratios are necessary for the decomposition of N_2O and this is because of the formation of α-Fe, that can only form on the Al moiety, hence more Al leads to the presence of more α-Fe species, and consequently more active sites. [8,11,12]

Here, catalysts have been prepared by CVI and when low weight loadings such as 0.16 % Fe-ZSM-5 were prepared there are only two species of Fe present, as framework Fe^{3+} and isolated extra-framework, confirmed by UV/Vis spectroscopy. At higher loadings two more species of Fe are present, as FeO_x nanoparticles and

large clusters; these are non-active species and therefore lead to an inefficient catalyst. In this work, it is confirmed that the species of Fe necessary for N_2O decomposition are framework and extra-framework species, as the 0.16 % Fe-ZSM-5 catalyst out-performs all other catalysts when a reductant is present in the gas feed even though it has the lowest percentage of Fe out of all the catalysts tested.

As discussed previously, the mechanism of N_2O decomposition involves the reduction of the surface to regenerate the active site by the removal of an absorbed oxygen species. This is the rate limiting step and without the presence of a reductant the higher weight loadings (1.25 and 2.5 wt.% Fe) out-perform the lower weight loadings. This is due to the increase in the density of active sites and the subsequent increase in oxygen recombination. As soon as a reductant is added to the gas feed the activity of all three weight loadings is similar at 600 °C. The effect of the density of active sites is removed when a reductant is added to the gas feed, as the reductant will cleave any oxygen atoms that are present on the surface and reduce the active site ready for another incoming N_2O molecule.

Acid washing had been shown in literature to be a suitable technique to selectively remove FeO_x nano-particles and clusters from the surface of a catalyst. [13] This was not the case when performed on 0.4 wt.% Fe-ZSM-5, with Fe being extracted from the pores in the extra-framework position and deposited on the surface of the catalysts instead as nano-particles and clusters. This results in a decrease in conversion due to the removal of active α-Fe species and an increase in TOF due to the removal of around 60 % of weight loading of Fe. A catalyst with the same weight loading was prepared by CVI, for comparison to the acid washed catalyst, and it was discovered that it was possible to produce a low weight loading catalyst that has only the two active species of Fe present, producing the most active catalyst. This catalysts had a TOF of 2.59 $x10^3$ s^{-1} and has a superior activity to all other catalysts in the series. When compared to literature, the TOF is far higher than that reported by Park *et al.* who achieved a TOF of 1.8 $x10^{-3}$ s^{-1} for N_2O decomposition at 550 °C using 1.96 wt. % Fe-ZSM-5 (27).[14] At similar conditions and the same temperature the 0.16 wt.% Fe-ZSM-5 catalysts achieves a TOF of 1.44 $x10^6$ s^{-1}, demonstrating the greater activity of the low loaded catalyst when propane is present.

6.2.2 Future Work

The scope of this study did not extend to the use of steaming pre-treatments which have been shown in literature to enhance Fe-ZSM-5 catalysts for N_2O decomposition. Literature has shown that the reason for this increase in activity is due to the removal of Fe from the pores and into the extra-framework sites. [15–19] This in turn creates the α-Fe species that have been shown in this work to be the active species for N_2O decomposition and would therefore be predicted to produce a more active catalyst. It would be interesting to study whether it is possible to prepare a low loading catalyst by CVI that has only framework and extra-framework species that, following a steaming pre-treatment, would produce a catalysts with only α-Fe species present, and what effect this has on the catalytic activity for N_2O decomposition.

Finally, to confirm that in fact the species of Fe that are active for N_2O decomposition is α-Fe, it would be possible to prepare a catalyst with the same weight loading on a silicate support as the α-Fe moiety can only form on the Al sites in the ZSM-5 framework. In silicates these species will not be produced and would therefore lead to an inactive catalyst.

6.3 Pd-Al_2O_3 Catalysts

6.3.1 Conclusions

The effect of heat treatment conditions, reaction cycling and chlorine concentration on 2.6 wt. % Pd-Al_2O_3 catalysts have been investigated for the catalytic decomposition of N_2O into N_2 and O_2 in the absence and presence of a reducing agent (C_3H_8). After several reaction cycles, the conversion of N_2O increased from 58 % after the first use to 96 % during the fourth use at 600 °C. These multiple use catalysts also show improved stability on-stream. By calcining the support before catalyst preparation, it is possible to achieve the same conversion in the first use of the support calcined catalyst, therefore, showing it is possible to attain high activity on the initial use rather than after multiple reaction cycles. It is hypothesised that this is due to the removal of water species, lowering the PZC of the support, due to the Pd solution containing $PdCl_3(H_2O)^-$ ions, there is

reduced interaction between the Pd ion and the support surface, which leads to the formation of smaller nanoparticles. As the pH of the solution is lower than that of the PZC, the surface is protonated and will strongly interact with anions; therefore with the decrease in PZC as the support is calcined, the surface is less positively charged and this leads to a weaker interaction between the nanoparticles and the surface, as a result smaller well dispersed nanoparticles. [20,21]

When a reductant is added to the gas feed, the temperature at which 100 % N_2O conversion is seen is shifted from 550 °C to 350 °C. The reductant enriches the decomposition of N_2O to N_2, however, a limited amount of O_2 is measured. This, alongside the presence of CO_2 and CO indicate that the propane is acting as a scavenger of oxygen to form cracked, oxidation products and water. During the decomposition of N_2O, the recombination of oxygen is the rate limiting step, therefore oxygen remains on the surface blocking the active site. The presence of a reductant increases the conversion of N_2O by acting as an oxygen scavenger regenerating the active site.

When the support was calcined before catalyst preparation, and deposited with Pd, the species formed were small Pd nanoparticles. The improvement in conversion of N_2O seen with these catalysts indicates that the small nanoparticles are the active species. When the particle size is controlled, by using a modified impregnation technique, the activity of both the untreated and treated support catalysts is the same. This adds further weight to the hypothesis that the particle size (and subsequently dispersion) control the activity of Pd-Al_2O_3 catalysts for N_2O decomposition.

6.3.2 Future Work

The effect of metal support interaction can be studied further by altering the PZC of a series of reducible and non-reducible supports to measure the interaction of the metal precursor and support. Differing interactions of the metal and support can lead to the formation of different particle size ranges as seen in the discussion of Chapter 4. This can be investigated in different supports to see if a single preparation method that controls particle size can be produced, following on from the work of Regabulto and co-workers.[21] They have determined that, if the pH of the precursor solution is below that of the PZC, the hydroxyl groups are protonated,

and then the surface can absorb anionic metal complexes; above the PZC, the hydroxyl groups are deprotonated and become negatively charged and cations will be strongly absorbed. The increase in difference between the PZC and pH of the precursor solution effects the strength of interaction and subsequently particle size. The production of a preparation technique with strict controls can be used to predict and control particle size. Particle size has shown to be a prevailing factor in catalysis,[22–26] therefore a method that could reliably predict and control the effect of metal precursor and support interaction leading to particle size would be of interest to the entire catalysis field.

In the Chapter there was a lot of discussion about the existence of Cl in the catalysts and the presence of PdCl species that were possibly limiting the activity of the catalysts. One way to investigate this further is to use a chlorine free preparation, which is possible by using Chemical Vapour Impregnation (CVI), where $Pd(acac)_2$ is used as the metal precursors. The support and the precursor are mixed together and heated under vacuum until the precursor ligands sublime and removed, leaving the deposited metal behind. This removes the effect of the Cl^- ions and will give a further understanding of the effect. Another interesting thing about this preparation method is that it is solvent free, meaning the interaction between the metal and the support cannot be hindered by the presence of water species. This is interesting as water is removed during the support calcination, which can be reabsorbed from the solvent, which could mean a better metal support interaction. This is just a hypothesis that needs testing to fully understand, but it would be important to be mindful that there are now two factors at play in this preparation method and they would both need to be investigated thoroughly.

Finally, another avenue of interesting work to investigate would be the effect of alternative reductants. A variety of reductants have been used in literature, such as methane, ethane, propane and CO. [11,27–35] it would be interesting to explore the effect on conversion of N_2O using alternative reductants. For example if methane improves the activity as much as propane then there is scope for removing two greenhouse gases, methane and N_2O in one reaction.

6.4 Perovskites

6.4.1 Conclusions

Perovskites have shown a literature precedent to be used as catalysts for the decomposition of N_2O into nitrogen and oxygen.[36–45] Based on this work, a study was performed by altering the A and B site ratios to in perovskites with the aim of improving purity and surface area, using three different preparation methods, with the effect on surface area and purity noted. By altering the A and B site ratios, it is possible to produce a pure phase perovskite at temperatures lower than the literature norm. When the preparation method was altered, it was noted that the oxygen species differed between methods even though the components were the same. This work has further highlighted the importance of lattice oxygen species and the requirement for a high oxygen mobility in the decomposition of N_2O. The rate limiting step for the decomposition of N_2O is the recombination of absorbed molecular oxygen to form oxygen. The recombination is limited due to the distance between the molecular oxygen species; therefore, highly mobile lattice oxygen is required to bridge these distances and enable recombination and regeneration of the active sites.

In the LSCF catalysts the activity closely follows the trend that the more mobile lattice oxygen is present in the more active the catalyst. The catalyst with the largest response during O_2-TPD, and therefore the more mobile the oxygen, was attained by using citric acid preparation method and resulted in the most active catalyst with a T_{50} of 432 °C. A similar trend was also noted in the PBC series of catalysts, but there was also the factor of oxygen vacancies to compare. More oxygen vacancies lead to a more active catalysts, which illustrates that oxygen vacancies are one of the active sites. The most active catalyst was prepared via the SAS preparation method and achieved a T_{50} of 410 °C, which was the catalysts with the highest amount of mobile lattice oxygen. Compared to literature (Section 5.1, Table 5.1), both these catalysts outperform the most active perovskite for N_2O decomposition, $Pr_{0.2}Ba_{0.8}MnO_3$, which has a T_{50} at 442 °C under similar conditions.[41]

6.4.2 Future Work

Catalyst reducibility has been shown to be a key factor in the decomposition of N_2O by Russo *et al.*[46] Therefore to understand how the perovskite catalysts operate, H_2-TPR should be performed to give an insight to the reducibility of the catalyst. The following mechanism is generally accepted for the decomposition of N_2O into $N_2$and O_2. [46,47]

$$N_2O + * \rightarrow N_2O* \quad (1)$$

$$N_2O* \rightarrow N_2 + O* \quad (2)$$

$$2\,O* \rightarrow O_2 + 2* \quad (3)$$

$$O* + N_2O* \rightarrow O_2 + N_2 + 2* \quad (4)$$

Mechanism 3. Decomposition of N_2O at an oxygen vacancy on the surface of a perovskite. * = O_{vac}

In step 2 of the reaction mechanism, the catalyst becomes oxidised and needs to be able to reduce the active site by removing oxygen that enables the active site to be regenerated and allow further reactions to take place. The reduction process can take place either through step 3, a Langmuir Hinshelwood, or by step 4 an Eley Rideal mechanism. Therefore high reducibility is an advantageous property of the catalyst, H_2-TPR can give an indication of the reducibility of the perovskite. Russo and co-workers tested a $LaCoO_3$ catalyst and stated that the catalyst "exhibited the highest activity as a consequence of its greater capability to be reduced at comparatively low temperature during TPR runs, a key requirement for nitrous oxide catalytic decomposition." [46] Secondly the recombination of oxygen species (the rate limiting step) can also be aided by oxygen mobility. Recombination usually takes place at vacancy sites and lattice oxygen is used to fill these vacancies and aid recombination, hence mobile oxygen is crucial. The study of reduction profiles would easily be able to select an active catalyst for N_2O decomposition.

6.5 Final Comments and Comparisons

Throughout this thesis different reaction conditions have been used meaning that it has not been completely clear which catalysts are the most active. Therefor for clarity, the rate of the most active catalysts in each chapter have been normalised

for comparison (Table 7). As you can see in Table 7 the most active catalyst is the 0.16 wt.% Fe-ZSM-5 (23) catalyst, has a higher rate of reaction, even though this catalysts does not have the highest conversion. This is due to the gas feed containing 5 times the number of moles of N_2O as the other catalysts, and therefore has the opportunity to convert more N_2O. The perovskite catalysts, LCSF Citric and PBC SAS both convert 100 % of the N_2O present, it would be interesting to test these catalysts under a regime whereby they are exposed to more N_2O, as is the case with the Fe-ZSM-5 catalysts. Finally, the Pd-Al_2O_3 catalyst do not show great promise when compared to the other catalysts in this thesis. These catalysts do not convert enough N_2O with out propane present to be deemed active catalysts, but this does change when propane is present and these catalysts would then be in the same ball park as the perovskite catalysts, converting 100 % N_2O at 550 °C.

Table 7. Comparison of most active catalysts in this thesis by a normalised rate.

Catalyst	**Conversion at 550 °C (%)**	**Rate in $mol_{N2O}\ kg_{cat}^{-1}\ h^{-1}$**
0.16 wt.% Fe-ZSM-5 (23)	30	67
2.6 wt.% Pd-Al_2O_3 **4R**	67	28.7
2.6 wt.% Pd-Al_2O_3 5**R**	57	24.4
LSCF Citric	98	43.8
PBC SAS	100	44.6

6.6 References

1 J. Pérez-Ramírez, F. Kapteijn, K. Schöffel and J. A. Moulijn, *Appl. Catal. B Environ.*, 2003, **44**, 117–151.

2 J. Weimann, *Best Pract. Res. Clin. Anaesthesiol.*, 2003, **17**, 47–61.

3 P. Grace and L. Barton, *http://theconversation.com/meet-n2o-the-greenhouse-gas-300-times-worse-than-co2-35204*, 2015-10–29.

4 Intergovernmental Panel on Climate Change, *Climate Change 2007 Synthesis Report*, 2008.

5 R. W. Portmann, J. S. Daniel and a. R. Ravishankara, *Philos. Trans. R. Soc. B*

Biol. Sci., 2012, **367**, 1256–1264.

6 A. R. Ravishankara, J. S. Daniel and R. W. Portmann, *Science*, 2009, **326**, 123–125.

7 M. I. Konsolakis, *ACS Catal.*, 2015, **5**, 6397–6421.

8 M. Rauscher, K. Kesore, R. Mönnig, W. Schwieger, A. Tißler and T. Turek, *Appl. Catal. A Gen.*, 1999, **184**, 249–256.

9 B. M. Abu-Zied, W. Schwieger and A. Unger, *Appl. Catal. B Environ.*, 2008, **84**, 277–288.

10 S. Sklenak, P. C. Andrikopoulos, B. Boekfa, B. Jansang, J. Nováková, L. Benco, T. Bucko, J. Hafner, J. Ddeek and Z. Sobalík, *J. Catal.*, 2010, **272**, 262–274.

11 H. Abdulhamid, E. Fridell and M. Skoglundh, *Top. Catal.*, 2004, **30/31**, 161–168.

12 I. Melián-Cabrera, E. R. H. van Eck, S. Espinosa, S. Siles-Quesada, L. Falco, A. P. M. Kentgens, F. Kapteijn and J. A. Moulijn, *Appl. Catal. B Environ.*, 2017, **203**, 218–226.

13 V. Peneau, R. D. Armstrong, G. Shaw, J. Xu, R. L. Jenkins, D. J. Morgan, N. Dimitratos, S. H. Taylor, H. W. Zanthoff, S. Peitz, G. Stochniol, Q. He, C. J. Kiely and G. J. Hutchings, *ChemCatChem*, 2017, **9**, 642–650.

14 J. H. Park, J. H. Choung, I. S. Nam and S. W. Ham, *Appl. Catal. B Environ.*, 2008, **78**, 342–354.

15 K. Sun, H. Zhang, H. Xia, Y. Lian, Y. Li, Z. Feng, P. Ying and C. Li, *Chem. Commun.*, 2004, **216**, 2480–2481.

16 K. A. Dubkov, N. S. Ovanesyan, A. A. Shteinman, E. V. Starokon and G. I. Panov, *J. Catal.*, 2002, **207**, 341–352.

17 A. Ribera, I. W. C. E. Arends, S. De Vries, J. Pérez-Ramírez and R. A. Sheldon, *J. Catal.*, 2000, **195**, 287–297.

18 G. I. Panov, A. K. Uriarte, M. A. Rodkin and V. I. Sobolev, *Catal. Today*, 1998, **41**, 365–385.

19 Q. Zhu, E. J. Hensen, B. L. Mojet, J. H. van Wolput and R. A. van Santen, *Chem*

Commun, 2002, 1232–1233.

20 J. Park and J. R. Regalbuto, *J. Colloid Interf. Sci.*, 1995, **175**, 239–252.

21 K. P. De Jong, *Synthesis of Solid Catalysts*, Wiley-VCH Verlag GmbH & Co. KGaA, 1st edn., 2009, vol. 39.

22 G. C. Bond, *Surf. Sci.*, 1985, **156**, 966–981.

23 M. Arenz, K. J. J. Mayrhofer, V. Stamenkovic, B. B. Blizanac, T. Tomoyuki, P. N. Ross and N. M. Markovic, *J. Am. Chem. Soc.*, 2005, **127**, 6819–6829.

24 K. J. J. Mayrhofer, B. B. Blizanac, M. Arenz, V. R. Stamenkovic, P. N. Ross and N. M. Markovic, *J. Phys. Chem. B*, 2005, **109**, 14433–14440.

25 G. L. Bezemer, J. H. Bitter, H. P. C. E. Kuipers, H. Oosterbeek, J. E. Holewijn, X. Xu, F. Kapteijn, A. J. Van Diilen and K. P. De Jong, *J. Am. Chem. Soc.*, 2006, **128**, 3956–3964.

26 M. K. Min, J. Cho, K. Cho and H. Kim, *Electrochim. Acta*, 2000, **45**, 4211–4217.

27 H. Ohtsuka, T. Tabata, O. Okada, L. M. F. Sabatino and G. Bellussi, *Catal. Letters*, 1997, **44**, 265–270.

28 H. Ohtsuka, T. Tabata, O. Okada, L. M. . Sabatino and G. Bellussi, *Catal. Today*, 1998, **42**, 45–50.

29 R. W. Van Den Brink, S. Booneveld, M. J. F. M. Verhaak and F. A. De Bruijn, *Catal. Today*, 2002, **75**, 227–232.

30 G. Centi and F. Vazzana, *Catal. Today*, 1999, **53**, 683–693.

31 G. Djéga-Mariadassou, F. Fajardie, J. F. Tempère, J. M. Manoli, O. Touret and G. Blanchard, *J. Mol. Catal. A Chem.*, 2000, **161**, 179–189.

32 L. He, L. C. Wang, H. Sun, J. Ni, Y. Cao, Y. He and K. N. Fan, *Angew. Chemie - Int. Ed.*, 2009, **48**, 9538–9541.

33 K. Teramura, T. Tanaka, H. Ishikawa, Y. Kohno and T. Funabiki, *J. Phys. Chem. B*, 2004, **108**, 346–354.

34 K. Yogo, M. Ihara, I. Terasaki and E. Kikuchi, *Chem. Lett.*, 1993, **22**, 229–232.

35 R. Burch and P. K. Loader, *Appl. Catal. B Environ.*, 1994, **5**, 149–164.

36 H. Tanaka and M. Misono, *Curr. Opin. Solid State Mater. Sci.*, 2001, **5**, 381–387.

37 L. Marchetti and L. Forni, *Appl. Catal. B Environ.*, 1998, **15**, 179–187.

38 R. J. H. Voorhoeve, J. P. Remeika and L. E. Trimble, *Ann. N. Y. Acad. Sci.*, 1976, **272**, 3–21.

39 J. Il Jung, H. Y. Jeong, J. S. Lee, M. G. Kim and J. Cho, *Angew. Chemie - Int. Ed.*, 2014, **53**, 4582–4586.

40 N. Russo, D. Mescia, D. Fino, G. Saracco and V. Specchia, *Ind. Eng. Chem. Res.*, 2007, **46**, 4226–4231.

41 S. Kumar, A. Vinu, J. Subrt, S. Bakardjieva, S. Rayalu, Y. Teraoka and N. Labhsetwar, *Catal. Today*, 2012, **198**, 125–132.

42 T. Ishihara, M. Ando, K. Sada, K. Takiishi, K. Yamada, H. Nishiguchi and Y. Takita, *J. Catal.*, 2003, **220**, 104–114.

43 D. V. Ivanov, E. M. Sadovskaya, L. G. Pinaeva and L. A. Isupova, *J. Catal.*, 2009, **267**, 5–13.

44 D. V. Ivanov, L. G. Pinaeva, L. A. Isupova, A. N. Nadeev, I. P. Prosvirin and L. S. Dovlitova, *Catal. Letters*, 2011, **141**, 322–331.

45 D. V. Ivanov, L. G. Pinaeva, L. A. Isupova, E. M. Sadovskaya, I. P. Prosvirin, E. Y. Gerasimov and I. S. Yakovleva, *Appl. Catal. A Gen.*, 2013, **457**, 42–51.

46 N. Russo, D. Mescia, D. Fino, G. Saracco and V. Specchia, *Ind. Eng. Chem. Res.*, 2007, **46**, 4226–4231.

47 F. Kapteijn, J. Rodriguez-Mirasol and J. A. Moulijn, *Appl. Catal. B Environ.*, 1996, **9**, 25–64.